TESE DE DOUTORAMENTO

NANOSIZED METALLIC OXIDES GOVERNING THE CHEMICAL AND BIOCHEMICAL OXIDATION OF POLLUTANTS PRESENT IN WASTEWATER

María Gamallo Mirón

ESCOLA DE DOUTORAMENTO INTERNACIONAL

PROGRAMA DE DOUTORAMENTO EN ENXEÑARÍA QUÍMICA E AMBIENTAL

SANTIAGO DE COMPOSTELA

2020

DECLARACIÓN DEL AUTOR/A DE LA TESIS

Nanosized metallic oxides governing the chemical and biochemical oxidation of pollutants present in wastewater

Para defensas telemáticas

Dna. María Gamallo Mirón

Presento mi tesis, siguiendo el procedimiento adecuado al Reglamento y declaro que:

1) La tesis abarca los resultados de la elaboración de mi trabajo.
2) De ser el caso, en la tesis se hace referencia a las colaboraciones que tuvo este trabajo.
3) La tesis es la versión definitiva presentada para su defensa y coincide con la enviada en formato electrónico.
4) Confirmo que la tesis no incurre en ningún tipo de plagio de otros autores ni de trabajos presentados por mi para la obtención de otros títulos.

Y me comprometo a presentar el ejemplar impreso de la tesis en el plazo de un mes desde que la EDIUS me lo requiera, así como del Compromiso Documental de Supervisión en el caso que el original no esté depositado en la Escuela.

En Santiago de Compostela, 30 de julio de 2020.

Asdo. María Gamallo Mirón

AUTORIZACIÓN DEL DIRECTOR / TUTOR DE LA TESIS

Nanosized metallic oxides governing the chemical and biochemical oxidation of pollutants present in wastewater

Dna. María Teresa Moreira Vilar, Catedrática de Enxeñaría Química e D. Gumersindo Feijoo Costa, Catedrático de Enxeñaría Química

INFORMA/N:

Que la presente tesis, corresponde con el trabajo realizado por Dña. ***María Gamallo Mirón****, bajo mi dirección, y autorizo su presentación, considerando que reúne los requisitos exigidos en el Reglamento de Estudios de Doctorado de la USC, y que como los directores de ésta no incurren en las causas de abstención establecidas en Ley 40/2015.*

En Santiago de Compostela, 29 de julio de 2020.

Asdo. María Teresa Moreira *Asdo. Gumersindo Feijoo Costa*

TABLE OF CONTENTS

ABBREVIATIONS AND ACRONYMS

ABTS	2,2'-azinobis-3-ethylbenzothiazoline-6-sulfonate
can	acetonitrile
AH_2	ascorbic acid
AOP	advanced oxidation process
APTES	(3-aminopropyl) triethoxysilane
ARB	antibiotic-resistant bacteria
ARG	antibiotic-resistant gen
A_0	unit cell parameter
BPA	bisphenol A
BQ	benzoquinone
CB	conduction band
CBZ	carbamazepine
CCD	central composite design
CdS	cadmium sulfide
CLD	chemiluminescence detector
CLEA	cross-linked enzyme aggregate
CMC	carboxymethyl cellulose
cNF	chitosan-based nanofiber
COD	chemical oxygen demand
DEG	diethylene glycol
DMP	2,6-dimethoxyphenol
DMSO	dimethyl sulfoxide
DNA	deoxyribonucleic acid
E_0	redox potential
E1	estrone
E2	17β-estradiol
e^-	electron

EC	European Commission
EDS	energy dispersive X-ray detector
EDC	endocrine disrupting compounds
EE2	17α-ethinylestradiol
EL	enzyme loading
EQS	Environmental Quality Standards
EU	European Union
FAAS	flame atomic absorption spectroscopy
FAS	ferrous ammonium sulphate
Fe^{2+}	ferrous iron
Fe^{3+}	ferric iron
Fe_2O_3	ferric oxide
Fe_3O_4	magnetite
fsMP	fumed silica microparticle
fsNP	fumed silica nanoparticle
h^+	electron hole
HAADF-STEM	field-scanning transmission electron micrographs
H_2O_2	hydrogen peroxide
$HO_2\cdot$	hydroperoxyl radical
HPLC	high performance liquid chromatography
h_{vb}^+	valence band holes
IBP	ibuprofen
ICG	ion chromatography
IC	inorganic carbon
ICP-OES	inductively coupled plasma-optical emission spectrometry
IY	immobilization yield
JCPDS	Joint committee on powder diffraction standards
K_{ads}	adsorption constant
K_M	Michaelis-Menten constant
KI	potassium iodide
K_{obs}	pseudo-first-order kinetic rate constants

LiP	lignin peroxidase
MeOH	methanol
MG	Methyl Green
MMCRC	mesoporous magnetite/carboxylate-rich carbon
MnP	manganese peroxidase
Mt	*Myceliophthora thermophila*
MR	Methyl Red
MSFBR	magnetically stabilized fluidized bed reactors
Mw	molecular weight
NaN_3	sodium azide
NC	nanocomposite
NDIR	non-dispersive infrared
NdFeB	neodymium-iron-boron
NO	nitric oxide
NP	nanoparticle
NSAID	non-steroidal anti-inflammatory drug
O_2	molecular oxygen
$^1O_2$	singlet oxygen
$O_2^{\cdot-}$	superoxide radicals
O_3	ozone
OD	optical density
OII	Orange II
OMP	organic micropollutant
PAH	polycyclic aromatic hydrocarbon
PANI	polyaniline
PAP	polyaspartate
PEI	polyethylenimine
pK_a	negative logarithm of the acid dissociation constant (K_a)
PLC	programmable logic controller
PPCP	pharmaceutical and personal care product
PPMS	physical property measurement system

PS_{DFT}	pore size by NLDFT method
PYR	pyrene
PZC	point of zero-charge
RB19	Reactive Blue 19
RhB	Rhodamine B
ROS	reactive oxygen species
R123	Rhodamine 123
R^2	correlation coefficient
SAI	sorption-assisted immobilization
Si	silicon
SBA	mesoporous silica
S_{BET}	surface area obtained by BET multipoint analysis
SBR	sequential batch reactor
SEM	scanning electron microscopy
SMX	sulfamethoxazole
SRM	surface response methodology
SnO_2	tin (IV) oxide
SPR	surface plasmon resonance
TAE	tris-acetate-EDTA buffer
TC	total carbon
TCE	trichloroethene
TEM	transmission electron microscopy
TEOS	tetraethyl orthosilicate
TGA	thermogravimetric analysis
TiO_2	titanium dioxide
TMAOH	tetramethylammonium hydroxide solution
TN	total nitrogen
TOC	total organic carbon
TSS	total suspended solids
Tv	*Trametes versicolor*
t_{wall}	wall thickness

$t_{1/2}$	half-life time
UV	ultraviolet
UVP	ultraviolet Pen-Ray® lamp
V_0	volume of sample
VB	valence band
V_{max}	maximum reaction velocity
VP	versatile peroxidase
V_P	pores volume
VSM	vibrating sample magnetometer
VSS	volatile suspended solid
WFD	Water framework directive
W_{Fe}	iron weight
WL	washing loss
WWTP	wastewater treatment plant
XRD	X-ray diffraction
XTT	sodium salt-based cell proliferation colorimetric assay
ZnO	zinc oxide
ZnS	zinc sulfide

USC
UNIVERSIDADE
DE SANTIAGO
DE COMPOSTELA

RESUMEN EXTENDIDO

En un contexto global, la creciente industrialización de la sociedad hace que cada día cobre una mayor importancia el tratamiento y eliminación de los residuos industriales. Entre las industrias que generan los efluentes más contaminantes se encuentran la industria papelera, textil, de refinería, de curtiduría y farmacéutica, entre otras (Rodríguez 2012). Los compuestos recalcitrantes, como los productos farmacéuticos, los productos de cuidado personal, tensioactivos, productos químicos industriales, tintes, etc., presentes en el agua constituyen un grave peligro incluso a bajas concentraciones, causando problemas para la salud humana y el medio ambiente (Maszenan et al. 2011, Mascolo et al. 2010, Kiatkittipong and Assabumrungrat 2017).

Las etapas convencionales de tratamiento primarios basados en procesos de coagulación-floculación y secundarios en sistemas biológicos aerobios y anaerobios en plantas de tratamiento de aguas residuales (EDAR) eliminan parcialmente este tipo de contaminantes. En consecuencia, cuando se trata de implementar un sistema de tratamiento para contaminantes recalcitrantes, el enfoque de tratamiento terciario sigue siendo el más recomendado, una vez que se han eliminado los sólidos, la materia orgánica y los nutrientes en las etapas previas. Las tecnologías existentes para el tratamiento terciario en las EDAR dependen principalmente del uso de membranas, ozonización o desinfección, utilizando luz ultravioleta (UV). Los nuevos procesos terciarios están todavía en desarrollo y tienen que proporcionar evidencia de una eliminación eficiente de los contaminantes sin que suponga costes altos de inversión ni de operación.

En este marco, los procesos de oxidación avanzada basados en procesos físico-químicos capaces de producir cambios profundos en la estructura química de los contaminantes presentes en matrices acuosas se han consolidado como una tecnología versátil y eficaz para el tratamiento de aguas contaminadas y la eliminación de compuestos químicos, incluyendo orgánicos, inorgánicos y metales pesados, y microorganismos patógenos (Carmona 2008). Algunas de las tecnologías de oxidación para la eliminación de sustancias tóxicas presentes en el agua que más han destacado en los últimos años son tanto procesos biológicos mediante el uso de enzimas oxidativas como procesos de oxidación Fenton y UV mediante el uso de

catalizadores sólidos. Esto es, en el caso de la reacción Fenton convencional, o también denominado Fenton homogéneo, el peróxido de hidrógeno (H_2O_2) reacciona con los iones de Fe(II) en disolución, produciendo radicales hidroxilo (·OH), generalmente a valores de pH cercanos a 3 (Garrido-Ramírez et al. 2010). Estos radicales ·OH, con un alto potencial de oxidación, son capaces de oxidar o incluso mineralizar una gran selección de compuestos recalcitrantes. Sin embargo, la aplicación del proceso Fenton convencional para el tratamiento de efluentes reales presenta una serie de limitaciones, principalmente debido a la necesidad de eliminar los iones de hierro disueltos en el efluente (Huang et al. 2012, Ratanatamskul et al. 2011). Una alternativa para resolver este problema es el uso de catalizadores sólidos, tanto en el caso de Fenton como en otros procesos de oxidación avanzada, de forma que puedan recuperarse una vez finalizado el tratamiento. Este tipo de proceso se conoce como proceso heterogéneo (Zazo et al. 2006). El uso de este tipo de catalizadores permite aumentar el área superficial de las especies metálicas proporcionando una buena dispersión de las partículas dentro de la matriz a tratar, mejorando a su vez la estabilidad del catalizador.

Existe un amplio espectro de materiales que han sido probados como catalizadores o como soportes durante los procesos de oxidación. En este sentido, el auge de la nanotecnología ha estimulado un fuerte interés por las propiedades de las nanopartículas (NP), con tamaño característico entre 10 y 100 nm, una gran área superficial y una alta reactividad química, características que les confieren cualidades ideales para ser utilizadas en procesos catalíticos.

Existen varias referencias sobre el uso de diferentes tipos de NPs como catalizadores o soportes (Zhang et al. 2017, Fida et al. 2017, Singh et al. 2016). Sin embargo, su aplicación en el proceso de tratamiento de efluentes debe asegurar su completa retención en el sistema, típicamente mediante membranas de nanofiltración. La posibilidad de sintetizar las NPs mencionadas anteriormente sobre un soporte de magnetita simplificaría en gran medida su uso, ya que podrían separarse aplicando un campo magnético (Zhang et al. 2008, Cleveland et al. 2014).

Además, el uso de nanopartículas magnéticas presenta una buena compatibilidad con el medio ambiente, ya que prolonga, a través de los sucesivos ciclos de recuperación, la vida útil del catalizador. Por lo tanto, para el caso del proceso Fenton, el uso de nanopartículas de hierro magnéticas, en las que se

sustituye el uso de iones Fe(II) disueltos, surge como una tecnología muy prometedora para el tratamiento de efluentes contaminados (Sun et al. 2009, He et al. 2016).

En vista de los buenos resultados obtenidos para la eliminación de diferentes compuestos mediante diferentes procesos de oxidación avanzada, el uso de nanopartículas magnéticas, con diferentes características y funcionalizaciones, puede considerarse el punto de partida para el desarrollo y uso de reactores magnéticos. Apenas hay información en la literatura sobre el diseño o el funcionamiento de los reactores en los que no es necesario el uso de sistemas de electroimanes para la separación de las partículas magnéticas. Este tipo de reactor se denomina reactor de lecho fluidizado estabilizado magnéticamente (MSFBR) y requiere una fuente de alimentación de corriente eléctrica, lo que aumenta considerablemente los costes de operación del sistema (Arivizhivendhan et al. 2016, Chen et al. 2017). Además, este campo magnético proporcionado por electroimanes permite la separación magnética de micropartículas, si bien se requiere un campo magnético más fuerte para las nanopartículas magnéticas (Tang and Lo 2013). En ninguno de estos trabajos se propone un dispositivo automatizado que permita la separación de las nanopartículas para su aplicación en ciclos sucesivos. Con el objetivo de solucionar este inconveniente, el desarrollo de sistemas automatizados para llevar a cabo la separación de los catalizadores es uno de los principales retos a conseguir durante el desarrollo de la presente tesis doctoral.

Por tanto, el objetivo principal de este trabajo es el desarrollo e implementación de diferentes tecnologías viables para la eliminación de compuestos recalcitrantes procedentes de aguas residuales basadas en la catálisis química soportada en nanopartículas magnéticas. Se han investigado diferentes enfoques y materiales para el tratamiento de aguas residuales, desde perspectivas más consolidadas hasta el uso de nanomateriales en función de los requisitos de la aplicación. Los materiales a nanoescala pueden diseñarse mediante síntesis controlada y selectiva, con propiedades físicas y químicas mejoradas y ajustables (Jeevanandam et al. 2018).

La combinación de diferentes materiales como compuestos híbridos, que cumplen con las propiedades específicas deseadas de cada uno de sus componentes, puede representar un tipo de nanomaterial potencialmente más eficiente, selectivo

y estable, en comparación con los métodos basados en un solo tipo de nanopartícula. Las nanopartículas utilizadas para el tratamiento de aguas residuales se pueden clasificar según su mecanismo de acción como nanoadsorbentes y nanomateriales reactivos, que actúan a través de reacciones químicas como ácido-base, redox, precipitación, catálisis y fotocatálisis o como soportes (García-Morales et al. 2018, Bao et al. 2017). El uso de este tipo de materiales debe enfrentar a varios retos fundamentales, como la alta capacidad de transformación/eliminación de los compuestos objetivo, coste aceptable, facilidad de síntesis desde una perspectiva de química verde, no toxicidad, biodegradabilidad, reciclabilidad y el potencial de recuperación después del uso (regeneración).

El estudio de los posibles riesgos ecológicos derivados de la liberación de nanomateriales en el medio ambiente es un área de investigación necesaria y complementaria en la perspectiva de la aplicación de estos procesos a gran escala. En este sentido, uno de los métodos más novedosos para estimar el posible impacto que las propiedades fisicoquímicas de estos nanocatalizadores pueden causar después de la exposición directa con una solución específica de ADN es un ensayo *in vitro* capaz de medir la degradación de ADN mediante electroforesis (Rivero et al. 2005). Otro método utilizado es la evaluación de la citotoxicidad, en la que se lleva a cabo la determinación del número de células vivas tras su exposición a posibles agentes tóxicos mediante el ensayo colorimétrico XTT (Roehm et al. 1991, Janus et al. 2019).

Para alcanzar el objetivo global de esta tesis, se definieron los siguientes objetivos específicos:

- Estudio de la transformación de compuestos recalcitrantes presentes en agua con el fin de explicar su comportamiento durante la etapa de eliminación mediante tratamientos de oxidación avanzados.
- Evaluación de diferentes procesos de oxidación avanzada basados en el uso de nano y micromateriales.
- Operación de diferentes configuraciones de reactores con unidades de separación magnética.

- Evaluación de la toxicidad asociada al uso de catalizadores sólidos en los procesos de oxidación avanzada para el tratamiento de aguas contaminadas.

En el Capítulo 3 se evaluaron nano y micropartículas de sílice (fsNP y fsMP) y nanofibras de quitosano (cNF) como soportes para la inmovilización de dos enzimas producidas por hongos ligninolíticos, en concreto, hongos de podredumbre blanca: lacasa de *Myceliophthora thermophila* (*Mt*) y *Trametes versicolor* (*Tv*) y la enzima Peroxidasa Versátil (VP) de *Bjerkandera* sp. (anamorfo R1). Una vez obtenido los diferentes biocatalizadores enzimáticos, se procedió a la caracterización de las enzimas inmovilizadas y a la evaluación de sus potenciales de oxidación frente a dos compuestos modelo: un colorante catiónico Verde de Metilo (MG) y un colorante aniónico Azul Reactivo 19 (RB19). Los materiales considerados como soporte mostraron una excelente biocompatibilidad con las enzimas, de modo que los bioconjugados obtenidos después de la inmovilización mostraron una mayor tolerancia a las variaciones de pH y temperatura, así como una mayor estabilidad operativa y de almacenamiento en comparación con la enzima libre. La mejora de las propiedades de las enzimas inmovilizadas se hizo evidente incluso en presencia de disolventes orgánicos e inhibidores de enzimas. Una vez seleccionado el biocatalizador más adecuado, se investigó su aplicación en una configuración de reactor enzimático de membrana que funciona en modo secuencial para la eliminación de diferentes compuestos recalcitrantes como Bisfenol A (BPA) y Estrona (E1), 17β-estradiol (E2) y 17α-etinilestradiol (EE2) y se llevó a cabo la eliminación eficaz del BPA durante varios ciclos de operación del reactor.

En el Capítulo 4 se explora el uso de diferentes agentes estabilizadores de nanopartículas de magnéticas (mNPs), incluyendo el ácido poliacrílico (PAA), polietilenimina (PEI) y SiO_2, con el objetivo principal de seleccionar el catalizador óptimo para su aplicación en el proceso de oxidación avanzada Fenton, utilizando el tinte RB19 como compuesto recalcitrante modelo. La influencia de las principales variables operacionales, como las concentraciones de mNPs y de peróxido de hidrógeno (H_2O_2), se evaluaron utilizando la Metodología de Superficie de Respuesta (SRM) según un diseño compuesto central, con el fin de optimizar las condiciones de degradación de RB19 con el nanocatalizador óptimo previamente seleccionado. Además, se lleva a cabo un estudio para eliminar el colorante modelo mediante el uso del catalizador inmovilizado en el material mesoporoso SBA-15. Finalmente, se

evalúa el catalizador de mayor potencial en la degradación de los estrógenos naturales E1, E2 y los estrógenos sintéticos EE2, BPA, el antibiótico sulfametoxazol (SMX) y el pireno (PYR). Sobre la base de los resultados de decoloración de RB19, se demostró que la estabilización de nanocatalizadores desempeña un papel crucial durante su aplicación en el proceso de oxidación Fenton. Las mNP recubiertas por PAA mostraron una buena estabilidad estructural y pueden separarse fácil y rápidamente mediante la aplicación de un campo magnético. Además, la inmovilización de estos mNP estabilizados con PAA en una matriz de sílice mesoporosa SBA-15 confiere al nanocatalizador excelentes propiedades como catalizador para los procesos Fenton, ya que logran una alta eficiencia en la eliminación de los contaminantes orgánicos a través de la recuperación y reutilización completa de nanocatalizadores.

El capítulo 5 tiene como objetivo dar un paso adelante en la aplicación de nanopartículas magnéticas mediante el uso de fotocatalizadores formulados como nanocompuestos (NC) para llevar a cabo la degradación de diferentes contaminantes, desde disruptores endocrinos como los ya utilizados BPA, E1, E2 y EE2 hasta diferentes colorantes, elegidos como modelos de contaminantes orgánicos. En este sentido, la excelente capacidad de los radicales ·OH de oxidar compuestos orgánicos sugiere también la utilidad de explorar su generación fotoquímica. La fotocatálisis heterogénea es un proceso basado en la absorción directa o indirecta de energía radiante (visible o UV) por un sólido (el fotocatalizador heterogéneo que normalmente es un semiconductor de banda ancha). Las reacciones fotocatalíticas en los materiales semiconductores se producen mediante la promoción de un electrón desde la banda de valencia (VB) a la banda de conducción (CB). La energía mínima necesaria para que se produzca esta promoción la proporcionan los fotones que inciden en la superficie de la fotocatálisis y se denomina "band gap". Esto crea un par electrón-agujero que promueve la formación de las especies reactivas mediante reacciones de reducción y oxidación respectivamente.

El sistema fotocatalítico heterogéneo que se plantea en este capítulo utiliza como fotocatalizadores nanopartículas de óxido de titanio (TiO_2) y de óxido de zinc (ZnO) en combinación con nanopartículas de magnetita, lo que facilita su recuperación y reutilización en ciclos de degradación consecutivos de los contaminantes presentes en matrices acuosas. El fotocatalizador de TiO_2 es el más

empleado a nivel industrial, sin embargo, el ZnO posee unas características similares y es más barato, lo que lo convierte en un catalizador óptimo para aplicaciones industriales a gran escala. Sin embargo, la inmovilización de estos materiales semiconductores sobre soportes sólidos magnéticos reduce la actividad del catalizador y disminuye el rendimiento de eliminación de microcontaminantes. Durante el desarrollo de este estudio se evaluaron diferentes condiciones experimentales, estudiando además el potencial de reutilización de los diferentes fotocatalizadores y comparando el proceso de fotocatálisis con el proceso de oxidación de Fenton heterogéneo estudiado previamente en el Capítulo 4.

En el capítulo 6 se avanzará en el desarrollo de reactores bajo diferentes configuraciones, con el objetivo de integrar la etapa de reacción con la etapa de separación magnética que asegura la retención del catalizador en el sistema. Para ello, se han evaluado diferentes configuraciones de dispositivos de separación magnética, desde una unidad de separación interna hasta dos sistemas externos diferentes, comparando los principales parámetros operacionales que influyen en el funcionamiento del reactor, tales como la tasa de eliminación de los contaminantes persistentes objetivo y la eficiencia de retención del catalizador dentro del sistema para la eliminación del colorante RB19 como modelo recalcitrante mediante el proceso de oxidación heterogénea Fenton.

Se operó la configuración óptima para la eliminación simultánea de una amplia gama de compuestos recalcitrantes presentes en el efluente de un reactor biológico de una EDAR, proporcionando una combinación efectiva de unidades de reacción y separación. Además, se evaluó la configuración de un fotorreactor sobre la base de la configuración óptima utilizada anteriormente para su funcionamiento con una etapa de luz ultravioleta externa. La eficiencia de la eliminación fotoquímica de compuestos orgánicos puede alterarse drásticamente en función del diseño del reactor (tipo de lámpara, geometría o hidrodinámica), lo cual repercute de manera directa en el consumo de energía eléctrica y por tanto, en los costes de operación.

Por último, en el capítulo 7 del presente trabajo se comparan diferentes nanocatalizadores basados en magnetita, previamente estudiados en los Capítulos 4 y 5, con el fin de investigar el impacto que las propiedades fisicoquímicas de estos nanocatalizadores pueden causar después de su liberación al medio ambiente y que pueden causar daños tanto ecológicos como en los seres humanos directamente en

una amplia gama de concentraciones. Para ello, se realiza en primer lugar un estudio *in vitro* de genotoxicidad para determinar la degradación del ADN mediante ensayos de electroforesis. Este estudio genotóxico consiste en la exposición directa de los nanomateriales utilizados a lo largo de esta tesis con una solución de ADN, y así estimar los efectos pro-oxidantes de estos materiales o el posible efecto que pueden tener los agentes estabilizadores presentes en la superficie de las diferentes NPs en las cadenas de ADN. Posteriormente, se realizan también ensayos de citotoxicidad con el objetivo principal de analizar, en un segundo nivel de toxicidad, el impacto de los mismos nanomateriales en la función de las células mitocondriales de dos líneas celulares humanas diferentes (HaCaT y Caco2), ya sea mediante su acumulación o mediante su penetración directa en la membrana celular.

Por lo tanto, este trabajo contribuye a la comprensión de los posibles efectos sobre la genotoxicidad y la citotoxicidad de diferentes catalizadores nanoestructurados basados en magnetita a diferentes concentraciones. Además, subraya la importancia de seguir investigando los mecanismos y factores que afectan e influyen en la toxicidad de los catalizadores sólidos aplicados en los procesos de oxidación avanzada para garantizar una mejor utilización de los nanomateriales y aumentar la conciencia con su correcta utilización en diferentes aplicaciones ambientales.

En resumen, esta tesis contribuye a ampliar los conocimientos actuales sobre la eficacia de diversas tecnologías de postratamiento para la eliminación de compuestos persistentes presentes en los efluentes líquidos mediante el enfoque de la utilización de la nanotecnología, identificando diferentes estrategias para mejorar la eliminación de esos compuestos. Además, se analiza la influencia de los factores operacionales no sólo con el propósito de maximizar la eficacia de estas tecnologías para eliminar los compuestos objetivo, sino también con el objetivo de garantizar la máxima retención de los nanocatalizadores en el sistema de reacción mediante tecnologías económicamente competitivas y sencillas, tratando de responder a la creciente demanda ambiental de descontaminación de las aguas residuales de origen tanto urbano como industrial.

Bibliografía

Arivizhivendhan, K., Mahesh, M., Boopathy, R. and Sekaran, G. (2016) A novel method for the extraction of prodigiosin from bacterial fermenter integrated with sequential batch extraction reactor using magnetic iron oxide. Process Biochemistry 51(10), 1731-1737.

Bao, S., Li, K., Ning, P., Peng, J., Jin, X. and Tang, L. (2017) Highly effective removal of mercury and lead ions from wastewater by mercaptoamine-functionalised silica-coated magnetic nano-adsorbents: behaviours and mechanisms. Applied Surface Science 393, 457-466.

Carmona, P.B. (2008) Tratamiento de aguas residuales de la industria cosmética mediante el proceso Fenton y con el sistema Fe/g-Al_2O_3/H_2O_2, Universidad Autónoma de Madrid.

Chen, G., Liu, J., Yao, J., Qi, Y. and Yan, B. (2017) Biodiesel production from waste cooking oil in a magnetically fluidized bed reactor using whole-cell biocatalysts. Energy Conversion and Management 138, 556-564.

Cleveland, V., Bingham, J.-P. and Kan, E. (2014) Heterogeneous Fenton degradation of bisphenol A by carbon nanotube-supported Fe3O4. Separation and Purification Technology 133, 388-395.

Fida, H., Zhang, G., Guo, S. and Naeem, A. (2017) Heterogeneous Fenton degradation of organic dyes in batch and fixed bed using La-Fe montmorillonite as catalyst. Journal of Colloid and Interface Science 490, 859-868.

García-Morales, R., García-García, A., Orona-Navar, C., Osma, J.F., Nigam, K. and Ornelas-Soto, N. (2018) Biotransformation of emerging pollutants in groundwater by laccase from P. sanguineus CS43 immobilized onto titania nanoparticles. Journal of Environmental Chemical Engineering 6(1), 710-717.

Garrido-Ramírez, E., Theng, B. and Mora, M. (2010) Clays and oxide minerals as catalysts and nanocatalysts in Fenton-like reactions-a review. Applied Clay Science 47(3-4), 182-192.

He, J., Yang, X., Men, B. and Wang, D. (2016) Interfacial mechanisms of heterogeneous Fenton reactions catalyzed by iron-based materials: A review. Journal of Environmental Sciences 39, 97-109.

Huang, R., Fang, Z., Yan, X. and Cheng, W. (2012) Heterogeneous sono-Fenton catalytic degradation of bisphenol A by Fe_3O_4 magnetic nanoparticles under neutral condition. Chemical Engineering Journal 197, 242-249.

Janus, Ł., Piątkowski, M., Radwan-Pragłowska, J., Bogdał, D. and Matysek, D. (2019) Chitosan-based carbon quantum dots for biomedical applications: synthesis and characterization. Nanomaterials 9(2), 274.

Jeevanandam, J., Barhoum, A., Chan, Y.S., Dufresne, A. and Danquah, M.K. (2018) Review on nanoparticles and nanostructured materials: history, sources, toxicity and regulations. Beilstein Journal of Nanotechnology 9(1), 1050-1074.

Kiatkittipong, K. and Assabumrungrat, S. (2017) A comparative study of sodium/hydrogen titanate nanotubes/nanoribbons on destruction of recalcitrant compounds and sedimentation. Journal of Cleaner Production 148, 905-914.

Mascolo, G., Balest, L., Cassano, D., Laera, G., Lopez, A., Pollice, A. and Salerno, C. (2010) Biodegradability of pharmaceutical industrial wastewater and formation of recalcitrant organic compounds during aerobic biological treatment. Bioresource Technology 101(8), 2585-2591.

Maszenan, A., Liu, Y. and Ng, W.J. (2011) Bioremediation of wastewaters with recalcitrant organic compounds and metals by aerobic granules. Biotechnology Advances 29(1), 111-123.

Ratanatamskul, C., Narkwittaya, S., Masomboon, N. and Lu, M.C. (2011) Effect of carrier composition on 2, 6-dimethylaniline degradation in aqueous solution by fluidized-bed Fenton process. Environmental Technology 32(11), 1233-1237.

Rivero, D., Pérez-Magariño, S., González-Sanjosé, M.L., Valls-Belles, V., Codoñer, P. and Muñiz, P. (2005) Inhibition of induced DNA oxidative damage by beers: Correlation with the content of polyphenols and melanoidins. Journal of Agricultural and Food Chemistry 53(9), 3637-3642.

Rodríguez, G.P. (2012) Intensificación del Proceso Fenton para el tratamiento de aguas residuales industriales, Universidad Autónoma de Madrid.

Roehm, N.W., Rodgers, G.H., Hatfield, S.M. and Glasebrook, A.L. (1991) An improved colorimetric assay for cell proliferation and viability utilizing the tetrazolium salt XTT. Journal of Immunological Methods 142(2), 257-265.

Singh, L., Rekha, P. and Chand, S. (2016) Cu-impregnated zeolite Y as highly active and stable heterogeneous Fenton-like catalyst for degradation of Congo red dye. Separation and Purification Technology 170, 321-336.

Sun, X., Zheng, C., Zhang, F., Yang, Y., Wu, G., Yu, A. and Guan, N. (2009) Size-controlled synthesis of magnetite (Fe_3O_4) nanoparticles coated with glucose and gluconic acid from a single Fe (III) precursor by a sucrose bifunctional hydrothermal method. The Journal of Physical Chemistry C 113(36), 16002-16008.

Tang, S.C. and Lo, I.M. (2013) Magnetic nanoparticles: essential factors for sustainable environmental applications. Water research 47(8), 2613-2632.

Zazo, J., Casas, J., Mohedano, A. and Rodríguez, J. (2006) Catalytic wet peroxide oxidation of phenol with a Fe/active carbon catalyst. Applied Catalysis B: Environmental 65(3-4), 261-268.

Zhang, J., Zhuang, J., Gao, L., Zhang, Y., Gu, N., Feng, J., Yang, D., Zhu, J. and Yan, X. (2008) Decomposing phenol by the hidden talent of ferromagnetic nanoparticles. Chemosphere 73(9), 1524-1528.

Zhang, N., Huang, Y., Zong, M., Ding, X., Li, S. and Wang, M. (2017) Synthesis of ZnS quantum dots and $CoFe_2O_4$ nanoparticles co-loaded with graphene nanosheets as an efficient broad band EM wave absorber. Chemical Engineering Journal 308, 214-221.

1. Chapter 1

GENERAL INTRODUCTION

OUTLINE

1.1 Wastewater management: a challenge for technology developers

Pressures such as water scarcity, increasingly stringent regulations, aging infrastructure, the prospect of climate change, volatility of energy prices, the need to engage with local communities and governments in promoting circular economy, among others, have a major role to play in the wastewater treatment sector, which is undergoing a transformational evolution in order to address existing and future challenges effectively and innovatively. Over the recent years, different wastewater management policies have been defined. Based on the 2030 Agenda for Sustainable Development, adopted by the Member States of the United Nations in 2015, one of the objectives is "Ensure the availability and sustainable management of water and sanitation for all" (UNICEF 2017). Moreover, the removal of organic micropollutants (OMPs) and the recovery of resources for reuse are key challenges in the water cycle management (WWAP 2017).

The presence of OMPs in aquatic environments has become an issue of growing concern due to their potential adverse effects on humans and natural ecosystems (McCallum et al. 2017). These compounds have been detected in the environment at trace level concentrations ranging from ng L^{-1} to µg L^{-1}. OMPs are released into the environment through a variety of sources, mainly agriculture, industry, hospitals and domestic residues, and may include a vast series of chemically different compounds, such as pharmaceuticals and personal care products (PPCPs), pesticides, illicit drugs, hormones, polycyclic aromatic hydrocarbons (PAHs) and household and industrial chemicals (Barbosa et al. 2016, Murray et al. 2010, Siddique et al. 2014). Additionally, these compounds can be classified as well-known regulated contaminants (e.g., PAHs, industrial compounds and pesticides) and chemicals of emerging concern with scarce regulation (e.g., pharmaceuticals and personal care products).

The Water Framework Directive (WFD) 2000/60/EC defined "Strategies against pollution in water" and Directives 2008/105/EC and 2013/39/EU establish Priority Lists of substances of special concern as well as a Watch List (WL) in order to monitor and gather information on the potential risks of OMPs for the aquatic environment. The WL is a list of potential water pollutants that European Union (EU) Member States must carefully monitor to determine the risk they pose to the aquatic

environment and whether EU Environmental Quality Standards (EQS) should be established for them.

Currently, the presence of emerging pollutants in aquatic environments has already been considered by the Commission Implementing Decision (EU) 2018/840 establishing a WL of substances for Union-wide monitoring in the field of water policy in accordance with Directive 2008/105/EC of the European Parliament and of the Council and repealing Commission Implementing Decision (EU) 2015/495. It included ten substances or groups of substances: one synthetic and two natural hormones, three antibiotics, two herbicides and two pesticides. Despite these efforts, the number of emerging pollutants is steadily increasing as industries develop, and it is therefore necessary to update frequently the legislation on OMPs to guarantee human and environmental health.

The presence of these OMPs in the influents of the wastewater treatment plants (WWTPs) is a major challenge. Since conventional treatments such as coagulation, flocculation, sedimentation or filtration in WWTPs are not designed to remove them, these pollutants may persist in the effluent and be released into receiving waters as trace pollutants (Kolpin et al. 2002, Lapworth et al. 2012). Recent studies noted that this type of facilities is the main responsible for the presence of OMPs in the aquatic environment (Kosma et al. 2014, Tijani et al. 2013). A large number of chemical compounds have been detected in WWTP effluents in a wide range of concentrations. Certain active endocrine compounds such as pesticides, halogenated and aromatic compounds, alkyl phenols, phthalates, preservatives, natural and synthetic steroids, etc., can be determined and alter the hormonal and homeostatic systems of the organisms causing disturbance in the reproduction of humans and wildlife (Colborn et al. 1993, Diamanti-Kandarakis et al. 2009).

A recent review recorded data on the occurrence of 60 emerging contaminants including antibiotics, anticonvulsants, artificial sweeteners, lipid regulators, non-steroidal anti-inflammatory drugs (NSAIDs), hormones, among others, in the influent, treated effluent, sludge and biosolids in municipal WWTPs of different geographical regions (Asia, Europe and North America). The results revealed a high occurrence of antibiotics both in the influent and the effluent, reaching values of a few tens of $\mu g\ L^{-1}$ (Tran et al. 2018). Moreover, antibiotics have been postulated as a

new class of water contaminants of emerging interest, mainly due to the evolution of antibiotic-resistant bacteria (ARB) and antibiotic-resistant genes (ARGs) (Bouki et al. 2013). Although WWTPs remove some OMPs during the treatment processes, removal efficiencies vary from plant to plant, leading to the disposal of certain compounds, causing persistent pollution on receiving waters (Kümmerer 2010). Therefore, the best available technology in tertiary treatment stages of WWTPs should be developed and adopted in order to meet present and future water treatment expectations (Paredes et al. 2018).

1.2 Tertiary treatment systems for the removal of OMPs

In recent decades, different strategies have been researched to control water pollution in WWTP effluents in order to improve the quality of the effluents treated before their discharge into the environment, from physicochemical to biological processes. Despite the efficiency of physicochemical alternatives, these methods are often very costly, and the accumulation of concentrated sludge creates a disposal problem. In the search of effective removal of micropollutants from large volumes of effluents with low-cost systems, biological processes were approached, but with limited efficiency.

Beyond conventional processes, different advanced treatment methods for the removal of contaminants from wastewater have been investigated as a potential solution to achieve these challenges. These methods can be classified into two separate categories: consolidated and advanced treatment methods (Figure 1.1) (Rizzo et al. 2018).

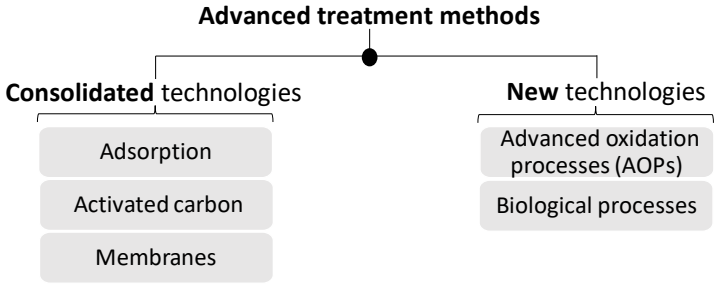

Figure 1.1 Classification of different advanced treatment methods for the removal of contaminants from WWTPs (Crittenden et al. 2012).

One of the most widely applied consolidated technologies is adsorption. Adsorption processes based on the retention of OMPs on the surface of a solid material have been widely studied, mainly because the formation of transformation products is avoided (Jiang et al. 2018). In this sense, activated carbon has proven to be a highly effective alternative material for removing target OMPs (Altmann et al. 2014). However, once the adsorbent is saturated, the material needs to be replaced and regenerated (Reungoat et al. 2012, Alvarino et al. 2018). Regarding membrane filtration processes, the main objectives are the removal of total suspended solids and microorganisms by implementing a physical barrier with pore sizes ranging 0.1-10 μm and 0.1-0.001 μm for micro and nanofiltration, respectively (Crittenden et al. 2012).

On the contrary, new technologies involving advanced oxidation processes (AOPs) and biological process approaches are considered as potential new alternatives. On the one hand, AOPs perform the oxidation of organic contaminants through reactions with hydroxyl radicals (·OH) (Glaze et al. 1987). On the other hand, biological process such as the use of microorganisms as bacteria, algae or fungi represent an environmentally friendly alternative for the removal of persistent OMPs (Falås et al. 2016, Muñoz et al. 2006, Arca-Ramos et al. 2012). Both AOPs and biological process were two alternatives assessed in the current research, as will be presented and detailed in the following sections.

1.2.1 Advanced oxidation processes (AOPs)

AOPs are powerful oxidative methods that provide efficient removal rates of recalcitrant pollutants from water. AOPs involve the *in-situ* generation and use of highly reactive oxygen species (ROS), whose high oxidation potential makes them much stronger than other conventional oxidizing species, such as hydrogen peroxide (H_2O_2) and ozone (O_3). ROS include ·OH radicals, superoxide radicals ($O_2^{\cdot-}$) and singlet oxygen ($^1O_2$), which are involved in the degradation of organic matter, ideally to its mineralization, producing carbon dioxide and water (Koppenol et al. 2010).

AOPs typically comprise two stages: i) the formation of ·OH (E_0 = 2.73 V) and ii) the reaction of these oxidants with organic contaminants present in water. AOPs are considered a highly competitive technology for the removal of organic pollutants which, due to their high chemical stability and/or low biodegradability, are not

successfully removed by conventional techniques (Oller et al. 2011). According to their mechanism of action, AOPs can be classified as non-photochemical treatments, such as Fenton and Fenton-like processes, electrochemical oxidation, ultrasound, ozonation, etc., and photochemical treatments, including homogeneous and heterogeneous photocatalysis, photo-Fenton, or ultraviolet light (UV) treatment (Munter 2001, Domínguez et al. 2014). Moreover, AOPs can be classified as homogeneous and heterogeneous processes, energy-dependent or non-energy-dependent (Figure 1.2).

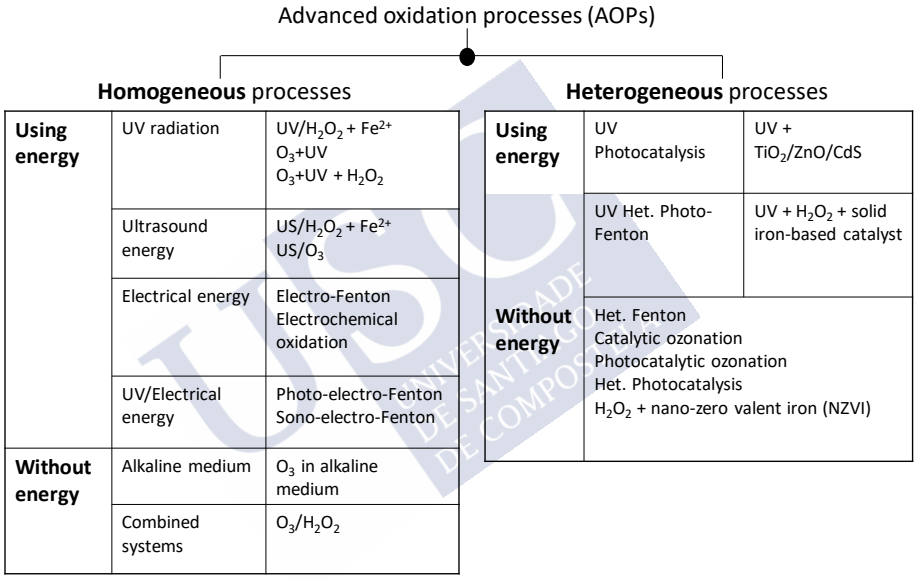

Figure 1.2 Classification of Advanced oxidation processes (AOPs). Adapted from Matavos-Aramyan and Moussavi (2017).

Ozonation

One of the most common advanced oxidation processes is ozonation, used for sanitization or removal of chemical contaminants (Von Gunten 2003). The reaction with a large number of organic compounds occurs by direct oxidation as an ozone molecule or by indirect reaction through the formation of secondary oxidants such as ·OH radical (Baig and Liechti 2001). The use of ozone presents a number of

drawbacks, such as relatively low solubility and stability in water, and requires an additional filtration step to remove biodegradable organic carbon from water (Somensi et al. 2010).

Sonolysis

During acoustic sonication, bubbles grow and collapse implosively, producing unusual chemical and physical phenomena. This collapse generates hotspots with a transient temperature of around 5000 K and pressures of about 1000 atm. Under such extreme conditions, water molecules dissociated into ·OH radicals and H atom. Radical species react with other molecules to induce sonochemical degradations (Özdemir et al. 2011). Joseph et al. (2000) applied a sonochemical treatment for different azo compounds, such as C.I. Reactive Red 22 and Methyl Orange. The results showed that the removal of both dyes was rapid (>90% in 30 min). However, in the pursuit of better process efficiency and color removal, it is a common strategy to combine different AOPs. This is the case study carried out by Chung and Kim (2011), in which the efficiency of ozonation combined with three AOPs (O_3/H_2O_2, O_3/UV and O_3/H_2O_2/UV) for the removal of dye-containing synthetic effluents were evaluated. Similarly, the treatment of a textile industry effluent by different advanced oxidation processes (O_3, O_3/UV, H_2O_2/UV, O_3/H_2O_2/UV, Fe^{2+}/H_2O_2) was also investigated (Azbar et al. 2004). The results showed that AOPs provide higher color removal than conventional chemical precipitation. Among the different AOPs, the O_3/H_2O_2/UV combination showed the best results (99% chemical oxygen demand (COD) elimination and 96% color removal). Moreover, the Fenton process also showed good results (96 % COD removal and 94% color removal) but proved to be more economical.

With the aim of investigating the relevance of the different AOPs technologies, a search for bibliographic references published between 2012 and 2017 was conducted (Figure 1.3). As for the different types of dyes, azo dyes are by far the most studied, with 81% of the bibliographical references; carbonyl dyes accounted for 14%, which corresponds to the sum of two individualized searches for anthraquinone dyes and indigo dyes and, finally, for phthalocyanine dyes (5%). Among the different AOPs used to remove dyes, the most studied with 51% of the

bibliographical references is the Fenton process followed by photocatalysis (11%) and ozonation (9%).

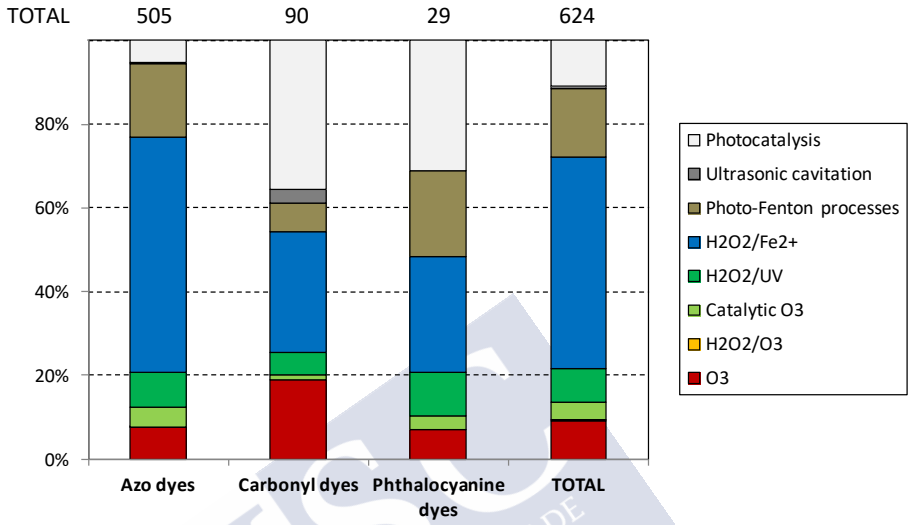

Figure 1.3 Scientific papers related to the application of AOPs for the removal of dyes (ISI Web of Knowledge; Years 2012 to 2017).

Fenton (H_2O_2/Fe^{2+}) and Photo-Fenton processes

The Fenton process is a widely studied AOP due to its efficiency and low reaction time (Pignatello et al. 2006). Fenton reactions are initiated with an electron transfer, in which ferrous iron (Fe^{2+}) reacts with H_2O_2 to generate ·OH radicals (Equation 1), which are the species responsible for the oxidation of organic matter, ideally resulting in complete mineralization to CO_2 and H_2O. The main types of reaction of ·OH with organic compounds include hydrogen atom abstraction from aliphatic carbon, the addition to double bonds and aromatic rings, and electron transfers (Bauer and Fallmann 1997).

Then, ferric iron (Fe^{3+}) is reduced to Fe^{2+}, forming a hydroperoxyl radical (HO_2·), which is also an oxidizing agent towards organic compounds (Equation 2). "R" is used to describe the reacting organic compound:

$$Fe^{2+} + H_2O_2 \xrightarrow{k = 76\ Lmol^{-1}s^{-1}} Fe^{3+} + \cdot OH + OH^- \quad (1)$$

$$Fe^{3+} + H_2O_2 \xrightarrow{k = 0.01\ Lmol^{-1}s^{-1}} Fe^{2+} + HO_2 \cdot + H^+ \quad (2)$$

$$RH + \cdot OH \rightarrow R \cdot + H_2O \quad (3)$$

$$R \cdot + Fe^{3+} \rightarrow R^+ + Fe^{2+} \quad (4)$$

$$R + OH \rightarrow R - OH \quad (5)$$

A modified configuration corresponds to the Photo-Fenton process, which can also produce hydroxyl radicals.

$$Fe^{2+} + H_2O_2 \rightarrow Fe^{3+} + OH^- + \cdot OH \quad (6)$$

$$Fe^{3+} + H_2O \xrightarrow{h\nu} Fe^{2+} + H^+ + \cdot OH \quad (7)$$

$$\cdot OH + RH \rightarrow H_2O + R \cdot \quad (8)$$

A number of advantages are associated to the Fenton process to eliminate organic pollutants: no energy is required to activate hydrogen peroxide, low cost and easy operation, short reaction time and no mass transfer limitation due to its homogeneous catalytic nature. However, this process has some drawbacks that must be taken into account, such as low pH requirements (2-3), consumption of ferrous salts due to ineffective regeneration and the presence of residual iron in the effluent and the production of chemical sludge.

The efficiency of Fenton processes for the treatment of polluted wastewater is widely reported in the literature. The combination of chemical oxidation using the Fenton reagent (H_2O_2/Fe^{2+}) achieved the partial removal of organic content (COD) of the contaminated effluents (Papadopoulos et al. 2007). When Fenton oxidation was coupled to either an aerobic Sequencing Batch Reactor (Blanco et al. 2012) or aerobic biological treatment (Pérez et al. 2002a), not only COD removal but also efficient pathogen removal was observed.

Fenton-like process

Although the Fenton process has been broadly studied for the treatment of a wide range of scenarios, the process has serious drawbacks, with the unfeasible separation of the homogeneous catalyst (Fe^{2+}) from the treated water being the most notable, as well as the subsequent large volume of iron sludge produced that poses adverse effects on the environment and waste disposal (Cheng et al. 2004, Luo et al. 2010). Moreover, EU directives limit the discharge of iron ions into the environment to 2 ppm (Kiwi 2001). According to previous works, the steps associated with the post-treatment of these undesirable sludge costs can reach up to 50% of the total operating costs of wastewater treatment (Munoz et al. 2015).

In this sense, the use of solid catalysts may represent a promising alternative to overcome these disadvantages, due to their easier separation from the effluent. The proposed mechanisms of action during Fenton-like process were the decomposition of H_2O_2 to ·OH radicals by binding H_2O_2 to the iron species present on the surface of the solid catalyst of the chemisorption of probe molecule on the surface of the catalyst.

Several works include the use of nanomaterials with higher performance in contaminant removal due to their high surface/volume ratio (Zhang et al. 2008, Navalon et al. 2010, Yang et al. 2013, Xu and Wang 2012). Among these nanomaterials, the use of magnetite (Fe_3O_4) as a potentially benign material for the environment is a promising heterogeneous nanocatalyst of the Fenton type due to its easy and economical recovery through the application of a magnetic field, which allows its repeated use (Zang et al. 2018, Velichkova et al. 2013, Hou et al. 2016, Nidheesh et al. 2014).

Ultraviolet (UV) irradiation

Direct UV treatment and UV-based AOPs have received considerable attention in recent decades due to their application for microbial disinfection in the treatment of drinking and wastewater. However, UV light can also carry out the degradation of organic compounds by direct photolysis as a consequence of UV light absorption or

by indirect processes assisted by the addition of oxidizing or photosensitizing agents such as hydrogen peroxide (Equation 9-13).

$$H_2O_2 \xrightarrow{h\nu} 2 \cdot OH \quad (9)$$

$$H_2O_2 + \cdot OH \rightarrow HO_2 \cdot + H_2O \quad (10)$$

$$HO_2 \cdot \rightarrow H^+ + O_2^{\cdot -} \quad (11)$$

$$H_2O_2 + O_2^{\cdot -} \rightarrow O_2 + OH^- \quad (12)$$

$$\cdot OH + O_2^{\cdot -} \rightarrow O_2 + OH^- \quad (13)$$

The efficacy of UV photolysis of micropollutants varies among compounds with different UV absorption and its quantum yield (Giannakis et al. 2017).

UV photocatalysis oxidation

Photocatalysis relies on the capacity of semiconducting materials to act as sensitizers for light-reduced redox processes due to their electronic structure. A photocatalyst is a chemical that produces electron-hole pairs by absorption of light quanta and makes chemical transformations of the reaction participants that come into contact with it and regenerates its chemical composition after each cycle (Fox and Dulay 1993).

Photocatalysts include titanium dioxide (TiO_2), zinc oxide (ZnO), zinc sulfide (ZnS), ferric oxide (Fe_2O_3), silicon (Si), tin (IV) oxide (SnO_2) and cadmium sulfide (CdS), among others. TiO_2 has been the most widely cited photocatalyst in the literature due to its properties: considerable activity, high stability, no environmental impact and low cost (Augugliaro et al. 2006). However, homogeneous catalysts react quickly and provide good conversion rates per molecule, but using heterogeneous photocatalysis, the reaction rate is restricted to the limited surface area of the catalyst (Govan and Gun'ko 2014).

1.2.2 Biological processes

The ability of biological agents such as plants and microorganisms, both bacteria and fungi, to degrade or detoxify substances hazardous to human health and/or the environment is a well-known alternative to the methods described above for the removal of OMPs from wastewater, which is gaining increasing interest. Bioremediation is defined as the process by which organic waste is degraded biologically under controlled conditions to a safe state, or at levels below the concentration limit established by regulatory authorities (Mueller et al. 1996, Megharaj et al. 2011).

The scientific justification for bioremediation derives from a relatively new and emerging concept of Green Engineering, defined as the design, commercialization, and use of processes and products that are feasible and economical while minimizing source contamination and risk to human health and the environment (Kirchhoff 2003).

White rot fungi and oxidative enzymes

White-rot fungi differ from other microorganisms in their ability to mineralize all components of lignin to CO_2 and water. Lignin constitutes the most abundant natural-origin renewable aromatic polymer in the world (Kirk and Farrell 1987). It is found in the cell wall of most plants, forming a matrix together with cellulose and hemicellulose, which provides rigidity and natural protection against extreme temperatures and a certain hydrophobic character (Higuchi 1990). Of the three components of wood (cellulose, hemicellulose and lignin), lignin is the most recalcitrant compound, as it has a complex structure derived from the coupling of monolignols and three primary hydroxycinnamyl alcohols: *p*-coumaryl, coniferyl, and sinapyl alcohols (Wong 2009). In addition, it has a high molecular weight and is very insoluble, which hinders its degradation (Martínez et al. 2005, Pérez et al. 2002b).

Enzymes produced by ligninolytic fungi are oxidoreductases produced in secondary metabolism that catalyze the transfer of electrons from one substrate to another for the depolymerization and mineralization of lignin (Cabana et al. 2007). These oxidative enzymes act by generating highly reactive free radicals that attack the lignin molecule by breaking covalent bonds and giving rise to phenolic

compounds. The generation of these radicals makes lignin-modifying enzymes attractive for the development of advanced oxidation processes of recalcitrant compounds. In addition, ligninolytic fungi secrete high molecular weight mediators, increasing the number of potentially biodegradable compounds (Kersten and Cullen 2007).

In recent years, numerous studies have been carried out to evaluate the oxidative capacity of white rot fungi to oxidize organic compounds (Cabana et al. 2007, Blánquez and Guieysse 2008). The use of these enzymes in environmental technology presents a series of advantages over the use of microbial cultures, since high concentrations of contaminants can be maintained, there is no inhibition of microbial growth due to these substances, the control of the process is easier, the production of sludge does not exist, it can work in conditions of non-sterility and in addition, the easy control process (Duran and Esposito 2000). The main limitations that must be taken into account in the enzymatic system are the cost of production of the enzyme and its instability, due to changes in environmental conditions (Wariishi et al. 1988). Since the interaction of the enzyme with the substrate may be limited by the size of the biocatalyst, it is sometimes desirable to use enzymes that spread easily or act through mediators. In this sense, extracellular enzymes are also preferred, whose production is simpler and cheaper (Eibes et al. 2006). The main types of extracellular lignin-modifying enzymes are peroxidases and laccases (Touahar et al. 2014).

On the one hand, peroxidases are a group of enzymes that require the presence of H_2O_2 as an electron acceptor to carry out oxidation (Mester and Tien 2000). Among the best-known peroxidases, lignin peroxidase (LiP), manganese peroxidase (MnP) and versatile peroxidase (VP) stand out (Touahar et al. 2014). Lignin peroxidase (LiP, EC 1.11.1.14) was the first identified ligninolytic peroxidase produced by *Phanerochaete chrysosporium* capable of oxidizing the non-phenolic units of lignin (representing up to 90% of the total polymer content) (Janusz et al. 2013).

MnP (EC 1.11.1.13) was also first described in *P. chrysosporium* (Wariishi et al., 1988). This enzyme is considered the most common ligninolytic peroxidase produced by most basidiomycetes (Wesenberg et al. 2003). MnP requires Mn^{2+} to close its

active cycle, and it is Mn^{3+} that acts as a diffusible agent oxidizing both phenolic and non-phenolic units through lipid peroxidation (Hofrichter 2002). As for VP, it is considered a hybrid between MnP and LiP, since it is capable of oxidizing Mn^{2+} and also non-phenolic compounds with high redox potential such as veratryl alcohol (Wong 2009, Wesenberg et al. 2003, Taboada-Puig et al. 2015).

On the other hand, laccases (EC 1.10.3.2) are enzymes with phenol-oxidase activity that contain copper atoms in their active center (Reinhammar 1972). These enzymes catalyze the oxidation of a wide variety of organic substances, in a process coupled to the reduction of molecular oxygen to water (Kunamneni et al. 2008). These enzymes are known and studied since the end of the 19th century. They were first discovered in the latex of the *Rhus vernicifera* tree (Yoshida 1883). However, it was not until 1986, when their presence was demonstrated in fungi and their existence is now known in insects, bacteria and archaea (Baldrian 2006, Dittmer et al. 2009, Claus et al. 2002, Uthandi et al. 2010).

This demonstrates its wide distribution in nature, as well as its involvement in many different biological processes. Laccase alone or through the laccase-mediator system have great technological potential in different processes such as pulp and paper production, food treatment, bioremediation of environmental contaminants and in the treatment of industrial effluents (Zucca et al. 2011). Regarding their application in the removal of recalcitrant compounds, numerous studies have been published (Marco-Urrea et al. 2010, Gasser et al. 2014, Rodríguez-Delgado and Ornelas-Soto 2017). From the reports available, the use of laccase is considered a promising technology for the elimination of contaminants.

Laccase enzymes have great potential as industrial catalysts, due to their excellent functional properties (activity, selectivity, specificity), in many areas of the chemical industry: fine chemistry, food, among others (Koeller and Wong 2001). However, the use of free laccase is limited by their inactivation with inhibitory compounds, extreme pH values or elevated temperatures (Kunamneni et al. 2008, Bornscheuer 2003, Osma et al. 2010). Therefore, in many cases they have to be improved for their application. Enzyme engineering for this purpose considers different techniques to improve properties such as molecular biology and immobilization techniques (Illanes et al. 2008, Ba et al. 2013).

For technical and economic reasons, in most enzyme-catalyzed processes it is necessary to use the biocatalyst continuously for prolonged periods and to reuse it for different cycles (Katchalski-Katzir and Kraemer 2000). In this context, enzyme immobilization can be defined as a technique that allows reuse or continuous use of the biocatalyst. Moreover, immobilization allows for greater stability and storage time of the enzyme (Lloret et al. 2011). Furthermore, to avoid enzyme losses in the continuous output flow of the reactor, the enzyme reactor configuration must include a retention system. Other reactor configurations, in addition to those using membranes, are those based on the immobilization of enzymes, by processes of ionic interaction, covalent bonding, cross-linking, encapsulation or entrapment (Ba et al. 2013). The immobilization method to be applied should provide the best conditions to ensure maximum enzymatic stability and easy separation of the reaction products for possible use in sequential batch and continuous reactors.

1.3 Nano-based technologies for water treatment

In the last two decades, the growing interest in nanoscience and materials with improved functionality has led to the preparation of nanomaterials with a characteristic surface and size, between 10 and 100 nm. Several approaches have been proposed for use in the removal of a wide range of contaminants, including heavy metals, algae, organic products, bacteria, viruses, nutrients, cyanide and antibiotics (Bethi et al. 2016).

Different approaches and materials for wastewater treatment have been investigated, from more consolidated perspectives to the use of nanomaterials. The characteristic large surface area of nanostructured materials allows a higher density of reactive sites on particle surfaces, which increases decontamination rates and overall efficiency. Depending on the application requirements, nanoscale materials can be designed by controlled and selective synthesis, with improved and adjustable physical and chemical properties (Jeevanandam et al. 2018). Engineered nanomaterials can be functionalized on their surface so that they can specifically interact with molecules of interest (pollutants) for efficient remediation.

The combination of different materials as hybrid composites, which meet the desired specific properties of each of their components, may represent a potentially more efficient, selective and stable type of nanomaterial, compared to methods

based on a single type of nanoparticle (NP). The NPs used for wastewater treatment can be classified according to their mechanism of action as nanoadsorbents and reactive nanomaterials, which act through chemical reactions such as acid-base, redox, precipitation, catalysis and photocatalysis or as supports (Rabbani et al. 2016, García-Morales et al. 2018). In this sense, heterogeneous catalysis based on the use of NPs seems to be a promising technology in the treatment of different types of effluents using new advanced treatment methods. Within the framework of the application of nanotechnology, this section aims to provide an overview of the latest advances in the field of functional NPs and hybrid nanocomposites (NCs) used for this purpose. The use of this type of materials must face several key challenges, such as the high transformation/elimination capacity of the target compounds, acceptable cost, ease of synthesis from a green chemistry perspective, non-toxicity, biodegradability, recyclability and the potential for recovery after use (regeneration).

Nanomaterials based on metals and oxides

Magnetite (Fe_3O_4) is one of the main iron ores. It is the most magnetic of all the natural minerals on Earth (Cornell and Schwertmann 2004). Fe_3O_4 particles are superparamagnetic when reduced to the nanoscale, allowing their easy separation and recovery from the medium simply by applying an external magnetic field. In addition, Fe_3O_4 NPs are non-toxic and biocompatible (Wei et al. 2012). They have been used in different environmental applications, such as the removal of organic pollutants and heavy metals by adsorption (Li et al. 2018, Shipley et al. 2010, Gutierrez et al. 2017) and/or by chemical methods (He et al. 2015, Tyre et al. 1991, Fang et al. 2012, Yang and Wu 2011).

In addition to the synthetic Fe_3O_4 NPs, He et al. (2015) recently demonstrated that natural Fe_3O_4 containing different impurities can catalyze the decomposition of H_2O_2 to produce ·OH and achieve the consequent degradation of p-nitrophenol (p-NP) (He et al. 2015). Similar results were obtained in Fenton-type mineral-catalyzed treatment in wastewater and even in natural soils (Watts et al. 1999, Xu et al. 2009). In a recent article, Luo et al. (2018) reported the removal of phenanthrene from a contaminated soil by a photo-Fenton process based on mesoporous

magnetite/carboxylate-rich carbon (MMCRC) composites, under visible light irradiation and circumneutral pH (Luo et al. 2018).

Other nanostructured metallic materials frequently applied in wastewater and soil remediation are ZnO and TiO_2 (Gu et al. 2012, Arana et al. 2002, Modirshahla et al. 2011). For example, if TiO_2 is illuminated with light ($h\nu$) of an appropriate wavelength, electrons (e^-) are promoted from the valence band (VB) to the conduction band (CB), and thus and photo-induced holes (h^+) are generated (Equation 14). In the valence band, h^+ can react with H_2O or OH^- ions and form ·OH (Equations 15-16), while e^- in the conduction band can react with O_2 and produce superoxide ions ($O_2^{\bullet-}$) (Equation 17). The reactive oxygen species, ·OH and $O_2^{\bullet-}$, along with photo-induced h^+, present a high oxidation potential and react with organic pollutants, causing their degradation, and with microorganism, leading to cell death (Elmolla and Chaudhuri 2010).

$$TiO_2 + h\nu \rightarrow e^-_{cb} + h^+_{vb} \quad (14)$$

$$h^+ + H_2O \rightarrow H^+ + \cdot OH \quad (15)$$

$$h^+ + OH^- \rightarrow \cdot OH \quad (16)$$

$$e^- + O_2 \rightarrow O_2^{\bullet-} \quad (17)$$

However, TiO_2 has some limitations as a photocatalyst, since most of the excited e^-/h^+ pairs recombine rapidly in the bulk or on the surface of the particle dissipating heat, and its absorption capacity in the visible-light range is restricted. Therefore, TiO_2 requires some modifications to increase its photocatalytic performance (Fagan et al. 2016). Some noble metals, such as silver (Ag), gold (Au), platinum (Pt) and palladium (Pd), have been studied for their contribution in visible-light absorption of titania-based photocatalysts by depositing them on TiO_2 NPs with oxygen vacancies (Pan and Xu 2013). This is related to the capability if these metals to act as e^- traps, thus reducing the recombination rate of photo-generated e^-/h^+ pairs in TiO_2, as well as to enhance the capture of visible light (Figure 1.4).

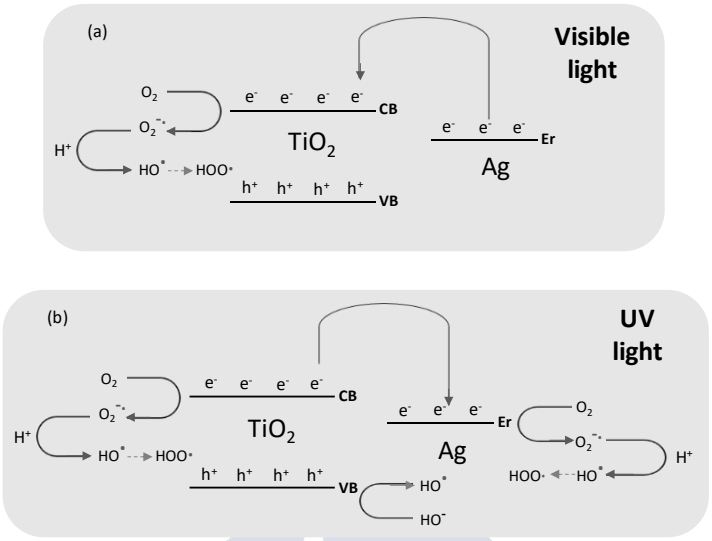

Figure 1.4 Schemes of the photocatalytic mechanism: (a) under visible light and (b) under UV light. Adapted from He et al. (2013).

Nolan et al. (2010) conducted a systematic study of the effect of silver on TiO_2, concluding that the surface plasmon resonance (SPR) of Ag NPs and the oxidized surface of Ag are responsible for the visible-light response of TiO_2 (Nolan et al. 2010). Zhang et al. (2014) prepared Pt/C-TiO_2 NPs with a Pt content of 0.5-5 wt% and demonstrated that the loaded Pt NPs enhanced the visible-light response by inhibiting recombination of the photo-generated charge carrier and promoting interfacial charge transfer, compared to C-TiO_2. Pt/C-TiO_2 NPs were successfully evaluated as photocatalysts in the degradation of toluene and Rhodamine B (RhB) in water (Zhang et al. 2014). In a similar study, Salami et al. (2012) investigated the photocatalytic properties of Ag-doped TiO_2 in the visible-light driven degradation of Methylene Blue and 4-chlorophenol in water, as well as benzene gas, obtaining high photocatalytic efficiencies.

More recently, the use of titanates has also been considered in photocatalysis. In particular, bismuth titanate ($Bi_{12}TiO_{20}$) is one of the most frequently investigated titanates due to its interesting properties of high photosensitivity in the visible red region and the potential for practical environmental applications (Mihailova et al. 1999). The photocatalytic activity of $Bi_{12}TiO_{20}$ has been successfully investigated

under visible-light irradiation below 500 nm in the degradation of methanol (Zhou et al. 2007), Methyl Orange (Skiker et al. 2018, Fang et al. 2018), Acid Orange 7 (Zhu et al. 2011) and RhB (Nogueira et al. 2015), among others.

Polymer-Based Nanomaterials

The benefits of nanomaterials are related to their higher surface/volume ratio, which provides them high catalytic activity and/or efficient adsorption capacity. However, this characteristic may also promote the aggregation and low stability of NPs due to particle interactions, which limits their application in the field. The use of polymers as a matrix or support has been widely proposed to avoid the obstacles related to nanomaterials. In addition, polymers can also contribute other desirable physicochemical properties, such as improved mechanical strength, thermal stability, moisture stability, durability and recyclability (Singh and Ambika 2018, Rong et al. 2002). Depending on the formation processes, these polymeric nanocomposites can be synthesized through different methods, such as melt intercalation, where the polymer, above its softening point, is in contact with the host in the absence of any solvent; in situ polymerization, which provides better dispersion of the NPs, thus obtaining stronger interactions between the nanomaterial and the polymer; or by direct mixing, simply bringing the NPs and the polymer into contact (Sinsawat et al. 2003, Kalaitzidou et al. 2007).

Polymer-based nanomaterials have been used in various environmental media, such as groundwater, industrial effluents, gases and soils, which were contaminated with different pollutants, including heavy metals, organic compounds or dyes (Manju et al. 2002, He et al. 2009). Inert organic polymers, such as carboxymethyl cellulose (CMC), polyaspartate (PAP) or poly(acrylic acid) (PAA) (Jiemvarangkul et al. 2011, Kumari and Singh 2016, Saleh et al. 2005), among others, can be used as surface coatings of NPs to act as stabilizers, creating electronically negative charges that promote particle repulsion with each other and with other particles (Cameselle et al. 2013). In this sense, Radoičić et al. (2017) prepared a novel photocatalytic nanocomposite designated as PANI/TiO_2, which was based on the chemical oxidative polymerization of polyaniline (PANI) in the presence of TiO_2 NPs. PANI/TiO_2 nanocomposites were applied in the degradation of Rhodamine B and Methylene

Blue, obtaining higher photocatalytic efficiency compared to bare TiO_2 NPs (Radoičić et al. 2017).

Polymeric graphitic carbon nitride (g-C_3N_4) is an earth-abundant, metal-free photocatalyst, which has recently captured the attention of researchers due to its success in increasing solar energy conversion into electricity and fuels, and its use in environmental applications (Iqbal et al. 2018). However, its relatively large bandgap (≈2.7 eV) and high recombination rate of e^-/h^+ pairs makes its use under visible light constrained. Recently, Wang et al. (2019) reported a new nanocomposite constituted by g-C_3N_4 coupled to Fe_3O_4 NPs with extended photocatalytic activity in the visible-light region, lower recombination rate of photo-induced e^-/h^+ and low toxicity, for its application in phenanthrene-contaminated soil remediation. The high conductivity (1.9×10^6 S m^{-1}) of Fe_3O_4 allows it to act as photo-induced e^- acceptor from g-C_3N_4 and thereby, decrease the recombination of the e^-/h^+ pairs. On the other hand, different polymers, such as polypyrrole, cellulose, poly(methyl methacrylate) or polythiophene, among others, have been used as adsorbents for the removal of heavy metal ions (Yan et al. 2007, Mthombeni et al. 2015, Ansari et al. 2015, Türkmen et al. 2009). In the removal of Cd(II), Pb(II), Co(II) and Ni(II), a new magnetic nanocomposite synthesized by reverse microemulsion of acrylamide polymerization in the presence of a magnetic fluid, using N,N'-methylene-bis-(acrylamide) as cross-linker was investigated. This nanocomposite (M-PAM-HA) was relatively selective with selected cations through its polymeric matrices, with the advantage of being easy to separate from the medium in the presence of an external magnetic field. A proposed divalent metal ion adsorption mechanism in M-PAM-HA suggested the formation of coordination complexes (Zhao et al. 2014).

Additionally, a novel chitosan based nanosized material have been employed as an environment-friendly nanomaterial due to its characteristic properties of non-toxicity, biocompatibility, biodegradability, and anti-microbial activity for the treatment of contaminated effluents (Dutta et al. 2004, Nasreen et al. 2013, Qian and Zhang 2010). In this sense, Aliabadi et al. (2013) investigated the use of chitosan-based nanofiber (cNF) membranes for adsorption of nickel (Ni), cadmium (Cd), lead (Pb) and copper (Cu) from aqueous solution and performing successive sorption-desorption cycles of the different metal ions, pointing out the potential of this technology for the treatment of contaminated effluents.

Silica-based nanomaterials

The hydroxyl groups present on the surface of silica-based nanomaterials, such as fumed silica NPs, silica-coated magnetic NPs or mesoporous silica materials, allow their modification for use as adsorbents and/or as immobilization supports of other active moieties. In particular, mesoporous silica materials have gained much attention due to their large surface area and adjustable pore size, that provide them great versatility. Figure 1.5 represents a schematic structure of mesoporous silica NPs decorated with polyethylenimine (PEI) moieties, being PEI a consolidated polymeric adsorbent of organic pollutants due to its high content of primary, secondary and tertiary amine groups (Thakur et al. 2017, Shi et al. 2018).

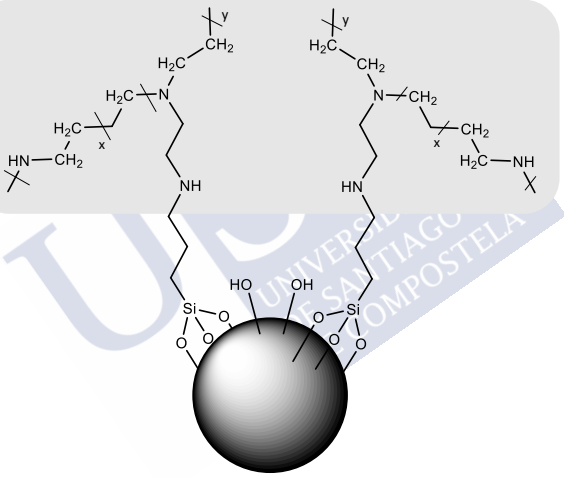

Figure 1.5 Representation of grafted PEI on mesoporous silica NPs. Adapted from (Thakur et al. 2017).

Mesoporous silica materials may also act as a support for the immobilization of catalytic enzymes applied in biological remediation. Wang et al. (2010) reported the preparation of large-pore magnetic mesoporous silica particles and their use as laccase support, which improved catalytic activity and stability properties over consecutive reuse cycles. Meeks et al. (2012) evaluated the immobilization of iron oxide NPs onto sulfonated silica particles with the aim of preventing NPs aggregation, for its application in the oxidative degradation of trichloroethene (TCE).

In this case, silica NPs were functionalized with sulfonate groups that provided an ion exchange platform for ferric/ferrous ions (Meeks et al. 2012).

Recent studies introduce the use of a novelty ordered mesoporous materials (SBA-15 and SBA-16), whose characteristic morphology makes them ideal supports for heterogeneous catalysis processes. The results obtained by Klimova et al. (2010), confirmed that use of the SBA-15 silica as metal species: Ni and molybdenum (Mo) support improves the dispersion of the active phase and its activity for hydrodesulphurization catalysts.

1.4 Objectives and scope of this thesis

With the general objective of the extensive degradation of chemical compounds present in water and wastewater, various advanced tertiary treatments based on nanotechnologies are proposed:

a) *Oxidative enzymes*: due to the ability of ligninolytic fungi to degrade the lignin present in the tree bark, this work proposes the use of enzymes produced by ligninolytic fungi, specifically white rot fungi, as an alternative to the methods described above for the elimination of emerging pollutants. Two different laccases from *Myceliophthora thermophila* (*Mt*) and *Trametes versicolor* (*Tv*) and VP from *Bjerkandera* sp were immobilized onto micro and nano supports (Chapter 3).

b) *Fenton oxidation*: different magnetite protecting agents, including PAA, PEI and SiO_2 were evaluated in order to select the optimum iron-based catalyst for the removal of a wide range of recalcitrant compounds during the application of heterogeneous Fenton process treatment (Chapter 4).

c) *Photocatalysis oxidation*: two different novel magnetic NCs based on magnetite and two metal oxides (ZnO and TiO_2) efficiency were investigated for its application in photocatalytic degradation experiments of persistent organic pollutants (Chapter 5).

Moreover, in Chapter 6, a specific objective was carried out for the development and operation of different configurations of magnetic separation devices with the objective of complete retention of the nanostructured magnetic

catalysts described in the previous chapters, during the the removal of recalcitrant compounds present in a water matrix by different oxidation processes.

In addition, Chapter 7 presents the results of the different magnetite-based nanocatalysts geno and cytotoxicity results after the direct exposure of the selected nanomaterials with a specific deoxyribonucleic acid (DNA) solution and human cells. These experiments aim to estimate the pro-oxidant effects of these nanoparticles on cells metabolism disorder. Finally, Chapter 8 encompasses the main conclusions obtained throughout this work, highlighting the most outstanding results.

1.5 References

Aliabadi, M., Irani, M., Ismaeili, J., Piri, H. and Parnian, M.J. (2013) Electrospun nanofiber membrane of PEO/Chitosan for the adsorption of nickel, cadmium, lead and copper ions from aqueous solution. Chemical Engineering Journal 220, 237-243.

Altmann, J., Ruhl, A.S., Zietzschmann, F. and Jekel, M. (2014) Direct comparison of ozonation and adsorption onto powdered activated carbon for micropollutant removal in advanced wastewater treatment. Water Research 55, 185-193.

Alvarino, T., García-Sandá, E., Gutiérrez-Prada, I., Lema, J., Omil, F. and Suárez, S. (2018) A new decentralized biological treatment process based on activated carbon targeting organic micropollutant removal from hospital wastewaters. Environmental Science and Pollution Research.

Ansari, M.O., Khan, M.M., Ansari, S.A. and Cho, M.H. (2015) Polythiophene nanocomposites for photodegradation applications: Past, present and future. Journal of Saudi Chemical Society 19(5), 494-504.

Arana, J., Melián, J.H., Rodrıguez, J.D., Dıaz, O.G., Viera, A., Pena, J.P., Sosa, P.M. and Jiménez, V.E. (2002) TiO_2-photocatalysis as a tertiary treatment of naturally treated wastewater. Catalysis Today 76(2-4), 279-289.

Arca-Ramos, A., Eibes, G., Moreira, M.T., Feijoo, G. and Lema, J.M. (2012) Mass transfer enhancement by the addition of surfactant in a two phase partitioning bioreactor for the degradation of anthracene by laccase. Chemical Engineering 27.

Augugliaro, V., Litter, M., Palmisano, L. and Soria, J. (2006) The combination of heterogeneous photocatalysis with chemical and physical operations: A tool for

improving the photoprocess performance. Journal of Photochemistry and Photobiology C: Photochemistry Reviews 7(4), 127-144.

Azbar, N., Yonar, T. and Kestioglu, K. (2004) Comparison of various advanced oxidation processes and chemical treatment methods for COD and color removal from a polyester and acetate fiber dyeing effluent. Chemosphere 55(1), 35-43.

Ba, S., Arsenault, A., Hassani, T., Jones, J.P. and Cabana, H. (2013) Laccase immobilization and insolubilization: from fundamentals to applications for the elimination of emerging contaminants in wastewater treatment. Critical Reviews in Biotechnology 33(4), 404-418.

Baig, S. and Liechti, P. (2001) Ozone treatment for biorefractory COD removal. Water Science and Technology 43(2), 197-204.

Baldrian, P. (2006) Fungal laccases–occurrence and properties. FEMS microbiology reviews 30(2), 215-242.

Barbosa, M.O., Moreira, N.F., Ribeiro, A.R., Pereira, M.F. and Silva, A.M. (2016) Occurrence and removal of organic micropollutants: an overview of the watch list of EU Decision 2015/495. Water Research 94, 257-279.

Bauer, R. and Fallmann, H. (1997) The Photo-Fenton Oxidation - A cheap and efficient wastewater treatment method. Research on Chemical Intermediates 23(4), 341-354.

Bethi, B., Sonawane, S.H., Bhanvase, B.A. and Gumfekar, S. (2016) Nanomaterials based advanced oxidation processes for waste water treatment: a review. Chemical Engineering and Processing: Process Intensification 109, 178-189.

Blanco, J., Torrades, F., De la Varga, M. and García-Montaño, J. (2012) Fenton and biological-Fenton coupled processes for textile wastewater treatment and reuse. Desalination 286, 394-399.

Blánquez, P. and Guieysse, B. (2008) Continuous biodegradation of 17β-estradiol and 17α-ethynylestradiol by Trametes versicolor. Journal of Hazardous Materials 150(2), 459-462.

Bornscheuer, U.T. (2003) Immobilizing enzymes: how to create more suitable biocatalysts. Angewandte Chemie International Edition 42(29), 3336-3337.

Bouki, C., Venieri, D. and Diamadopoulos, E. (2013) Detection and fate of antibiotic resistant bacteria in wastewater treatment plants: A review. Ecotoxicology and Environmental Safety 91, 1-9.

Cabana, H., Jones, J. and Agathos, S.N. (2007) Elimination of endocrine disrupting chemicals using white rot fungi and their lignin modifying enzymes: a review. Engineering in Life Sciences 7(5), 429-456.

Cameselle, C., Reddy, K.R., Darko-Kagya, K. and Khodadoust, A. (2013) Effect of Dispersant on Transport of Nanoscale Iron Particles in Soils: Zeta Potential Measurements and Column Experiments. Journal of Environmental Engineering 139(1), 23-33.

Cheng, M., Ma, W., Li, J., Huang, Y., Zhao, J., Wen, Y.x. and Xu, Y. (2004) Visible-Light-Assisted Degradation of Dye Pollutants over Fe(III)-Loaded Resin in the Presence of H2O2 at Neutral pH Values. Environmental Science & Technology 38(5), 1569-1575.

Chung, J. and Kim, J. (2011) Application of advanced oxidation processes to remove refractory compounds from dye wastewater. Desalination and Water Treatment 25(1-3), 233-240.

Claus, H., Faber, G. and König, H. (2002) Redox-mediated decolorization of synthetic dyes by fungal laccases. Applied microbiology and biotechnology 59(6), 672-678.

Colborn, T., Vom Saal, F.S. and Soto, A.M. (1993) Developmental effects of endocrine-disrupting chemicals in wildlife and humans. Environmental Health Perspectives 101(5), 378-384.

Cornell, R.M. and Schwertmann, U. (2004) The Iron Oxides. Cornell, R.M. and Schwertmann, U. (eds), Wiley-VCH, Weinheim.

Crittenden, J.C., Trussell, R.R., Hand, D.W., Howe, K.J. and Tchobanoglous, G. (2012) MWH's water treatment: principles and design, John Wiley & Sons.

Diamanti-Kandarakis, E., Bourguignon, J.-P., Giudice, L.C., Hauser, R., Prins, G.S., Soto, A.M., Zoeller, R.T. and Gore, A.C. (2009) Endocrine-disrupting chemicals: an Endocrine Society scientific statement. Endocrine Reviews 30(4), 293-342.

Dittmer, N.T., Gorman, M.J. and Kanost, M.R. (2009) Characterization of endogenous and recombinant forms of laccase-2, a multicopper oxidase from the tobacco

hornworm, Manduca sexta. Insect biochemistry and molecular biology 39(9), 596-606.

Domínguez, J.R., González, T., Palo, P. and Cuerda-Correa, E.M. (2014) Advanced photochemical oxidation of emergent micropollutants: carbamazepine. Journal of Environmental Science and Health, Part A 49(9), 988-997.

Duran, N. and Esposito, E. (2000) Potential applications of oxidative enzymes and phenoloxidase-like compounds in wastewater and soil treatment: a review. Applied Catalysis B: Environmental 28(2), 83-99.

Dutta, P.K., Dutta, J. and Tripathi, V. (2004) Chitin and chitosan: Chemistry, Properties and Applications.

Eibes, G., Cajthaml, T., Moreira, M.T., Feijoo, G. and Lema, J.M. (2006) Enzymatic degradation of anthracene, dibenzothiophene and pyrene by manganese peroxidase in media containing acetone. Chemosphere 64(3), 408-414.

Elmolla, E.S. and Chaudhuri, M. (2010) Degradation of amoxicillin, ampicillin and cloxacillin antibiotics in aqueous solution by the UV/ZnO photocatalytic process. Journal of Hazardous Materials 173(1), 445-449.

Fagan, R., McCormack, D.E., Dionysiou, D.D. and Pillai, S.C. (2016) A review of solar and visible light active TiO_2 photocatalysis for treating bacteria, cyanotoxins and contaminants of emerging concern. Mater. Sci. Semicond. Process. 42, 2-14.

Falås, P., Wick, A., Castronovo, S., Habermacher, J., Ternes, T.A. and Joss, A. (2016) Tracing the limits of organic micropollutant removal in biological wastewater treatment. Water Research 95, 240-249.

Fang, G., Si, Y., Tian, C., Zhang, G. and Zhou, D. (2012) Degradation of 2,4-D in soils by Fe_3O_4 nanoparticles combined with stimulating indigenous microbes. Environ. Sci. Pollut. Res. 19(3), 784-793.

Fang, G., Wang, L., Zhang, G., Yan, X. and Wang, D. (2018) Rapid microwave-assisted sol-gel synthesis and exceptional visible light photocatalytic activities of $Bi_{12}TiO_20$. Ceramics International 44(14), 16388-16393.

Fox, M.A. and Dulay, M.T. (1993) Heterogeneous photocatalysis. Chemical Reviews 93(1), 341-357.

García-Morales, R., García-García, A., Orona-Navar, C., Osma, J.F., Nigam, K. and Ornelas-Soto, N. (2018) Biotransformation of emerging pollutants in groundwater by laccase from P. sanguineus CS43 immobilized onto titania nanoparticles. Journal of environmental chemical engineering 6(1), 710-717.

Gasser, C.A., Ammann, E.M., Shahgaldian, P. and Corvini, P.F.-X. (2014) Laccases to take on the challenge of emerging organic contaminants in wastewater. Applied microbiology and biotechnology 98(24), 9931-9952.

Giannakis, S., Rtimi, S. and Pulgarin, C. (2017) Light-assisted advanced oxidation processes for the elimination of chemical and microbiological pollution of wastewaters in developed and developing countries. Molecules 22(7), 1070.

Glaze, W.H., Kang, J. and Chapin, D.H. (1987) The chemistry of water treatment processes involving ozone, hydrogen peroxide and ultraviolet radiation. Ozone: Science & Engineering 9(4), 335-352.

Govan, J. and Gun'ko, Y.K. (2014) Recent advances in the application of magnetic nanoparticles as a support for homogeneous catalysts. Nanomaterials 4(2), 222-241.

Gu, J., Dong, D., Kong, L., Zheng, Y. and Li, X. (2012) Photocatalytic degradation of phenanthrene on soil surfaces in the presence of nanometer anatase TiO_2 under UV-light. Journal of Environmental Sciences 24(12), 2122-2126.

Gutierrez, A.M., Dziubla, T.D. and Hilt, J.Z. (2017) Recent advances on iron oxide magnetic nanoparticles as sorbents of organic pollutants in water and wastewater treatment. Rev. environ. health 32(1-2), 111-117.

He, H., Zhong, Y., Liang, X., Tan, W., Zhu, J. and Yan Wang, C. (2015) Natural Magnetite: an efficient catalyst for the degradation of organic contaminant. Sci. Rep. 5, 10139.

He, T., Ma, H., Zhou, Z., Xu, W., Ren, F., Shi, Z. and Wang, J. (2009) Preparation of ZnS-Fluoropolymer nanocomposites and its photocatalytic degradation of methylene blue. Polymer Degradation and Stability 94(12), 2251-2256.

He, Y., Basnet, P., Murph, S.E.H. and Zhao, Y. (2013) Ag Nanoparticle Embedded TiO_2 Composite Nanorod Arrays Fabricated by Oblique Angle Deposition: Toward Plasmonic Photocatalysis. ACS Applied Materials & Interfaces 5(22), 11818-11827.

Higuchi, T. (1990) Lignin biochemistry: biosynthesis and biodegradation. Wood Science and Technology 24(1), 23-63.

Hofrichter, M. (2002) lignin conversion by manganese peroxidase (MnP). Enzyme and Microbial Technology 30(4), 454-466.

Hou, L., Wang, L., Royer, S. and Zhang, H. (2016) Ultrasound-assisted heterogeneous Fenton-like degradation of tetracycline over a magnetite catalyst. Journal of Hazardous Materials 302, 458-467.

Illanes, A., Fernández-Lafuente, R., Guisán, J.M. and Wilson, L. (2008) Enzyme Biocatalysis, pp. 155-203, Springer.

Iqbal, W., Yang, B., Zhao, X., Rauf, M., Waqas, M., Gong, Y., Zhang, J. and Mao, Y. (2018) Controllable synthesis of graphitic carbon nitride nanomaterials for solar energy conversion and environmental remediation: the road travelled and the way forward. Catalysis Science & Technology 8(18), 4576-4599.

Janusz, G., Kucharzyk, K.H., Pawlik, A., Staszczak, M. and Paszczynski, A.J. (2013) Fungal laccase, manganese peroxidase and lignin peroxidase: gene expression and regulation. Enzyme and Microbial Technology 52(1), 1-12.

Jeevanandam, J., Barhoum, A., Chan, Y.S., Dufresne, A. and Danquah, M.K. (2018) Review on nanoparticles and nanostructured materials: history, sources, toxicity and regulations. Beilstein Journal of Nanotechnology 9(1), 1050-1074.

Jiang, N., Shang, R., Heijman, S.G.J. and Rietveld, L.C. (2018) High-silica zeolites for adsorption of organic micro-pollutants in water treatment: A review. Water Research 144, 145-161.

Jiemvarangkul, P., Zhang, W.-x. and Lien, H.-L. (2011) Enhanced transport of polyelectrolyte stabilized nanoscale zero-valent iron (nZVI) in porous media. Chemical Engineering Journal 170(2), 482-491.

Joseph, J.M., Destaillats, H., Hung, H.M. and Hoffmann, M.R. (2000) The sonochemical degradation of azobenzene and related azo dyes: rate enhancements via Fenton's eeactions. Journal of Physical Chemistry A 104(2), 301-307.

Kalaitzidou, K., Fukushima, H. and Drzal, L.T. (2007) A new compounding method for exfoliated graphite–polypropylene nanocomposites with enhanced flexural

properties and lower percolation threshold. Composites Science and Technology 67(10), 2045-2051.

Katchalski-Katzir, E. and Kraemer, D.M. (2000) Eupergit® C, a carrier for immobilization of enzymes of industrial potential. Journal of Molecular Catalysis B: Enzymatic 10(1-3), 157-176.

Kersten, P. and Cullen, D. (2007) Extracellular oxidative systems of the lignin-degrading Basidiomycete Phanerochaete chrysosporium. Fungal Genetics and Biology 44(2), 77-87.

Kirchhoff, M.M. (2003) Promoting green engineering through green chemistry. Environmental Science & Technology 37(23), 5349-5353.

Kirk, T.K. and Farrell, R.L. (1987) Enzymatic" combustion": the microbial degradation of lignin. Annual Reviews in Microbiology 41(1), 465-501.

Kiwi, S.S.S.a.J. (2001) Degradation of 2,4-dichlorophenol by immobilized iron catalysts. Water Research 35(8), 1994-2002.

Klimova, T., Gutiérrez, O., Lizama, L. and Amezcua, J. (2010) Advantages of ZrO_2- and TiO_2-SBA-15 mesostructured supports for hydrodesulfurization catalysts over pure TiO_2, ZrO_2 and SBA-15. Microporous and Mesoporous Materials 133(1), 91-99.

Koeller, K.M. and Wong, C.-H. (2001) Enzymes for chemical synthesis. Nature 409(6817), 232.

Kolpin, D.W., Furlong, E.T., Meyer, M.T., Thurman, E.M., Zaugg, S.D., Barber, L.B. and Buxton, H.T. (2002) Pharmaceuticals, hormones, and other organic wastewater contaminants in US streams, 1999− 2000: A national reconnaissance. Environmental Science & Technology 36(6), 1202-1211.

Koppenol, W.H., Stanbury, D.M. and Bounds, P.L. (2010) Electrode potentials of partially reduced oxygen species, from dioxygen to water. Free Radical Biology and Medicine 49(3), 317-322.

Kosma, C.I., Lambropoulou, D.A. and Albanis, T.A. (2014) Investigation of PPCPs in wastewater treatment plants in Greece: occurrence, removal and environmental risk assessment. Science of the Total Environment 466, 421-438.

Kumari, B. and Singh, D.P. (2016) A review on multifaceted application of nanoparticles in the field of bioremediation of petroleum hydrocarbons. Ecological Engineering 97, 98-105.

Kümmerer, K. (2010) Pharmaceuticals in the environment. Annual Review of Rnvironment and Resources 35, 57-75.

Kunamneni, A., Ghazi, I., Camarero, S., Ballesteros, A., Plou, F.J. and Alcalde, M. (2008) Decolorization of synthetic dyes by laccase immobilized on epoxy-activated carriers. Process Biochemistry 43(2), 169-178.

Lapworth, D., Baran, N., Stuart, M. and Ward, R. (2012) Emerging organic contaminants in groundwater: a review of sources, fate and occurrence. Environmental Pollution 163, 287-303.

Li, L., Wang, F., Lv, Y., Liu, J., Zhang, D. and Shao, Z. (2018) Halloysite nanotubes and Fe3O4 nanoparticles enhanced adsorption removal of heavy metal using electrospun membranes. Appl. Clay Sci. 161, 225-234.

Lloret, L., Eibes, G., Feijoo, G., Moreira, M., Lema, J. and Hollmann, F. (2011) Immobilization of laccase by encapsulation in a sol-gel matrix and its characterization and use for the removal of estrogens. Biotechnology Progress 27(6), 1570-1579.

Luo, W., Zhu, L., Wang, N., Tang, H., Cao, M. and She, Y. (2010) Efficient removal of organic pollutants with magnetic nanoscaled BiFeO3 as a reusable heterogeneous Fenton-like catalyst. Environmental Science & Technology 44(5), 1786-1791.

Luo, Z., Wang, J., Song, Y., Zheng, X., Qu, L., Wu, Z. and Wu, X. (2018) Remediation of Phenanthrene Contaminated Soil by a Solid State Photo-Fenton Reagent Based on Mesoporous Magnetite/Carboxylate-Rich Carbon Composites and Its Phytotoxicity Evaluation. ACS Sustainable Chemistry & Engineering 6(10), 13262-13275.

Manju, G.N., Anoop Krishnan, K., Vinod, V.P. and Anirudhan, T.S. (2002) An investigation into the sorption of heavy metals from wastewaters by polyacrylamide-grafted iron(III) oxide. Journal of Hazardous Materials 91(1), 221-238.

Marco-Urrea, E., Pérez-Trujillo, M., Cruz-Morató, C., Caminal, G. and Vicent, T. (2010) Degradation of the drug sodium diclofenac by Trametes versicolor pellets and identification of some intermediates by NMR. Journal of Hazardous Materials 176(1-3), 836-842.

Martínez, Á.T., Speranza, M., Ruiz-Dueñas, F.J., Ferreira, P., Camarero, S., Guillén, F., Martínez, M.J., Gutiérrez Suárez, A. and Río Andrade, J.C.d. (2005) Biodegradation of lignocellulosics: microbial, chemical, and enzymatic aspects of the fungal attack of lignin.

Matavos-Aramyan, S. and Moussavi, M. (2017) Advances in Fenton and Fenton based oxidation processes for industrial effluent contaminants control-a review. International Journal of Environmental Sciences and Natural Resources 2(4), 1-18.

McCallum, E.S., Krutzelmann, E., Brodin, T., Fick, J., Sundelin, A. and Balshine, S. (2017) Exposure to wastewater effluent affects fish behaviour and tissue-specific uptake of pharmaceuticals. Science of the Total Environment 605, 578-588.

Meeks, N.D., Smuleac, V., Stevens, C. and Bhattacharyya, D. (2012) Iron-Based Nanoparticles for Toxic Organic Degradation: Silica Platform and Green Synthesis. Industrial & Engineering Chemistry Research 51(28), 9581-9590.

Megharaj, M., Ramakrishnan, B., Venkateswarlu, K., Sethunathan, N. and Naidu, R. (2011) Bioremediation approaches for organic pollutants: a critical perspective. Environment International 37(8), 1362-1375.

Mester, T. and Tien, M. (2000) Oxidation mechanism of ligninolytic enzymes involved in the degradation of environmental pollutants. International Biodeterioration & Biodegradation 46(1), 51-59.

Mihailova, B., Bogachev, G., Marinova, V. and Konstantinov, L. (1999) Raman spectroscopy study of sillenites. II. Effect of doping on Raman spectra of $Bi_{12}TiO_20$. Journal of Physics and Chemistry of Solids 60(11), 1829-1834.

Modirshahla, N., Hassani, A., Behnajady, M.A. and Rahbarfam, R. (2011) Effect of operational parameters on decolorization of Acid Yellow 23 from wastewater by UV irradiation using ZnO and ZnO/SnO_2 photocatalysts. Desalination 271(1-3), 187-192.

Mthombeni, N.H., Mbakop, S. and Onyango, M.S. (2015) Magnetic zeolite-polymer composite as an adsorbent for the remediation of wastewaters containing vanadium. International Journal of Environmental Science and Development 6(8), 602.

Mueller, J.G., Cerniglia, C.E. and Pritchard, P.H. (1996) Bioremediation of environments contaminated by polycyclic aromatic hydrocarbons. Biotechnology Research Series 6, 125-194.

Munoz, M., De Pedro, Z.M., Casas, J.A. and Rodriguez, J.J. (2015) Preparation of magnetite-based catalysts and their application in heterogeneous Fenton oxidation–a review. Applied Catalysis B: Environmental 176, 249-265.

Muñoz, R., Alvarez, M.T., Muñoz, A., Terrazas, E., Guieysse, B. and Mattiasson, B. (2006) Sequential removal of heavy metals ions and organic pollutants using an algal-bacterial consortium. Chemosphere 63(6), 903-911.

Munter, R. (2001) Advanced oxidation processes–current status and prospects. Proceedings of the Estonian Academy of Sciences. Chemistry 50(2), 59-80.

Murray, K.E., Thomas, S.M. and Bodour, A.A. (2010) Prioritizing research for trace pollutants and emerging contaminants in the freshwater environment. Environmental Pollution 158(12), 3462-3471.

Nasreen, S.A.A.N., Sundarrajan, S., Nizar, S.A.S., Balamurugan, R. and Ramakrishna, S. (2013) Advancement in electrospun nanofibrous membranes modification and their application in water treatment. Membranes 3(4), 266-284.

Navalon, S., Alvaro, M. and Garcia, H. (2010) Heterogeneous Fenton catalysts based on clays, silicas and zeolites. Applied Catalysis B: Environmental 99(1), 1-26.

Nidheesh, P., Gandhimathi, R., Velmathi, S. and Sanjini, N. (2014) Magnetite as a heterogeneous electro Fenton catalyst for the removal of Rhodamine B from aqueous solution. RSC Advances 4(11), 5698-5708.

Nogueira, A.E., Longo, E., Leite, E.R. and Camargo, E.R. (2015) Visible-light photocatalysis with bismuth titanate ($Bi_{12}TiO_20$) particles synthesized by the oxidant peroxide method (OPM). Ceramics International 41(9, Part B), 12073-12080.

Nolan, N.T., Seery, M.K., Hinder, S.J., Healy, L.F. and Pillai, S.C. (2010) A Systematic Study of the Effect of Silver on the Chelation of Formic Acid to a Titanium Precursor and the Resulting Effect on the Anatase to Rutile Transformation of TiO_2. The Journal of Physical Chemistry C 114(30), 13026-13034.

Oller, I., Malato, S. and Sánchez-Pérez, J.A. (2011) Combination of Advanced Oxidation Processes and biological treatments for wastewater decontamination-A review. Science of the Total Environment 409(20), 4141-4166.

Osma, J.F., Toca-Herrera, J.L. and Rodríguez-Couto, S. (2010) Biodegradation of a simulated textile effluent by immobilised-coated laccase in laboratory-scale reactors. Applied Catalysis A: General 373(1-2), 147-153.

Özdemir, C., Öden, M.K., Şahinkaya, S. and Güçlü, D. (2011) The sonochemical decolorisation of textile azo dye CI Reactive Orange 127. Coloration Technology 127(4), 268-273.

Pan, X. and Xu, Y. J. (2013) Defect-Mediated Growth of Noble-Metal (Ag, Pt, and Pd) Nanoparticles on TiO2 with Oxygen Vacancies for Photocatalytic Redox Reactions under Visible Light. The Journal of Physical Chemistry C 117(35), 17996-18005.

Papadopoulos, A.E., Fatta, D. and Loizidou, M. (2007) Development and optimization of dark Fenton oxidation for the treatment of textile wastewaters with high organic load. Journal of Hazardous Materials 146(3), 558-563.

Paredes, L., Omil, F., Lema, J.M. and Carballa, M. (2018) What happens with organic micropollutants during UV disinfection in WWTPs? A global perspective from laboratory to full-scale. Journal of Hazardous Materials 342, 670-678.

Pérez, J., Munoz-Dorado, J., De la Rubia, T. and Martinez, J. (2002b) Biodegradation and biological treatments of cellulose, hemicellulose and lignin: an overview. International Microbiology 5(2), 53-63.

Pérez, M., Torrades, F., Domènech, X. and Peral, J. (2002a) Fenton and photo-Fenton oxidation of textile effluents. Water Research 36(11), 2703-2710.

Pignatello, J.J., Oliveros, E. and MacKay, A. (2006) Advanced oxidation processes for organic contaminant destruction based on the fenton reaction and related chemistry. Critical Reviews in Environmental Science and Technology 36(1), 1-84.

Qian, L. and Zhang, H. (2010) Green synthesis of chitosan-based nanofibers and their applications. Green Chemistry 12(7), 1207-1214.

Rabbani, M.M., Ahmed, I. and Park, S.J. (2016) Environmental Remediation Technologies for Metal-Contaminated Soils. Hasegawa, H., Rahman, I. and Rahman, M. (eds), Springer, Tokyo.

Radoičić, M., Ćirić-Marjanović, G., Spasojević, V., Ahrenkiel, P., Mitrić, M., Novaković, T. and Šaponjić, Z. (2017) Superior photocatalytic properties of carbonized PANI/TiO2 nanocomposites. Applied Catalysis B 213, 155-166.

Reinhammar, B.R. (1972) Oxidation-reduction potentials of the electron acceptors in laccases and stellacyanin. Biochimica et Biophysica Acta (BBA)-Bioenergetics 275(2), 245-259.

Reungoat, J., Escher, B., Macova, M., Argaud, F., Gernjak, W. and Keller, J. (2012) Ozonation and biological activated carbon filtration of wastewater treatment plant effluents. Water Research 46(3), 863-872.

Rizzo, L., Malato, S., Antakyali, D., Beretsou, V.G., Đolić, M.B., Gernjak, W., Heath, E., Ivancev-Tumbas, I., Karaolia, P. and Ribeiro, A.R.L. (2018) Consolidated vs new advanced treatment methods for the removal of contaminants of emerging concern from urban wastewater. Science of the Total Environment.

Rodríguez-Delgado, M. and Ornelas-Soto, N. (2017) Green Technologies and Environmental Sustainability, pp. 45-65, Springer.

Rong, M.Z., Ji, Q.L., Zhang, M.Q. and Friedrich, K. (2002) Graft polymerization of vinyl monomers onto nanosized alumina particles. European Polymer Journal 38(8), 1573-1582.

Saleh, N., Phenrat, T., Sirk, K., Dufour, B., Ok, J., Sarbu, T., Matyjaszewski, K., Tilton, R.D. and Lowry, G.V. (2005) Adsorbed Triblock Copolymers Deliver Reactive Iron Nanoparticles to the Oil/Water Interface. Nano Letters 5(12), 2489-2494.

Shi, Y., Zhang, T., Ren, H., Kruse, A. and Cui, R. (2018) Polyethylene imine modified hydrochar adsorption for chromium (VI) and nickel (II) removal from aqueous solution. Bioresource Technology 247, 370-379.

Shipley, H., Engates, K. and M. Guettner, A. (2010) Study of iron oxide nanoparticles in soil for remediation of arsenic. J. Nanopart. Res. 13, 2387-2397.

Siddique, M., Farooq, R. and Price, G.J. (2014) Synergistic effects of combining ultrasound with the Fenton process in the degradation of Reactive Blue 19. Ultrasonics Sonochemistry 21(3), 1206-1212.

Singh, P.P. and Ambika (2018) New Polymer Nanocomposites for Environmental Remediation. Hussain, C.M. and Mishra, A.K. (eds), pp. 223-241, Elsevier.

Sinsawat, A., Anderson, K.L., Vaia, R.A. and Farmer, B.L. (2003) Influence of polymer matrix composition and architecture on polymer nanocomposite formation: Coarse-

grained molecular dynamics simulation. Journal of Polymer Science B 41(24), 3272-3284.

Skiker, R., Zouraibi, M., Saidi, M. and Ziat, K. (2018) Facile coprecipitation synthesis of novel $Bi_{12}TiO_20/BiFeO_3$ heterostructure serie with enhanced photocatalytic activity for removal of methyl orange from water. Journal of Physics and Chemistry of Solids 119, 265-275.

Somensi, C.A., Simionatto, E.L., Bertoli, S.L., Wisniewski Jr, A. and Radetski, C.M. (2010) Use of ozone in a pilot-scale plant for textile wastewater pre-treatment: Physico-chemical efficiency, degradation by-products identification and environmental toxicity of treated wastewater. Journal of Hazardous Materials 175(1-3), 235-240.

Taboada-Puig, R., Lu-Chau, T.A., Eibes, G., Feijoo, G., Moreira, M.T. and Lema, J.M. (2015) Continuous removal of endocrine disruptors by versatile peroxidase using a two-stage system. Biotechnology Progress 31(4), 908-916.

Thakur, A.K., Nisola, G.M., Limjuco, L.A., Parohinog, K.J., Torrejos, R.E.C., Shahi, V.K. and Chung, W.-J. (2017) Polyethylenimine-modified mesoporous silica adsorbent for simultaneous removal of Cd(II) and Ni(II) from aqueous solution. Journal of Industrial and Engineering Chemistry 49, 133-144.

Tijani, J.O., Fatoba, O.O. and Petrik, L.F. (2013) A review of pharmaceuticals and endocrine-disrupting compounds: sources, effects, removal, and detections. Water, Air, & Soil Pollution 224(11), 1770.

Touahar, I.E., Haroune, L., Ba, S., Bellenger, J.-P. and Cabana, H. (2014) Characterization of combined cross-linked enzyme aggregates from laccase, versatile peroxidase and glucose oxidase, and their utilization for the elimination of pharmaceuticals. Science of the Total Environment 481, 90-99.

Tran, N.H., Reinhard, M. and Gin, K.Y.-H. (2018) Occurrence and fate of emerging contaminants in municipal wastewater treatment plants from different geographical regions-a review. Water Research 133, 182-207.

Türkmen, D., Yılmaz, E., Öztürk, N., Akgöl, S. and Denizli, A. (2009) Poly(hydroxyethyl methacrylate) nanobeads containing imidazole groups for removal of Cu(II) ions. Materials Science and Engineering: C 29(6), 2072-2078.

Tyre, W., Watts, B. J. and Miller, G. (1991) Treatment of Four Biorefractory Contaminants in Soils Using Catalyzed Hydrogen Peroxide. J. Environ. Qual. 20(4), 832-838.

UNICEF, W.a. (2017) Progress on drinking water, sanitation and hygiene: 2017 update and SDG baselines.

Uthandi, S., Saad, B., Humbard, M.A. and Maupin-Furlow, J.A. (2010) LccA, an archaeal laccase secreted as a highly stable glycoprotein into the extracellular medium by Haloferax volcanii. Appl. Environ. Microbiol. 76(3), 733-743.

Velichkova, F., Julcour-Lebigue, C., Koumanova, B. and Delmas, H. (2013) Heterogeneous Fenton oxidation of paracetamol using iron oxide (nano) particles. Journal of Environmental Chemical Engineering 1(4), 1214-1222.

Von Gunten, U. (2003) Ozonation of drinking water: Part I. Oxidation kinetics and product formation. Water Research 37(7), 1443-1467.

Wariishi, H., Akileswaran, L. and Gold, M.H. (1988) Manganese peroxidase from the basidiomycete Phanerochaete chrysosporium: spectral characterization of the oxidized states and the catalytic cycle. Biochemistry 27(14), 5365-5370.

Watts, R.J., Udell, M.M., Kong, S. and Leung, S.W. (1999) Fenton-Like Soil Remediation Catalyzed by Naturally Occurring Iron Minerals. Environmental Engineering Science 16(1), 93-103.

Wei, Y., Han, B., Hu, X., Lin, Y., Wang, X. and Deng, X. (2012) Synthesis of Fe3O4 Nanoparticles and their Magnetic Properties. Procedia Eng. 27, 632-637.

Wesenberg, D., Kyriakides, I. and Agathos, S.N. (2003) White-rot fungi and their enzymes for the treatment of industrial dye effluents. Biotechnology Advances 22(1-2), 161-187.

Wong, D.W.S. (2009) Structure and Action Mechanism of Ligninolytic Enzymes. Applied Biochemistry and Biotechnology 157(2), 174-209.

WWAP, U. (2017) Wastewater: the Untapped Resource, The United Nations World Water Development Report, UNESCO, Paris.

Xu, H.-y., Prasad, M. and Liu, Y. (2009) Schorl: A novel catalyst in mineral-catalyzed Fenton-like system for dyeing wastewater discoloration. Journal of Hazardous Materials 165(1-3), 1186-1192.

Xu, L. and Wang, J. (2012) Magnetic nanoscaled Fe3O4/CeO2 composite as an efficient Fenton-like heterogeneous catalyst for degradation of 4-chlorophenol. Environmental Science & Technology 46(18), 10145-10153.

Yan, Z., Haijia, S. and Tianwei, T. (2007) Adsorption behaviors of the aminated chitosan adsorbent. Korean Journal of Chemical Engineering 24(6), 1047-1052.

Yang, G.C.C. and Wu, M.-Y. (2011) Injection of nanoscale Fe3O4 slurry coupled with the electrokinetic process for remediation of NO_3^- in saturated soil: Remediation performance and reaction behavior. Sep. Purif. Technol. 79(2), 272-277.

Yang, X., Tian, P.-F., Zhang, C., Deng, Y.-q., Xu, J., Gong, J. and Han, Y. F. (2013) Au/carbon as Fenton-like catalysts for the oxidative degradation of bisphenol A. Applied Catalysis B: Environmental 134, 145-152.

Yoshida, H. (1883) LXIII.—chemistry of lacquer (Urushi). Part I. communication from the chemical society of Tokio. Journal of the Chemical Society, Transactions 43, 472-486.

Zang, H., Miao, C., Shang, J., Liu, Y. and Liu, J. (2018) Structural effects on the catalytic activity of carbon-supported magnetite nanocomposites in heterogeneous Fenton-like reactions. RSC Advances 8(29), 16193-16201.

Zhang, J., Zhuang, J., Gao, L., Zhang, Y., Gu, N., Feng, J., Yang, D., Zhu, J. and Yan, X. (2008) Decomposing phenol by the hidden talent of ferromagnetic nanoparticles. Chemosphere 73(9), 1524-1528.

Zhang, L., Tse, M.S. and Tan, O.K. (2014) Facile in situ synthesis of visible light-active Pt/C–TiO_2 nanoparticles for environmental remediation. Journal of Environmental Chemical Engineering 2(2), 1214-1220.

Zhao, F., Tang, W.Z., Zhao, D., Meng, Y., Yin, D. and Sillanpää, M. (2014) Adsorption kinetics, isotherms and mechanisms of Cd(II), Pb(II), Co(II) and Ni(II) by a modified magnetic polyacrylamide microcomposite adsorbent. Journal of Water Process Engineering 4, 47-57.

Zhou, J., Zou, Z., Ray, A.K. and Zhao, X.S. (2007) Preparation and Characterization of Polycrystalline Bismuth Titanate $Bi_{12}TiO_20$ and Its Photocatalytic Properties under Visible Light Irradiation. Industrial & Engineering Chemistry Research 46(3), 745-749.

Zhu, X., Zhang, J. and Chen, F. (2011) Study on visible light photocatalytic activity and mechanism of spherical $Bi_{12}TiO_20$ nanoparticles prepared by low-power hydrothermal method. Applied Catalysis B 102(1), 316-322.

Zucca, P., Rescigno, A., Olianas, A., Maccioni, S., Sollai, F.A. and Sanjust, E. (2011) Induction, purification, and characterization of a laccase isozyme from Pleurotus sajor-caju and the potential in decolorization of textile dyes. Journal of Molecular Catalysis B: Enzymatic 68(2), 216-222.

USC
UNIVERSIDADE
DE SANTIAGO
DE COMPOSTELA

2 Chapter 2

MATERIALS AND METHODS

SUMMARY

This chapter summarizes a detailed description of the chemicals and the methodology used during the experimental work carried out in this thesis. From the characterization techniques of the catalyst and supports to organic micropollutants analysis and conventional parameters of physical-chemical characterization of wastewater, such as chemical oxygen demand, total nitrogen and organic carbon, total and volatile suspended solids, pH, which were determined according to the Standard Methods for the Examination of Water and Wastewater. The specific analytical methods or the calculations used in a single part of the research work and the corresponding experimental set-ups are described in the corresponding chapters.

OUTLINE

2.1 Chemicals

All chemicals were purchased from commercial suppliers and used without further purification. For the enzyme immobilization procedure: 2,2'-azinobis-3-ethylbenzothiazoline-6-sulfonate (ABTS) ($C_{18}H_{24}N_6O_6S_4$, ≥98%), (3-aminopropyl) triethoxysilane (APTES) ($H_2N(CH_2)_3Si(OC_2H_5)_3$, ≥98%), glutaraldehyde ($OHC(CH_2)_3CHO$, 25%) and sodium malonate (≥98%) were obtained from Sigma-Aldrich. 2,6-dimethoxyphenol (DMP; 97%) was provided by Fluka (Buchs, Switzerland). Manganese (II) sulphate 1-hydrate ($MnSO_4.H_2O$) from Panreac.

The chemicals in the buffer solution were anhydrous sodium hydrogen phosphate (≥99% of purity) and anhydrous sodium di-hydrogen phosphate (≥99% of purity) from Panreac, acetic acid (98% of purity) from J.T. Baker, citric acid from Vorquimia and sodium acetate (≥99% of purity) from Sigma-Aldrich.

The chemicals used during the synthesis of catalysts, Fenton and photocatalysts reactions were tetraethyl orthosilicate (TEOS) ($Si(OC_2H_5)_4$, 98%), iron(III) chloride hexahydrate ($FeCl_3{\cdot}6H_2O$, 99%), hydrochloric acid (HCl, 37%), ferrocene ($Fe(C_5H_5)_2$, 98%), cyclohexane (C_6H_{12}, ≥99.8%), IGEPAL CO-520 (polyoxyethylene (5) nonylphenylether, branched; $(C_2H_4O)_n{\cdot}C_{15}H_{24}O$, n~5), isooctane (2,2,4-Trimethylpentane, $(CH_3)_2CHCH_2C(CH_3)_3$, ≥99%), iron(II) sulphate heptahydrate ($FeSO_4{\cdot}7H_2O$, 99%), zinc(II) acetate dihydrate ($Zn(CH_3CO_2)_2{\cdot}2H_2O$, >98%), absolute ethanol (CH_3CH_2OH, >99.8%), tetramethylammonium hydroxide solution (TMAOH, 10% wt in water), dimethyl sulfoxide (DMSO) $(CH_3)_2SO$, ≥99.7%), *tert*-butanol (*t*-butanol) ($(CH_3)_3COH$, ≥99.5%), L-ascorbic acid (AH_2) ($C_6H_8O_6$, 99%), tetrachloro-1,4-benzoquinone (BQ) ($C_6Cl_4O_2$, 99%) and 2-propanol ($(CH_3)_2CHOH$, ≥99.5%) were obtained from Sigma-Aldrich; methanol (MeOH) (CH_3OH) from J.T. Baker; hydrogen peroxide solution (H_2O_2, 30% wt), sodium azide (NaN_3, 99%) and potassium iodide (KI) from Panreac; ortho phosphoric acid (85%) and ammonium hydroxide solution (NH_4OH, 28% wt in water) from Fluka; diethylene glycol ($(HOCH_2CH_2)_2O$, DEG, 99%) was provided by Alfa Aesar; acetone (≥99%) was purchased from Scharlau and oleic acid (extra pure) from Merck.

Recalcitrant model compounds: C.I. Reactive Blue 19 (RB19) ($C_{22}H_{16}N_2Na_2O_{11}S_3$, ~50%), Methyl Green (MG) ($C_{27}H_{35}BrClN_3{\cdot}ZnCl_2$, ~85%), C.I. Orange II (OII)

($C_{16}H_{11}N_2O_4SNa$, ~85%), C.I. Methyl Red (MR) ($C_{15}H_{15}N_3O_2$, ACS grade reagent), Rhodamine 123 (R123) ($C_{21}H_{17}ClN_2O_3$), Bisphenol A (BPA) ($(CH_3)_2C(C_6H_4OH)_2$, ≥99%), estrone (E1, ≥99%), 17β-estradiol (E2, ≥98%), 17α-ethynylestradiol (EE2, ≥98%), sulfamethoxazole (SMX) ($C_{10}H_{11}N_3O_3S$, analytical standard), carbamazepine (CBZ) ($C_{15}H_{12}N_2O$) and ibuprofen (IBP) ($C_{13}H_{18}O_2$) were purchased from Sigma-Aldrich. Pyrene (PYR, ≥98%) was obtained from Janssen Chimica. Chemical structures and main physicochemical properties of selected compounds are displayed in Table A2.1 (dyes) and Table A2.2, in Annex section.

2.2 Catalyst and supports characterization

The nanostructured catalyst tested in Chapters 4-7 were synthetized by the Laboratory of Magnetism and Nanotechnology of the Departments of Applied Physics and Physical Chemistry, Universidade de Santiago de Compostela (USC) and the characterization were made by the Scientific-Technological Support Center, CACTUS, USC.

2.2.1 X-ray diffraction

The X-ray diffraction (XRD) study of the crystalline phases was carried out on powder samples using a Philips (Amsterdam, Holland) PW-1710 diffractometer (Cu Kα radiation source, λ= 1.54186 Å).

Measurements were performed in air at room temperature and collected in the 2θ angle range between 10° and 80°, with steps of 0.021 and 5-10 s per step. In the case of mesoporous matrix structure, the characterization of the crystalline phases was analyzed by low-angle XRD in a PANalytical X'Pert Powder Empyrean, in a 2θ range between 0.25° and 6°, and a step size of 0.01° (5 s per step).

2.2.2 Thermogravimetry

The dispersion concentration of the magnetic nanocatalysts was obtained by thermogravimetric analysis (TGA). The thermogravimetric curves were recorded with a Perkin-Elmer TGA 7 analyzer, operating under N_2 atmosphere, with increasing temperature up to 850 °C, at a scanning rate of 10 °C min^{-1}.

2.2.3 Morphological study

Materials were characterized by scanning electron microscopy (SEM) using a Zeiss FE-SEM ULTRA Plus (5 kV) microscope in order to determine their morphology. Moreover, transmission electron microscopy (TEM) images were taken with a JEOL JEM-1011 transmission electron microscope (Tokyo, Japan) operating at an accelerating voltage of 100 kV. High-angle annular dark field-scanning transmission electron micrographs (HAADF-STEM) and elemental mapping were taken with a Zeiss Libra 200 FE OMEGA TEM operating at an accelerating voltage of 200 kV and equipped with an energy dispersive X-ray detector (EDS). One drop of a diluted sample solution was deposited on an amorphous carbon film on 400 mesh copper grids and allowed to evaporate at room temperature.

2.2.4 Pore size distribution

Pore size distribution and specific surface area in the case of SBA-15 nanostructured catalysts of Chapter 4 were calculated from N_2 adsorption-desorption isotherms obtained using a Quantachrome Autosorb IQ2 instrument.

2.2.5 Magnetization curves

Magnetization curves as a function of the applied magnetic field (up to 10 kOe) were obtained with a DMS Model 1660 Vibrating Sample Magnetometer (VSM) for Chapter 4 catalyst and with a Quantum Design Physical Property Measurement System (PPMS) for Chapter 5 photocatalysts, both in dry samples at room temperature.

2.2.6 Zeta potential

The zeta potential values of selected catalyst were measured at different pH with a Malvern Panalytical Zetasizer Nano at 20 °C.

2.2.7 Iron content

The iron content in the nanostructured catalysts samples was determined by Flame Atomic Absorption Spectroscopy (FAAS) in a Perkin-Elmer 3110 Atomic Absorption Spectrometer. Inductively coupled plasma-optical emission

spectrometry (ICP-OES) was used for the determination of Fe, Zn and TiO_2 in the photocatalysts, with a Perkin-Elmer Optima 3300 DV equipped with an auto-sampler Perkin-Elmer AS91. To determine the possible loss of the catalyst expressed as iron concentration (mg Fe L^{-1}) in the treated effluent, Fe was also determined by ICP-OES with a Perkin-Elmer Optima 3300 DV equipped with an autosampler Perkin-Elmer AS91.

2.3 Organic micropollutants analysis

2.3.1 Spectrophotometry

Absorbance measurements were performed on a BioTek PowerWave XS2 microplates spectrophotometer (Winooski, VT, USA) to monitor laccase activity in Chapter 3 and the color removal spectrum in the case of dyes removal tests. Moreover, peroxidase activity was obtained by monitoring DMP oxidation in a UV-Visible spectrophotometer UV-1603 Shimadzu (Japan).

2.3.2 Liquid chromatography

The liquid chromatography system consisted in a Jasco XLC High Performance Liquid Chromatography (HPLC) (Jasco Analitica, Madrid, Spain) equipped with a diode array detector 3110 MD and a Gemini reversed-phase column (150 mm × 4.6 mm, particle size: 3 µm) from Phenomenex (supplied by Jasco Analitica, Madrid, Spain). Aliquots (200 µL) of the aqueous samples collected during the degradation processes were quantified by HPLC and processed using HP ChromNav data software.

For E1, E2, EE2, BPA, CBZ, IBP and SMX, the detection wavelength in the range of 210-278 nm and the gradient elution flow (0.8 mL min^{-1}) started with 20% acetonitrile in water, which was kept for 1 min, followed by an increase to 90% acetonitrile within 4 min. This concentration remained constant for 5 min, and then linearly decreased back to the initial concentration after 14 min. In the case of PYR, the detection wavelength was 254 nm and the gradient elution flow (1.0 mL min^{-1}) started with 20% acetonitrile in water, followed by an increase to 90%.

2.4 Conventional physicochemical parameters

This section describes the analytical methods used to measure the conventional parameters to characterize the liquid phase. When measuring soluble compounds, liquid samples are filtered through a mixed cellulose ester filter of 0.45 µm pore size (HA, Millipore) to remove suspended solids.

2.4.1 Chemical Oxygen Demand

Chemical Oxygen Demand (COD) is defined as the amount of oxygen required to oxidize the organic matter present in a sample using a chemical oxidant (potassium dichromate, $K_2Cr_2O_7$) under controlled conditions, and is determined following the method described by Soto et al. (1989), which is a modification of the method 5220-D described in the *Standard Methods for the Examination of Water and Wastewater* (APHA-AWWA-WEF 2012). A catalyst (silver sulphate, Ag_2SO_4) in acid medium is used to improve the oxidation of some organic compounds during the digestion of the samples. After digestion, the remaining unreduced $K_2Cr_2O_7$ is titrated with ferrous ammonium sulphate (FAS) solution to determine the amount of $K_2Cr_2O_7$ consumed, being the amount of oxidable matter calculated in terms of oxygen equivalents. The overall reaction is:

$$Cr_2O_7^{2-} + \text{Organic matter} + 14\ H^+ \xrightarrow{Ag_2SO_4} 2\ Cr^{3+} + CO_2 + 7H_2O$$

Reagents

- Concentrated potassium dichromate digestion solution: 10.23 g of $K_2Cr_2O_7$ and 33 g of $HgSO_4$ are dissolved into 500 mL of distilled water. Afterwards, 167 mL of concentrated H_2SO_4 is added. The solution obtained is cooled down to room temperature before dilution to 1 L.
- Diluted potassium dichromate digestion solution: 2.44 g of $K_2Cr_2O_7$ and 17 g of $HgSO_4$ are dissolved into 500 mL of distilled water. Afterwards, 167 mL of concentrated H_2SO_4 is added. The obtained solution was cooled down to room temperature before dilution to 1 L.
- Sulfuric acid catalytic solution: 10.70 g of Ag_2SO_4 are dissolved into 1 L of concentrated H_2SO_4. The solution should be prepared at least two days before use.

- Ferroin indicator solution: 1.49 g of $C_{18}H_8N_2.H_2O$ (phenanthroline monohydrate) and 0.69 g of $FeSO_4.7H_2O$ are dissolved in 100 mL of distilled water.
- Standard potassium dichromate solution 0.05 N: 1.23 g of $K_2Cr_2O_7$, previously dried at 105 °C for 2 h, are dissolved in 500 mL of distilled water.
- Concentrated FAS solution (0.035 N): 13.72 g of $Fe(NH)_4(SO)_2.6H_2O$ are dissolved in distilled water and 20 mL of concentrated H_2SO_4 are added. Finally, distilled water is added to reach a total volume of 1 L.
- Diluted FAS solution (0.016 N): 6.28 g of $Fe(NH)_4(SO)_2.6H_2O$ are dissolved in distilled water and 20 mL of concentrated H_2SO_4 are added. Finally, distilled water is added to reach a total volume of 1 L.

Determination procedure

A volume of 2.5 mL of sample is placed in a 10-mL Pyrex® glass tube. Then, 1.5 mL of digestion solution (concentrated or diluted according to the organic matter content of the sample) is added, and 3.5 mL of sulfuric acid reagent is slowly added on the wall of the tube slightly inclined. A blank sample using distilled water is prepared in the same way and it acts as "reference" value. Pyrex® glass tubes are tightly sealed with Teflon® and covered with Bakelite® caps to avoid the leakage of produced gases. Then, the tubes are shaken and placed in the thermodigester (VELP ECO16) preheated to 150 °C. After 2 h of digestion, the tubes are cooled to room temperature, transferred to a beaker and, after the addition of 1-3 drops of ferroin indicator, the solution is titrated under rapid stirring with the corresponding standard FAS solution. The end-point is visualized by a sharp color change from blue-green to reddish brown.

The COD value (mg COD L^{-1}) of the samples is calculated using the equation below,

$$COD = \frac{(A-B)\cdot N_{FAS}\cdot 8000}{V} \quad (1)$$

where A is the volume (mL) of FAS consumed by the blank; B is the volume of FAS consumed by the analyzed sample; 8000 is the milliequivalent weight of oxygen in 1,000 mL L^{-1}; N_{FAS} is the normality of the FAS and V is the volume (mL) of the sample.

The concentration of the FAS solution, expressed as normality, is calculated using Equation 2,

$$N_{FAS} = \frac{V_{K_2Cr_2O_7} N_{K_2Cr_2O_7}}{V_{FAS}} \quad (2)$$

where V_{FAS} is volume of FAS solution consumed in the titration (mL); $V_{K_2Cr_2O_7}$ is the added volume of the standard $K_2Cr_2O_7$ solution (5 mL) and $N_{K_2Cr_2O_7}$ is the normality of the standard $K_2Cr_2O_7$ solution (0.05 N).

The FAS solutions were daily standardized as follows: 3.5 mL of H_2SO_4 was mixed with 5 mL of distilled water, cooled down, and then 5 mL of standard $K_2Cr_2O_7$ solution was added. Then, the mixture was titrated after the addition of 1-3 drops of ferroin solution, to visualize the end-point by the color change.

2.4.2 Total Organic Carbon

Organic carbon in water and wastewater samples may include a variety of organic compounds in different oxidation states. Total Organic Carbon (TOC) measurement is performed according to method 5310 of the *Standard Methods for the Examination of Water and Wastewater* (APHA-AWWA-WEF 2012). To determine the quantity of organically bound carbon in a liquid sample, the organic molecules must be broken down and converted to a single carbon molecular form that can be measured quantitatively. The TOC concentration is determined by a Shimadzu analyzer (TOC-L CSN) as the difference between the Total Carbon (TC) and the Inorganic Carbon (IC) concentrations. The instrument is connected to an automated sampler (Shimadzu, ASI-L). Dissolved carbon forms are measured as the equipment only accepts filtered samples.

TC concentrations are determined from the amount of CO_2 produced during the combustion of the sample at 720 °C, using platinum as the catalyst. High purity air is used as carrier gas with a flow of 150 mL min^{-1}. The streams are cooled and dried at room temperature. The CO_2 produced is detected with a non-dispersive infrared (NDIR) analyzer, which generates a peak with an area related to the concentration of the compounds. The IC concentration is obtained from the CO_2 produced with HCl 1 N reaction at room temperature. Then, the produced CO_2 is

detected with the NDIR analyzer. The detection limits of the equipment for TC and IC are 50 and 4 µg C L^{-1}, respectively.

A curve comprising calibration points in the range of 0.5 to 1,000 mg C L^{-1} is used for the quantification of the carbon compounds. Standard solutions of potassium phthalate ($C_8H_5KO_4$) and a mixture of sodium carbonate and bicarbonate (Na_2CO_3/$NaHCO_3$, 3:4 w/w) were used for TC and IC determination, respectively.

2.4.3 Total Nitrogen

Total nitrogen (TN) is determined on the same Shimadzu analyzer (TOC-L CSN) as the TOC concentration. The sample is injected into the combustion tube where oxidative pyrolysis occurs at 720 °C, to convert all nitrogen compounds into nitric oxide (NO) gas. Dinitrogen gas does not become NO under these conditions. The carrier gas together with the produced NO are cooled by an electronic dehumidifier to eliminate any possible condensation.

The NO obtained is forced to react with in-situ produced ozone (O_3) obtaining nitrogen dioxide in an unstable excited state (NO_2*). The NO_2* reaches its elemental state by emitting a photon in the range of 590 - 299 nm, which is detected by a chemiluminescence detector (CLD). The calibration is carried out by a standard commercial solution of ammonium (Merck) in the range of 0.5-777 mg N L^{-1}. The analyzer detection limit is 20 µg TN L^{-1}.

2.4.4 Inorganic ions

The anions nitrite (NO_2^-, NO_3^-, Cl^-, PO_4^{3-} and SO_4^{2-}) and the cations sodium (Na^+, K^+, Mg^{2+}, Br^-, Ca^{2+} and NH_4^+) in liquid phase were determined by using ion chromatography (ICG). An 816 Advanced Compact IC system equipped with CO_2 suppressor (MCS 853, Metrohm) and Advanced Sampler Procesor (Metrohm, Switzerland), were used for measuring anions and cations.

Furthermore, Metrosep A Supp 5-250 and Metrosep C3-250 columns were used for detecting cations and anions, respectively. Table 1.1 shows the calibration ranges for the different inorganic ions concentrations.

Table 1.1 Calibration range of concentrations for the different inorganic ions (m L^{-1})

	Cl^-	Br^-	PO_4^{3-}	SO_4^{2-}	NO_3^-	NO_2^-	Na^+	K^+	Mg^{2+}	Ca^{2+}	NH_4^+
Upper limit (mg L^{-1})	100	20	50	150	50	5	150	50	50	50	10
Lower limit (mg L^{-1})	1.0	0.2	0.5	1.5	0.5	0.05	1.5	0.5	0.5	0.5	0.1

2.4.5 pH

The pH measurements are performed with an electrode (Crison Instruments GLP-21, USA) equipped with an automatic compensatory temperature device and connected to a measurement instrument. The sensitivity of the instrument is 0.01 pH units. The electrode is calibrated at room temperature with two standard buffer solutions of pH 7.0 and 4.0.

2.4.6 Conductivity

The conductivity measurements were carried out with a SensION^{TM}+ EC5 portable (Hach, USA), consisting in a 2-pole platinum cell with a built-in temperature sensor for conductivity measurements in general aqueous samples in a range of 0.2 µS cm^{-1} to 200 mS cm^{-1}.

2.4.7 Solid concentration

The Total Suspended Solids (TSS) and the Volatile Suspended Solids (VSS) concentrations are determined according to the method 2540 described in the *Standard Methods for the Examination of Water and Wastewater* (APHA-AWWA-WEF 2012).

Determination procedure

For the determination of the TSS, a known volume of the sample is collected to obtain a residue. Firstly, a fibreglass filter (Merck Millipore APFC04700, 47 mm of diameter, 1.2 µm of pore size) is placed in a muffle furnace (J.P. Selecta, Select-Horn-TFT) at 550°C for half an hour to remove humidity and get a constant weight. Then, it is placed inside a desiccator to achieve room temperature and then weighed to obtain the value of F_0.

Then, a well-mixed volume of sample (V_0) is filtered through the dried fiberglass filter of known weight. The residue retained on the filter is dried for at least 2 hours at 105 °C in an oven (J.P. Selecta 2000210) to constant weight. After that, it is located inside a desiccator until it reaches room temperature. Finally, it is weighed to obtain the value of F_1. The increase in the weight of the filter represents the TSS. The concentration of TSS is determined according to Equation 3.

$$TSS = \frac{F_1 - F_0\ (mg)}{V_0\ (mL)} \quad (3)$$

Finally, for the determination of the VSS, the filter previously dried to obtain the TSS concentration is burned inside a muffle furnace at 550°C for half an hour. Then, it is located inside the desiccator to reach room temperature and weighed to obtain the value of F_2. The weight loss during ignition corresponds to the VSS content and its concentration is determined according to Equation 4.

$$VSS = \frac{F_1 - F_2\ (mg)}{V_0\ (mL)} \quad (4)$$

2.5 Annex

Table 2.1 Structures and physicochemical properties of selected dyes

Dye	Structure	Classification and characteristics	References
Reactive blue 19 (RB19)	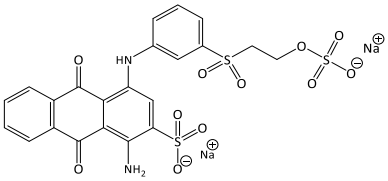	Anthraquinone *MW: 626.5 λ: 592	Liu et al. (2016)
Methyl Red (MR)	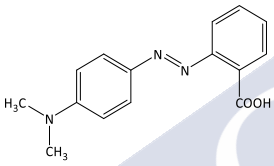	Azo MW: 269.3 λ: 520-540	Lachheb et al. (2002)
Methyl green (MG)	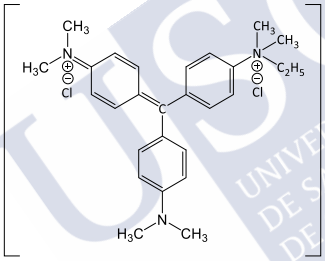	Triphenylmethane MW: 653.2 λ: 632	Nezamzadeh-Ejhieh and Shams-Ghahfarokhi (2012)
Rhodamine 123 (R123)	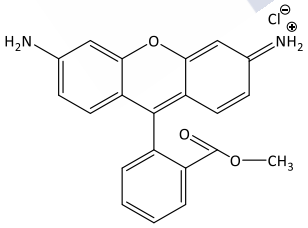	Rhodamine MW: 380.8 λ: 500	Ugwu et al. (2016), Van de Linde et al. (2011)
Orange II (OII)	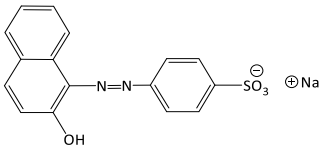	Azo MW: 350.3 λ: 473	Ong et al. (2005), Daneshvar et al. (2003)

*MW: g mol^{-1}; Maximum absorbance wavelength (λ): nm

Table 2.2 Structures and physicochemical characteristics of the selected compounds

Compound	Structure	MW* (g mol^{-1})	S_w* (mg L^{-1})	pK_a	References
Estrone (E1)	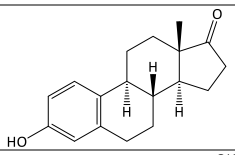	270.4	13	10.4	Hurwitz and Liu (1977), Racz and Goel (2010), Lai et al. (2000)
17α-Estradiol (E2)	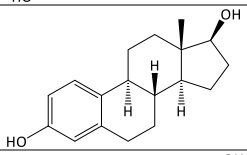	272.4	13	10.5	Hurwitz and Liu (1977), Racz and Goel (2010), Lai et al. (2000)
Ethinyl estradiol (EE2)	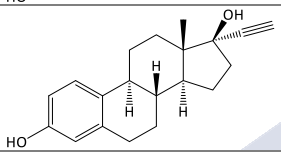	296.4	4.8	10.5-10.7	Hurwitz and Liu (1977), Racz and Goel (2010), Lai et al. (2000)
Bisphenol A (BPA)	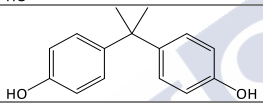	228.3	120-300	[1]9.6, [2]10.2	Lin et al. (2009), Zhang et al. (2006)
Sulfa-methoxazole (SMX)	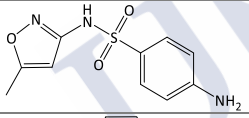	253.3	<1000	[1]1.8, [2]5.57	Dantas et al. (2008), NTP (1992)
Pyrene (PYR)	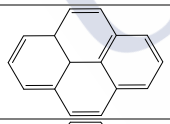	202.25	0.135	-	Miller et al. (1985)
Carbamazepine (CBZ)	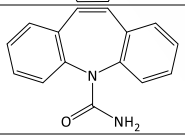	236.3	125	13.9	Deng et al. (2013), Wang and Wang (2016)
Ibuprofen (IBP)	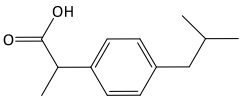	206.3	2.3 10^3**	4.4-4.9	Madhavan et al. (2010), Jallouli et al. (2018), Yazdanian et al. (2004)

*Molecular weight (MW); Solubility in water (S_w) at 20-25 °C (S_w);
**Ibuprofen S_w was measured at pH 7.4

2.6 References

APHA-AWWA-WEF (2012) Standard methods for the examination of water and wastewater, American Public Health Association, Washington DC.

Daneshvar, N., Ashassi-Sorkhabi, H. and Tizpar, A. (2003) Decolorization of orange II by electrocoagulation method. Separation and Purification Technology 31(2), 153-162.

Dantas, R.F., Contreras, S., Sans, C. and Esplugas, S. (2008) Sulfamethoxazole abatement by means of ozonation. Journal of Hazardous Materials 150(3), 790-794.

Deng, J., Shao, Y., Gao, N., Xia, S., Tan, C., Zhou, S. and Hu, X. (2013) Degradation of the antiepileptic drug carbamazepine upon different UV-based advanced oxidation processes in water. Chemical Engineering Journal 222, 150-158.

Hurwitz, A. and Liu, S., T (1977) Determination of aqueous solubility and pKa values of estrogens. Journal of Pharmaceutical Sciences 66(5), 624-627.

Jallouli, N., Pastrana-Martínez, L.M., Ribeiro, A.R., Moreira, N.F., Faria, J.L., Hentati, O., Silva, A.M. and Ksibi, M. (2018) Heterogeneous photocatalytic degradation of ibuprofen in ultrapure water, municipal and pharmaceutical industry wastewaters using a TiO2/UV-LED system. Chemical Engineering Journal 334, 976-984.

Lachheb, H., Puzenat, E., Houas, A., Ksibi, M., Elaloui, E., Guillard, C. and Herrmann, J.-M. (2002) Photocatalytic degradation of various types of dyes (Alizarin S, Crocein Orange G, Methyl Red, Congo Red, Methylene Blue) in water by UV-irradiated titania. Applied Catalysis B: Environmental 39(1), 75-90.

Lai, K., Johnson, K., Scrimshaw, M. and Lester, J. (2000) Binding of waterborne steroid estrogens to solid phases in river and estuarine systems. Environmental Science & Technology 34(18), 3890-3894.

Lin, K., Liu, W. and Gan, J. (2009) Oxidative removal of bisphenol A by manganese dioxide: efficacy, products, and pathways. Environmental Science & Technology 43(10), 3860-3864.

Liu, Y., Yan, M., Geng, Y. and Huang, J. (2016) Laccase immobilization on poly (p-phenylenediamine)/Fe_3O_4 nanocomposite for reactive blue 19 dye removal. Applied Sciences 6(8), 232.

Madhavan, J., Grieser, F. and Ashokkumar, M. (2010) Combined advanced oxidation processes for the synergistic degradation of ibuprofen in aqueous environments. Journal of Hazardous Materials 178(1-3), 202-208.

Miller, M.M., Wasik, S.P., Huang, G.L., Shiu, W.Y. and Mackay, D. (1985) Relationships between octanol-water partition coefficient and aqueous solubility. Environmental Science & Technology 19(6), 522-529.

Nezamzadeh-Ejhieh, A. and Shams-Ghahfarokhi, Z. (2012) Photodegradation of methyl green by nickel-dimethylglyoxime/ZSM-5 zeolite as a heterogeneous catalyst. Journal of Chemistry.

NTP (1992) Institute of Environmental Health Sciences, National Institutes of Health (NTP). National Toxicology Program Chemical Repository Database. Research Triangle Park, North Carolina: NTP via httn.

Ong, S.-A., Toorisaka, E., Hirata, M. and Hano, T. (2005) Decolorization of azo dye (Orange II) in a sequential UASB–SBR system. Separation and Purification Technology 42(3), 297-302.

Racz, L. and Goel, R.K. (2010) Fate and removal of estrogens in municipal wastewater. Journal of Environmental Monitoring 12(1), 58-70.

Soto, M., Veiga, M.C., Mendez, R. and Lema, J.M. (1989) Semi-micro C.O.D. determination method for high-salinity wastewater. Environmental Technology Letters 10(5), 541-548.

Ugwu, M.C., Oli, A., Esimone, C.O. and Agu, R.U. (2016) Organic cation rhodamines for screening organic cation transporters in early stages of drug development. Journal of Pharmacological and Toxicological Methods 82, 9-19.

Van de Linde, S., Krstić, I., Prisner, T., Doose, S., Heilemann, M. and Sauer, M. (2011) Photoinduced formation of reversible dye radicals and their impact on super-resolution imaging. Photochemical & Photobiological Sciences 10(4), 499-506.

Wang, J. and Wang, S. (2016) Removal of pharmaceuticals and personal care products (PPCPs) from wastewater: a review. Journal of Environmental Management 182, 620-640.

Yazdanian, M., Briggs, K., Jankovsky, C. and Hawi, A. (2004) The “high solubility” definition of the current FDA guidance on biopharmaceutical classification system may be too strict for acidic drugs. Pharmaceutical Research 21(2), 293-299.

Zhang, Y., Causserand, C., Aimar, P. and Cravedi, J.-P. (2006) Removal of bisphenol A by a nanofiltration membrane in view of drinking water production. Water Research 40(20), 3793-3799.

USC
UNIVERSIDADE
DE SANTIAGO
DE COMPOSTELA

3. Chapter 3

ENZYME-ASSISTED OXIDATION: Potentiality of enzymes immobilized onto different supports as biocatalysts

SUMMARY

From a bottom-up approach, the evaluation of the potentiality of immobilized enzymes as biocatalysts for the oxidation and removal of broad-spectrum emerging pollutants arises as a topic of increasing interest. To this end, this chapter evaluated the immobilization of two different laccases from *Myceliophthora thermophila* (*Mt*) and *Trametes versicolor* (*Tv*) and versatile peroxidase (VP) from *Bjerkandera* sp in micro- and nano-supports as biocatalysts to carry out the transformation of structurally diverse endocrine disrupting chemicals. The materials considered as support showed excellent biocompatibility with the enzymes, so that the bioconjugates obtained after immobilization showed greater tolerance to variations in pH and temperature, as well as greater operational and storage stability compared to the free enzyme. The enhanced properties of the immobilized enzymes became evident even in the presence of organic solvents and enzyme inhibitors. Once the most suitable biocatalyst was selected, its application was investigated in an enzymatic membrane reactor configuration operating in sequential mode throughout different operating cycles.

OUTLINE

3.1 Introduction

Enzymes are versatile biological catalysts that can potentially substitute conventional chemicals thanks to their high chemo-, regio- and enantioselectivity at ambient temperatures (Silverman 2002). Ligninolytic enzymes are capable of performing the selective degradation of lignin, which gives fungi access to cellulose and hemicellulose as their source of carbon and energy (Reddy et al. 2003, Salvachúa et al. 2011). Among the most widely studied ligninolytic enzymes, laccases and peroxidases stand out as they are capable of generating highly reactive and non-specific free radicals with high oxidative potential to perform the degradation of highly recalcitrant compounds (Taboada-Puig et al. 2013, Dashtban et al. 2010).

Laccases are the only ligninolytic enzymes already applied at industrial scale, for example in the food processing industry. From this starting point, the application in wastewater treatment is closer. Both their structure and the mechanism associated with their catalytic cycle have been described. Thus, they are multi-copper oxidases whose catalytic mechanisms involve two individual sites binding the reducing substrate and molecular oxygen (O_2) with four catalytic copper atoms (Mate and Alcalde 2017). In this sense, it is interesting to evaluate their structural modification of the target compounds in synthesis reactions, or their degradation based on oxidation reactions.

Peroxidases are hemoproteins that require the presence of hydrogen peroxide (H_2O_2) as electron acceptor to initiate their catalytic cycle, although it may also entail the participation of mediating compounds to oxidize lignin and lignin-related compounds (Ortiz de Montellano 1992, Mester and Tien 2000). Like all proteins, their activity range is restricted to mild pH and T values, as otherwise their activity would be lost due to protein denaturation. Furthermore, the active center of the enzyme can be deactivated by organic solvents, solutions with high salinity, presence of azides and metals. The restrictions imposed by these parameters must be controlled to ensure the stability of the enzyme in a given process (Bornscheuer 2003).

For this reason, the interest arises to develop strategies that allow the safe and efficient use of enzymes, even under conditions that could be regarded unfavorable in the case of considering the free enzyme in its native state. Beyond the potentiality

of protein engineering and directed evolution to change enzyme conformation (Illanes et al. 2008), immobilization on physical supports can be applied to enhance enzyme stability by prevention of autolysis or proteolysis, rigidification of the enzyme structure via multipoint covalent attachment (Hernandez and Fernández-Lafuente 2011, Rodrigues et al. 2013). The bonding of the enzyme on a support allows the stabilization of its tertiary structure (Othman et al. 2016).

On the other hand, it is foreseeable that there will be benefits not only in the activity and stability of the immobilized enzyme. The fact that the physical state of the enzyme is changed after immobilization will allow the recovery of the bioconjugate, a term that refers to the combination of enzyme and support, by physical methods such as centrifugation, sedimentation, filtration or magnetic separation methods. In particular, in recent years there has been growing interest in the use of support alternatives based on nanoparticles and microparticles, materials that ensure an ordered arrangement and high stability to chemical and mechanical forces. The main difference between both types of material is related to their characteristic dimensions, in the range of 10-100 nm in the case of nanoparticles and 100-1000 nm in the case of microparticles, which clearly influences the surface area they offer for immobilization (Cui et al. 2016, Ngomsik et al. 2005, Tratnyek and Johnson 2006).

A prerequisite for immobilization is the functionalization of th material. During this procedure, anchor points are distributed ensuring immobilization according to the combination of functional groups generated and the enzyme terminal groups. In particular, silica materials have been used as support materials for enzyme immobilization based on modification of the silica surface by amination of hydroxyl and reactive siloxane groups and addition of methyl or polyvinyl alcohol groups (Rao et al. 2000, Shioji et al. 2003, Pogorilyi et al. 2007). Other materials of growing interest are biodegradable and biocompatible nanomaterials. In this sense, chitosan polymeric nanofibers are prepared by the electrospinning technique and mixed with poly (vinyl alcohol) as a polymeric additive. This synthesis procedure has provided them with unique characteristics: high specific surface, high porosity and small pore size, which has allowed their application in multiple areas such as medical, pharmaceutical, cosmetic, metal ion recovery, filtration, biosensors, among others

(Dadras Chomachayi et al. 2018, Karavasili et al. 2018, Yoshimoto et al. 2003, Yan et al. 2011, Eroglu et al. 2012, Huang et al. 2003).

Although there are some reports on enzyme immobilization onto micro and nanosized carriers (Lu et al. 2007, Das et al. 2017, Marysková et al. 2016, Jia et al. 2002), very few publications focus on the application of the biocatalyst for environmental purposes under more realistic conditions, such as the removal of xenobiotics present in wastewater (Gasser et al. 2014, Arca-Ramos et al. 2016).

In this work, fumed silica nanoparticles (fsNPs), microparticles (fsMPs) and chitosan-based nanofibers (cNFs) were evaluated as support for the immobilization of laccase from *Myceliophthora thermophila* (*Mt*) and *Trametes versicolor* (*Tv*) and Versatile peroxidase (VP) from *Bjerkandera* sp. (anamorph R1) by covalent interaction on the functionalized structure of the support. Once the bio-conjugate was obtained, the characterization of the immobilized enzyme and its oxidation potential was evaluated towards two model compounds: a cationic dye Methyl green (MG) and an anionic dye Reactive Blue 19 (RB19). From the initial selection, the technical feasibility of using these biocatalysts for the elimination of different contaminants belonging to the group of endocrine disrupting chemicals (Bisphenol A (BPA) and Estrone (E1), 17β-estradiol (E2), and 17α-ethinylestradiol (EE2) was evaluated.

3.2 Materials and methods

3.2.1 Chemicals, supports and enzymes

All chemicals required in this chapter are listed in the chemicals Section 2.1 in Chapter 2. The supports selected for enzyme immobilization were the following: fsNPs (surface area: 390 ± 40 $m^2\ g^{-1}$; particle aggregates with a size of 7 nm) and fsMPs (surface area 200 ± 25 $m^2\ g^{-1}$; particle aggregates with a size of 200-300 nm) were purchased from Sigma-Aldrich (St. Louis, USA). cNFs (dry composition of 16.6% chitosan and 83.4% poly (vinyl alcohol), diameter of 213 ± 46 nm and an estimated surface area by image analysis of 1705 ± 591 $cm^2\ g^{-1}$) were kindly provided by the Food analysis laboratory (BUAP, Mexico).

These nanofibers were synthesized by electrospinning (28 kV; flow rate of 0.2 mL h^{-1}; collection distance of 20 cm and 100 rpm) from a solution of 3% (w/v) chitosan/acetic acid 1 M and 10% (w/v) poly (vinyl alcohol) in a ratio of 1:1.

Different types of enzymes were evaluated: two types of laccase and one peroxidase. Commercial laccase from *Mt* supplied by Novozymes (Denmark), namely Novozym 51003 (activity ≥1.2 10^6 U L^{-1}), was produced by submerged fermentation of genetically modified *Aspergillus oryzae*. This laccase has a size of 77 kDa (Bulter et al. 2003), a density of 1.05 g mL^{-1} and optimal activity at pH between 3.5 and 6.5, depending on the substrate. Commercial laccase from *Tv* (activity ≥ 0.5 U mg^{-1}) was purchased from Sigma-Aldrich (St. Louis, USA). Peroxidase VP (activity close to 10 U mL^{-1}) was obtained from submerged cultures of the anamorph R1 of *Bjerkandera* sp. (Taboada-Puig et al. 2011).

3.2.2 Determination of enzyme activity

Laccase activity was determined by the oxidation of 0.267 mM ABTS to its cation radical ($ABTS^{\bullet+}$) in citrate-phosphate buffer (pH 3) and 30 °C in a 96-well-plate (Zimmermann et al. 2011). Aliquots of 50 µL of immobilized laccase onto fsMP or fsNPs previously diluted in citrate-phosphate buffer was added to 0.2 mM of ABTS solution. Absorbance was measured at 420 nm (ε_{420}= 30,800 M^{-1} cm^{-1}) for 7 min at 6 s intervals in the BioTek PowerWave XS2 microplate spectrophotometer previously described in Chapter 2 (Section 2.3) and the Gen5 1.08 Data Analysis Software. One unit (U) of activity was defined as the amount of enzyme capable of oxidizing 1 µmol ABTS per minute, or at the same time, the amount of enzyme forming 1 µmol of $ABTS^{\bullet+}$ per minute.

Versatile Peroxidase presents manganese-dependent enzyme activity and it can be measured by monitoring the oxidation of 2,6-dimethoxyphenol (DMP) at 468 nm and ε_{468}= 49.6 mM cm^{-1} (referred to coerulignone) in a UV-Visible Spectrophotometer UV-1603 Shimadzu (Japan). The reaction mixture (in a total volume of 1 mL) contained 50 mM sodium malonate (pH 4.5), 1 mM DMP, 1 mM $MnSO_4$ and 50 µL of sample. The reaction was started by adding 0.4 mM H_2O_2. One enzyme unit was defined as the amount of enzyme producing 1 µmol of coerulignone per minute (Mester et al. 1995).

The determination of the activity of immobilized enzymes in the support of activated cNFs was performed as described above using an equivalent sample of nanofibers instead of a diluted sample containing enzymes (50 µL), such as fsMPs and fsNPs.

3.2.3 Immobilization of enzymes by covalent binding onto fumed silica micro and nanoparticles and chitosan nanofibers

Prior to immobilization, surface modification of fsNPs and fsMPs was performed according to Hommes et al. (2012). In order to optimize the immobilization results, different doses of 3-aminopropyl triethoxysilane (APTES): 0.4, 0.8 and 1.2 mmol g^{-1} fsMP, were tested, selecting fsMPs as the immobilization support model. Briefly, APTES was mixed with the microparticles and incubated in an orbital shaker (C24 Incubator shaker, New Brunswick Scientific) at 150 rpm and room temperature for at least 12 h, and then washed in three cycles of centrifugation/re-suspension with phosphate buffer (100 mM, pH 7). The amino-functionalized microparticles were stored at 4 °C.

Laccase immobilization was performed following the sorption-assisted immobilization (SAI) method described by Zimmermann et al. (2011), which combines enzyme sorption to the surface of the particles and the crosslinking of enzymes on the aminopropylated carrier. As a first step of the process, aliquots of 1 mL of the amino-functionalized particles were withdrawn and *Mt* laccase (1 U mg^{-1} fsMP) was added in most of the experiments, except in those in which different doses of laccase were investigated. The solution was incubated by stirring (150 rpm) at 4 °C for 2 h. After this period, different doses of glutaraldehyde (1, 4, 8 and 12 mmol g^{-1} fsMPs) from a 5% stock solution prepared in 100 mM sodium phosphate buffer (pH 7) were added dropwise as a cross-linking agent to the mixture of fsMPs and laccase and incubated under agitation (150 rpm) at 4 °C for 24 h.

Thereafter, the excess of glutaraldehyde and the non-covalently bound enzyme were washed with phosphate buffer in five centrifugation/re-suspension steps for 7 min at 4000 rpm. The same methodological approach was followed for fsNPs. For cNFs functionalization, the first step is not necessary since the amine groups present in chitosan can react directly with the glutaraldehyde cross-linking solution. For this

case, cNFs were reticulated with 25% glutaraldehyde for 48 h at room temperature in order to activate the nanofiber surface.

Following the above-mentioned protocol, the enzymatic activities of the suspension and supernatants of fsMP-laccase conjugates were measured to determine the immobilization yield (%), enzyme loading (U mg^{-1} fsMP) and washing loss (%). Immobilization yield (IY) was defined as the apparent laccase activity of the fsMP suspensions after immobilization and washing in relation to the initially applied laccase activity (100%), reflecting the binding efficiency during the immobilization process. Enzyme loading (EL) was defined as the apparent laccase activity bound to fsMPs per mg fsMPs after thorough washing (U mg^{-1}). Washing loss (WL) was calculated based on the enzyme activity before and after washing. All experiments were conducted in triplicate to ensure the reproducibility of the results.

3.2.4 Characterization of biocatalysts

Both free and immobilized *Mt* laccase onto fsMPs were biochemically characterized by evaluating their catalytic activity and stability over a wide range of conditions. The effect of pH on the instantaneous enzyme activity was assessed by measuring laccase activity at pH values between 2.4 and 8. The results were expressed as relative activity (calculated as the ratio between the activity at each pH and the maximum at pH 3).

The effect of pH on the stability of free and immobilized enzyme (*Mt*) onto fsMPs was studied after incubating the enzyme in buffer solutions (100 mM): citrate-phosphate (pH 3-4), acetate buffer (pH 5) and phosphate (pH 6-7) at room temperature. Likewise, pH stability effect between 3 and 8 was studied for VP immobilized onto fsNPs and fsMPs in sodium malonate buffer solutions. Samples were periodically withdrawn at specific intervals for 24 h to determine residual activity (calculated as the ratio between the activity measured at specific conditions and the activity measured at time zero).

Immobilization can be a useful approach of increasing enzyme stability when operating under conditions far from the optimal described for the free enzyme. Thermal stability was evaluated in experiments performed under agitation (150 rpm) in phosphate buffer (100 mM, pH 7) in a temperature range of 10 to 50 °C and 24 h.

The stability of free and immobilized enzymes onto fsMPs against different inactivating agents was tested by incubating the enzyme in the presence of salts (2.5 mM NaCl, 90 mM NaCl and 10 µM $CaCl_2$) and organic solvents (methanol, ethanol and acetone at 25% v/v) in 100 mM sodium acetate buffer (pH 5) at 150 rpm, room temperature and 24 h. The long-term stability of both immobilized and free laccase (*Mt*) was investigated when the enzyme was incubated at 4 °C in phosphate buffer (pH 7 and in the secondary effluent from a municipal wastewater treatment plant (WWTP) for 30 days. Before measuring the residual activity, the collected wastewater was filtered (0.45 µm) to remove suspended solids. The kinetic parameters of the free and immobilized enzyme were determined by measuring *Mt* laccase activity using ABTS as a substrate at concentrations ranging from 1.2 to 750 µM in McIlvaine buffer (80 mM citric acid, 40 mM Na_2HPO_4, pH 3) at room temperature. The Michaelis-Menten constant (K_M) and the maximum reaction velocity (V_{max}) were determined by using a non-linear least square fit routine.

3.2.5 Determination of the concentration of pollutants

As described in Chapter 2 (Section 2.3), bisphenol A (BPA) and E1, E2 and EE2 estrogens were quantified by high performance liquid chromatography (HPLC) at a detection wavelength of 278 nm on a Jasco XLC HPLC (Jasco Analitica, Madrid, Spain) equipped with a 3110 MD diode array detector and a Gemini reversed-phase column (150 x 4.6 mm, particle size: 3 µm) from Phenomenex (supplied by Jasco Analitica, Madrid, Spain) and an HP ChromNav data processor. Color removal of RB19 and MG was determined in the BioTek PowerWave XS2 microplate spectrophotometer.

3.2.6 Batch experiments of enzyme immobilized silica nano and microparticles for recalcitrant pollutants transformation

An initial screening of the supports was carried out during the removal of persistent dyes as organic model compounds by free and immobilized biocatalysts. First catalytic tests were performed to assess dye colorization of MG and RB19 at an initial concentration of 25 mg L^{-1} and incubation in 10 mL of aqueous samples (phosphate buffer pH 6-7) containing 200 U L^{-1} of both *Mt* and *Tv* laccase (free and immobilized onto fsNPs, fsMPs and cNFs). Batch experiments were conducted at room temperature and continuous orbital agitation (150 rpm). At regular intervals, spectrophotometric measurements were performed to monitor laccase activity and

color removal. Color removal yield (%) was determined as the extent of color removal, calculated by the following equation,

$$\text{Degradation yield (\%)} = \frac{(C_0 - C_t)}{C_0} \times 100 \quad (1)$$

where C_0 and C_t represent the organic compound concentration (mg L^{-1}) before and after the reaction time, respectively.

The enzymatic oxidation of BPA (10 mg L^{-1}) and estrogens (0.35 mg L^{-1}) was conducted in batch experiments (10 mL) at room temperature and continuous agitation. *Mt* laccase immobilized onto both fsMP with initial activity of 1000 U L^{-1} were tested to transform BPA and E1, E2 and EE2 present in 100 mM sodium phosphate buffer (pH 7) and in the secondary effluent from a municipal WWTP. Complete solubility of BPA and estrogens was ensured by the addition of 10% and less than 1% (v/v) methanol, respectively. Samples were periodically withdrawn to measure laccase activity and contaminant concentration. To verify that transformation occurred only by enzymatic catalysis, parallel control tests were run in the absence of laccase but in the presence of functionalized supports. Degradation yield (%) was determined using Equation 1.

3.2.7 Enzymatic membrane reactor for the transformation of recalcitrant compounds

The enzymatic reactor consisted of a 10-mL stirred tank coupled to an ultrafiltration polyethersulfone membrane (Cell Amicon Millipore) with a nominal molecular weight cut-off of 500 kDa, which allowed the retention of the immobilized laccase inside the reaction vessel. The operation of the reactor was sequential according to the fill-and-draw principle, which consists of the following steps: fill, reaction, membrane retention of the biocatalyst and withdrawal of the reaction medium. The selected biocatalyst (*Mt*) immobilized on the fsMPs was added in a single initial pulse of 1000 U L^{-1} to perform the transformation of contaminants in 100 mM sodium phosphate buffer (pH 7) in a series of consecutive 24-hour cycles (10 mg BPA L^{-1} in 10% methanol).

Thereafter, inert nitrogen under pressure was passed through the membrane to discharge around 80% of the effluent. In subsequent cycles, the same immobilized

enzyme was reused and fresh medium with contaminants was added for a new cycle. Samples were withdrawn at the beginning and end of each cycle to measure laccase activity and contaminants concentrations. The adsorption of contaminants on the polymeric membrane was evaluated at conditions similar to those of the enzymatic reaction, but in the absence of laccase.

3.3 Results and discussion

3.3.1 Laccase and peroxidase immobilization onto micro and nano-sized materials

The approach followed for laccase and peroxidase immobilization pursues the immobilization of the enzymes onto silica nano and microparticles and chitosan-based nanofibers through covalent binding. In order to obtain a biocatalyst with high activity, the support must be biocompatible with the enzyme and favor the access of substrates for oxidative catalysis. Porous inorganic materials, especially porous silica, have been used as enzyme support due to their large specific surface area, high stability and low cost (Hudson et al. 2008, Rekuć et al. 2010).

The silanol groups, Si-OH, on the silica surface can be easily modified to primary amine functions through the addition of APTES (Zimmermann et al. 2011). This reaction allows the formation of one or few additional molecular layers on the surface of the particles, which changes the surface potential charge of the particles from a negative value of -50 mV for bare particles to a value of 33 mV for the APTES treated ones; thus confirming the desired functionalization on their surface (Galliker et al. 2010). A distinct advantage of cNFs is that the first step of functionalization may be circumvented in order to continue with enzyme immobilization procedure. In a further step, the immobilization of laccase and peroxidase by covalent bonding requires the use of a crosslinking agent such as glutaraldehyde to carry out the bonding of functional groups of enzymes and functionalized supports (Fernández-Fernández et al. 2013).

Mt laccase-bioconjugate was selected as first approach for the optimization of the functionalization and immobilization procedure. Table 3.1 depicts the results of the optimization of *Mt* immobilization onto fsMPs in terms of immobilization yield (%), enzyme loading (U mg^{-1} fsMPs) and washing loss (%) for different doses of APTES, glutaraldehyde and laccase.

Table 3.1 *Mt* laccase immobilization on fsMPs at different doses of APTES, glutaraldehyde and laccase.

	Immobilization yield (%)	Enzyme loading (U mg^{-1} fsMP)	Washing loss (%)
APTES (mmol g^{-1} fsMPs)[1]			
0.4	41.1 ± 8.8	0.49 ± 0.05	62.0 ± 7.0
0.8*	58.7 ± 3.2	0.58 ± 0.01	27.1 ± 7.0
1.2	48.3 ± 8.0	0.58 ± 0.06	53.3 ± 4.0
Glutaraldehyde (mmol g^{-1} fsMPs)[2]			
1	13.3 ± 2.4	0.10 ± 0.007	88.5 ± 2.2
4	42.9 ± 3.8	0.34 ± 0.045	60.9 ± 7.6
8*	58.7 ± 3.2	0.58 ± 0.013	27.1 ± 7.0
12	44.0 ± 8.4	0.40 ± 0.058	31.5 ± 13.4
Laccase (U mg^{-1} fsMPs)[3]			
1*	**58.7 ± 3.2**	**0.58 ± 0.013**	**27.1 ± 7.0**
2.4	29.9 ± 2.6	0.61 ± 0.034	39.4 ± 5.7
3.7	20.4 ± 2.5	0.59 ± 0.061	53.5 ± 1.1

[1] Fixed doses of laccase (1 U mg^{-1} fsMP) and glutaraldehyde (8 mmol g^{-1} fsMP)

[2] Fixed doses of laccase (1 U mg^{-1} fsMP) and APTES (0.8 mmol g^{-1} fsMP)

[3] Fixed doses of glutaraldehyde (8 mmol g^{-1} fsMPs) and APTES (0.8 mmol g^{-1} fsMPs)

* Optimal doses of APTES, glutaraldehyde and laccase for its immobilization onto fsMPs

The influence of the APTES dose was evaluated with fixed doses of laccase (1 U mg^{-1} fsMPs) and glutaraldehyde (8 mmol g^{-1} fsMPs). The addition of 0.8 mmol g^{-1} APTES fsMPs showed the best results in terms of the three variables (Table 3.1), implying an 80% reduction in the use of APTES compared to the protocol described by Zimmermann et al. (2011). Similarly, for the addition of the cross-linker, 8 mmol glutaraldehyde g^{-1} fsMPs led to the best results in the three indexes, which, compared to the conditions reported in Zimmermann et al. (2011), represents a 20% reduction for glutaraldehyde consumption. Finally, the dose of *Mt* laccase was evaluated, and the concentration of 1 U mg^{-1} fsMPs was selected, since it provided a balance between enzyme dose, high immobilization yield (58.7 ± 3.2%) and low washing loss (27.1 ± 7.0%). The immobilization of *Mt* onto fsNPs and the immobilization of laccase from *Tv* onto both fsNPs and fsMPs were carried out with the optimal doses of chemicals and laccase previously obtained for fsMPs, which

enabled similar results in terms of *Mt* immobilization yield for fsNPs (62.4 ± 2.6%) and *Tv* immobilization yield for fsNPs (75.8 ± 5.3%) and fsMPs (70.3 ± 2.1%). A similar percentage of immobilization (49%) was obtained for *Trametes versicolor* laccase immobilized on magnetic microparticles coated with cellulose (Jořenek and Zajoncová 2015).

Accordingly, the immobilization of VP was performed with the initial functionalization of fsNPs and fsMPs with APTES before their incubation with peroxidase and glutaraldehyde. The results obtained, using optimal doses of chemicals and enzymes previously applied for fsMPs, achieved immobilization yields close to 30% for both fsNPs and fsMPs supports. Aiming at improving performance, the initial VP dose was varied to a range between 100-500 U L^{-1}, resulting in a negligible improvement with maximum immobilization yields of 37.4 ± 3.4% and 33.9 ± 2.6% for fsNPs and fsMPs, respectively, for an initial VP activity of 200 U L^{-1}.

In parallel, both *Mt* and *Tv* laccase and VP immobilization onto cNFs were also carried out, varying the doses previously obtained for the fsMPs supports to lower doses (100-500 U·L^{-1}) of laccase and peroxidase, in order to optimize the immobilization results. Stabilized cNFs demonstrated excellent biocompatibility as support for enzyme immobilization. Figure 3.1 presents a summary of the results obtained in terms of enzyme immobilization performance for the three enzymes evaluated in cNFs. The enzyme immobilization results for cNFs reflect that the maximum percentage of immobilization is achieved with an initial enzyme dose of 100 U L^{-1}. For the three enzyme scenarios, the immobilization yield remained below 100%, with values between 65 and 90%, with the highest value corresponding to the Tv enzyme (90.3 ± 4.2%). These values decreased as the enzyme dose increased, while simultaneously higher washout losses were obtained. Previous research has also used chitosan/poly(vinyl alcohol) nanofibers as support for immobilized lipase from *Candida rugosa* using glutaraldehyde as coupling reagent obtaining similar immobilization percentages: 49.8% (Huang et al. 2007).

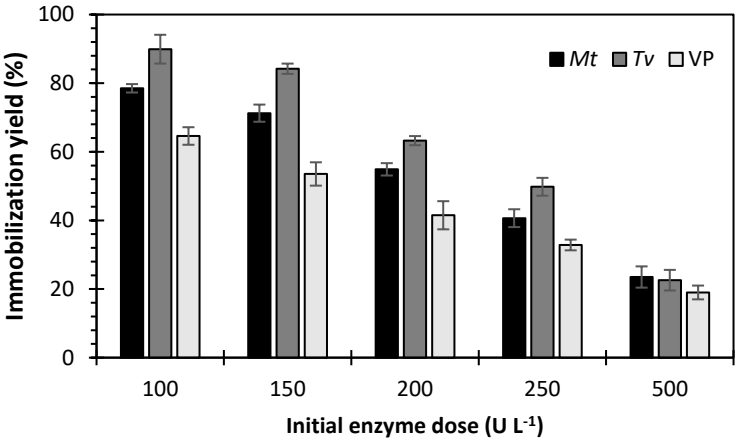

Figure 3.1 Enzyme immobilization (*Mt*, *Tv* and VP) percentages obtained for different enzyme doses (100-500 U L^{-1}).

3.3.2 Characterization of *Mt*-fsMPs biocatalysts

Research on catalytic mechanisms have shown that the catalytic cycle of laccases involves a sequence of reactions: i) the abstraction of electrons from the substrate to the T1 copper and the sequential reduction of the T1 copper and ii) the internal electron transfer from the T1 to the T2/T3 copper cluster, with the consequent oxidation of the target substrate (Xu 1997, Gianfreda et al. 1999, Kurniawati and Nicell 2008). During the catalytic cycle, the pH can affect the structure of the active center as well as the charge of the substrates and therefore affect the efficiency of the reaction mechanism. (Xu 1997). Besides, pH may influence the redox potential of reacting species, affecting the overall oxidation extent.

The optimal pH for laccase activity was generally reported in the acidic region, with values ranging from 2.7 to 7.5, but typically in the range of 3.5-6, depending on the substrate (Gianfreda et al. 1999, Call and Mücke 1997). The immobilized laccase (*Mt*) was active in a range of pH 2.4-8, exhibiting a maximum activity at pH 3 (Figure 3.2), similarly to the profile of the free enzyme.

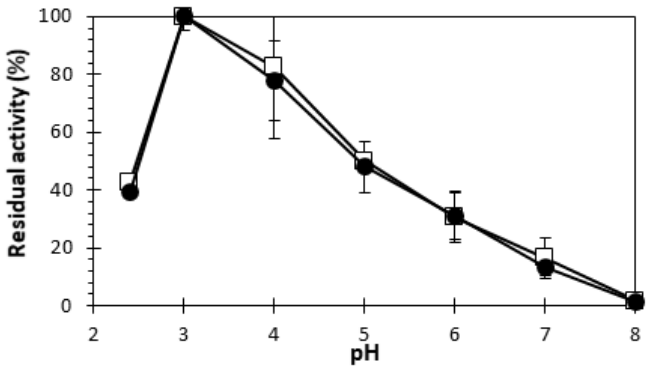

Figure 3.2 Influence of pH on residual activity of free (□) and immobilized *Mt* laccase (●).

Regarding the stability of the immobilized biocatalyst towards a broader pH range, Table 3.2 shows that the pH stability was superior for immobilized laccase than for free laccase after 24 h.

Table 3.2 Stability of free and immobilized laccase onto fsMP at different pH and temperature after 24 h.

		Residual activity (%)	
		Free enzyme	***fsMPs***
pH	**3**	1.10 ± 0.58	20.20 ± 2.91
	4	25.01 ± 12.67	66.02 ± 4.26
	5	48.19 ± 10.70	80.25 ± 0.88
	6	78.92 ± 0.00	95.48 ± 0.00
	7	90.81 ± 0.00	92.84 ± 0.00
		Free enzyme	***fsMPs***
Temperature (°C)	**10**	107.87 ± 2.68	109.73 ± 1.48
	20	101.68 ± 0.76	101.83 ± 3.35
	30	68.73 ± 2.59	100.87 ± 2.35
	40	60.47 ± 1.67	80.66 ± 11.43
	50	8.31 ± 1.61	22.06 ± 2.36

*100% activity corresponds to 1000 U L^{-1}.

At neutral pH, the fsMPs-laccase exhibited an apparent activity similar to that of the free enzyme, around 90% for both cases, as shown in Table 3.2. However, there is a drastic reduction in enzyme activity for acidic pH, which results in a strong drop of 78% to pH 4 and a complete deactivation of the free enzyme at pH 3 after 24 h. Nevertheless, the residual activity of the fsMPs enzyme at pH 3 and 4 was superior: 20 and 66%, respectively. Therefore, this biocatalyst shows maximum enzymatic activity and significant stability at pH 3 in comparison with the free enzyme. However, in the pH range of 5-7, the stability of the biocatalyst was lower than that of the free enzyme. Lloret et al. (2012) also observed enhanced stability at low pH after immobilization of *Mt* laccase onto Eupergit supports and Nguyen et al. (2016) found that the immobilization of laccase onto granular activated carbon strongly enhanced its stability at acidic pH, which could be particularly suitable for the removal of some recalcitrant micropollutants. Similar results were observed by Kunamneni et al. (2008), where laccase was covalently immobilized on polymethacrylate-based polymers activated with epoxy groups and exhibited higher stability than the free form, especially in the pH range of 3-5. The thermostability of free and immobilized laccases onto fsMPs was tested when measuring the enzyme activity between 10 and 50 °C. After 24 h, the maximum activity was observed at low T (10 and 20 °C) with a percentage of residual activity close to 100% for the two biocatalysts (Table 3.2). Above 30 °C, free laccase activity began to decrease, with virtually total deactivation at 50 °C after 24 h.

In contrast, the immobilized laccase maintained an enzymatic activity superior to that of free laccase, especially in the case of fsMPs (from 1.33 to 2.60 times superior to that of free laccase). Jermann et al. (2009) reported that laccase immobilization led to a significant stabilizing effect towards heat denaturation at 60 and 70 °C, where stability increased by 15 and 10%, respectively, relative to the free one. Other studies reported that the immobilization affects the conformational flexibility of the enzyme since it causes an increase in enzyme rigidity and enhances stability towards denaturation at high temperature (Osma et al. 2010). The stability of free and immobilized laccase onto fsMPs in the presence of different inhibitors was also evaluated. Figure 3.3 depicts the residual activity after 24 h at 25 °C in sodium acetate (pH 5) and different inhibitors: NaCl (2.5 and 90 mM), $CaCl_2$ (10 μM) and organic solvents (methanol, ethanol and acetone, 25% v/v).

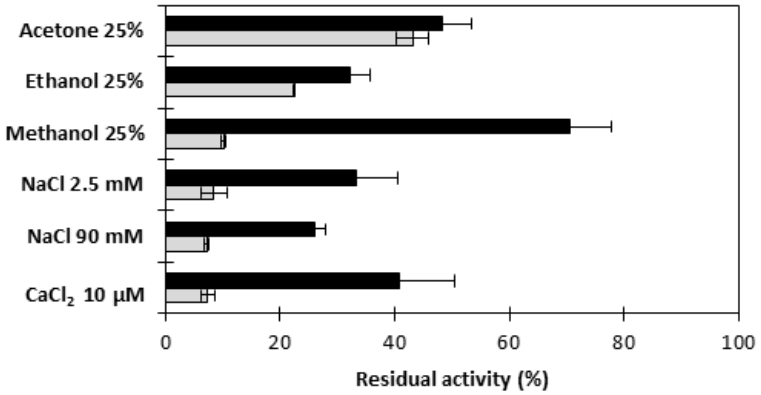

Figure 3.3 Stability of free ( ) and immobilized laccase onto fsMPs ( ) in the presence of different inhibitors.

The presence of inhibitors was detrimental for laccase stability, although to a lesser extent for the enzyme immobilized onto fsMP, which maintained a higher residual activity. The presence of 90 mM NaCl caused the greatest drop (26% of residual activity) compared to other inhibitors (Figure 3.3).

These results are in agreement with the findings reported by Hassani et al. (2013), where laccase-based cross-linked enzyme aggregates (CLEAs) showed higher residual activity than the unmodified biocatalyst against 25% methanol (up to 15 times) and 25% acetone (up to 20 times). The tolerance to chloride concentrations becomes especially important when considering the use of the biocatalyst for industrial wastewaters, which may contain significant concentrations of salts: 2.5-5 mM, and even much higher in the pharmaceutical industry, up to 90 mM (Margot et al. 2013).

A similar behavior has been reported by Margot et al. (2013), who evaluated the stability of free and immobilized laccase at NaCl concentrations ranging from 0 to 600 mM. Chaotropic salts such as $CaCl_2$ had a similar effect on laccase stability and the immobilized enzyme was comparably more stable than the free enzyme in the presence of 10 µM $CaCl_2$.

Another important feature for possible industrial application is the matrix effect on enzyme stability. The composition of the secondary effluent could play a

role on the enzyme inactivation, possibly due to proteolytic attack as well as to the inhibitory action of halides and metal cations (Cabana et al. 2007). This factor was assessed in experiments performed with the secondary effluent of a municipal WWTP (Table 3.3) and compared with those using phosphate buffer (Figure 3.4).

Table 3.3 Composition of the secondary effluent.

Parameter	Value
Chemical oxygen demand (**COD**)	15.36 mg L^{-1}
Total organic carbon (**TOC**)	8.85 mg L^{-1}
pH	7.2
Cations	
K^+	3.19 mg L^{-1}
Mg^{2+}	1.54 mg L^{-1}
Ca^{2+}	6.86 mg L^{-1}
Na^+	11.86 mg L^{-1}
NH_4^+	0.79 mg L^{-1}
Anions	
Cl^-	13.73 mg L^{-1}
NO_2^-	0.12 mg L^{-1}
Br^-	0.29 mg L^{-1}
NO_3^-	13.97 mg L^{-1}
PO_4^{3-}	1.13 mg L^{-1}
SO_4^{2-}	11.31 mg L^{-1}

After 60 days at 4 °C, it was observed that free laccase was inactivated in both matrices (76 and 66% inactivation for phosphate buffer and real wastewater matrix, respectively). However, enzyme inactivation was faster in the case of the secondary effluent; after 11 days, the residual activity was 50%, whereas in the phosphate buffer it remained at 76%.

On the contrary, immobilized laccases were much more stable, with residual laccase activity after 60 days of 99% in the phosphate buffer and 90% in the secondary effluent for fsMP. These values suggest that immobilized laccases in fsMP are stable for up to 2 months at 4 °C with minor loss of laccase activity.

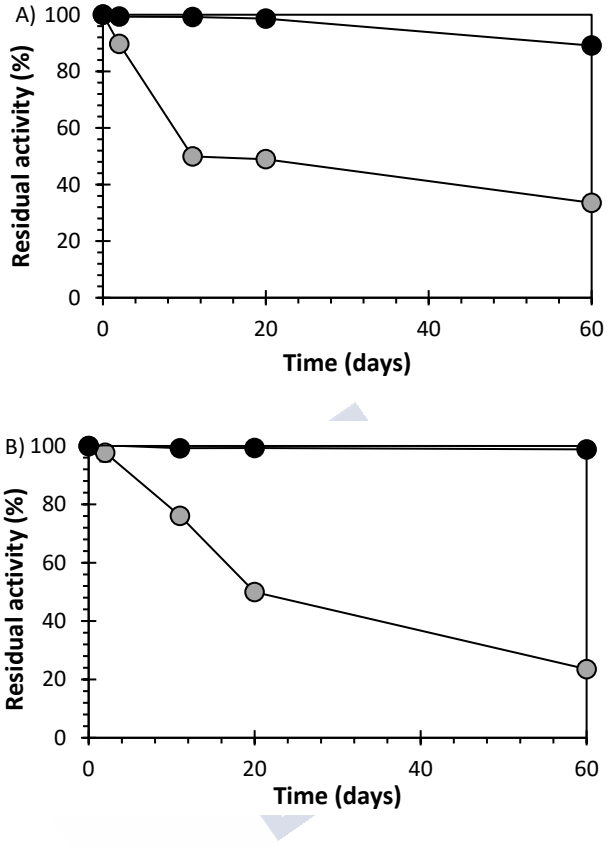

Figure 3.4 Residual activity of the free laccase (●), fsMP-laccase (●) in the secondary effluent from a wastewater treatment plant (WWTP) (A) and in phosphate buffer (B).

Michaelis-Menten kinetic parameters (K_M, V_{max}) of immobilized laccase in fsMPs and free laccases were determined with ABTS as substrate (1.2-750 µM) aiming to evaluate the effect of the immobilization method on the catalytic efficiency of laccase (Table 3.4). It is noted that the K_M value for the free enzyme (9.23 mM) is only slightly lower compared with the K_M values of the immobilized one, indicating that the potential protein conformational changes due to immobilization hardly affect the accessibility of the substrate to the active site.

Table 3.4 Experimental kinetic data of free and immobilized laccase in the oxidation of ABTS Michaelis-Menten constants.

Laccase	K_M (μM)	V_{max}(μM min^{-1})
Free	9.23 ± 0.01	183.5 ± 7.8
fsMPs	10.48 ± 2.10	133.3 ± 21.4

R^2: 0.984 for free laccase regression
R^2: 0.986 for fsMP-laccase regression

3.3.3 Batch experiments of enzyme immobilized onto silica nano and microparticles and chitosan nanofibers for recalcitrant pollutants transformation

The enzymes selected to perform the experiments were *Mt* and *Tv* laccases. Though the laccases present a lower redox potential (0.4 and 0.8 V for *Mt* and *Tv*, respectively) compared to ligninolytic peroxidases (> 1 V), laccases use molecular oxygen as the final electron acceptor instead of hydrogen peroxide (H_2O_2) required by peroxidases (Xu et al. 1996, Ivnitski and Atanassov 2007, Camarero et al. 2005). Another advantage of these enzymes over the selected peroxidase is their commercial availability.

Prior to the evaluation of the degradation of recalcitrant compounds of interest, the biotransformation of two model dyes was carried out. Experiments were performed in phosphate buffer medium (pH 7 and 6 for RB19 and MG, respectively) samples containing 200 U L^{-1} of enzyme and 25 mg L^{-1} of RB19 or MG, as model compounds of organic pollutants. RB19 belongs to the group of anthraquinones, widely used in the textile industry and identified as a persistent compound (Jen-Mao Fanchiang 2009). MG is a synthetic cationic dye molecule used as DNA labelling of cells or electrophoretic gels (Bel Hadjltaief et al. 2016, Prieto et al. 2014).

According to the results, the most efficient dye removal yields for both RB19 and MG by enzymatic bio-catalysis process reached values around 70 and 90% of RB19 and MG, respectively, after 24 h of treatment using cNFs as enzyme support for both *Mt* and *Tv* laccases (Figure 3.5). The enzymatic activity remained constant during experiments with barely perceptible enzyme deactivation (<10%). However, controls with cNFs lacking laccase showed that the target model dyes were absorbed

onto the support and little improvement in the enzyme biotransformation was observed. Previous studies have demonstrated the ability of chitosan nanofibers as suitable adsorbents with high dye adsorption capacity (Mahmoodi and Mokhtari-Shourijeh 2015, Dotto et al. 2017).

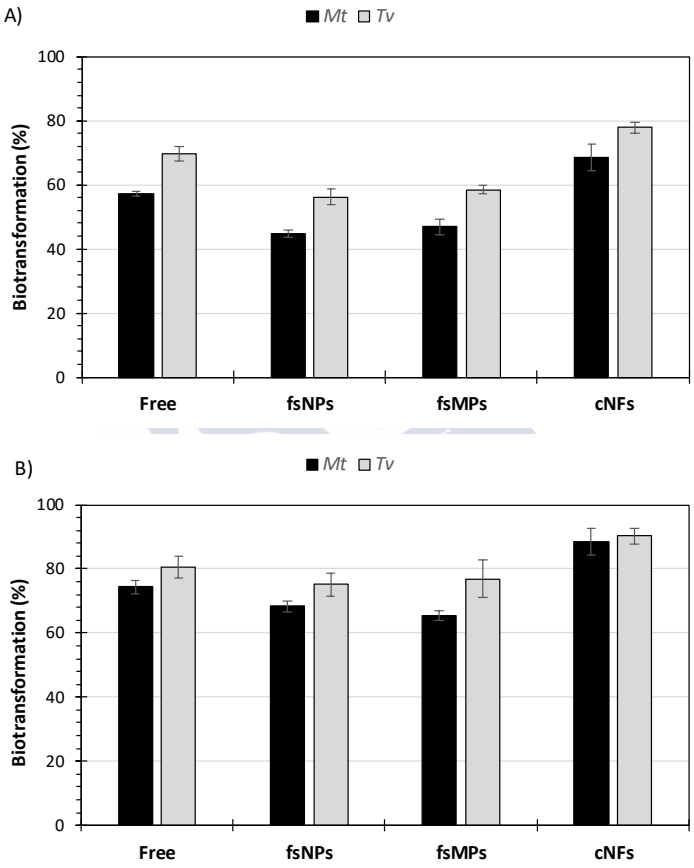

Figure 3.5 RB19 (A) and MG (B) dye color removal by enzymatic treatment with Mt and Tv laccase free and immobilized onto fsMPs, fsMPs and cNFs.

FsMPs demonstrated similar RB19 and MG removal percentages (46.9 ± 2.6% and 65.5 ± 1.58%, respectively) compared to free (57.2 ± 0.8% and 74.3 ± 2.15%, respectively) and immobilized fsNPs (44.8 ± 1.3% and 68.3 ± 1.69%, respectively) and cNFs bioconjugates (68.5 ± 4.2% and 88.5 ± 4.3%, respectively) for the two dyes and

as stated earlier, the use of fsMPs instead of fsNPs significantly reduces the cost of the process. Similarly, *Tv* presents higher redox potential than *Mt* and therefore little higher color removal percentages, but the cost of *Tv* is superior to the *Mt* cost. In this sense, the selected biocatalyst for the subsequent experiments was *Mt*-fsMP.

The capacity of free and immobilized enzymes (*Mt*-fsMP) to carry out the biotransformation of recalcitrant compounds was evaluated in phosphate buffer and in the secondary effluent of a municipal WWTP (Table 3.3). Four recalcitrant compounds of interest: BPA, the natural estrogens E1 and E2, and the synthetic estrogen EE2 were evaluated. Figure 3.6 shows that BPA (10 mg L^{-1}) removal was nearly complete with the free enzyme (>98%), whereas the removal was slightly inferior for fsMP-laccase (>76%). Adsorption control of BPA in fsMP is barely significant (<10%). Furthermore, the presence of the secondary effluent did not affect the removal of BPA by laccase, even when working at nearly neutral pH. These results are in agreement with previous reports on free laccase (Arca-Ramos et al. 2015), where nearly complete removal of BPA (95%) was attained in experiments in a continuous enzymatic reactor operated with real wastewater (pH≈7.2).

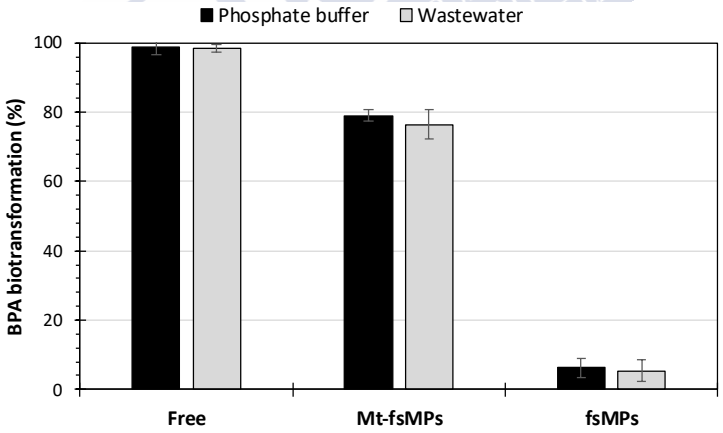

Figure 3.6 BPA transformation (24 h) with free and immobilized enzyme onto fsMP and fsMP lacking enzyme in synthetic matrix (■) and secondary effluent from a wastewater treatment plant (WWTP) (■).

The results depicted in Figure 3.7 show that the efficiency of E1, E2 and EE2 removal by laccase immobilized onto fsMP reached transformation percentages

close to 80% for free *Mt* enzyme (78.85 ± 1.05%, 87.44 ± 2.89% and 80.44 ± 0.20%, respectively) after 8 h of treatment. In phosphate buffer matrix *Mt*-fsMPs biotransformation capacity dropped to 27.49 ± 4.72 and 46.97 ± 5.13% for E1 and E2 but maintained stable for EE2 removal (77.05 ± 7.67). In real wastewater matrix, estrogens removal by fsMP-laccase behavior was comparable with the E1, E2 and EE2 estrogens removal in phosphate buffer matrix (27.35 ± 0.41%, 49.88 ± 0.28% and 71.05 ± 10.05%, respectively). Controls run with functionalized particles lacking laccase showed that the target pollutants (E1, E2 and EE2) did not absorb significantly onto the support (<5%).

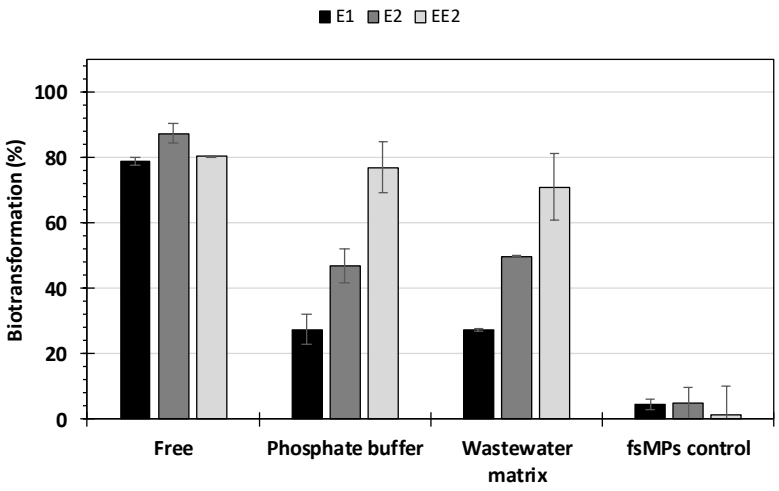

Figure 3.7 Estrogens (E1, E2 and EE2; 350 µg L^{-1}) transformation (8 h) with free and immobilized enzyme (1000 U L^{-1}) onto fsMP in synthetic matrix and secondary effluent from a wastewater treatment plant (WWTP).

Auriol et al. (2007) also studied the effect of wastewater matrices on enzymatic removal of estrogens, and observed that the degree of reactivity of the laccase-catalyzed system was not significantly affected by the municipal wastewater matrix. Furthermore, the potential laccase inhibitors (e.g., sulfide, nitrite, mercury, cyanide, chloride, and fluoride) in wastewater were limiting in a lesser extent than reported by Kim and Nicell (2006) to be inhibiting.

3.3.4 Enzymatic membrane reactor for the transformation of recalcitrant compounds

The proposed reactor consisted of a stirred tank reactor coupled to an ultrafiltration polyethersulfone membrane. The capacity of the immobilized enzymes onto fsMPs to remove recalcitrant compounds was assessed in repeated batches of 24 h. The reactors were operated for a total of 10 cycles without fouling of the membrane. In the sequential operation of the membrane reactor, the highest percentages of removal were reached in the first cycle, with complete removal of BPA (Figure 3.8). Partial adsorption of BPA (30%) onto the polymeric membrane was also evidenced in a control experiment (in the absence of biocatalyst). This is in accordance with other works that reported adsorption of BPA in polyethersulfone membranes (Su-Hua et al. 2010). The reuse of the membrane in consecutive cycles may lead to the saturation of the membrane or, at least, a decrease in its adsorption capacity.

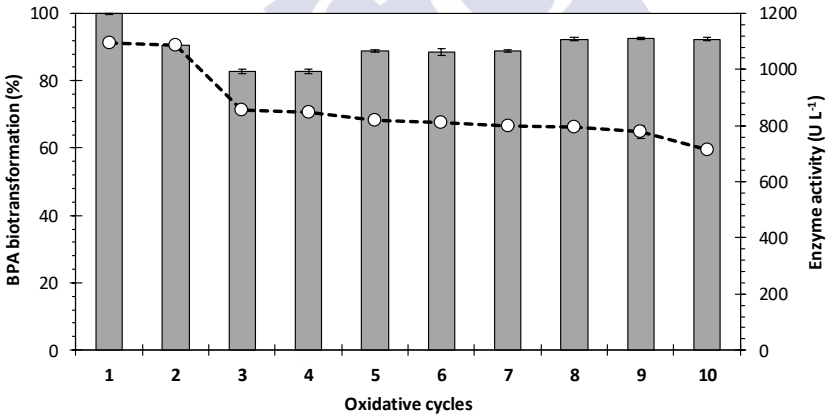

Figure 3.8 Biotransformation of BPA (10 mg L^{-1}) (■) and enzyme activity (□) in subsequent cycles of enzyme treatment with *Mt* laccase immobilized onto fsMPs.

In the second and subsequent cycles, BPA removal remained quite constant in percentages close to 90% (except for cycles 3 and 4, which slightly diminished to 82.79 ± 0.67% and 82.72 ± 0.78%, respectively). On the contrary, a progressive decrease of the initial enzyme activity was observed (34.73% loss of activity after 10

cycles) and was possibly associated the higher percentage of methanol in the reaction medium (10%).

3.4 Conclusions

In this chapter, the efficient covalent immobilization of three different laccase enzymes onto nano and microsupports was performed. Immobilized laccase showed broader pH and temperature range, and satisfactory stability in secondary effluents. The different biocatalysts were applied for the removal of two model dyes and Mt laccase immobilized onto fsNPs and fsMPs was selected for the removal of BPA and E1, E2 and EE2 estrogens from phosphate buffer medium and from the secondary effluent of a wastewater treatment plant with high transformation values. Furthermore, the biocatalysts were easily recovered using different configurations of enzymatic reactor. The enzymatic reactor coupled to the polymeric membrane was effective in the removal of the target pollutant thanks to partial adsorption and enzymatic transformation. Additionally, the consecutive use of the biocatalyst during the removal assays did not affect their removal capacity allowing their reuse for at least ten cycles. Furthermore, the decrease of the enzymatic activity did not lead to a reduction of the removal percentage, suggesting that the initial enzyme activity could be reduced to lower the operational costs. Hence, this reactor system shows a great potential for the removal of water contaminants.

3.5 References

Arca-Ramos, A., Ammann, E.M., Gasser, C.A., Nastold, P., Eibes, G., Feijoo, G., Lema, J.M., Moreira, M.T. and Corvini, P.F.X. (2016) Assessing the use of nanoimmobilized laccases to remove micropollutants from wastewater. Environmental Science and Pollution Research 23(4), 3217-3228.

Arca-Ramos, A., Eibes, G., Feijoo, G., Lema, J.M. and Moreira, M.T. (2015) Potentiality of a ceramic membrane reactor for the laccase-catalyzed removal of bisphenol A from secondary effluents. Applied Microbiology and Biotechnology 99(21), 9299-9308.

Auriol, M., Filali-Meknassi, Y., Tyagi, R.D. and Adams, C.D. (2007) Laccase-catalyzed conversion of natural and synthetic hormones from a municipal wastewater. Water Research 41(15), 3281-3288.

Bel Hadjltaief, H., Ben Zina, M., Galvez, M.E. and Da Costa, P. (2016) Photocatalytic degradation of methyl green dye in aqueous solution over natural clay-supported ZnO–TiO2 catalysts. Journal of Photochemistry and Photobiology A: Chemistry 315, 25-33.

Bornscheuer, U.T. (2003) Imobilizing enzymes: How to create a more suitable biocatalyst. Ange. Chem. Int. Ed. 42(29), 3336-3337.

Bulter, T., Alcalde, M., Sieber, V., Meinhold, P., Schlachtbauer, C. and Arnold, F.H. (2003) Functional Expression of a Fungal Laccase in *Saccharomyces cerevisiae* by Directed Evolution. Applied and Environmental Microbiology 69(2), 987-995.

Cabana, H., Jones, J.P. and Agathos, S.N. (2007) Elimination of Endocrine Disrupting Chemicals using White Rot Fungi and their Lignin Modifying Enzymes: A Review. Engineering in Life Sciences 7(5), 429-456.

Call, H.P. and Mücke, I. (1997) History, overview and applications of mediated lignolytic systems, especially laccase-mediator-systems (Lignozym®-process). Journal of Biotechnology 53(2–3), 163-202.

Camarero, S., Ibarra, D., Martínez, M.J. and Martínez, Á.T. (2005) Lignin-derived compounds as efficient laccase mediators for decolorization of different types of recalcitrant dyes. Appl. Environ. Microbiol. 71(4), 1775-1784.

Cui, J., Hibbs, B., Gunawan, S.T., Braunger, J.A., Chen, X., Richardson, J.J., Hanssen, E. and Caruso, F. (2016) Immobilized Particle Imaging for Quantification of Nano- and Microparticles. Langmuir 32(14), 3532-3540.

Dadras Chomachayi, M., Solouk, A., Akbari, S., Sadeghi, D., Mirahmadi, F. and Mirzadeh, H. (2018) Electrospun nanofibers comprising of silk fibroin/gelatin for drug delivery applications: Thyme essential oil and doxycycline monohydrate release study. Journal of Biomedical Materials Research Part A 106(4), 1092-1103.

Das, A., Singh, J. and K.N., Y. (2017) Laccase immobilized magnetic iron nanoparticles: Fabrication and its performance evaluation in chlorpyrifos degradation. International Biodeterioration & Biodegradation 117, 183-189.

Dashtban, M., Schraft, H., Syed, T.A. and Qin, W. (2010) Fungal biodegradation and enzymatic modification of lignin. International Journal of Biochemistry and Bolecular Biology 1(1), 36-50.

Dotto, G.L., Santos, J.M.N., Tanabe, E.H., Bertuol, D.A., Foletto, E.L., Lima, E.C. and Pavan, F.A. (2017) Chitosan/polyamide nanofibers prepared by Forcespinning® technology: A new adsorbent to remove anionic dyes from aqueous solutions. Journal of Cleaner Production 144, 120-129.

Eroglu, E., Agarwal, V., Bradshaw, M., Chen, X., Smith, S.M., Raston, C.L. and Iyer, K.S. (2012) Nitrate removal from liquid effluents using microalgae immobilized on chitosan nanofiber mats. Green Chemistry 14(10), 2682-2685.

Fernández-Fernández, M., Sanromán, M.A. and Moldes, D. (2013) Recent developments and applications of immobilized laccase. Biotechnology Advances 31, 1808–1825.

Galliker, P., Hommes, G., Schlosser, D., Corvini, P.F.X. and Shahgaldian, P. (2010) Laccase-modified silica nanoparticles efficiently catalyze the transformation of phenolic compounds. Journal of Colloid and Interface Science 349(1), 98-105.

Gasser, C.A., Yu, L., Svojitka, J., Wintgens, T., Ammann, E.M., Shahgaldian, P., Corvini, P.F.-X. and Hommes, G. (2014) Advanced enzymatic elimination of phenolic contaminants in wastewater: a nano approach at field scale. Applied Microbiology and Biotechnology 98, 3305–3316.

Gianfreda, L., Xu, F. and Bollag, J.M. (1999) Laccases: a useful group of oxidoreductive enzymes. Bioremediation Journal 3(1), 1-26.

Hassani, T., Ba, S. and Cabana, H. (2013) Formation of enzyme polymer engineered structure for laccase and cross-linked laccase aggregates stabilization. Bioresource Technology 128(-), 640-645.

Hernandez, K. and Fernández-Lafuente, R. (2011) Control of protein immobilization: Coupling immobilization and site-directed mutagenesis to improve biocatalyst or biosensor performance. Enzyme and Microbial Technology 48(2), 107-122.

Hommes, G.G., Christoph A.; Howald, Chaim B. C.; Goers, Roland;, Schlosser, D., Shahgaldian, P. and Corvini, P.F.X. (2012) Production of a robust nanobiocatalyst for municipal wastewater treatment. Bioresource Technology 115, 8-15.

Huang, X.-J., Ge, D. and Xu, Z.-K. (2007) Preparation and characterization of stable chitosan nanofibrous membrane for lipase immobilization. European Polymer Journal 43(9), 3710-3718.

Huang, Z.-M., Zhang, Y.Z., Kotaki, M. and Ramakrishna, S. (2003) A review on polymer nanofibers by electrospinning and their applications in nanocomposites. Composites Science and Technology 63(15), 2223-2253.

Hudson, S., Cooney, J. and Magner, E. (2008) Proteins in Mesoporous Silicates. Angewandte Chemie Int. Ed. 47(- 45), 8582-8594.

Illanes, A., Fernández-Lafuente, R., Guisán, J.M. and Wilson, L. (2008) Enzyme Biocatalysis, Springer.

Ivnitski, D. and Atanassov, P. (2007) Electrochemical studies of intramolecular electron transfer in laccase from Trametes versicolor. Electroanalysis: An International Journal Devoted to Fundamental and Practical Aspects of Electroanalysis 19(22), 2307-2313.

Jen-Mao Fanchiang, D.-H.T. (2009) Degradation of anthraquinone dye C.I. Reactive Blue 19 in aqueous solution by ozonation. Chemosphere 77, 214-221

Jermann, D., Pronk, W., Boller, M. and Schäfer, A.I. (2009) The role of NOM fouling for the retention of estradiol and ibuprofen during ultrafiltration. Journal of Membrane Science 329, 75-84.

Jia, H., Zhu, G., Vugrinovich, B., Kataphinan, W., Reneker, D.H. and Wang, P. (2002) Enzyme-carrying polymeric nanofibers prepared via electrospinning for use as unique biocatalysts. Biotechnology Progress 18(5), 1027-1032.

Jořenek, M. and Zajoncová, L. (2015) Immobilization of laccase on magnetic carriers and its use in decolorization of dyes. Chemical and Biochemical Engineering Quarterly 29(3), 457-466.

Karavasili, C., Panteris, E., Vizirianakis, I.S., Koutsopoulos, S. and Fatouros, D.G. (2018) Chemotherapeutic Delivery from a Self-Assembling Peptide Nanofiber Hydrogel for the Management of Glioblastoma. Pharmaceutical Research 35(8), 166.

Kim, Y.-J. and Nicell, J.A. (2006) Impact of reaction conditions on the laccase-catalyzed conversion of bisphenol A. Bioresource Technology 97(12), 1431-1442.

Kunamneni, A., Ghazi, I., Camarero, S., Ballesteros, A., Plou, F.J. and Alcalde, M. (2008) Decolorization of synthetic dyes by laccase immobilized on epoxy-activated carriers. Process Biochemistry 43(2), 169-178.

Kurniawati, S. and Nicell, J.A. (2008) Characterization of Trametes versicolor laccase for the transformation of aqueous phenol. Bioresource Technology 99(16), 7825-7834.

Lloret, L., Hollmann, F., Eibes, G., Feijoo, G., Moreira, M.T. and Lema, J.M. (2012) Immobilisation of laccase on Eupergit supports and its application for the removal of endocrine disrupting chemicals in a packed-bed reactor. Biodegradation 23, 373–386.

Lu, L., Zhao, M. and Wang, Y. (2007) Immobilization of laccase by alginate–chitosan microcapsules and its use in dye decolorization. World Journal of Microbiology and Biotechnology 23, 159–166.

Mahmoodi, N.M. and Mokhtari-Shourijeh, Z. (2015) Preparation of PVA-chitosan blend nanofiber and its dye removal ability from colored wastewater. Fibers and Polymers 16(9), 1861-1869.

Margot, J., Bennati-Granier, C., Maillard, J., Blánquez, P., Barry, D.A. and Holliger, C. (2013) Bacterial versus fungal laccase: potential for micropollutant degradation. AMB Express 3(1), 63.

Marysková, M., Ardao, I., García-González, C.A., Martinová, L., Rotková, J. and Sevc, A. (2016) Polyamide 6/chitosan nanofibers as support for the immobilization of *Trametes versicolor* laccase for the elimination of endocrine disrupting chemicals. Enzyme and Microbial Technology 89, 31-38.

Mate, D.M. and Alcalde, M. (2017) Laccase: a multi-purpose biocatalyst at the forefront of biotechnology. Microbial Biotechnology 10(6), 1457-1467.

Mester, T. and Tien, M. (2000) Oxidation mechanism of ligninolytic enzymes involved in the degradation of environmental pollutants. International Biodeterioration & Biodegradation 46(1), 51-59.

Mester, T., de Jong, E. and Field, J.A. (1995) Manganese regulation of veratryl alcohol in white rot fungi and its indirect effect on lignin peroxidase. Applied and Environmental Microbiology 61(5), 1881-1887.

Ngomsik, A.-F., Bee, A., Draye, M., Cote, G. and Cabuil, V. (2005) Magnetic nano- and microparticles for metal removal and environmental applications: a review. Comptes Rendus Chimie 8(6), 963-970.

Nguyen, L.N., Hai, F.I., Dosseto, A., Richardson, C., Price, W.E. and Nghiem, L.D. (2016) Continuous adsorption and biotransformation of micropollutants by granular activated carbon-bound laccase in a packed-bed enzyme reactor. Bioresource Technology 210, 108–116.

Ortiz de Montellano, P.R. (1992) Catalytic sites of hemoprotein peroxidases. Annual Review of Pharmacology and Toxicology 32(1), 89-107.

Osma, J.F., Toca-Herrera, J.L. and Rodríguez-Couto, S. (2010) Biodegradation of a simulated textile effluent by immobilised-coated laccase in laboratory-scale reactors. Applied Catalysis A: General 373(1–2), 147-153.

Othman, A.M., González-Domínguez, E., Sanromán, Á., Correa-Duarte, M. and Moldes, D. (2016) Immobilization of laccase on functionalized multiwalled carbon nanotube membranes and application for dye decolorization. RSC Advances 6(115), 114690-114697.

Pogorilyi, R.P., Siletskaya, E.Y., Goncharik, V.P., Kozhara, L.I. and Zub, Y.L. (2007) Immobilization of Urease on the Silica Gel Surface by Sol-Gel Method. Russian Journal of Applied Chemistry 80(2), 330–334.

Prieto, D., Aparicio, G., Morande, P.E. and Zolessi, F.R. (2014) A fast, low cost, and highly efficient fluorescent DNA labeling method using methyl green. Histochemistry and Cell Biology 142(3), 335-345.

Rao, M.N., Kembhavi, A.A. and Pant, A. (2000) Immobilization of endo-polygalacturonase from *Aspergillus ustus* on silica gel. Biotechnology Letters 22, 1557–1559.

Reddy, G.V.B., Sridhar, M. and Gold, M.H. (2003) Cleavage of nonphenolic β-1 diarylpropane lignin model dimers by manganese peroxidase from Phanerochaete chrysosporium: Evidence for a hydrogen abstraction mechanism. European Journal of Biochemistry 270(2), 284-292.

Rekuć, A., Bryjak, J., Szymańska, K. and Jarzębski, A.B. (2010) Very stable silica-gel-bound laccase biocatalysts for the selective oxidation in continuous systems. Bioresource Technology 101(7), 2073-2083.

Rodrigues, R.C., Ortiz, C., Berenguer-Murcia, Á., Torres, R. and Fernández-Lafuente, R. (2013) Modifying enzyme activity and selectivity by immobilization. Chem. Soc. Rev. 42(15), 6290-6307.

Salvachúa, D., Prieto, A., López-Abelairas, M., Lu-Chau, T., Martínez, Á.T. and Martínez, M.J. (2011) Fungal pretreatment: An alternative in second-generation ethanol from wheat straw. Bioresource Technology 102(16), 7500-7506.

Shioji, S., Hanada, M., Yasuhiro;, H., Tokami, K. and Yamamoto, H. (2003) Continuous surface modication of silica particles for enzyme immobilization. Advanced Powder Technol. 14, 231–245.

Silverman, R.B. (2002) The Organic Chemistry of Enzyme-catalyzed Reactions, pp. 1-38, Academic Press, San Diego.

Su-Hua, W., Bing-zhi, D. and Yu, H. (2010) Adsorption of bisphenol A by polysulphone membrane. Desalination 253, 22-29.

Taboada-Puig, R., Lú-Chau, T., Moreira, M.T., Feijoo, G., Martínez, M.J. and Lema, J.M. (2011) A new strain of Bjerkandera sp. production, purification and characterization of versatile peroxidase. World Journal of Microbiology and Biotechnology 27(1), 115-122.

Taboada-Puig, R., Lú-Chau, T.A., Moreira, M.T., Feijoo, G. and Lema, J.M. (2013) Activation of Kraft Lignin by an Enzymatic Treatment with a Versatile Peroxidase from Bjerkandera sp. R1. Applied Biochemistry and Biotechnology 169(4), 1262-1278.

Tratnyek, P.G. and Johnson, R.L. (2006) Nanotechnologies for environmental cleanup. Nano Today 1(2), 44-48.

Xu, F. (1997) Effects of Redox Potential and Hydroxide Inhibition on the pH Activity Profile of Fungal Laccases. The Journal of Biological Chemistry 272(10), 924–928.

Xu, F., Shin, W., Brown, S.H., Wahleithner, J.A., Sundaram, U.M. and Solomon, E.I. (1996) A study of a series of recombinant fungal laccases and bilirubin oxidase that exhibit significant differences in redox potential, substrate specificity, and stability. Biochimica et Biophysica Acta (BBA)-Protein Structure and Molecular Enzymology 1292(2), 303-311.

Yan, X., Tai, Z., Chen, J. and Xue, Q. (2011) Fabrication of carbon nanofiber–polyaniline composite flexible paper for supercapacitor. Nanoscale 3(1), 212-216.

Yoshimoto, H., Shin, Y., Terai, H. and Vacanti, J. (2003) A biodegradable nanofiber scaffold by electrospinning and its potential for bone tissue engineering. Biomaterials 24(12), 2077-2082.

Zimmermann, Y.-S., Shahgaldian, P., Corvini, P.F.X. and Hommes, G. (2011) Sorption-assisted surface conjugation: a way to stabilize laccase enzyme. Applied Microbiology and Biotechnology 92(1), 169-178.

4. Chapter 4

HETEROGENEOUS FENTON catalysis using iron-based nanomaterials

SUMMARY

With the recent development of nanotechnology, magnetic nanoparticles (mNPs) have received increasing attention as potential heterogeneous Fenton catalysts in wastewater treatment applications, as an alternative to the conventional Fenton process using dissolved iron salts. Due to their superparamagnetic properties, magnetite-based NPs can be easily recovered and reused by applying a magnetic field. In the present study, the superparamagnetic magnetite (Fe_3O_4) NPs play a crucial role, being themselves the catalytic Fenton agents. In other words, mNPs have not been used as support, Fe^{2+} and Fe^{3+} ions present on the surface of nanoparticles interact with hydrogen peroxide (H_2O_2) in the generation of hydroxyl (·OH) radicals, which can oxidize most organic molecules as heterogeneous Fenton process. More than that, these mNPs can be easily recovered by applying an external magnetic field. An initial screening will be performed for the removal of RB19 dye as model pollutant by free and immobilized catalysts. The catalyst with the greatest potential will be evaluated in the degradation of a wide range of organic micropollutants.

OUTLINE

4.1 Introduction

Advanced oxidation processes (AOPs) are wastewater treatment technologies based on the oxidation of pollutants by reactive oxygen species (ROS), mainly hydroxyl radicals (·OH). This type of powerful and non-selective oxidants can attack nearly all organic complexes, causing their decomposition. AOPs include photochemical methods, such as photocatalysis, photo-Fenton and the combination of ozone-hydrogen peroxide-ultraviolet radiation ($O_3/H_2O_2/UV$), as well as non-photochemical methods, including ozonation, wet peroxide ozonation (O_3/H_2O_2), catalytic ozonation and Fenton processes (Bethi et al. 2016). Due to the strong oxidative capacity of ROS, AOPs have been considered to treat different types of water bodies containing persistent pollutants, such as pharmaceuticals and personal care products (PPCPs), endocrine disrupting compounds (EDCs), dyes, or nitroaromatic explosives (Andreozzi et al. 2004, Tayo et al. 2018, Ning et al. 2007, Sathishkumar et al. 2016, Ayoub et al. 2010).

Among AOPs, Fenton catalysis is a well-known and simple technology, which has shown to be more efficient in terms of operating costs for the degradation of a wide range of organic compounds at low and high concentrations (Sable et al. 2015, Krishnan et al. 2017). Fenton reaction starts with an electron transfer process, in which ferrous iron (Fe^{2+}) reacts with hydrogen peroxide (H_2O_2) to form ·OH (Eq. 1), so that it oxidizes organic matter, ideally resulting in complete mineralization to carbon dioxide (CO_2) and water (H_2O). The ferric iron (Fe^{3+}) is then reduced to Fe^{2+} by H_2O_2, forming a hydroperoxyl radical (·OOH) (Eq. 2).

$$Fe^{2+} + H_2O_2 \rightarrow Fe^{3+} + \cdot OH + H^+ \quad (1)$$

$$Fe^{3+} + H_2O_2 \rightarrow Fe^{2+} + \cdot OOH + H^+ \quad (2)$$

However, the conventional Fenton process has important drawbacks, among which is the impossibility of viable separation of the homogeneous catalyst (Fe^{2+}) from the treated effluent and, therefore, the need for treatment of the ferric hydroxide sludge produced (Álvarez et al. 2010). In this context, the cost associated with post-treatment can represent up to 50% of the total operating costs (Munoz et al. 2015).

To overcome these obstacles, the heterogeneous Fenton approach, which uses solid phase catalysts that can be easily separated from the effluent, represents a promising alternative. However, heterogeneous catalysts have only a small fraction of iron on their surface, presenting slower reaction kinetics and mass transfer limitations compared to homogeneous catalysts (Bae et al. 2013, Mirzaei et al. 2017). The link between heterogeneous and homogeneous catalysts can be accomplished using nanostructured materials. Previous works have reported the use of engineered magnetic nanoparticles (mNPs), whose high surface/volume ratio compared to bulk materials enhances the contact between the reactants and the catalyst, making them efficient catalysts in water treatment applications (Zang et al. 2018, Sun et al. 2013, Truskewycz et al. 2016). Magnetite (Fe_3O_4) is an environmentally benign material containing Fe^{2+} and Fe^{3+} in its structure, and presents superparamagnetism when reduced to the nanoscale, allowing easy and cost-effective recovery of the medium simply by applying an external magnetic field. This feature ensures a safe discharge of the treated effluent free of mNPs and the reuse of Fe_3O_4 in a subsequent cycle, ideally without significant loss of catalytic activity (Velichkova et al. 2013). However, the superparamagnetic nature of Fe_3O_4 mNPs in aqueous media leads to interparticle interactions, causing the formation of large aggregates with lower surface/volume ratios, directly affecting their catalytic activity (Mehdaoui et al. 2017). This shortcoming can be avoided by modifying the surface of mNPs with stabilizing agents, such as coatings of surfactants, silica or oleic acid derivatives, preventing mNPs from agglomeration by steric or electrostatic forces (Kim et al. 2003). However, high stability of colloidal Fe_3O_4 mNPs suspensions can result in a difficult recovery of the material, which would require an additional separation process between water treatment cycles, limiting the reuse of the catalyst (Wang et al. 2013). The immobilization of mNPs on a suitable matrix is relevant, not only to improve their dispersion and separability, but also to preserve their properties for widespread application (Zubir et al. 2014).

The ordered mesoporous material SBA-15 has been widely used as support for active moieties due to its uniform hexagonally arrayed channels with a narrow pore size distribution, thick pore walls, high surface area and hydrothermal stability. Typically, the pore size of SBA-15 ranges from 4 to 12 nm, but can be increased up to 30 nm by adding organic additives during its preparation (Chaudhary and Sharma 2017). Besides, the mechanical and chemical stability of this material makes SBA-15

an ideal support for the incorporation of catalytic mNPs on its surface or in its pores for wastewater treatment applications (Singh et al. 2015, Aliyan et al. 2013, Santos et al. 2017).

This chapter explores the use of different magnetite protecting agents, including polyacrylic acid (PAA), polyethylenimine (PEI) and SiO_2 in order to formulate coated NPs to be used as catalyst for the removal of Reactive Blue 19 (RB19) as the compound model. The influence of the main operational variables (concentrations of Fe_3O_4 mNPs and H_2O_2) has been evaluated using the Surface Response Methodology (SRM) according to a central compound design, in order to parameterize the optimal conditions to degrade RB19 with the previously selected nanocatalyst. Subsequently, a screening will be carried out in order to test the application of free and immobilized catalysts onto ordered mesoporous material SBA-15 to remove the dye. The catalyst with the greatest potential will be evaluated in the degradation of the natural estrogens estrone (E1), 17β-estradiol (E2), and the synthetic estrogen 17α-ethynylestradiol (EE2), bisphenol A (BPA), sulfamethoxazole (SMX) antibiotic and pyrene (PYR).

4.2 Materials and methods

4.2.1 Chemicals and nanostructured catalysts

All chemicals used in this chapter have been previously described in Section 2.1 of Chapter 2. Selected Fenton-like nanocatalysts (listed in Tables 4.1 and 4.2) were synthesized and provided by Laboratory of Magnetism and Nanotechnology (Nanomag, Universidade de Santiago de Compostela), except Fe_3O_4@PAA mNPs which were supplied by Nanogap (Milladoiro, Spain).

Table 4.1 Magnetic nanoparticles characteristics

Catalyst	Characteristics
Fe_3O_4	Magnetite stabilized in TMAOH
Fe_3O_4@PAA	Magnetite stabilized with PAA
Fe_3O_4@PEI	PEI-coated magnetite NPs
Fe_3O_4@SiO_2	Silica coated magnetite mNPs

Table 4.2 Magnetic nanoparticles supported onto SBA-15 characteristics

Catalyst	Characteristics
Fe_3O_4@PAA/SBA-15	PAA-coated magnetic NPs supported onto SBA-15
Fe_3O_4@PEI/SBA-15	PEI-coated magnetic NPs supported onto SBA-15
Fe_3O_4@SiO_2/SBA-15	Silica coated magnetic NPs supported onto SBA-15
Fe_3O_4@C/SBA-15	Fe_3O_4@C NPs functionalized with carboxylic groups supported onto SBA-15

4.2.2 Description of the different production processes

Sterically-stabilized Fe_3O_4 nanoparticles were prepared by the co-precipitation of Fe^{2+} and Fe^{3+} salts, following the Massart (1981) method. In a typical synthesis, 12.15 g of $FeCl_3.6H_2O$ (45 mmol) and 8.35 g of $FeSO_4.7H_2O$ (30 mmol, molar ratio $Fe^{3+}/Fe^{2+}\approx 1.5$) were placed in a 250 mL round-bottom flask and dissolved in 100 mL of 0.01 M HCl solution with mechanical stirring. Temperature was increased to 60 °C and 30 mL of 28% wt ammonia solution were added to the mixture, with the immediate formation of black magnetite nanoparticles. The nanoparticles were washed four times with deionized water and, finally, a solution of tetramethylammonium hydroxide (TMAOH) (10% by weight) was added to raise pH to 10 for the sterically stabilized magnetite. On this basis, mNPs with different coatings (PAA, PEI and SiO_2) were prepared (Table 4.1).

PEI-coated magnetite nanoparticles and PAA-coated magnetite nanoparticles: The production process starts with the addition of PEI or PAA to Fe_3O_4 NPs, with the addition of HCl to lower pH to 4 before the addition of tetraethyl orthosilicate (TEOS) to produce the mNPs (Vargas-Osorio et al. 2016). Silica-coated magnetic nanoparticles: Fe_3O_4@SiO_2 core-shell nanoparticles are prepared through a water-in-cyclohexane reverse microemulsion starting from the oleic-acid-coated magnetite nanoparticles, using as main chemicals: polyoxyethylene(5)nonylphenyl ether (Igepal CO-520), cyclohexane, NH_4OH, TEOS and isopropanol (IPA) (Vargas-Osorio et al. 2017).

The synthetic procedure of mesoporous silica SBA-15 has been previously by Acton (2012), based on the Colilla et al. (2007) method. The product was dried and subjected to different washing cycles with organic solvents to remove the remaining block copolymer.

Preparation of Fe_3O_4@PAA/SBA-15 and Fe_3O_4@PEI/SBA-15 nanocomposites (NCs): Fe_3O_4@PAA/SBA-15 and Fe_3O_4@PEI/SBA-15 were synthesized by incorporating the SBA-15 matrix into a container with an aqueous HCl solution, hexahydrate ferric chloride and tetrahydrate ferrous sulphate under mechanical stirring. The temperature was increased and ammonium hydroxide and PAA (Mw 2000 Da) (Fe_3O_4@PAA/SBA-15) or PEI (Mw 25000 Da) were incorporated to the mixture. The reaction was allowed to progress, and the resulting precipitate was acidified to pH 4 with HCl (9%) and then magnetically separated. Finally, the NCs were repeatedly washed with distilled water and ethanol and dried at 60 °C for 12 h (Vargas-Osorio et al. 2016).

Preparation of Fe_3O_4@SiO_2/SBA-15 NC: This procedure is based on the formation of silica-coated core-shell NPs in water-in-oil microemulsion systems, but including the SBA-15 matrix to favor the anchoring of Fe_3O_4@SiO_2 on the outer surface of the SBA-15 matrix (Vargas-Osorio et al. 2017). Magnetic mesoporous Fe_3O_4@C/SBA-15 were prepared by adding mesoporous silica to the solvothermal preparation of multicore magnetic aggregates described by Wang et al. (2011).

4.2.3 Characterization of nanostructured catalysts

The analytical methods used to measure the conventional parameters for characterizing the selected catalysts (Tables 4.1 and 4.2): X-ray diffraction (XRD) study of crystalline phases, transmission electron microscopy (TEM) images, scanning electron microscopy (SEM), particle size distribution, thermogravimetric analysis (TGA) and magnetization curves have been previously described in Section 2.2 of Chapter 2.

4.2.4 Benchmarking between different nano-structured materials: Experimental set-up for dye removal by heterogenous Fenton

Batch experiments were performed in 20-mL glass reactors containing 10 mL of an aqueous solution of RB19 (25 mg L^{-1}) at pH 3. RB19 degradation was initiated by adding H_2O_2 to the reaction medium. Then, samples were then incubated at room temperature and continuously stirred at 150 rpm in an orbital shaker (C24 Incubator shaker, New Brunswick Scientific, NJ, USA). At regular time intervals, aliquots (200 µL) were taken after magnetic separation of the nanocatalyst from the treated solution, and absorbance measurements were performed on a BioTek PowerWave XS2 micro-plates spectrophotometer (Winooski, VT, USA) to monitor the color removal of RB19 (λ= 592 nm), as described in Section 2.3 of Chapter 2. The degradation yield (%) was determined as the extent of color removal, calculated by Equation 3:

$$\text{Degradation yield (\%)} = \frac{(C_0 - C_t)}{C_0} \times 100 \quad (3)$$

where C_0 and C_t represent the concentration of the organic compound (mg L^{-1}) before and after the reaction time, respectively. To clarify the influence of mNPs on dye removal, control experiments containing RB19 and H_2O_2 were conducted in parallel experiments lacking catalyst. Adsorption control assays without H_2O_2 dosage were also carried out.

4.2.5 Experimental design and optimization for dye removal by heterogeneous Fenton catalysis with Fe_3O_4@PAA mNPs

Color removal of RB19 (25 mg L^{-1}) by the heterogeneous Fenton process was evaluated following a factorial, centered second-order experimental design for the optimization of the main experimental conditions. The concentrations of Fe_3O_4@PAA mNPs (100-300 mg L^{-1}) and H_2O_2 (100-400 mg L^{-1}) were selected as independent variables for the experimental design to obtain information, both single and combined, on their effect on the decolorization of RB19 (Table 4.3). The central composite design (CCD) contains the complete factorial design and star design at the five factor levels: -α, -1, 0, 1 y α, where $|\alpha| = (2^f)^{1/4}$, i.e. 1.414 in the case of two factors (f=2). Eleven series of batch experiments were carried out, and three replicates were conducted at the central point.

Table 4.3 Variables and levels applied to the RB19 decolorization through an experimental design of the Fenton process

Variables	Levels				
	-1.414	**-1**	**0**	**1**	**1.414**
Fe_3O_4@PAA mNPs (mg L^{-1})	58.6	100	200	300	341.4
H_2O_2 (mg L^{-1})	250	100	250	400	462.1

The experimental data were tested according to the proposed model using the commercial IBM® SPSS Statistics® 20 software. To predict the decolorization percentage of the dye, the experimental data were fitted using a second-order polynomial equation described by the following mathematical model:

$$y_j=\beta_{0j}+\sum_{i=1}^{2}\beta_i x_i+\sum_{i=1}^{2}\sum_{k=1}^{2}\beta_{ikj}x_i x_k \quad (4)$$

where y_j is the dependent variable (j=1), β_{0j}, β_{ij} and β_{ikj} are the regression coefficients calculated from the experimental results by the least-squares method, and x_i or x_k (k≥i) are the dimensionless, normalized independent variables.

The RB19 decolorization kinetics in a batch system was explained by a pseudo-first order equation:

$$\ln\left(\frac{C_t}{C_0}\right)=-k_{obs}t \quad (5)$$

where k_{obs} is the observed rate constant (h^{-1}) and t is the time (h). A Total Organic Carbon (TOC) analyzer with autosampler (Shimadzu TOC 5000) was used to determine TOC concentrations in samples at mg L^{-1} levels and to calculate the percentage of mineralization after treatment. This parameter is defined in Section 2.4 of Chapter 2.

4.2.6 Evaluation of the different immobilized mNPs onto SBA-15 for dye removal

Different immobilized nanocatalyst supported on the SBA-15 mesoporous silica matrix (Table 4.2) were tested for RB19 dye decolorization by heterogeneous Fenton-like reaction in a 20-mL glass reactor. A stock solution of RB19 was diluted in

H_2O (pH 3-7) to a final concentration of 25 mg L^{-1} and incubated under previously optimized conditions (Section 4.2.4): 200 mg L^{-1} of Fe_3O_4 and 100 mg L^{-1} of H_2O_2. Batch experiments were conducted at room temperature and continuous orbital agitation (150 rpm). Dye removal was initiated by adding H_2O_2 to the reactor (up to a final volume of 10 mL). At regular time intervals, absorbance measurements were performed to monitor the color removal of RB19. The decolorization yield (%) was determined as the rate of color disappearance, calculated using Equation 3. To clarify the influence of the magnetic catalysts on the dye decolorization, adsorption control experiments lacking H_2O_2 were conducted.

Active species (·OH and $O_2^{\cdot-}$) scavengers were also studied during the color removal of RB19 using Fe_3O_4@PAA/SBA-15 as catalyst to further explore the underlying degradation mechanism. The selected hydroxyl radical scavengers were *tert*-butanol (*t*-Butanol), methanol (MeOH), dimethyl sulfoxide (DMSO) and potassium iodide (KI) at 50 mM. Superoxide radical contribution was examined quenching experiments by adding benzoquinone (BQ; 1 mM) and ascorbic acid (AH_2; 1 mM) separately as O_2^- radical scavenger.

4.2.7 Reuse of catalysts

The reuse of the Fe_3O_4@PAA/SBA-15 catalyst was evaluated in a sequential operation of a magnetic reactor (10 mL), according to the fill-and-draw principle. After each Fenton-like cycle, the liquid fraction was removed by separating the catalyst with an external magnetic field. Then, fresh medium containing RB19 at 25 mg L^{-1} was added to the catalyst for a new cycle. Aliquots were taken at the beginning and end of each cycle to determine the dye concentration. TOC was determined in the supernatant after magnetic separation of the catalyst. Normalized TOC concentration (%TOC removal) was used to quantitatively characterize the compound mineralization (Section 4.2, Chapter 2).

4.2.8 Experimental set-up for recalcitrant compounds removal by Fenton heterogenous using Fe_3O_4@PAA/SBA-15 as catalyst

Prior to the evaluation of a wide range of organic pollutants (BPA, PYR and SMX), catalytic tests for the degradation of 350 µg L^{-1} E1, E2 and EE2 were performed on 10 mL of aqueous samples containing 100-1000 mg L^{-1} of Fe_3O_4@PAA/SBA-15 at

pH 3, with different H_2O_2 concentrations (200-500 mg L^{-1}). Chemical structures and main physicochemical properties of selected compounds are displayed in Table 2.2 of Chapter 2. Batch experiments were conducted at room temperature and continuous orbital agitation (150 rpm). Aliquots (200 µL) of the aqueous samples collected at different times during the degradation processes were taken and the compounds were quantified by high performance liquid chromatography (HPLC) (Section 2.3 of Chapter 2). Degradation yield (%) was determined using Equation 3. Adsorption and H_2O_2 control experiments were also conducted.

4.3 Results and discussion

4.3.1 Characterization of catalysts

The catalysts were structurally characterized by X-ray diffraction (XRD) patterns to evaluate the degree of crystallinity. The position and relative intensities of the peaks observed in Figure 4.1 for Fe_3O_4, Fe_3O_4@SiO_2, Fe_3O_4@PEI and Fe_3O_4@PAA mNPs indicate that the main crystalline phase present in the sample corresponds to magnetite (Joint Committee of Powder Diffraction Standards (JCPDS) card number 19-0629). Additionally, Fe_3O_4@SiO_2 showed a broad hump between 18° and 29° corresponding to the amorphous silica coating.

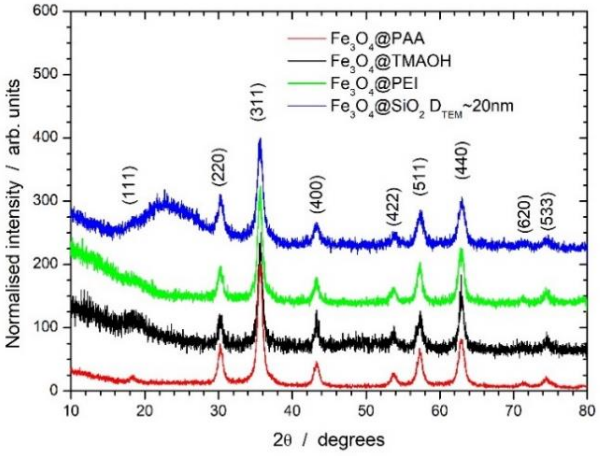

Figure 4.1 X-ray diffraction (XRD) pattern of naked and stabilized-Fe_3O_4 mNPs.

In the case of mesoporous silica composites, position and relative intensities of the main reflection peaks revealed the presence of Fe_3O_4 in Fe_3O_4@PAA/SBA-15 (Figure 4.2a). Additionally, mesoporous matrix structures were evaluated by low-angle XRD (Figure 4.2b). The disruption in the structural arrangement of SBA-15 with the disappearance of reflections (110) and (200) is related to the random distribution of Fe_3O_4 in the NC, which causes a loss of order. Similarly, Fe_3O_4@PEI/SBA-15, Fe_3O_4@SiO_2/SBA-15 and Fe_3O_4@C/SBA-15 NCs were previously structurally characterized by XRD measurements by Vargas-Osorio et al. (2016) and (2017).

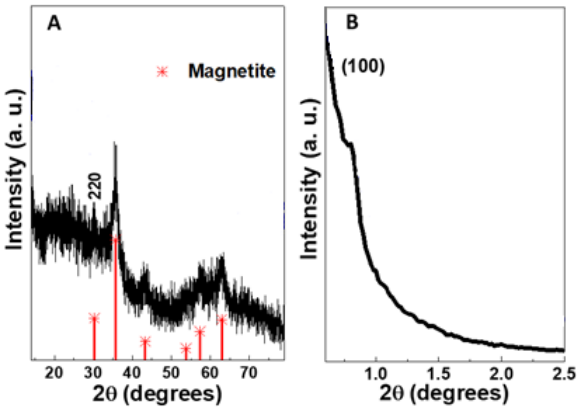

Figure 4.2 (a) X-ray diffraction (XRD) pattern and (b) low angle XRD patterns for the Fe_3O_4@PAA-SBA-15 mesoporous material.

Figure 4.3 shows the TEM micrograph of non-coated Fe_3O_4, Fe_3O_4@PAA Fe_3O_4@PEI and Fe_3O_4@SiO_2. The mNPs sample presented a regular, almost spherical morphology, with an average diameter of 8.2, 7.6 and 10.9 nm for Fe_3O_4, Fe_3O_4@PAA Fe_3O_4@PEI, respectively. The average particle size of Fe_3O_4@SiO_2 mNPs is around 20 nm, which evidences the effect of surface silica coating. The thickness of the silica layer was not determined; however, it can be differentiated in the TEM micrograph as it is lighter in color than Fe_3O_4.

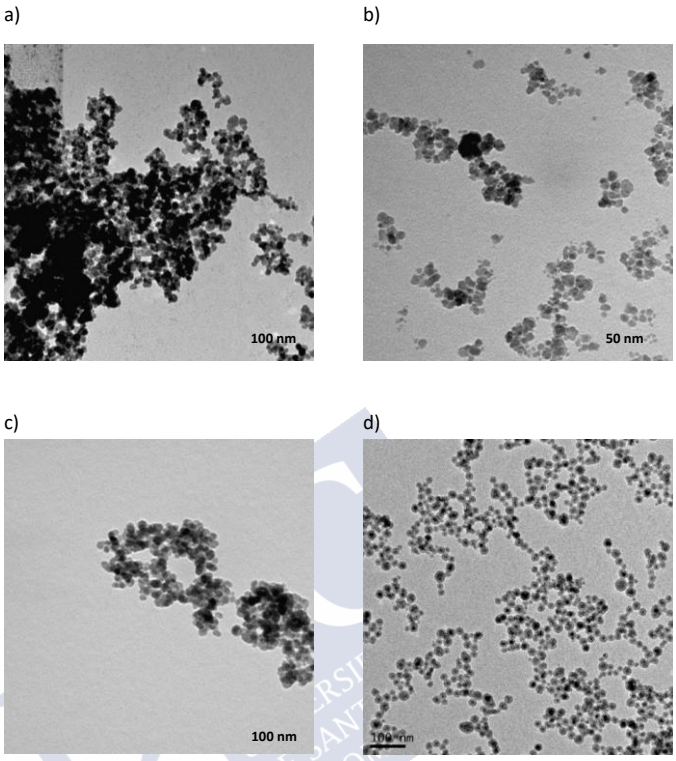

Figure 4.3 TEM images of a) Fe_3O_4-TMAOH (average size: 8.2 ± 3.8 nm), b) Fe_3O_4@PAA (average size: 7.6 ± 2.7 nm), c) Fe_3O_4@PEI (average size: 10.9 ± 3.0 nm) and d) Fe_3O_4@SiO_2 (average size: ≈20 nm).

The total solid content in mNPs was determined by thermogravimetry (TGA), obtaining mNPs concentrations of 0.83, 2.05, 1.02 and 0.69% by weight in the stock solution for Fe_3O_4, Fe_3O_4@PAA Fe_3O_4@PEI and Fe_3O_4@SiO_2, respectively. The morphology of NCs was analyzed by SEM (Figure 4.4).

In Fe_3O_4@PAA/SBA-15 and Fe_3O_4@PEI/SBA-15 NCs, magnetite is found both inside the channels and as aggregates on the outside, while in Fe_3O_4@SiO_2/SBA-15 and Fe_3O_4@C/SBA-15 magnetite NPs are found only anchored onto the outer surface, by the amorphous SiO_2 coating in the case of Fe_3O_4@SiO_2/SBA-15.

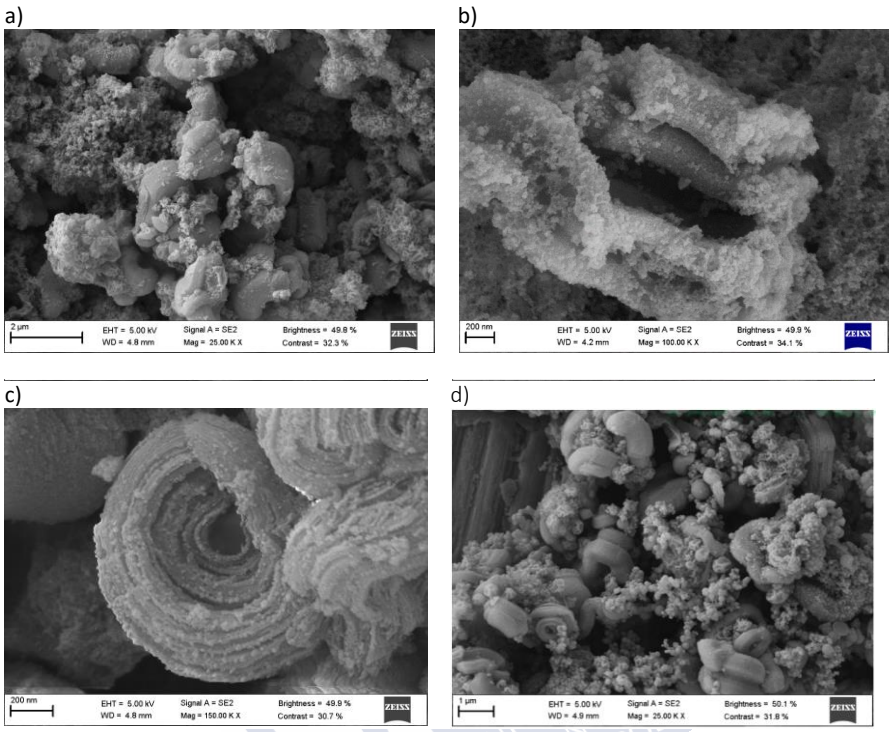

Figure 4.4 SEM images of a) Fe_3O_4@PEI/SBA-15, b) Fe_3O_4@PAA/SBA-15, c) Fe_3O_4@SiO_2/SBA-15 and d) Fe_3O_4@C/SBA-15.

The pore size distribution and specific surface area of NCs were estimated from N_2 adsorption isotherms. Figure 4.5a displayed the characteristic type IV isotherms of Fe_3O_4@PAA/SBA-15 mesoporous material. The boundary hysteresis loop with two-steep parallel branches (type H1) confirmed the presences of the cylindrical pores of SBA-15 NC. The pore size distribution of mesoporous samples is presented in Figure 4.5b.

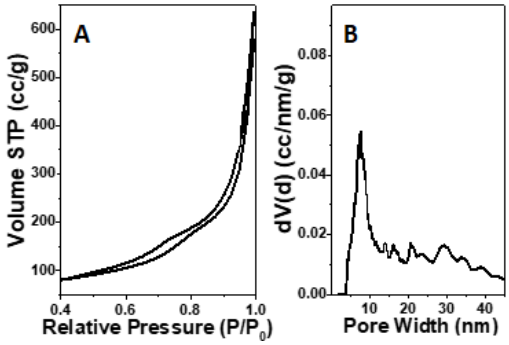

Figure 4.5 (a) N_2 sorption isotherms for the SBA-15 and Fe_3O_4@PAA/SBA-15. (b) Pore size distribution of Fe_3O_4@PAA/SBA-15.

The textural and structural values of all selected magnetic NCs (Fe_3O_4@PAA/SBA-15, Fe_3O_4@PEI/SBA-15, Fe_3O_4@SiO_2/SBA-15 and Fe_3O_4@C/SBA-15) are compiled in Table 4.4, where S_{BET} is the surface area obtained by BET multipoint analysis, V_p represents the total volume of pores and W_{Fe} is the iron content in the NC.

Table 4.4 Textural and structural values of magnetic mesoporous nanocomposites (NCs). Surface area (S_{BET}), pore volume (V_p) and iron weight percentage (W_{Fe}).

Sample	S_{BET} (m^2 g^{-1})	V_p (cm^3 g^{-1})	W_{Fe} (%)
Fe_3O_4@PAA/SBA-15	220.29	0.65	24.0
Fe_3O_4@PEI/SBA-15	157.32	0.44	15.0
Fe_3O_4@SiO_2/SBA-15	235.90	0.35	6.3
Fe_3O_4@C/SBA-15	156.00	0.38	8.0

Pore size by NLDFT method (PS_{DFT}), unit cell parameter (a_0) and thickness of the wall of the mesopores (t_{wall}) was also estimated for Fe_3O_4@PAA/SBA-15 NC, obtaining values of 9.09 nm of PS_{DFT}, 12.77 nm of a_0 and 3.67 nm of t_{wall}.

Magnetization studies of Fe_3O_4 mNPs and magnetic NCs (Fe_3O_4@PAA/SBA-15) were conducted by measuring the variation of the magnetization as a function of the applied magnetic field at 300 K (Figures 4.6 and 4.7).

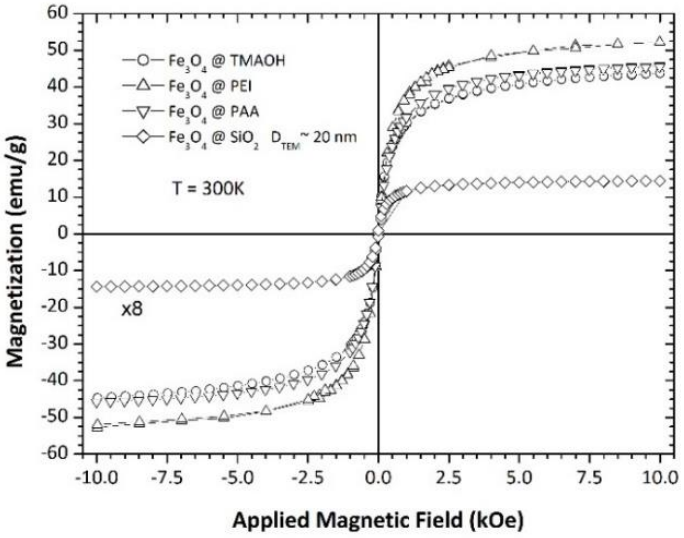

Figure 4.6 Magnetization study of stabilized-Fe_3O_4 mNPs.

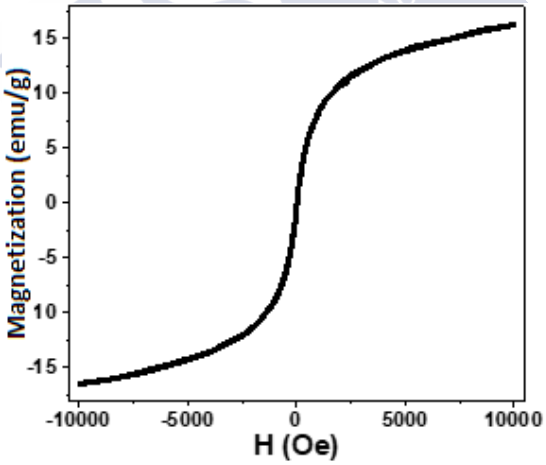

Figure 4.7 Vibrating sample magnetometer (VSM) curves of Fe_3O_4@PAA/SBA-15.

The obtained magnetization curves (Figures 4.6 and 4.7) confirms the superparamagnetic behavior (negligible coercive forces and remanence) of the magnetite-based samples. In the case of Fe_3O_4@SiO_2 mNPs, a decrease in saturation

magnetization can be observed (Figure 4.6). According to Moldes-Diz et al. (2018), this significant drop can be attributed to the silica shell, which is non-magnetic and may affect the magnetization values. For Fe_3O_4@PEI/SBA-15, Fe_3O_4@SiO_2/SBA-15 and Fe_3O_4@C/SBA-15 NCs, similar magnetization curves (Figure 4.7) were previously obtained by Vargas-Osorio et al. (2017).

4.3.2 Analysis of different iron-based nanomaterials for the removal of a model dye by heterogeneous Fenton

The objective of this study is to carry out a preliminary benchmarking between the different nano-structured materials. To optimize Fenton reaction, experiments were performed on aqueous samples containing RB19, as a model compound of organic pollutant to be degraded. The initial conditions selected: Fe_3O_4-TMAOH catalyst dosage (100-1000 mg L^{-1}), H_2O_2 concentration (50-500 mg L^{-1}), 25 mg L^{-1} of RB19 and pH 3 were assumed according to similar previous works (Siddique 2014, Zhang et al. 2014, Hu et al. 2011).

Briefly, the best results of dye decolorization results using Fe_3O_4-TMAOH as catalyst was obtained at pH 3, with Fe_3O_4 in the range of 200-300 mg L^{-1} (Figure 4.8a) and H_2O_2 at 100-300 mg L^{-1} (Figure 4.8b), obtaining 43.59 ± 0.72% of RB19 removal after 2 h (100 mg L^{-1} H_2O_2 and 200 mg L^{-1} Fe_3O_4).

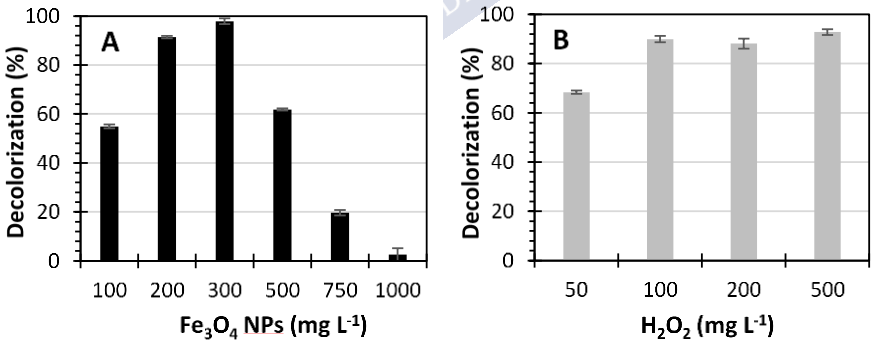

Figure 4.8 RB19 color removal (%) at: (a) different initial Fe_3O_4-TMAOH mNPs concentrations (100-1000 mg L^{-1}) and (b) different initial H_2O_2 concentration (50-500 mg L^{-1}). Other conditions: 25 mg L^{-1} RB19 and pH 3.

These conditions were applied for the selection of different coatings (Table 4.1). Under these conditions, 8.19 ± 1.89% of RB19 was removed in control samples that did not contain Fe_3O_4, as a consequence of exposure to H_2O_2 (Table 4.5). The pH stability control samples did not show significant decrease in dye concentration after 2 h.

Table 4.5 Dye decolorization (%) after 2 h (RB19) using different stabilized-Fe_3O_4 mNPs as heterogenous Fenton catalysts. Operational conditions: Fe_3O_4: 200 mg L^{-1}, H_2O_2: 100 mg L^{-1}, pH 3 and V=10 mL.

Sample	Decolorization (%)	Adsorption (%)
Fe_3O_4-TMAOH	43.59 ± 0.72	2.02 ± 0.55
Fe_3O_4@PAA	74.76 ± 1.28	0.89 ± 0.82
Fe_3O_4@PEI	-	100.00 ± 0.00
Fe_3O_4@SiO_2	21.50 ± 1.30	1.09 ± 0.50

Considering the influence of the different coatings used for the stabilization of Fe_3O_4 mNPs (PAA, PEI and SiO_2), the results after 2 h of heterogeneous Fenton treatment achieved rates ranging from 74.76% (Fe_3O_4@PAA), 0% (Fe_3O_4@PEI) and 21.50% (Fe_3O_4@SiO_2), reaching the conclusion that Fe_3O_4@PAA mNPs are the most suitable alternative (Table 4.5). Fe_3O_4@PAA mNPs demonstrate that the water-stability provided by the PAA coating greatly enhances catalytic efficiency. Controls of RB19 adsorption onto mNPs in the absence of H_2O_2 showed no significant removal (0.89%) (Table 4.5).

In catalysis, pH is a key parameter that determines the interaction between the surface of the catalyst and the target compounds. Considering the dissociation constant of PAA (pK_a= 4.3), the surface of the nanoparticle is neutral at pH 3, which explains why the adsorption is negligible due to the absence of electrostatic forces. However, the effect of the cationic-polymer PEI coating during the oxidation of the anionic dye RB19 demonstrated its well-known adsorption capacity, resulting in a strong mutual attraction between Fe_3O_4@PEI mNPs and the selected dye, even under acidic conditions (Treweek and Morgan 1977). This electrostatic interaction led to 100% of color removal by adsorption in less than 1 min.

In the case of Fe_3O_4@SiO_2, a relatively low decolorization percentage (21.50 ± 1.30) and marginal adsorption (1.09 ± 0.50) were observed (Table 4.5). In general, SiO_2 coating shell thickness is higher than in the previous cases as well as dense and solid, obstructing the access of H_2O_2 to iron deposited on the surface. Henceforth, Fe_3O_4@PAA coated mNPs were selected as the optimum nanocatalyst for the removal of organic molecules through heterogeneous Fenton oxidations.

4.3.3 Searching for optimal Fenton-like parameters for dye decolorization using Fe_3O_4@PAA mNPs

The experimental results used for the optimization of the independent variables (mNPs and H_2O_2 concentrations) are shown in Table 4.6.

Table 4.6 Factors and levels in the design matrix and data on the residual RB19 color from experiments 1-11.

Exp no.	Dimensional independent variables		Dimensionless independent variables		Dependent variable
	H_2O_2 (mg L^{-1})	mNPs (mg L^{-1})	x1	x2	y1 or RB19 (%)
1	100	100	-1	-1	44.49
2	400	100	1	-1	37.79
3	100	300	-1	1	52.20
4	400	300	1	1	41.23
5	250	200	0	0	28.95
6	250	200	0	0	31.17
7	250	200	0	0	31.92
8	37.9	200	-1.414	0	52.69
9	250	341.4	0	1.414	45.04
10	462.1	200	1.414	0	38.06
11	250	58.6	0	-1.414	39.10

The suitability of the model was validated through the value of the determination coefficient (R^2= 0.99) and the significance value of the test F, obtained from the ANOVA variance analysis (89.97). Additionally, it was confirmed that the concentrations of mNPs and H_2O_2 have a significant effect on dye degradation at the 5% of significance level.

According to the response surface graph built on these data, the most efficient RB19 removal yields by the heterogeneous Fenton process reached values around 70% after 2 h of treatment (Figure 4.9). Optimal operating ranges between 220 and 240 mg L^{-1} of mNPs and between 190 and 235 mg L^{-1} of H_2O_2 were determined, obtaining maximum dye decolorization (70.4%) with 230 mg L^{-1} of Fe_3O_4@PAA mNPs and 220 mg L^{-1} of H_2O_2.

Total organic carbon (TOC) analysis revealed that partial mineralization (32.7± 4.0%) was obtained after 4 h of treatment. In view of the results obtained (Figure 4.9), it can be observed that an insufficient concentration of H_2O_2 leads to a decrease in the effectiveness of RB19 removal due to the reduction of hydroxyl radicals generated, while high doses of H_2O_2 above the optimal concentrations (>235 mg L^{-1}) can destroy the ·OH radicals in situ formed acting as scavenger themselves (Eq. 6) (Liang et al. 2013).

$$H_2O_2 + \cdot OH \rightarrow H_2O + HO_2 \cdot \quad (6)$$

The concentration of mNPs also has a significant effect on the catalytic efficiency. With increasing concentrations of Fe_3O_4@PAA mNPs between 100 and 220 mg L^{-1}, the removal of RB19 dye increased, as the number of active sites in the catalyst is greater, which intensifies the production of hydroxyl radicals.

However, this phenomenon occurs to a certain extent, obtaining that above 240 mg L^{-1} of Fe_3O_4@PAA mNPs, the catalytic efficiency decreases. A high concentration of mNPs can produce not only the agglomeration of nanoparticles, which leads to a reduction of the effective surface area, but also the behavior of Fe_3O_4@PAA mNPs acting as ·OH scavenger species (Eq. 7) (Wang et al. 2016).

$$Fe^{2+} + \cdot OH \rightarrow Fe^{2+} + OH^- \quad (7)$$

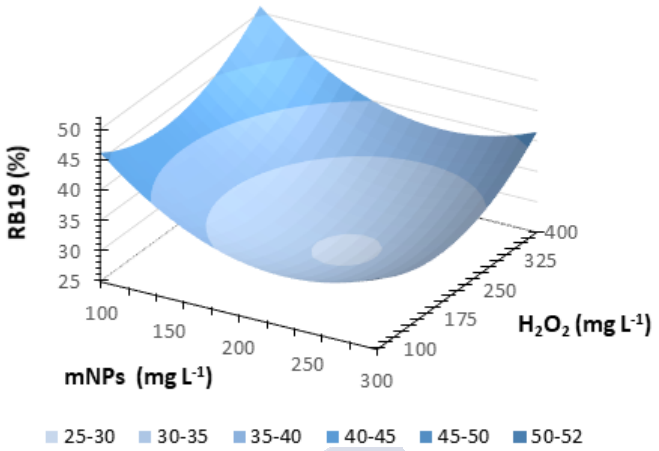

Figure 4.9 3D plot showing the effect of the concentration (mg L^{-1}) of hydrogen peroxide (H_2O_2) and catalyst (mNPs) on the color removal of RB19.

In relation to RB19 concentration, dye decolorization in the range of 25-100 mg L^{-1} was investigated using optimal operation conditions (230 mg L^{-1} of Fe_3O_4@PAA mNPs and 220 mg L^{-1} H_2O_2). The kinetic parameters were determined by adjusting a pseudo first-order kinetic model (Eq. 5, Section 4.2.5). Table 4.7 shows the correlation coefficients (R^2), the apparent constants of pseudo-first order rate (k_{obs}) and the half-life times ($t_{1/2}$).

Table 4.7 Pseudo-first-order kinetic rate constants (k_{obs}), half-life time ($t_{1/2}$) and regression coefficients (R^2) for RB19 (25-100 mg L^{-1}) decolorization by heterogeneous Fenton.

Dye (mg L^{-1})	R^2	k_{obs} (h^{-1})	$t_{1/2}$ (h)
25	0.995	0.631	1.098
50	0.983	0.408	1.698
100	0.996	0.177	3.909

The fittings of the experimental data to this kinetic model are presented in Figure 4.10. After 2 h of treatment, RB19 decolorization decreased from 59.6 to 29.2% with the increase of the dye concentration from 50 to 100 mg L^{-1}. Consequently, the kinetic constant decreased from 0.408 to 0.117 h^{-1}. Similar findings of RB19 removal have been previously reported (Naimi and Bellakhal 2012, Siddique et al. 2014). On the other hand, it was found that the percentage of RB19

removal determined in the batch experiment with an initial concentration of RB19 of 25 mg L^{-1} (68.2%) matches the predicted value of the model (70.4%).

Finally, these results agree with the previous results obtained in Section 4.3.2, for RB19 color removal using non-coated Fe_3O_4 mNPs (43.59 ± 0.72%) and Fe_3O_4@PAA mNPs (74.76 ± 1.28%) which reached high removal values at 200 mg L^{-1} of Fe_3O_4@PAA mNPs and 100 mg L^{-1} of H_2O_2. Therefore, in subsequent assays the selected operation conditions will be 200 mg L^{-1} of Fe_3O_4@PAA mNPs and 100 mg L^{-1} of H_2O_2.

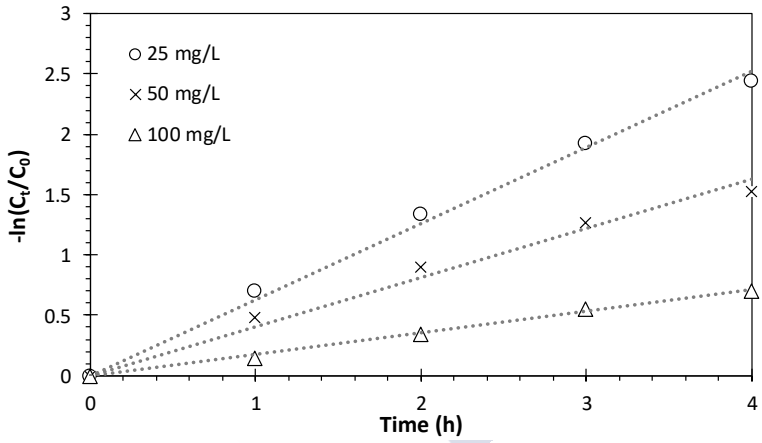

Figure 4.10 Pseudo-first-order reaction of RB19 decolorization at different initial dye concentrations (25-100 mg L^{-1}). Other conditions: 230 mg L^{-1} of Fe_3O_4@PAA mNPs, 220 mg L^{-1} of H_2O_2, pH 3.

4.3.4 Evaluation of the different immobilized mNPs onto SBA-15 for dye removal

A broad spectrum of stabilized Fe_3O_4 mNPs, immobilized onto mesoporous silica SBA-15 matrix, has been considered for the decolorization of RB19 (25 mg L^{-1}) by the heterogeneous Fenton process, following the previously optimized conditions (Section 4.3.2): 200 mg L^{-1} of catalyst on the basis of Fe_3O_4 and 100 mg L^{-1} H_2O_2. Table 4.8 identifies PAA as the best stabilization agent for the coating of Fe_3O_4 mNPs before immobilization onto the mesoporous material, reaching values of 98.86 ± 1.48% of RB19 decolorization after 2 h.

Table 4.8 Dye decolorization (%) after 2 h (RB19) using different stabilized-Fe_3O_4 mNPs immobilized on SBA-15 matrix as heterogenous Fenton catalysts. Operational conditions: Fe_3O_4: 200 mg L^{-1}, H_2O_2: 100 mg L^{-1}, pH: 3 and V: 10 mL.

Sample	Decolorization (%)	Adsorption (%)
Fe_3O_4@PAA/SBA-15	98.86 ± 1.48	6.27 ± 0.06
Fe_3O_4@PEI/SBA-15	-	56.56 ± 7.80
Fe_3O_4@SiO_2/SBA-15	50.87 ± 0.50	0.75 ± 1.07
Fe_3O_4@C/SBA-15	76.50 ± 2.46	24.23 ± 3.44

Compared with the non-immobilized mNPs decolorization results (Table 4.5), it is evident that immobilization in the SBA-15 matrix confers greater stabilization to the nanocatalysts improving decolorization percentages (Table 4.8). The results of this study suggest that PAA-coated magnetic nanoparticles are the most suitable option for their applications in heterogeneous Fenton processes.

Ordered mesoporous material SBA-15 has been widely used as support of active chemical agents due to its large surface area. In addition, the mechanical and chemical stability of SBA-15 makes it an ideal support for the incorporation of Fe_3O_4 NPs for wastewater treatment applications.

For PEI coating, similar results have been obtained in comparison with non-immobilized PEI mNPs (Table 4.5 of Section 4.3.2), being the adsorption the predominant phenomenon (56.56 ± 7.80%). In the case of silica-coated mNPs (Fe_3O_4@SiO_2/SBA-15) and those functionalized with carboxylic groups (Fe_3O_4@C/SBA-15), RB19 removal percentages have reached relatively high values, 50.87 ± 0.50 and 76.50 ± 2.46%, respectively. Furthermore, in these cases, Fe_3O_4 mNPs are only present outside the NC and not inside the channels. In the case of Fe_3O_4@C/SBA-15 catalyst, a significant adsorption can be observed (24.23 ± 3.44%), while in the case of Fe_3O_4@SiO_2/SBA-15 NC, the silica layer covering the mNPs can be acting as an impediment for the Fenton reaction, making iron ions less accessible and therefore decreasing the effectiveness of the oxidation reaction.

Additionally, the evaluation of pH in the range of 3 to 7 was carried out in order to analyze the possible circumneutral pH application. However, as previously reported, the optimal pH for Fenton reactions was in the acidic region, with values

ranging from 96.02 ± 2.45% to 79.13 ± 1.3% for pH 3 and 5, respectively (Figure 4.11) (Sedlak and Andren 1991).

Above pH 5, the decrease in dye removal efficiency could be attributed to the ·OH oxidation potential reduction and the lower Fe^{3+} reduction as the pH increases (de la Plata et al. 2012). Moreover, mechanical stability is a key parameter, which plays an important role in particle agglomeration and in the working pH value. The zeta potential value of Fe_3O_4@SiO_2/SBA-15 NC at pH 3 was calculated, obtaining a value of -3.28 ± 1.46 mV. Above or below this point, particle agglomeration has an effect on the oxidation reaction.

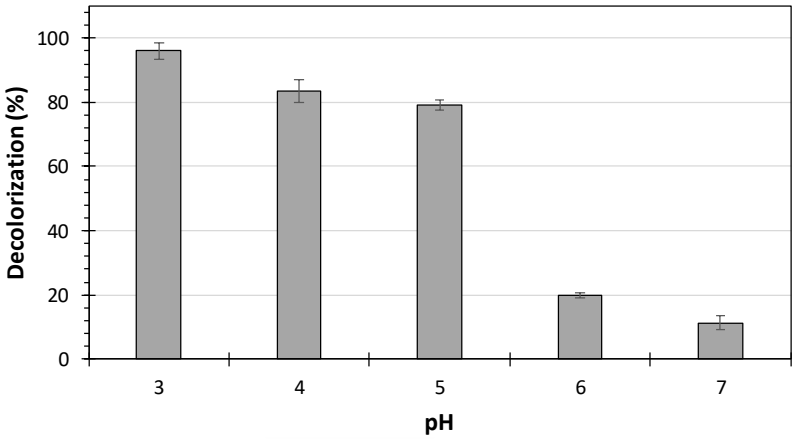

Figure 4.11 RB19 decolorization (%) after 2 h using Fe_3O_4@PAA/SBA-15 nanocomposite (NC) as heterogenous Fenton catalyst. Operational conditions: Fe_3O_4: 200 mg L^{-1}, H_2O_2: 100 mg L^{-1}, pH: 3-7, V: 10 mL.

The degradation process was also studied by examining some radical scavengers to elucidate the reaction mechanism. The results shown in Figure 4.12 revealed differences between hydroxyl radical trends. The addition of *t*-butanol, MeOH and DMSO had a low impact on the catalytic removal of RB19, although their presence decreases the reaction velocity compared to reaction control without any type of radical scavenger. These three scavenger agents have in common that their presence inhibit RB19 transformation by quenching free ·OH present in the reaction medium during the first 30 minutes (5-15%).

Nevertheless, when KI was introduced to the degradation system, significant changes occurred on dye color removal, indicating that the iodide ion (I^-) acts as ·OH scavenger on the surface of the catalyst (Eq. 8) (Li et al. 2011, Xu and Wang 2011). As shown in Figure 4.12, the addition of KI completely inhibits the RB19 transformation. Similar hydroxyl radical scavenger studies confirm this premise, corroborating that the presence of I^- anion generates an electron transfer with the dye as electron donor interfering also with the cationic radicals of the dye (Yin et al. 2009).

$$I^- + \cdot OH \rightarrow I^{\cdot} + OH^- \quad (8)$$

In addition, when using iron oxide catalyst in a Fenton-like reaction, it is common to generate not only ·OH radicals from H_2O_2 but also $\cdot OOH/O_2^{\cdot-}$ reactive species. In this regard, BQ and AH_2 were added to the reaction medium as free and surface adsorbed O_2^- radical scavengers.

The decrease in the RB19 removal in the presence of BQ was 68.60% compared to the control test under the same conditions, reaching transformation values of 30.10% after 2 h of Fenton-like treatment (Figure 4.12). These results agree with previous studies in which BQ was used as a superoxide scavenger, where this chemical inhibits but to a certain extent, indicating that other oxidant species besides O_2^- radicals are also being generated (Li et al. 2014).

However, no dye transformation was detected when AH_2 was introduced in the reaction system (Figure 4.12). Although the initial concentration of BQ is 50 lower, AH_2 is a well-known superoxide scavenger used as protective agent in biomedical applications, and it is responsible of the Fenton reaction quenching through the oxidation of ascorbic acid by superoxide radical (Nandi and Chatterjee 1987, Nishikimi 1975). In summary, the probable pathway for heterogeneous Fenton dye removal involves an oxidative reaction that occurs on the surface of the catalyst rather than the free radicals present in the reaction medium.

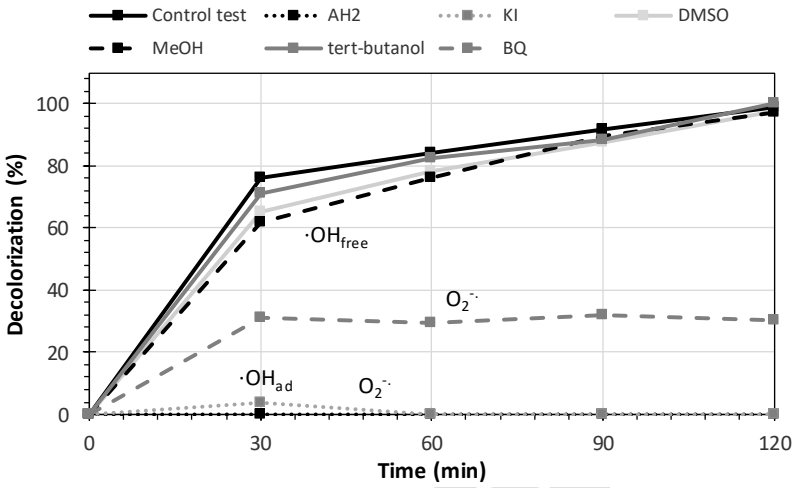

Figure 4.12 Quenching experiments using t-butanol, MeOH, DMSO, KI and AH_2 at 50 mM and BQ at 1mM as ·OH and O_2^{-} radical scavengers during the decolorization of RB19 (25 mg L^{-1}) by heterogeneous Fenton process (H_2O_2: 100 mg L^{-1}; Fe_3O_4@PAA/SBA-15: 200 mg Fe_3O_4 L^{-1}; pH 3).

4.3.5 Catalyst reuse study

The reuse of Fe_3O_4@PAA/SBA-15 catalyst was studied in a 10 mL reactor according to the fill-and-draw principle. Fenton-like operational conditions applied for the decolorization of RB19 (25 mg L^{-1}) in 2 h of sequential batch operation were 200 and 100 mg L^{-1} for catalyst and H_2O_2 concentrations, respectively. The decolorization results obtained after each cycle were between 97.68 and 84.06% after 2 h of oxidative treatment (Figure 4.13).

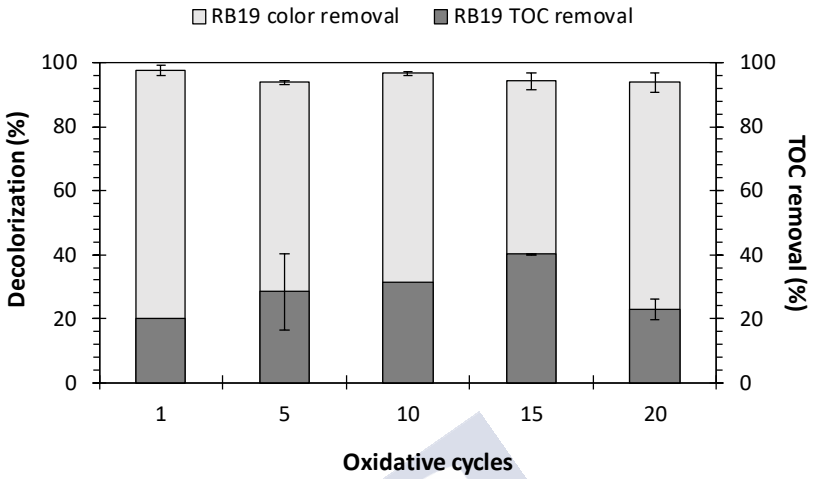

Figure 4.13 Decolorization of RB19 (25 mg L^{-1}) by heterogeneous Fenton (H_2O_2: 100 mg L^{-1}; Fe_3O_4@PAA/SBA-15: 200 Fe_3O_4 mg L^{-1}) process after 2 h of treatment in subsequent cycles (gray bars) and TOC (%) removal after the treatment (black bars).

Additionally, the mineralization of compound RB19 was evaluated by measuring TOC removal in each effluent cycle. The results expressed as RB19 TOC removal percentage revealed that partial mineralization (31.11 ± 8.49% on average) was obtained after 2 h of treatment during 20 cycles of catalyst reuse (Figure 4.13). These results are better than those obtained using non-immobilized Fe_3O_4@PAA mNPs (32.7 ± 4.0% after 4 h of treatment in Section 4.3.3) and are also consistent with previous studies in which the removal rate of RB19 involving only color disappearance is faster than the complete cleavage of the chromophore. The characteristic blue color of RB19 is mainly due to a main absorption band in the visible region, with a maximum of 592 nm. The RB19 dye also presents another intense band in the UVA region, corresponding to the anthraquinone structure (Fanchiang and Tseng 2009).

The proposed pathway for RB19 degradation during the oxidation process in the presence of ·OH has been previously reported, suggesting an initial breakdown of the molecule by an attack on the C-N bond (Figure 4.14). Other mechanistic aspects would imply the cleavage of the quinone ring obtained in route a), eventually

to phthalic acid as final product, and the transformation of the sulfonate-transformation product obtained in route b) (Bilal et al. 2018).

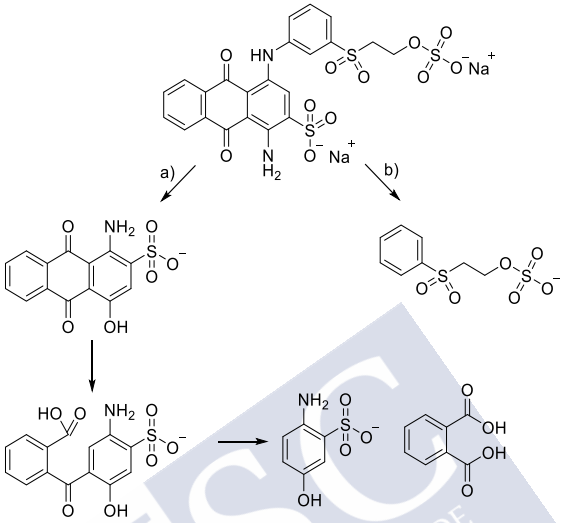

Figure 4.14 Proposed pathway of RB19 degradation by ·OH oxidation process (Bilal et al. 2018).

4.3.6 Removal of recalcitrant compounds by Fenton heterogenous using Fe_3O_4@PAA/SBA-15 as catalyst

The oxidative capacity of Fe_3O_4@PAA/SBA-15 was independently evaluated in the degradation of different recalcitrant compounds (Estrogens, BPA, SMX and pyrene). The operational conditions were preliminary evaluated for the removal of three estrogens (E1, E2 and EE2) as model compounds.

Initial concentrations of 350 µg L^{-1} E1, E2 and EE2 were performed on 10 mL of aqueous samples containing 100-1000 mg L^{-1} of Fe_3O_4@PAA/SBA-15 on the basis of Fe at pH 3, with 300 mg L^{-1} H_2O_2 concentrations. Removal rates ranged values from 37.55-79.42% (E1), 50.77-86.63% (E2) and 55.88-86.99% (EE2), after 6 h of treatment. The highest values achieved correspond in all cases to the nanocatalyst concentration of 750 mg L^{-1} (1.04 g Fe_3O_4 L^{-1}) (Figure 4.15).

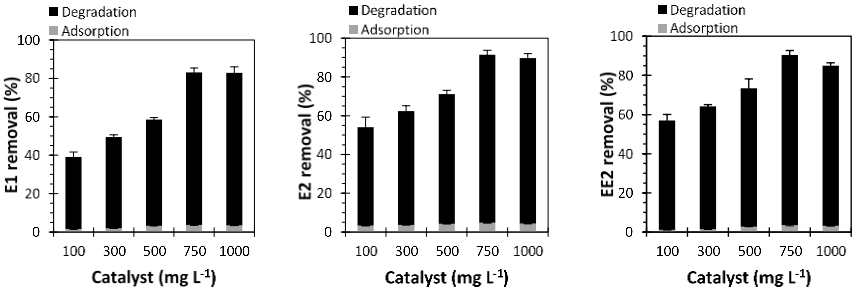

Figure 4.15 Catalyst effect on removal of E1, E2 and EE2 (each at 350 µg L^{-1}), using Fe_3O_4@PAA/SBA-15, at pH 3, after 6 h of oxidative treatment. Black bars represent estrogens removal by Fenton reaction; grey bars represent estrogens removal by adsorption.

With regard to the previously optimized concentration of nanocatalyst (200 mg Fe_3O_4 L^{-1}) for the removal of the RB19 dye, recent data demonstrates that the most complex compounds, which displays greater relatively stability against hydroxyl and/or superoxide radicals from Fenton reaction, requires additional charge of nanocatalyst to achieve relative high removal values (5-fold increase).

It was found that beyond the optimum value (750 mg Fe L^{-1}), the catalytic efficiency gradually decreased, which can be attributed to NC aggregation. The adsorption control samples showed the same trend, obtaining higher rates using 750 mg L^{-1} of NC (Figure 4.15). H_2O_2 control samples were conducted in the absence of Fe_3O_4@PAA/SBA-15, and no significant estrogens removal was observed after 6 h of reaction.

The effect of H_2O_2 concentration was evaluated in the range of 200-500 mg L^{-1}, to degrade E1, E2 and EE2 (350 µg L^{-1}) in presence of Fe_3O_4@PAA/SBA-15 (750 mg Fe L^{-1}), at pH 3. It was found that catalytic efficiency increased with H_2O_2 concentration up to 400 mg L^{-1}, obtaining degradation rates of 84.86% (E1), 88.18% (E2) and 86.51% (EE2) (Figure 4.16).

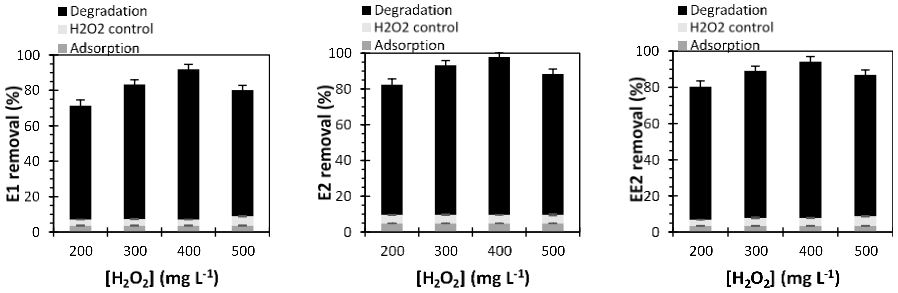

Figure 4.16 H_2O_2 effect on removal of E1, E2 and EE2 (each at 350 µg L^{-1}), using nanocatalyst (Fe) at 750 mg L^{-1}, at pH 3, after 6 h of oxidative treatment. Black bars represent estrogens removal by Fenton reactions; white bars represent estrogens removal by adsorption; grey bars represent H_2O_2 controls.

Consequently, to study the rate of the oxidative degradation of different organic compounds (BPA, PYR and SMX), optimized conditions have been selected: Fe_3O_4@PAA/SBA-15 with a concentration of 750 mg Fe L^{-1} of NC and 400 mg L^{-1} of H_2O_2 (Figure 4.17).

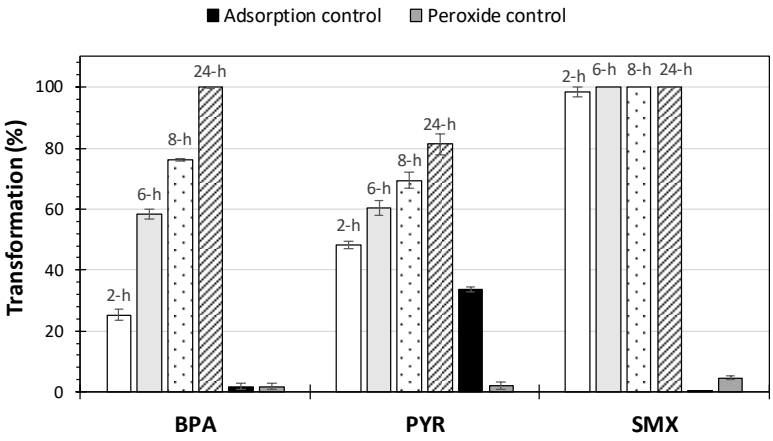

Figure 4.17 Recalcitrant micropollutants removal (BPA, PYR and SMX) at different time intervals by heterogenous Fenton treatment. Operational conditions: Initial micropollutant concentration of 350 µg L^{-1}, 750 mg Fe L^{-1} of Fe_3O_4@PAA/SBA-15 nanocomposite (NC) and 400 mg L^{-1} of H_2O_2.

Briefly, the complete degradation of BPA was obtained after 24 h, whereas in the case of SMX almost complete removal was achieved after 2 h of treatment (98.31 ± 1.63%). Pyrene proved to be the most recalcitrant compound with a percentage removal of 81.26 after 24 h and also with a relative high adsorption value (33.58 ± 0.90%).

4.4 Conclusions

The current chapter delves into different operating conditions to optimize the removal of a recalcitrant compound (RB19) from aqueous media by heterogeneous Fenton catalysis. The central composite design selected as the Response Surface Methodology allowed to determine the optimal conditions to perform dye degradation. From the outcomes of the analysis of RB19 decolorization, it was proven that nanocatalyst stabilization plays a crucial role. Fe_3O_4@PAA mNPs exhibit good structural stability and can be easily separated by a magnetic field. Furthermore, the immobilization of these mNPs onto a mesoporous silica matrix confers the nanocatalyst excellent properties as Fenton-like catalyst in achieving high efficiency in the removal of organic microcontaminants through the recovery and complete reuse of nanocatalysts.

4.5 References

Acton, A. (2012) Advances in Nanotechnology Research and Application. Editions™, S. (ed), p. 1378.

Aliyan, H., Fazaeli, R. and Jalilian, R. (2013) Fe3O4@mesoporous SBA-15: A magnetically recoverable catalyst for photodegradation of malachite green. Applied Surface Science 276, 147-153.

Álvarez, P.M., Jaramillo, J., Lopez-Pinero, F. and Plucinski, P.K. (2010) Preparation and characterization of magnetic TiO_2 nanoparticles and their utilization for the degradation of emerging pollutants in water. Applied Catalysis B: Environmental 100(1-2), 338-345.

Andreozzi, R., Campanella, L., Fraysse, B., Garric, J., Gonnella, A., Lo Giudice, R., Marotta, R., Pinto, G. and Pollio, A. (2004) Effects of advanced oxidation processes (AOPs) on the toxicity of a mixture of pharmaceuticals. Water Science and Technology 50(5), 23-28.

Ayoub, K., Van Hullebusch, E.D., Cassir, M. and Bermond, A. (2010) Application of advanced oxidation processes for TNT removal: a review. Journal of Hazardous Materials 178(1-3), 10-28.

Bae, S., Kim, D. and Lee, W. (2013) Degradation of diclofenac by pyrite catalyzed Fenton oxidation. Applied Catalysis B: Environmental 134-135, 93-102.

Bethi, B., Sonawane, S.H., Bhanvase, B.A. and Gumfekar, S.P. (2016) Nanomaterials-based advanced oxidation processes for wastewater treatment: A review. Chemical Engineering and Processing-Process Intensification 109, 178-189.

Bilal, M., Rasheed, T., Iqbal, H.M., Li, C., Wang, H., Hu, H., Wang, W. and Zhang, X. (2018) Photocatalytic degradation, toxicological assessment and degradation pathway of CI Reactive Blue 19 dye. Chemical Engineering Research and Design 129, 384-390.

Chaudhary, V. and Sharma, S. (2017) An overview of ordered mesoporous material SBA-15: synthesis, functionalization and application in oxidation reactions. Journal of Porous Materials 24(3), 741-749.

Colilla, M., Balas, F., Manzano, M. and Vallet-Regí, M. (2007) Novel method to enlarge the surface area of SBA-15. Chemistry of Materials 19(13), 3099-3101.

de la Plata, G.B.O., Alfano, O.M. and Cassano, A.E. (2012) 2-Chlorophenol degradation via photo Fenton reaction employing zero valent iron nanoparticles. Journal of Photochemistry and Photobiology A: Chemistry 233, 53-59.

Fanchiang, J.-M. and Tseng, D.-H. (2009) Degradation of anthraquinone dye CI Reactive Blue 19 in aqueous solution by ozonation. Chemosphere 77(2), 214-221.

Hu, X., Liu, B., Deng, Y., Chen, H., Luo, S., Sun, C., Yang, P. and Yang, S. (2011) Adsorption and heterogeneous Fenton degradation of 17α-methyltestosterone on nano Fe3O4/MWCNTs in aqueous solution. Applied Catalysis B: Environmental 107(3), 274-283.

Kim, D.K., Mikhaylova, M., Zhang, Y. and Muhammed, M. (2003) Protective Coating of Superparamagnetic Iron Oxide Nanoparticles. Chemistry of Materials 15(8), 1617-1627.

Krishnan, S., Rawindran, H., Sinnathambi, C. and Lim, J. (2017) Comparison of various advanced oxidation processes used in remediation of industrial wastewater laden with recalcitrant pollutants, p. 012089, IOP Publishing.

Li, W., Wang, Y. and Irini, A. (2014) Effect of pH and H2O2 dosage on catechol oxidation in nano-Fe3O4 catalyzing UV–Fenton and identification of reactive oxygen species. Chemical Engineering Journal 244, 1-8.

Li, Y., Wang, J., Yao, H., Dang, L. and Li, Z. (2011) Efficient decomposition of organic compounds and reaction mechanism with BiOI photocatalyst under visible light irradiation. Journal of Molecular Catalysis A: Chemical 334(1-2), 116-122.

Liang, X., He, Z., Zhong, Y., Tan, W., He, H., Yuan, P., Zhu, J. and Zhang, J. (2013) The effect of transition metal substitution on the catalytic activity of magnetite in heterogeneous Fenton reaction: In interfacial view. Colloids and Surfaces A: Physicochemical and Engineering Aspects 435, 28-35.

Massart, R. (1981) Preparation of aqueous magnetic liquids in alkaline and acidic media. IEEE Trans. Magn. 17(2), 1247-1248.

Mehdaoui, R., El Ghali, A., Cheikhrouhou, W., Beyou, E. and Baouab, M.H.V. (2017) Fe3O4 nanoparticles coated by new functionalized tetraaza-2,3 dialdehyde micro-crystalline cellulose: synthesis, characterization, and catalytic application for degradation of Acid Yellow 17. Iranian Polymer Journal 26(8), 597-613.

Mirzaei, A., Chen, Z., Haghighat, F. and Yerushalmi, L. (2017) Removal of pharmaceuticals from water by homo/heterogonous Fenton-type processes – A review. Chemosphere 174, 665-688.

Moldes-Diz, Y., Gamallo, M., Eibes, G., Vargas-Osorio, Z., Vazquez-Vazquez, C., Feijoo, G., Lema, J. and Moreira, M. (2018) Development of a Superparamagnetic Laccase Nanobiocatalyst for the Enzymatic Biotransformation of Xenobiotics. Journal of Environmental Engineering 144(3), 04018007.

Munoz, M., de Pedro, Z.M., Casas, J.A. and Rodriguez, J.J. (2015) Preparation of magnetite-based catalysts and their application in heterogeneous Fenton oxidation – A review. Applied Catalysis B: Environmental 176-177, 249-265.

Naimi, I. and Bellakhal, N. (2012) Removal of 17β-Estradiol by electro-fenton process. Materials Sciences and Applications 3(12), 880.

Nandi, A. and Chatterjee, I.B. (1987) Scavenging of superoxide radical by ascorbic acid. Journal of Biosciences 11(1), 435-441.

Ning, B., Graham, N., Zhang, Y., Nakonechny, M. and Gamal El-Din, M. (2007) Degradation of endocrine disrupting chemicals by ozone/AOPs. Ozone: Science and Engineering 29(3), 153-176.

Nishikimi, M. (1975) Oxidation of ascorbic acid with superoxide anion generated by the xanthine-xanthine oxidase system. Biochemical and Biophysical Research Communications 63(2), 463-468.

Sable, S.S., Ghute, P.P., Álvarez, P., Beltrán, F.J., Medina, F. and Contreras, S. (2015) FeOOH and derived phases: efficient heterogeneous catalysts for clofibric acid degradation by advanced oxidation processes (AOPs). Catalysis Today 240, 46-54.

Santos, F.S.d., Lago, F.R., Yokoyama, L. and Fonseca, F.V. (2017) Synthesis and characterization of zero-valent iron nanoparticles supported on SBA-15. Journal of Materials Research and Technology 6(2), 178-183.

Sathishkumar, P., Mangalaraja, R.V. and Anandan, S. (2016) Review on the recent improvements in sonochemical and combined sonochemical oxidation processes–A powerful tool for destruction of environmental contaminants. Renewable and Sustainable Energy Reviews 55, 426-454.

Sedlak, D.L. and Andren, A.W. (1991) Oxidation of chlorobenzene with Fenton's reagent. Environmental Science & Technology 25(4), 777-782.

Siddique, M., Farooq, R. and Price, G.J. (2014) Synergistic effects of combining ultrasound with the Fenton process in the degradation of Reactive Blue 19. Ultrasonics Sonochemistry 21(3), 1206-1212.

Siddique, M.R.F.G.J.P. (2014) Synergistic effects of combining ultrasound with the Fenton process in the degradation of Reactive Blue 19. Ultrasonics Sonochemistry 21, 1206-1212.

Singh, S., Srivastava, V.C. and Mandal, T.K. (2015) Treatment of fertilizer industry wastewater by catalytic peroxidation process using copper-loaded SBA-15. Journal of Environmental Science and Health, Part A 50(14), 1468-1478.

Sun, S.-P., Zeng, X. and Lemley, A.T. (2013) Nano-magnetite catalyzed heterogeneous Fenton-like degradation of emerging contaminants carbamazepine and ibuprofen in

aqueous suspensions and montmorillonite clay slurries at neutral pH. Journal of Molecular Catalysis A: Chemical 371, 94-103.

Tayo, L.L., Caparanga, A.R., Doma, B.T. and Liao, C.-H. (2018) A review on the removal of pharmaceutical and personal care products (PPCPs) using advanced oxidation processes. Journal of Advanced Oxidation Technologies 21, 196-214.

Treweek, G.P. and Morgan, J.J. (1977) The mechanism of E. coli aggregation by polyethyleneimine. Journal of Colloid and Interface Science 60(2), 258-273.

Truskewycz, A., Shukla, R. and Ball, A.S. (2016) Iron nanoparticles synthesized using green tea extracts for the fenton-like degradation of concentrated dye mixtures at elevated temperatures. Journal of Environmental Chemical Engineering 4(4, Part A), 4409-4417.

Vargas-Osorio, Z., González-Gómez, M., Piñeiro, Y., Vázquez-Vázquez, C., Rodríguez-Abreu, C., López-Quintela, M. and Rivas, J. (2017) Novel synthetic routes of large-pore magnetic mesoporous nanocomposites (SBA-15/Fe 3 O 4) as potential multifunctional theranostic nanodevices. Journal of Materials Chemistry B 5(47), 9395-9404.

Vargas-Osorio, Z., Piñeiro, Y., Vázquez-Vázquez, C., Rodríguez-Abreu, C., Á lvarez-Pérez, M., López-Quintela, M. and Rivas, J. (2016) Magnetic nanocomposites based on mesoporous silica for biomedical applications. International Journal of Nanotechnology 13(8-9), 648-658.

Velichkova, F., Julcour-Lebigue, C., Koumanova, B. and Delmas, H. (2013) Heterogeneous Fenton oxidation of paracetamol using iron oxide (nano)particles. Journal of Environmental Chemical Engineering 1(4), 1214-1222.

Wang, H., Chen, Q.-W., Yu, Y.-F., Cheng, K. and Sun, Y.-B. (2011) Size- and Solvent-Dependent Magnetically Responsive Optical Diffraction of Carbon-Encapsulated Superparamagnetic Colloidal Photonic Crystals. The Journal of Physical Chemistry C 115(23), 11427-11434.

Wang, H., Dong, Z. and Na, C. (2013) Hierarchical Carbon Nanotube Membrane-Supported Gold Nanoparticles for Rapid Catalytic Reduction of p-Nitrophenol. ACS Sustainable Chemistry & Engineering 1(7), 746-752.

Wang, N., Zheng, T., Zhang, G. and Wang, P. (2016) A review on Fenton-like processes for organic wastewater treatment. Journal of Environmental Chemical Engineering 4(1), 762-787.

Xu, L. and Wang, J. (2011) A heterogeneous Fenton-like system with nanoparticulate zero-valent iron for removal of 4-chloro-3-methyl phenol. Journal of Hazardous Materials 186(1), 256-264.

Yin, M., Li, Z., Kou, J. and Zou, Z. (2009) Mechanism investigation of visible light-induced degradation in a heterogeneous TiO_2/Eosin Y/Rhodamine B system. Environmental Science & Technology 43(21), 8361-8366.

Zang, H., Miao, C., Shang, J., Liu, Y. and Liu, J. (2018) Structural effects on the catalytic activity of carbon-supported magnetite nanocomposites in heterogeneous Fenton-like reactions. RSC Advances 8(29), 16193-16201.

Zhang, X., He, M., Liu, J.H., Liao, R., Zhao, L., Xie, J., Wang, R., Yang, S.T., Wang, H. and Liu, Y. (2014) Fe_3O_4@C nanoparticles as high-performance Fenton-like catalyst for dye decoloration. Chinese Science Bulletin 59(27), 3406-3412.

Zubir, N.A., Yacou, C., Motuzas, J., Zhang, X. and Diniz da Costa, J.C. (2014) Structural and functional investigation of graphene oxide–Fe3O4 nanocomposites for the heterogeneous Fenton-like reaction. Scientific Reports 4, 4594.

5. Chapter 5

PHOTOCATALYSIS OXIDATION: UV catalysis using iron-based nanomaterials

SUMMARY

This chapter approaches the validity of different novel nanocomposites (NCs) based on magnetite (Fe_3O_4) and two metal oxides (ZnO and TiO_2). The most typical nanoparticles used in photocatalysis are metal oxide nanoparticles. Their principal advantages are the high surface area and their exceptional optoelectronic, catalytic and photochemical properties. The objective is the removal of a wide range of recalcitrant compounds present in water by a photocatalysis process. In a photocatalytic reaction, the photocatalyst is illuminated with light (hv) of appropriate wavelengths, thus electrons (e^-) in the valence band are excited to the conduction band to form photo-induced electron/holes (e^-/h^+) pairs. The holes in the valence band can subtract a hydrogen atom from water and form hydroxyl (·OH) radicals. The development of these wastewater treatment systems has enabled the photocatalytic degradation of persistent organic pollutants, such as pharmaceuticals and personal care products (PPCPs) and dyes. It is not only interesting to demonstrate the capacity of magnetic NCs for the removal of recalcitrant compounds present in water, but also to ensure full recovery of the nanocatalyst and that its catalytic potential is maintained in different cycles, demonstrating its reuse.

OUTLINE

5.1 Introduction

Photocatalysis relies on the capacity of semiconducting materials to act as sensitizers for light-reduced redox processes due to their electronic structure. A photocatalyst is a chemical that produces electron-hole pairs by absorption of light quanta and makes chemical transformations of the elements participating in the reaction that come into contact with it in a way that ensures the regeneration of the catalyst after each cycle (Fox and Dulay 1993). Photocatalysts include titanium dioxide (TiO_2), zinc oxide (ZnO), zinc sulfide (ZnS), ferric oxide (Fe_2O_3), silicon (Si), tin (IV) oxide (SnO_2) and cadmium sulfide (CdS), among others. TiO_2 has been the most widely cited photocatalyst in the literature due to characteristic aspects: considerable activity, high stability, low environmental impact and reduced cost (Augugliaro et al. 2006).

Heterogeneous photocatalysis has been reported to perform the oxidation of the target organic contaminants within a short contact time generating solid waste (Neppolian et al. 2007). Among the different types of nanomaterials, semiconductors can act as photocatalysts, favoring the oxidation of organic compounds (Mohapatra et al. 2014, Hoffmann et al. 1995). If a semiconductor is irradiated, photons with energy higher than the band gap energy of the semiconductor can excite electrons from the valence band to the conduction band, leaving a positively charged vacancy or hole in the valence band. The combination of both is referred to as an electron-hole pair. Many electron-hole pairs will recombine as the electron returns to its original state, emitting light or heat. However, some pairs may migrate to the catalyst surface, where they can participate in redox reactions that lead to the decomposition of compounds adsorbed on the surface (Parsons 2004, Nguyen and Juang 2015).

Diverse nanocatalysts has been investigated for the treatment of a wide range of contaminants, obtaining high degradation percentages in most cases. In particular, TiO_2 and ZnO are preferred because they are relatively inexpensive, non-toxic, stable and present a high oxidization potential (Sousa-Castillo et al. 2016, Gmurek et al. 2017, Gaya and Abdullah 2008). In particular, TiO_2 has been applied in the photocatalytic treatment of polluted wastewaters (Oros-Ruiz et al. 2013, Khodja et al. 2001, Barka et al. 2013, Khataee and Kasiri 2010). The immobilization of TiO_2

or ZnO NPs onto magnetic nanoparticles (mNPs) provides not only an easy recovery of the photocatalyst, but also a nanocomposite with a double potential, particularly interesting in water treatment applications, so that the Fenton effect and the photocatalytic potential are combined. Magnetite (Fe_3O_4) nanoparticles (NPs) have been also widely applied as supports of photocatalytic agents, including semiconductors such as ZnO or TiO_2 (Beydoun et al. 2000, Xie et al. 2018, Banić et al. 2019, de O. Pereira et al. 2019, Heshmatpour and Abdikhani 2019).

This chapter aims to take a step forward in the application of magnetic nanoparticles and photocatalysts formulated as nanocomposites to perform the degradation of different compounds, from endocrine disruptor chemicals to different dyes, chosen as models of organic pollutants. The heterogeneous photocatalytic system using TiO_2 and ZnO NPs was assessed under different experimental conditions, evaluating the potential reuse of the nanocatalysts and comparing the process with heterogeneous Fenton oxidation processes previously studied in Chapter 4.

5.2 Materials and methods

5.2.1 Chemicals and nanostructured catalysts

In the present chapter, all chemicals used have been previously mentioned in Section 2.1 of Chapter 2. Selected photocatalysts, listed in Table 5.1, were synthesized and kindly provided by Laboratory of Magnetism and Nanotechnology (Nanomag, Universidade de Santiago de Compostela).

Table 5.1 Photocatalysts

Catalyst	Description
Fe_3O_4/ZnO	Zinc oxide magnetic NC
Fe_3O_4/TiO_2	Titanium dioxide magnetic NC

5.2.2 Description of the photocatalysts synthesis

Preparation of Fe_3O_4 nanoparticles

Fe_3O_4 NPs can be prepared through different chemical approaches, such as co-precipitation, microemulsion, sol-gel, sonochemical and thermal decomposition or

laser pyrolysis. Among them, chemical co-precipitation is probably the most common approach, which is based on the reaction of an aqueous mixture of ferrous and ferric salts in alkaline medium that renders into Fe_3O_4 NPs with a broad size distribution, ranging from 4 to 20 nm. In order to produce NPs with a more homogeneous size distribution, water-in-oil (w/o) microemulsion can be considered, which consists of forming nano-sized water droplets dispersed in an oily phase, which are stabilized by a surfactant at the w/o interface. This nano-cavities are typically in the range of 10 nm and provide a confinement effect that limits the nucleation, growth and agglomeration of particles (Akbarzadeh et al. 2012).

As previously described (Chapter 4, Section 4.2.2), sterically stabilized Fe_3O_4 NPs were prepared by the co-precipitation of Fe^{2+} and Fe^{3+} salts, following the Massart's method (Massart 1981).

Synthesis of Fe_3O_4/ZnO nanocomposite

The synthesis of Fe_3O_4/ZnO NC is based on the polyol-mediated preparation of ZnO NPs (Feldmann and Jungk 2001). The previously synthesized Fe_3O_4 NPs were dispersed with diethyleneglycol (DEG) and added to a Zn(II) acetate solution in DEG. The mixture was heated at 180 °C for 2 h under mechanical agitation. The prepared NC were centrifuged and washed with ethanol.

Synthesis of Fe_3O_4/TiO_2 nanocomposite

The synthesis of Fe_3O_4@TiO_2 is based on the hydrolysis and polycondensation of titanium alkoxide in the presence of Fe_3O_4 NPs (Chemseddine and Moritz 1999). In particular, Fe_3O_4 NPs were added to a solution of TMAOH in water and cooled to 2 °C using an ice/water bath. Then, Ti (IV) isopropoxide in 2-propanol were dropwise added to the mixture and stirred vigorously. After 10 min, the mixture was heated, and the reaction continued for 24 h. Finally, the prepared NCs were centrifuged, washed and dispersed.

5.2.3 Characterization of photocatalysts

The analytical methods used to measure the conventional parameters for characterizing the selected catalysts (Table 5.1): X-ray diffraction (XRD) study of the

crystalline phases, transmission electron microscopy (TEM) images, high-angle dark field-scanning transmission electron micrographs (HAADF-STEM), thermogravimetric analysis (TGA), magnetization curves and inductively coupled plasma-optical emission spectrometry (ICP-OES) have been described earlier in Section 2.2 of Chapter 2.

5.2.4 Experimental set-up for the evaluation of different nano-structured photocatalysts

The evaluation of the photocatalytic activity of Fe_3O_4/ZnO and Fe_3O_4/TiO_2 was carried out for the removal of four organic micropollutants evaluated in the degradation of the natural estrogens estrone (E1), 17β-estradiol (E2), and bisphenol A (BPA), (Table 2.2, Chapter 2), at an initial concentration of 350 μg L^{-1}. Each sample was exposed to UVA radiation in 100 ml glass beakers (365 nm wavelength UVP Pen-Ray® Lamp 50 W model 11SC-1L from Analytik Jena (Cambridge, United Kingdom), Figure 5.1). The radiation power was measured with a UV light meter provided by PCE Group Iberica S. L. (Tobarra, Spain), model UVA-UVB PCE-UV34.

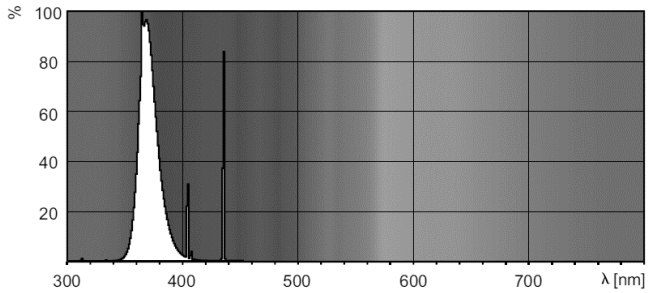

Figure 5.1 Emission spectrum of the photocatalytic reactor lamp, Philips MASTER Actinic BL TL-D(-K). The emission line of the lamp used in this study corresponds to 365.0/366.3 nm.

The lamp was inserted into a quartz tube of 18.0 mm outer diameter and immersed in the glass beaker with an inner diameter of 22.5 mm (Figure 5.2). Photocatalytic experiments were performed on 20 mL of aqueous samples with a pH of 7 and under magnetic agitation. The concentration of catalyst and oxidizing agent experimentally found as optimal: 100 mg L^{-1} were considered (Fernández et al. 2019).

Prior to initiating photocatalytic reactions, the target contaminants were kept in the dark in contact with each NC for 30 min for adsorption-desorption equilibria. Control samples of dark adsorption, direct photolysis, peroxide oxidation and photocatalysis lacking H_2O_2 were carried out in parallel under the same conditions. In addition, control experiments using non-magnetic ZnO and TiO_2 NPs were evaluated under the same photocatalytic conditions.

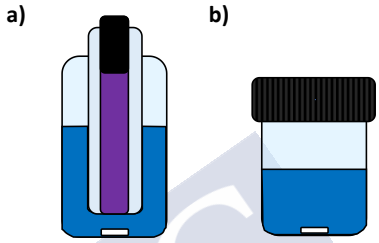

Figure 5.2 Experimental set-up for a) UV experiments and b) control tests.

Aliquots (200 µL) of the aqueous samples collected at regular intervals during the degradation processes were taken and the compounds were quantified by high performance liquid chromatography (HPLC) (Section 2.3 of Chapter 2). The photodegradation yield (%) was determined using the following equation:

$$\text{Photodegradation yield (\%)} = \frac{(C_0 - C_t)}{C_0} \times 100 \quad (1)$$

where C_0 and C_t represent the contaminant concentration (µg L^{-1}) before and after the reaction time, respectively.

5.2.5 Evaluation of photocatalytic active species

The different intermediate active species such as singlet oxygen ($^1O_2$), superoxide radical anions ($O_2^{\cdot-}$) and hydroxyl radicals, including also surface valence band holes (h_{vb}^+) interactions, were studied during the color removal of a selected model dye: Orange II (OII; 5 mg L^{-1}). The reaction conditions of the photocatalyst were chosen according to previous studies throughout this chapter (100 mg L^{-1} of NCs and H_2O_2 and pH 7) in 20 mL reactors. Fe_3O_4/ZnO NC was used as catalyst to further explore the underlying degradation mechanism. The selected ·OH scavengers

were methanol (MeOH) and dimethyl sulfoxide (DMSO). The contribution of superoxide radicals and singlet oxygen was evaluated by the addition of ascorbic acid (AH_2) and sodium azide (NaN_3), respectively. The initial concentration selected for each radical scavenger was 50 mM. At regular time intervals, aliquots (200 µL) were taken after magnetic separation of the nanocatalyst, and absorbance measurements were performed on a BioTek PowerWave XS2 micro-plates spectrophotometer (Winooski, VT, USA) to monitor OII color removal (λ= 473 nm) (Section 2.3, Chapter 2). The degradation yield (%) was determined as the extent of color disappearance, calculated by equation 1.

5.2.6 Comparison of oxidation technologies for the removal of different dyes

The evaluation of different dyes decolorization by photocatalysis were performed for the color removal of Reactive Blue 16 (RB19), Methyl Green (MG), Methyl Red (MR), OII and Rhodamine 123 (R123). The main physicochemical properties of the different dyes used in this study are presented in Table 2.1 of Chapter 2. Efficiency comparison between photocatalysis and heterogeneous Fenton oxidation processes was also conducted for the decolorization of selected dyes.

Dye color removal at an initial concentration of 25 mg L^{-1} both by photocatalysis and heterogeneous Fenton process was evaluated under concentrations of Fe_3O_4/ZnO and Fe_3O_4@PAA/SBA15 NCs of 100 and 200 mg L^{-1}, respectively, for a final volume of 20 mL. Once the adsorption-desorption equilibrium had been reached (approximately 30 minutes, depending on the dye), H_2O_2 (100 mg L^{-1}) was added to the reaction medium. Color removal was monitored spectrophotometrically as described in the previous sections. To clarify that the influence of the magnetic NCs on dye removal, controls were conducted with H_2O_2 dosage but lacking mNPs. Finally, a total organic carbon (TOC) analyzer with autosampler, was used to determine TOC concentrations at mg L^{-1} levels in the samples and to calculate the percentage of mineralization after treatment.

5.2.7 Reuse of catalyst

The reuse of the nanocatalyst for the removal of OII (25 mg L^{-1}) was evaluated according to the fill-and-draw principle, in subsequent cycles under the previous

selected conditions (Section 5.2.4) in a sequential operation of a magnetic reactor (20 mL). After each cycle, the liquid fraction was removed by separating the catalyst with an external magnetic field. Then, fresh medium containing 25 mg L^{-1} of dye-contaminant was added to the catalyst (100 mg L^{-1}) for a new cycle starting the reaction with the addition of H_2O_2 (100 mg L^{-1}). Aliquots (200 µL) were taken at the beginning and at the end of each cycle to determine spectrophotometrically the dye concentration.

5.3 Results and discussion

5.3.1 Nanocomposites characterization

Sterically stabilized Fe_3O_4 NPs were prepared by the co-precipitation of iron salts, while NCs synthesis (Fe_3O_4/ZnO and Fe_3O_4/TiO_2) were carried out by the polyol-mediated preparation of ZnO NPs in the presence of Fe_3O_4 NPs and by hydrolysis and polycondensation of titanium alkoxide, respectively. After the synthesis reactions, the NCs were washed three times and recovered by magnetic separation. With this procedure, it is possible to ensure the magnetic nature of the final materials. The two NCs were structurally characterized by X-ray diffraction patterns. Figure 5.3 shows the position and relative intensities of the Fe_3O_4 (Joint Committee of Powder Diffraction Standards (JCPDS) card number 19-0629), zincite (ZnO, JCPDS card number 36-1451) and anatase (TiO_2, JCPDS card number 21-1272) peaks. Hexagonal wurtzite structure was identified as the two crystalline phases present in the Fe_3O_4/ZnO NC sample.

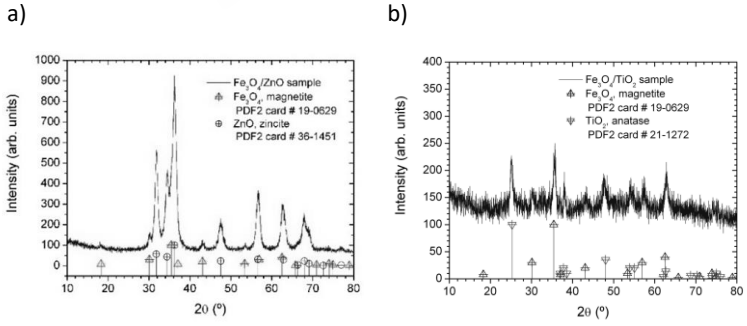

Figure 5.3 X-ray diffraction pattern of the nanocomposites Fe_3O_4/ZnO (a) and Fe_3O_4/TiO_2 (b). The main reflections of magnetite (Fe_3O_4, JCPDS card number 19-

0629), zincite (ZnO, JCPDS card number 36-1451) and anatase (TiO_2, JCPDS card number 21-1272) are included as drop lines.

The different morphology of both hybrid Fe_3O_4/ZnO and Fe_3O_4/TiO_2 NCs has been evaluated. Transmission electron micrographs show in the case of ZnO NC, a mixture of Fe_3O_4 NPs (approximate size 10 nm) with ZnO NPs (10-15 nm), with spherical aggregates (200-300 nm) coexisting with other non-spherical aggregates (Figure 5.4).

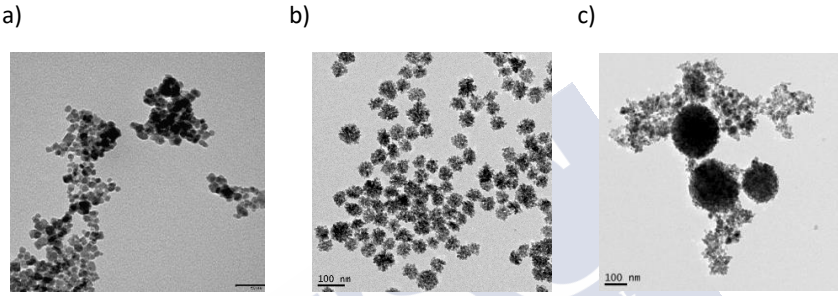

Figure 5.4 Transmission electron micrograph of a) Fe_3O_4 NPs, b) ZnO NPs and c) Fe_3O_4/ZnO.

Fe_3O_4/TiO_2 NCs present two different crystalline grades ("rods" and porous material) in the aggregates (approximate size 150-250 nm), with Fe_3O_4 NPs (approximate size 10 nm) and TiO_2 NPs (40-45 nm) (Figure 5.5).

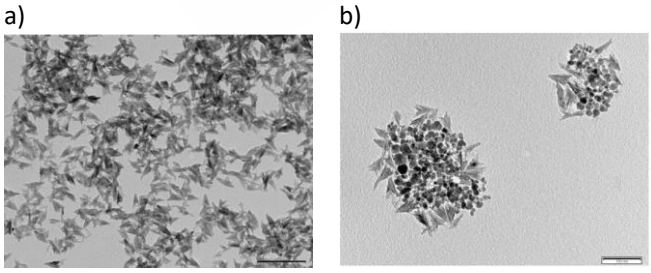

Figure 5.5 Transmission electron micrograph of nanocomposites of TiO_2 (a) and Fe_3O_4/TiO_2 (b).

Moreover, HAADF-STEM imaging and corresponding elemental maps have been provided to determine the dispersion of the NPs (Fe_3O_4, ZnO and TiO_2) in the Fe_3O_4/ZnO and Fe_3O_4/TiO_2 NCs (Figure 5.6). These maps demonstrated the presence

of Fe and Zn types of NPs in Fe_3O_4/ZnO NC and Fe and Ti NPs in the Fe_3O_4/TiO_2 hybrid NC.

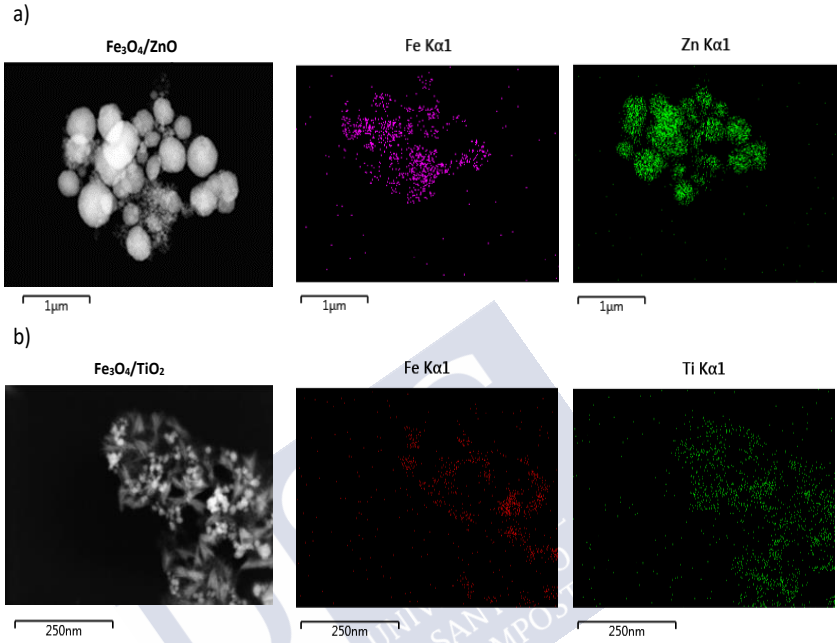

Figure 5.6 HAADF-STEM micrograph and elemental maps of Fe_3O_4/ZnO and Fe_3O_4/TiO_2 composites.

The inductively coupled plasma-optical emission spectrometry (ICP-OES) determined a composition of 87.2% ZnO and 12.8% Fe_3O_4 for Fe_3O_4/ZnO NC and 65.2% TiO_2 and 34.8% Fe_3O_4 for Fe_3O_4/TiO_2 NC. The total solids content was determined by thermogravimetry (TGA), obtaining a NCs concentration of 1.5% and 0.74% by weight in the stock solution for Fe_3O_4/ZnO and for Fe_3O_4/TiO_2, respectively.

Finally, magnetization studies were conducted by measuring the variation of the magnetization as a function of the applied magnetic field at 300 K. The magnetization curves obtained for both Fe_3O_4/ZnO and Fe_3O_4/TiO_2 NCs confirm the superparamagnetic behaviour of the sample, forming a hysteresis curve with a saturation magnetization of 4.3 and 16 emu g^{-1} at 10 kOe for Fe_3O_4/ZnO and Fe_3O_4/TiO_2 NCs, respectively (Figure 5.7).

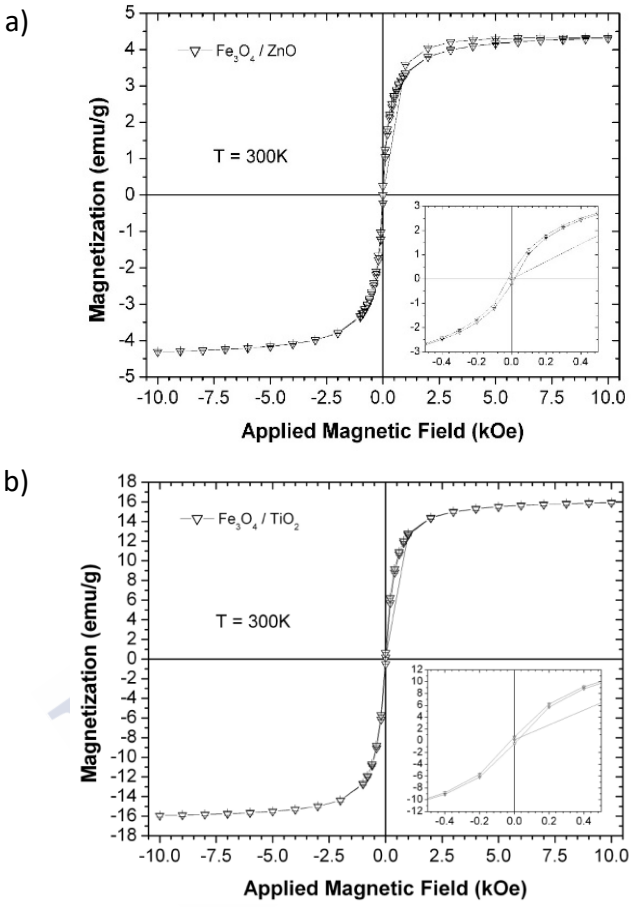

Figure 5.7 Variation of the magnetization with the applied magnetic field at 300 K of a) Fe_3O_4/ZnO and b) Fe_3O_4/TiO_2 composites.

5.3.2 Evaluation of different photocatalysts for the removal of micropollutants

In order to provide a preliminary comparison between two different nanostructured materials (Table 5.1), assays containing 350 µg L^{-1} of each contaminant to be degraded have been carried out under the operational conditions defined as optimal in the previous experiments: catalyst dosage, 100 mg L^{-1}, H_2O_2 concentration, 100 mg L^{-1} and pH 7 (Fernández et al. 2019). The irradiance on the outer surface of the quartz tube was 1.57 mW cm^{-2}. Both Fe_3O_4/ZnO and Fe_3O_4/TiO_2

NCs have been successfully employed to degrade in a first instance three estrogenic hormones (E1, E2 and EE2) (Figure 5.8).

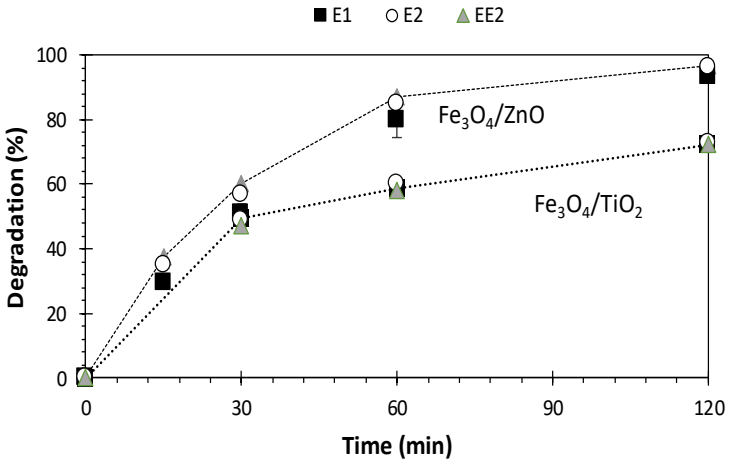

Figure 5.8 Photodegradation performance of Fe_3O_4/ZnO and Fe_3O_4/TiO_2 NCs under optimal conditions for the removal of E1, E2 and EE2 (each at 350 μg L^{-1}) after 120 min.

Figure 5.8 depicts the evolution of E1, E2 and EE2 removal (%) versus time (min). The selected hormones showed similar rates of photocatalytic degradation under the same conditions. However, the use of Fe_3O_4/ZnO NC as a catalyst allows a high photocatalytic efficiency to be achieved after 120 min (93-97% of E1, E2 and EE2 removal) compared with titanium NC (74-76% of E1, E2 and EE2 removal).

The photo-degradation of E1, E2 and EE2 under UV light irradiation was also investigated using the non-magnetic ZnO and TiO_2 NPs (original precursors of the Fe_3O_4/ZnO and Fe_3O_4/TiO_2 NCs) in order to understand the possible contribution of Fe_3O_4 material to the photocatalysis oxidation process. The best photocatalytic performance was obtained for the ZnO NPs (97-98% of E1, E2 and EE2 removal), closely followed by the hybrid Fe_3O_4/ZnO NCs and by non-magnetic TiO_2 NPs (94-96% of E1, E2 and EE2 removal) (Figure 5.9).

These results can be understood taking into account that the photocatalytic reaction occurs on the surface of the material and therefore the smaller NPs (non-magnetic ZnO and TiO_2) have a larger surface suitable for the chemical reaction. In the case of Fe_3O_4/ZnO and Fe_3O_4/TiO_2 NCs, the particle aggregates have similar size,

however, the two NCs present different composite nanostructure and arrangement and as consequence, the photocatalytic efficiency could be strongly affected by the surface area of photocatalyst material (ZnO or TiO_2) that is exposed to the light.

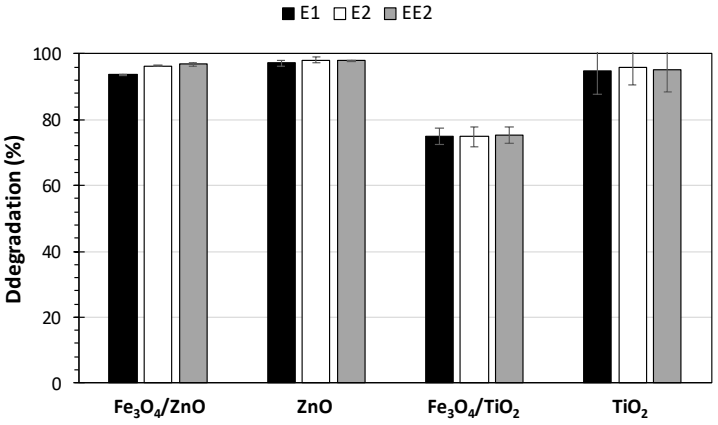

Figure 5.9 Photodegradation results of Fe_3O_4/ZnO and Fe_3O_4/TiO_2 NCs and ZnO and TiO_2 NPs under optimal conditions for the removal of E1, E2 and EE2 (each at 350 µg L^{-1}) after 120 min.

In the present case we can assume that the enhancement in the exposed surface of the Fe_3O_4/ZnO NC is responsible for the improvement of the photocatalytic performance. On the other hand, adsorption controls of E1, E2 and EE2 (350 µg L^{-1} of each contaminant) in the nanostructured catalyst have been evaluated in dark conditions applying the same operational conditions as in the experiments described above (catalyst dosage of 100 mg L^{-1}, H_2O_2 concentration 100 mg L^{-1} and pH 7).

Figure 5.10 shows the results of the adsorption control samples (Fe_3O_4/ZnO and Fe_3O_4/TiO_2 NCs and ZnO and TiO_2 NPs), where adsorption plays a significant role in the case of zinc containing catalysts, with adsorption values ranging from 15 to 20% for both Fe_3O_4/ZnO and ZnO materials. This adsorption may explain the good photodegradation percentages obtained for Fe_3O_4/ZnO NC in comparison with the titanium equivalent NC (Fe_3O_4/TiO_2), which contribute positively to the increase of the degradation kinetics and the final oxidation potential.

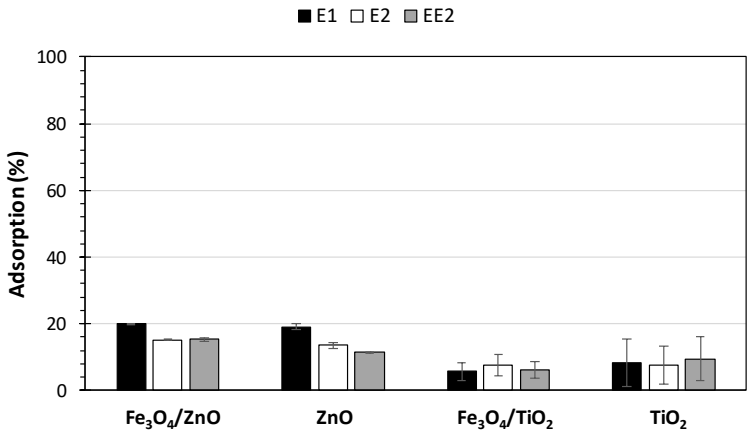

Figure 5.10 Adsorption results of Fe_3O_4/ZnO and Fe_3O_4/TiO_2 NCs and ZnO and TiO_2 NPs under optimal conditions for the removal of E1, E2 and EE2 (each at 350 µg L^{-1}) after 120 min.

The adsorption on the surface of nanocatalysts depends mainly on the physical-chemical properties of the material and its electrostatic behavior. Considering the amphoteric nature of most semiconductor oxides, pH is also an important factor affecting the stability of the surface charge and the interactions of the photocatalyst particles in solution, as well as determining the particle size of the colloids. Table 5.2 summarizes the corresponding zeta potential values of the selected catalyst at pH 7.

Table 5.2 Zeta potential of nanostructured photocatalysts at pH 7

Nanostructured catalyst	Zeta potential (mV)
Fe_3O_4/ZnO	-38.5
Fe_3O_4/TiO_2	-40.7
ZnO	-25.9
TiO_2	-21.6

Point of zero-charge (PZC) of ZnO is reported in a range between 8.3 and 10.5 (Fatehah et al. 2014). However, the PZC of Fe_3O_4/ZnO was found at pH 3.0, being negatively charged with charges ranging from -4 to -34 mV from pH 4 to 11 (Figure A5.1, Annex section). This value differs greatly from the reported PZC of pure ZnO NPs.

When pH is below the PZC of the catalyst, its surface is positively charged (Eq. 2), while at higher pH value the surface is negatively charged (Eq. 3).

$$ZnOH + H^{+} \leftrightarrows ZnOH_2^{+} \quad (2)$$

$$ZnOH + OH^{-} \leftrightarrows ZnO^{-} + H_2O \quad (3)$$

Additionally, the protonation/deprotonation of the target pollutants is based on their pK_a values, which control the adsorption process of the organic molecules on the surface of the catalyst due to electrostatic forces (Zhao et al. 2018). For a pH lower than the dissociation constant (pKa) values of E1, E2 and EE2 (Table 2.2, Chapter 2), these molecules have a predominantly neutral charge, presenting negligible electrostatic interaction with the NC. In addition, the synergistic effect between photocatalysis on ZnO/TiO_2 and Fenton or photo-Fenton on Fe_3O_4 for estrogens oxidation, the total on Fe_3O_4/ZnO and Fe_3O_4/TiO_2 NCs has been studied.

NCs consisting of 87.2% ZnO and 12.8% Fe_3O_4 for Fe_3O_4/ZnO NC and 65.2% TiO_2 and 34.8% Fe_3O_4 for Fe_3O_4/TiO_2 NC, can act as Fenton or photo-Fenton reagent in the presence of H_2O_2. The effect of these catalysts as Fenton contributor (at pH 7) is negligible compared to the photocatalysis process, reaching estrogen elimination values in the range of 15-20% and 6-8% for Fe_3O_4/ZnO and ZnO/TiO_2 NC (Table 5.3), respectively, which can be attributed to the adsorption process. Typically, these reactions are carried out at acidic pH, being ineffective under neutral conditions.

Table 5.3 Control experiments results (%) for the removal of E1, E2 and EE2 estrogens using Fe_3O_4/ZnO and ZnO/TiO_2 NCs after 2 h of treatment.

Control experiments	Description	E1 removal (%)	E2 removal (%)	EE2 removal (%)
Fenton Fe_3O_4/ZnO	Fenton-like reaction in dark conditions at pH 7	15.32 ± 5.20	19.71 ± 2.90	16.35 ± 1.03
Fenton Fe_3O_4/TiO_2	Fenton-like reaction in dark conditions at pH 7	6.56 ± 2.18	6.65 ± 2.83	7.60 ± 2.19
Estrogens stability	Estrogens stability in water matrix at pH 7	2.06 ± 1.80	1.65 ± 0.68	1.33 ± 1.28
Peroxide oxidation	Peroxide oxidation (100 mg L^{-1}) lacking catalyst and UV-light	3.44 ± 1.78	3.48 ± 2.97	2.12 ± 1.39

UV oxidation	Direct photolysis using UV-light	11.37 ± 4.89	8.86 ± 5.96	10.12 ± 5.75
Photocatalysis Fe_3O_4/ZnO	Photocatalysis oxidation at pH 7 and lacking H_2O_2	36.14 ± 1.48	29.08 ±4.59	41.32 ± 0.57
Photocatalysis Fe_3O_4/TiO_2	Photocatalysis oxidation at pH 7 and lacking H_2O_2	28.14 ± 3.26	25.36 ± 3.77	33.83 ± 3.25

Direct photolysis of estrogens under UVA irradiation, estrogens stability in aqueous media at neutral pH and H_2O_2 oxidation controls have been tested. Table 5.3 shows that the degradation of the three estrogens studied is almost negligible in terms of removal percentage within 2 h of treatment, reaching the highest degradation values with direct exposure to UV light (11.37%, 8.86% and 10.12% for E1, E2 and EE2, respectively).

Table 5.3 also summarizes the experimental results obtained for the performance of the photocatalysis of the removal control of E1, E2 and EE2 lacking H_2O_2 dosage in the photocatalytic reaction medium. Estrogen degradation increased in relation to previous removal control values, reaching percentages of the order of 25-40% for both Fe_3O_4/ZnO and ZnO/TiO_2 NCs. However, further degradation of hormones in the presence of H_2O_2 can be attributed to the electrons trapping by H_2O_2 through the reduction of e^- and h_{vb}^+ pairs and thus increasing the ROS formation (Gupta et al. 2006).

Finally, the selected optimal conditions were evaluated (catalyst dosage, 100 mg L^{-1}, H_2O_2 concentration, 100 mg L^{-1} and pH 7) for the removal of BPA (350 µg L^{-1}) as a known endocrine disruptor chemical of industrial origin with diphenolic structure (Table 2.2, Chapter 2). Figure 5.11 displays the BPA photodegradation results, the Fenton-like NC contribution and the dark adsorption controls for the four nanostructures catalysts being evaluated: Fe_3O_4/ZnO and Fe_3O_4/TiO_2 NCs and ZnO and TiO_2 NPs. As expected, similar results have been obtained for all types of catalysts.

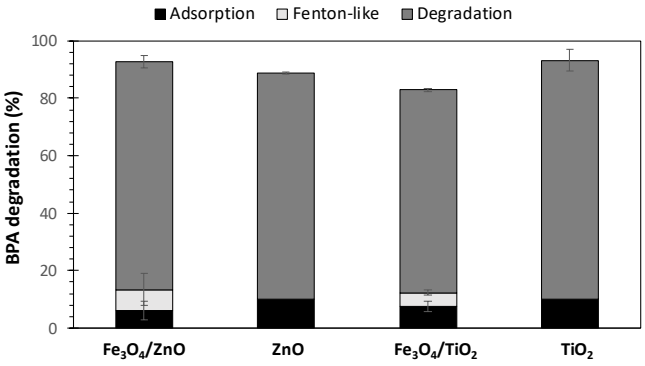

Figure 5.11 Photodegradation (grey bars), Fenton-like (white bars) and adsorption control (black bars) results of Fe_3O_4/ZnO and Fe_3O_4/TiO_2 NCs and ZnO and TiO_2 NPs under optimal conditions for the removal of BPA (350 μg L^{-1}) after 2 h.

The NCs of Fe_3O_4/ZnO and Fe_3O_4/TiO_2 and ZnO and the NPs of TiO_2 reached high BPA removal percentages (92.76%, 82.89%, 88.80% and 93.26%, respectively), while the results of the adsorption control were less than 10% of BPA removal. Regarding Fenton contribution evaluation of Fe_3O_4/ZnO and Fe_3O_4/TiO_2 NCs, the results rule out this option as a favorable contribution mechanism during the BPA photocatalysis process, although numerous studies corroborate that the presence of TiO_2 influenced the increase of the optimal pH towards an almost neutral level, through the chelation of the iron ions, during for example, Methylene Blue (MB) dye removal by Fenton-like reaction (Yang et al. 2015, Sun et al. 2019).

These results can also be explained by the similar bandgap of ZnO and TiO_2 (~3 eV) which theoretically provide the same photocatalytic efficiency (Lee et al. 2016). However, the ZnO magnetic compound has been selected for application in subsequent studies, not only because of its relatively better photocatalytic result, but also because of its economic cost, as ZnO is relatively cheaper compared to TiO_2, whereby the usage of TiO_2 is not cost-effective for large-scale water treatment operations (Daneshvar et al. 2004). In addition, although degradation rates were similar using non-magnetic NPs, these NPs could not be easily removed from the reaction medium, requiring an additional precipitation step or centrifugation.

5.3.3 Photocatalytic active species evaluation

The main objective of this section is to carry out a preliminary evaluation of the ability to generate intermediate active species of Fe_3O_4/ZnO by UVA-assisted photodegradation of a dye model (OII; 5 mg L^{-1}) in the presence of different scavenger agents. Figure 5.12 shows that the generation of adsorbed ·OH and $O_2^{\cdot-}$, as well as h_{vb}^+, plays a crucial role in photodegradation mechanisms, while ·OH in solution were not largely involved. It was also evidenced a partial contribution of $^1O_2$), which has an electrophilic character and reacts with organic compounds.

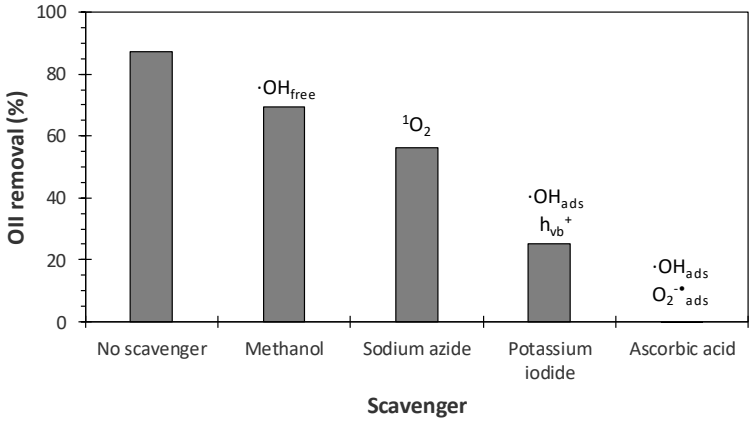

Figure 5.12 OII (5 mg L^{-1}) photodegradation in the presence of Fe_3O_4/ZnO and different scavengers of reactive oxygen species, after 60 min of reaction time.

5.3.4 Comparison of oxidation technologies for the removal of different dyes

The objective of this study is to perform the degradation of a wide range of dyes (RN19, MG, MR, OII and R123; 25 mg L^{-1}) with different structures and characteristics through the UV-assisted photodegradation process under the previously applied operating conditions (catalyst dosage of 100 mg L^{-1}, H_2O_2 concentration 100 mg L^{-1} and pH 7). Additionally, a comparison of the results obtained by photocatalysis with heterogeneous Fenton process for the color removal of the same studied dyes have been carried out. Fenton-like optimal operational conditions have been selected as in Section 4.3.2, Chapter 4 (Fe_3O_4@PAA/SBA15 NC dosage of 200 mg Fe_3O_4 L^{-1}, H_2O_2 concentration 100 mg L^{-1} and pH 3).

The results of the decolorization of different dyes using Fe_3O_4/ZnO NC under UV irradiation compared to Fenton-like process using Fe_3O_4@PAA/SBA15 are reported in Figure 5.13A. The experimental results indicate that color removal after 120 min of Fenton-like reaction undergoes to an acceptable decolorization rate, greater than 90% for RB19 and 70% for MR and OII, whereas for MG and R123 the decolorization results were lower than 50%. Control tests with H_2O_2 dosage but lacking mNPs and pH 3 stability tests did not show significant results (data not shown).

The pH parameter determines the interaction between the surface of the catalyst and the target compounds. Under acidic conditions, MR, MG and R123 (cationic dyes) are positively charged and RB19 and OII (anionic dyes) are negatively charged. Considering the dissociation constant of PAA (pK_a= 4.3), the surface of the catalyst particle is neutral at pH 3.

It has become evident that there is an influence of the chemical structure of the different dyes during the decolorization reactions. RB19 achieved the highest percentage of color removal, accounting for almost 100% of decolorization, whereas for OII, the decolorization yield was close to 60% (Figure 5.13A). In the case of cationic dyes, two different scenarios could be postulated. On the one hand, MR showed decolorization to certain extent (75%), attributed to the azo bond (–N=N–), which is prone to be oxidized by ·OH radicals (Cao et al. 1999).

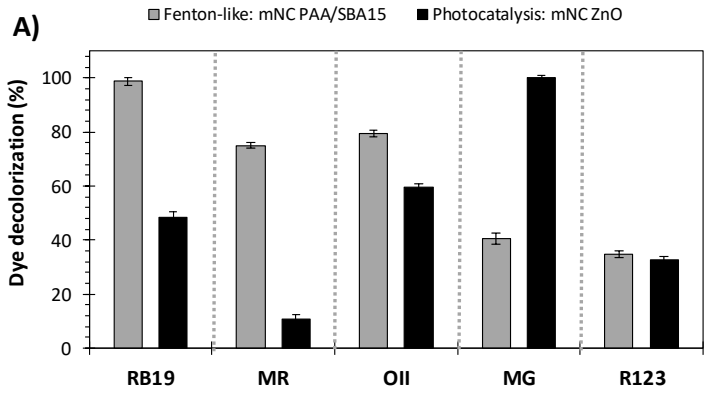

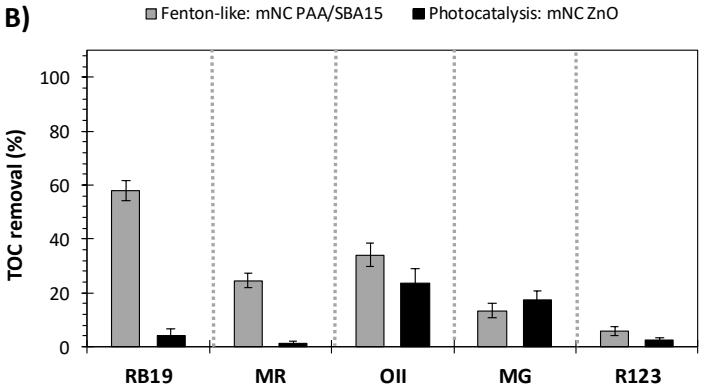

Figure 5.13 A) Dye decolorization (%) and B) TOC removal (%) after 120 min using Fe_3O_4@PAA/SBA-15 magnetic NC (mNC) as heterogenous Fenton catalyst ( ) and Fe_3O_4/ZnO mNC as photocatalyst ( ).

On the other hand, MG and R123 have scarcely shown any decolorization after 2 h of heterogeneous Fenton oxidation, with values between 35 and 40% (Figure 5.13A). These results can be explained on the hypothesis of an inhibitory effect of chloride ions (Cl^-) from dyes molecules, which act as ·OH scavenger contributing to reduce decolorization yield (Gupta et al. 2006). Moreover, the presence of methyl groups ($-CH_3$) in the molecular structure of MG tends to decrease the decolorization rate (Khataee and Kasiri 2010).

Dye-containing effluents were also evaluated for the heterogeneous photocatalytic system based on magnetic composites. The results indicate that RB19, MG and OII are subjected to a decolorization higher than 50% for the three cases, reaching complete MG color removal. However, dye stability tests at pH 7 show a significant decolorization of the MG dye (50.5%) after 2 h of control test. Some studies indicate that above neutral pH conditions (pH 7.5), MG fading becomes evident, being stable at low pH, in the range of 3-5 (Kurnick and Foster 1950). This phenomenon can be explained by the conversion of MG into the colorless carbinol base (triarylmethanol; Figure 5.14).

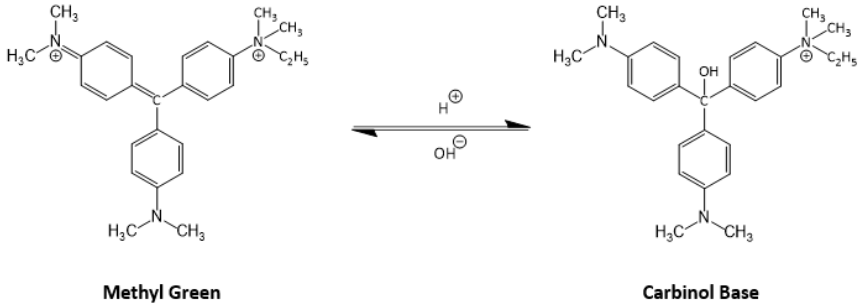

Figure 5.14 MG proposed pathway under basic pH solutions (Mai et al. 2008).

For MR and R123, the decolorization yield was 10 and 32%, respectively, which could be attributed to the recalcitrant nature of MR and R123 dyes. In a similar study, MR was found to have the higher adsorption constant (K_{ads}=18·10^3 L mol^{-1}) at the surface of titania compared to different representative dyes, which could be explained by the carboxylic substituent on one of the benzene rings (Lachheb et al. 2002). However, in the studied nanocatalyst (ZnO mNC) nearly no adsorption was observed (less than 5%).

Finally, TOC have been determined to estimate the percentage of mineralization after treatment. The results shown in Figure 5.13B revealed a decrease in the percentage of mineralization compared to the decolorization yield for the different dyes, obtaining the highest values after heterogeneous treatment with Fenton for almost all dyes, with values ranging from 6 to 60% of TOC removal. These results agree with a previous comparative study carried out by Arslan et al. (2000) that evaluated the oxidation of different reactive dyes in simulated dyeing effluents by ferrioxalate-Fenton/UVA and TiO_2/UVA processes. They achieved the highest TOC removal percentages (3 times higher decolorization rate constant) by the application of Fe^{3+}-oxalate-Fenton/UVA oxidation compared to TiO_2/UVA processes. The efficiency of Fenton type processes may be explained by effectiveness ·OH formation during the oxidation reactions (Spacek et al. 1995). However, from the results obtained, the different AOPs considered here emerge as highly competitive technologies for dye removal.

5.3.5 Reuse of the catalysts

The capacity of the Fe_3O_4/ZnO NC as photocatalyst to remove 25 mg L^{-1} of the recalcitrant azo dye OII was evaluated in a 2 h repeated batch operation. The results obtained are shown in Figure 5.15, where, under selected conditions (catalyst and H_2O_2 dosage of 100 mg L^{-1} and pH 7), 52.1% of OII was removed after ten decolorization cycles. Heterogeneous photocatalysis reached a decolorization percentage close to 60% in the first cycle and was maintained during 10 cycles, decreasing slightly after cycle 5, reaching values between 52 and 57% of OII removal.

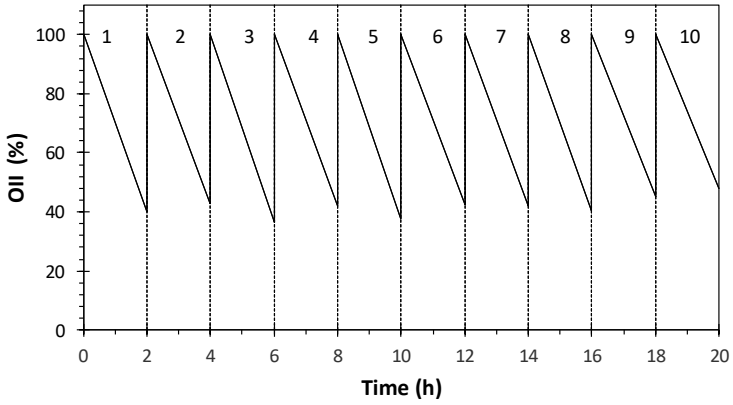

Figure 5.15 OII (25 mg L^{-1}) decolorization yield in subsequent cycles of Fe_3O_4/ZnO heterogeneous photocatalysis treatment after 2 h. Catalyst and H_2O_2 dosage of 100 mg L^{-1} and pH 7.

This slight decay could be due to the reduction of the mNC activity but also these positive results demonstrate the recovery of the catalyst by means of the magnetic field, assuring the reuse of the catalysts in different oxidation cycles without replacement of additional material.

5.4 Conclusions

In the present chapter, two different nanostructured photoactive materials based on hybrid NCs, Fe_3O_4/ZnO and Fe_3O_4/TiO_2, have been prepared and evaluated for wastewater treatment applications. Degradation experiments were performed

with the aim of explore its photocatalytic activity for the removal of a variety of water pollutants, which were selected as model of persistent organic compounds in water.

In this sense, results have demonstrated the feasibility of these mNCs as photocatalysts for water treatment in the presence of UV-light. These findings also suggest that various operating parameters such as type of photocatalyst and contaminant, among other parameters, may influence the photocatalytic oxidation process. The optimization of these conditions is crucial from the perspective of efficient design and application of heterogeneous photocatalysis processes.

5.5 References

Akbarzadeh, A., Samiei, M. and Davaran, S. (2012) Magnetic nanoparticles: preparation, physical properties, and applications in biomedicine. Nanoscale research letters 7(1), 144.

Arslan, İ., Balcioğlu, I.A. and Bahnemann, D.W. (2000) Advanced chemical oxidation of reactive dyes in simulated dyehouse effluents by ferrioxalate-Fenton/UV-A and TiO2/UV-A processes. Dyes and Pigments 47(3), 207-218.

Augugliaro, V., Litter, M., Palmisano, L. and Soria, J. (2006) The combination of heterogeneous photocatalysis with chemical and physical operations: A tool for improving the photoprocess performance. Journal of Photochemistry and Photobiology C: Photochemistry Reviews 7(4), 127-144.

Banić, N.D., Abramović, B.F., Krstić, J.B., Šojić Merkulov, D.V., Finčur, N.L. and Mitrić, M.N. (2019) Novel WO3/Fe3O4 magnetic photocatalysts: Preparation, characterization and thiacloprid photodegradation. Journal of Industrial and Engineering Chemistry 70, 264-275.

Barka, N., Bakas, I., Qourzal, S., Assabbane, A. and Ait-Ichou, Y. (2013) Degradation of phenol in water by titanium dioxide photocatalysis. Oriental Journal of Chemistry 29(3), 1055-1060.

Beydoun, D., Amal, R., Low, G.K.-C. and McEvoy, S. (2000) Novel photocatalyst: titania-coated magnetite. Activity and photodissolution. The Journal of Physical Chemistry B 104(18), 4387-4396.

Cao, J., Wei, L., Huang, Q., Wang, L. and Han, S. (1999) Reducing degradation of azo dye by zero-valent iron in aqueous solution. Chemosphere 38(3), 565-571.

Chemseddine, A. and Moritz, T. (1999) Nanostructuring titania: control over nanocrystal structure, size, shape, and organization. European Journal of Inorganic Chemistry 1999(2), 235-245.

Daneshvar, N., Salari, D. and Khataee, A. (2004) Photocatalytic degradation of azo dye acid red 14 in water on ZnO as an alternative catalyst to TiO2. Journal of Photochemistry and Photobiology A: Chemistry 162(2-3), 317-322.

de O. Pereira, L., de Moura, S.G., Coelho, G.C.M., Oliveira, L.C.A., de Almeida, E.T. and Magalhães, F. (2019) Magnetic photocatalysts from industrial residues and TiO2 for the degradation of organic contaminants. Journal of Environmental Chemical Engineering 7(1), 102826.

Fatehah, M.O., Aziz, H.A. and Stoll, S. (2014) Stability of ZnO nanoparticles in solution. Influence of pH, dissolution, aggregation and disaggregation effects. Journal of Colloid Science and Biotechnology 3(1), 75-84.

Feldmann, C. and Jungk, H.O. (2001) Polyol-mediated preparation of nanoscale oxide particles. Angewandte Chemie International Edition 40(2), 359-362.

Fernández, L., Gamallo, M., González-Gómez, M.A., Vázquez-Vázquez, C., Rivas, J., Pintado, M. and Moreira, M.T. (2019) Insight into antibiotics removal: Exploring the photocatalytic performance of a Fe3O4/ZnO nanocomposite in a novel magnetic sequential batch reactor. Journal of Environmental Management 237, 595-608.

Fox, M.A. and Dulay, M.T. (1993) Heterogeneous photocatalysis. Chemical Reviews 93(1), 341-357.

Gaya, U.I. and Abdullah, A.H. (2008) Heterogeneous photocatalytic degradation of organic contaminants over titanium dioxide: a review of fundamentals, progress and problems. Journal of Photochemistry and Photobiology C: Photochemistry Reviews 9(1), 1-12.

Gmurek, M., Olak-Kucharczyk, M. and Ledakowicz, S. (2017) Photochemical decomposition of endocrine disrupting compounds–A review. Chemical Engineering Journal 310, 437-456.

Gupta, A., Pal, A. and Sahoo, C. (2006) Photocatalytic degradation of a mixture of Crystal Violet (Basic Violet 3) and Methyl Red dye in aqueous suspensions using Ag+ doped TiO2. Dyes and Pigments 69(3), 224-232.

Heshmatpour, F. and Abdikhani, M.S. (2019) Ce-Ag-ZnO/Fe_3O_4 nanocomposites: a novel magnetically separable photocatalyst for highly efficient photodegradation of contaminants. Physica B: Condensed Matter.

Hoffmann, M.R., Martin, S.T., Choi, W. and Bahnemann, D.W. (1995) Environmental applications of semiconductor photocatalysis. Chemical Reviews 95(1), 69-96.

Khataee, A. and Kasiri, M.B. (2010) Photocatalytic degradation of organic dyes in the presence of nanostructured titanium dioxide: Influence of the chemical structure of dyes. Journal of Molecular Catalysis A: Chemical 328(1-2), 8-26.

Khodja, A.A., Sehili, T., Pilichowski, J.-F. and Boule, P. (2001) Photocatalytic degradation of 2-phenylphenol on TiO2 and ZnO in aqueous suspensions. Journal of Photochemistry and Photobiology A: Chemistry 141(2-3), 231-239.

Kurnick, N. and Foster, M. (1950) METHYL GREEN: III. Reaction with Desoxyribonucleic Acid, Stoichiometry, and Behavior of the Reaction Product. The Journal of General Physiology 34(2), 147-159.

Lachheb, H., Puzenat, E., Houas, A., Ksibi, M., Elaloui, E., Guillard, C. and Herrmann, J.-M. (2002) Photocatalytic degradation of various types of dyes (Alizarin S, Crocein Orange G, Methyl Red, Congo Red, Methylene Blue) in water by UV-irradiated titania. Applied Catalysis B: Environmental 39(1), 75-90.

Lee, K.M., Lai, C.W., Ngai, K.S. and Juan, J.C. (2016) Recent developments of zinc oxide based photocatalyst in water treatment technology: a review. Water Research 88, 428-448.

Mai, F.D., Chen, C.C., Chen, J.L. and Liu, S.C. (2008) Photodegradation of methyl green using visible irradiation in ZnO suspensions: Determination of the reaction pathway and identification of intermediates by a high-performance liquid chromatography–photodiode array-electrospray ionization-mass spectrometry method. Journal of Chromatography A 1189(1), 355-365.

Massart, R. (1981) Preparation of aqueous magnetic liquids in alkaline and acidic media. IEEE Transactions on Magnetics 17(2), 1247-1248.

Mohapatra, D.P., Brar, S.K., Tyagi, R.D., Picard, P. and Surampalli, R.Y. (2014) Analysis and advanced oxidation treatment of a persistent pharmaceutical compound in wastewater and wastewater sludge-carbamazepine. Science of the Total Environment 470, 58-75.

Neppolian, B., Jung, H. and Choi, H. (2007) Photocatalytic degradation of 4-chlorophenol using TiO2 and Pt-TiO2 nanoparticles prepared by sol-gel method. Journal of Advanced Oxidation Technologies 10(2), 369-374.

Nguyen, A.T. and Juang, R.-S. (2015) Photocatalytic degradation of p-chlorophenol by hybrid H2O2 and TiO2 in aqueous suspensions under UV irradiation. Journal of Environmental Management 147, 271-277.

Oros-Ruiz, S., Zanella, R. and Prado, B. (2013) Photocatalytic degradation of trimethoprim by metallic nanoparticles supported on TiO2-P25. Journal of Hazardous materials 263, 28-35.

Parsons, S. (2004) Advanced oxidation processes for water and wastewater treatment, IWA publishing.

Sousa-Castillo, A., Comesaña-Hermo, M., Rodríguez-González, B., Pérez-Lorenzo, M.s., Wang, Z., Kong, X.-T., Govorov, A.O. and Correa-Duarte, M.A. (2016) Boosting hot electron-driven photocatalysis through anisotropic plasmonic nanoparticles with hot spots in Au–TiO_2 nanoarchitectures. The Journal of Physical Chemistry C 120(21), 11690-11699.

Spacek, W., Bauer, R. and Heisler, G. (1995) Heterogeneous and homogeneous wastewater treatment—comparison between photodegradation with TiO2 and the photo-Fenton reaction. Chemosphere 30(3), 477-484.

Sun, C., Yang, S.-T., Gao, Z., Yang, S., Yilihamu, A., Ma, Q., Zhao, R.-S. and Xue, F. (2019) Fe3O4/TiO2/reduced graphene oxide composites as highly efficient Fenton-like catalyst for the decoloration of methylene blue. Materials Chemistry and Physics 223, 751-757.

Xie, X., Liu, Y., Dong, X., Lin, C., Wen, X. and Yan, Q. (2018) Synthesis and characterization of Fe3O4/BiOI n-p heterojunction magnetic photocatalysts. Applied Surface Science 455, 742-747.

Yang, S., Yang, L., Liu, X., Xie, J., Zhang, X., Yu, B., Wu, R., Li, H., Chen, L. and Liu, J. (2015) TiO2-doped Fe3O4 nanoparticles as high-performance Fenton-like catalyst for dye decoloration. Science China Technological Sciences 58(5), 858-863.

Zhao, L., Deng, J., Sun, P., Liu, J., Ji, Y., Nakada, N., Qiao, Z., Tanaka, H. and Yang, Y. (2018) Nanomaterials for treating emerging contaminants in water by adsorption

and photocatalysis: Systematic review and bibliometric analysis. Science of the Total Environment 627, 1253-1263.

5.6 Annex

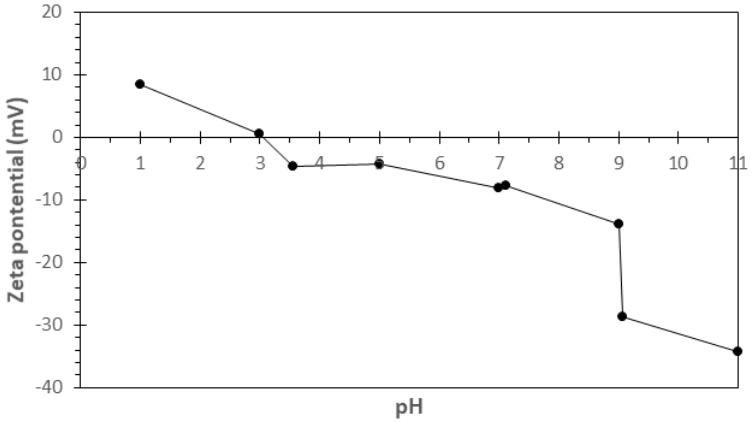

Figure A5.1 Zeta potential of Fe_3O_4/ZnO NC as a function of pH, at 20 °C. Line is only a visual guide to the data trend.

USC
UNIVERSIDADE
DE SANTIAGO
DE COMPOSTELA

6. Chapter 6

OPERATION OF DIFFERENT CONFIGURATIONS OF CATALYSIS REACTORS coupled with magnetic separation

SUMMARY

This chapter presents the development and operation of a magnetic catalytic reactor applied to the elimination of a wide range of recalcitrant compounds present in a water matrix by means of different oxidation processes based on the use of nanostructured based-magnetite catalyst (Fe_3O_4). Different configurations of magnetic separation devices, from an internal separation unit to two different external systems, have been evaluated, comparing the main operating parameters that influence the operation of the reactor, such as the removal rate of the pollutant and the retention efficiency of the catalyst. Finally, the optimal configuration was evaluated for its operation as photoreactor coupled with an UV-light external stage.

OUTLINE

6.1 Introduction

It is not only interesting to demonstrate the capacity of the previous nanostructured magnetic catalysts proposed for the removal of contaminants in water, but also to ensure the complete recovery of the nanocatalysts and that their catalytic potential is maintained during their application in different cycles, demonstrating their reuse. In the literature, there is hardly any information on the design or operation of reactors in which the use of electromagnet systems for the separation of magnetic particles is not necessary. These types of reactors called magnetically stabilized fluidized bed reactors (MSFBR) require a power supply, which greatly increases the operating costs of the system (Arivizhivendhan et al. 2016, Chen et al. 2017, Ou et al. 2019).

In addition, this magnetic field provided by electromagnets is limited to the magnetic separation of microparticles, while a stronger magnetic field is required for magnetic nanoparticles (Tang and Lo 2013). References are even scarcer in the operation of oxidation technologies such as Fenton heterogeneous catalysis reactors where the separation of the catalyst is carried out automatically.

He et al. (2014) describes the use of magnetite (Fe_3O_4) nanoparticles (NPs) in an electro-Fenton process to carry out the degradation of the dye Reactive Blue 19 (RB19) in an electrochemical reactor; another case is that described by Zhou et al. (2015), through the use of magnetic composites of $Cu_{0.3}Fe_{2.7-x}Ti_xO_4$ for the removal of mercury in a bubbling reactor. Regarding photocatalysis processes, photocatalytic reactors encounter unfavorable mass transfer conditions due to the need for catalyst immobilization and/or high operating costs associated with the recovery of the catalyst by ultrafiltration (Wang et al. 2014, Ahmari et al. 2018). In addition, none of these works proposes an automated device allowing the separation of nanoparticles for their application in successive cycles.

In this sense, a recent work developed by Moldes-Diz et al. (2018) proposed a novel sequential batch reactor (SBR) coupled to an internal magnetic separator. The main advantage of this technology is the simplicity in the separation of the nanocatalyst, since the unit requires a minimum investment and energy cost, as opposed to the use of high energy demand electromagnets.

Taking this work as a reference, the main objective of this chapter is the development and operation of a reactor coupled to different magnetic separation systems to perform the degradation of different recalcitrant compounds, guaranteeing the complete retention of magnetic NPs (mNPs) and photocatalysts formulated as nanocomposites (NCs).

In order to ensure the long term of the process and avoid the release of nanocatalysts into the effluent, different novel magnetic separation units are proposed and evaluated in terms of pollutant removal and NC recovery percentage in the effluent for the removal of RB19 dye as a recalcitrant model by heterogeneous Fenton oxidative treatment, providing an effective combination of reaction and separation units. The optimal configuration was operated for the simultaneous removal of a wide range of micropollutants present in real water matrix corresponding to the secondary effluent of a wastewater treatment plant (WWTP).

6.2 Materials and methods

6.2.1 Chemicals and nanostructured catalysts

In the present chapter, all chemicals used have been previously mentioned in Section 2.1 in Chapter 2. Selected mNPs and photocatalysts formulated as (NCs) synthesis and characteristics have been also previously described in Chapters 4 and 5 and are listed in Table 6.1. The selection of these catalysts has been based on the results obtained in the corresponding previous chapters.

Table 6.1 Selected nanostructured catalysts

Catalyst	Description
Fe_3O_4@PAA/SBA-15	PAA-coated magnetic NPs supported onto SBA-15
Fe_3O_4/ZnO	Zinc oxide magnetic NC

6.2.2 Experimental set-up and description of the magnetic separation units applied to the reactor performing the decolorization of RB19

Decolorization of RB19 (25 mg L^{-1}) by heterogeneous Fenton treatment were individually conducted in a 5-L reactor up to a final volume of 2 L, at room temperature, pH 3 and continuous stirring. The applied concentrations of mNPs (Fe_3O_4@PAA/SBA-15) and H_2O_2 were 200 mg L^{-1} based on Fe_3O_4 and 100 mg L^{-1},

respectively, followed by a reaction time of 2 h, previously established as the required conditions to accomplish the extensive decolorization of the target dye RB19 (Section 4.3.4).

At regular intervals, absorbance measurements were conducted in a UV-Vis spectrophotometer to monitor color removal of RB19 (λ=592 nm) (Section 2.3, Chapter 2). The degradation yield (%) was determined as the extent of color disappearance, calculated by Eq. 3:

$$\text{Degradation yield (\%)} = \frac{(C_0 - C_t)}{C_0} \times 100 \quad (1)$$

where C_0 and C_t represent the organic compound concentration (mg L^{-1}) before and after the reaction time, respectively.

The designed reactor was used to evaluate the next operating sequence, the magnetic separation of the nanostructured catalyst during several operating cycles. This stage has been tested for different configurations of magnetic separation equipment, developed in collaboration with the Laboratory of Magnetism and Nanotechnology belonging to the Departments of Applied Physics and Physical Chemistry of the University of Santiago de Compostela (Spain), which are described below.

The efficiency of color removal, the stability of the operation, the absence of magnetic catalysts in the effluent and the operability of the system have been determined and compared between the operation of the internal and both external magnetic reactors. In order to ensure that the effluent is free of magnetic catalysts, inductively coupled plasma-optical emission spectrometry (ICP-OES; Section 2.2, Chapter 2) was performed on the treated effluent to determine the possible loss of the catalyst expressed in iron concentration (mg L^{-1} Fe).

Internal magnetic separation unit

The configuration of the internal magnetic separator consists of an air pneumatic cylinder with a magnetic bar inside the reactor. The magnetic bar covered by a thin glass tube comprises permanent toroidal magnets (14 neodymium-iron-

boron (NdFeB) magnets of 6x15x6 mm) with axial magnetization and arranged with alternate polarity controlled by a programmable logic controller (PLC) system (previously described in Patents ES2 559111B2 and ES2558582B2). The operation of the reactor cycle involves four main stages: a) loading of untreated contaminated water into the reactor in the presence of nanocatalysts, b) reaction treatment phase, c) end of the oxidation treatment and d) retention of the nanocatalyst and effluent discharge (Figure 6.1).

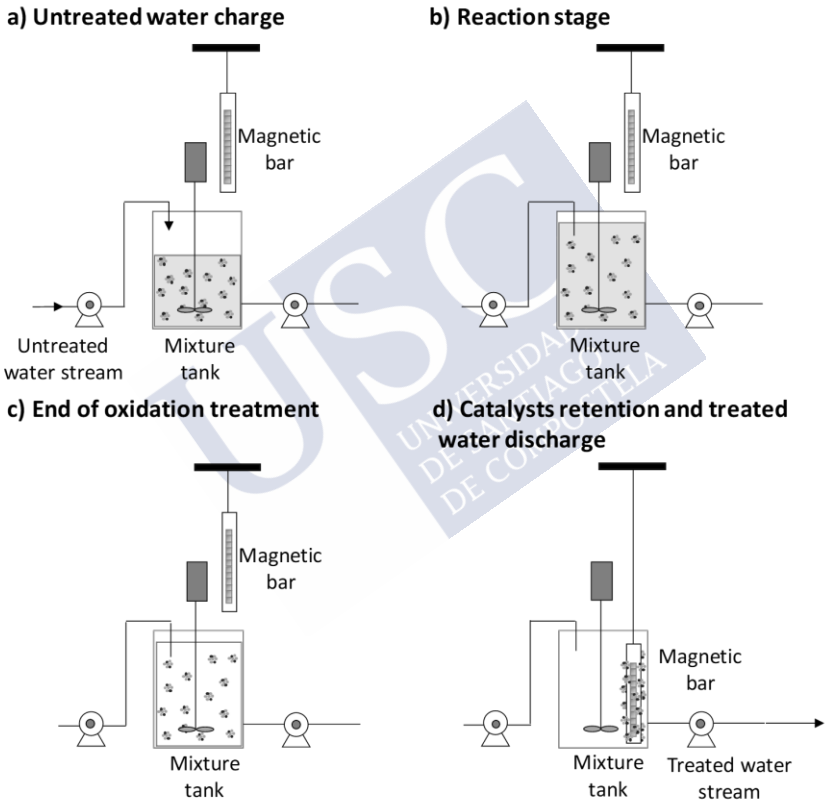

Figure 6.1 SBR operation stages: a) Influent charge, b) reaction stage, c) end of water treatment and d) retention of the catalyst/discharge of the treated effluent.

External magnetic separation unit

The unit for the external magnetic separation consisted of a system of Teflon tubes (internal and external diameters of 2 and 5 mm, respectively), on which an external magnetic field was applied. This magnetic field was produced by ten ring magnets (NdFeB; with the following dimensions of each of the toroidal magnets: internal diameter of 16 mm, external diameter of 26.8 mm and length of 5 mm).

Figure 6.3 shows the reaction system with Patent ES2670712B2; it starts when the untreated influent is pumped into the reactor vessel, where the magnetic nanocatalysts are in solution (Stage I). Once a reaction cycle is completed (Stage II), the output stream of the reactor is pumped through the external magnetic separation unit, with a flow similar to the influent stream.

The magnetic unit retains the magnetic catalysts and the treated effluent free of magnetic solids can be discharged (Stage III). Finally, a new contaminated effluent is pumped back through the pipeline by dragging the nanoparticles retained back into the system by the pushing effect of the inlet stream. This process can be repeated successively in different reaction cycles.

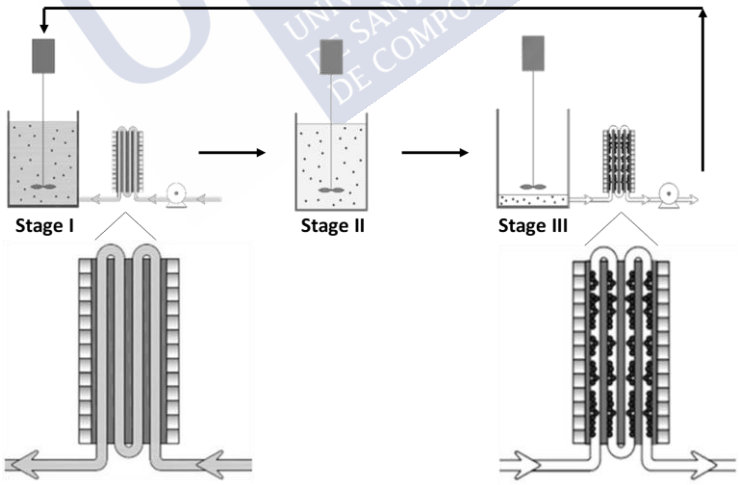

Figure 6.3 Diagram of reaction system with external magnetic separation and its application in the treatment of polluted water.

External magnetic rotatory separation unit

The reuse of the selected magnetic nanocatalysts was also explored during their use in consecutive removal cycles performed in a sequentially operating reactor (Figure 6.4). The magnetic separation unit consists of an external device, where the magnetic catalysts are kept in the maximum flow of a non-uniform magnetic field, while the magnetic system rotates on the same axis and in opposite directions, avoiding both dragging and accumulation on the walls. The magnetic field was created with an arrangement of radially and axially magnetized toroidal NdFeB magnets. Finally, the rotary separator coupled to the reactor divides the streams within the glass flow divider (Figure 6.5), to obtain one flow with the treated effluent and the other with the nanocatalyst that will be recirculated to the reactor.

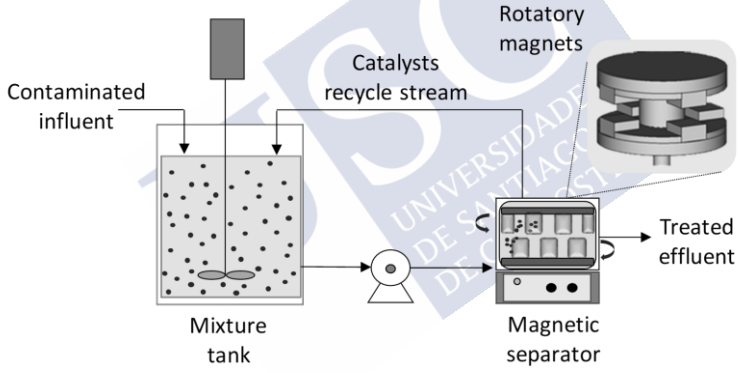

Figure 6.4 Scheme of reaction system with external rotating magnetic separation unit and its application in the treatment of contaminated water.

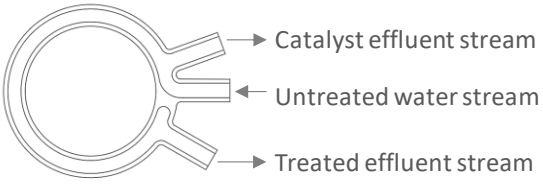

Figure 6.5 Glass flow divider located inside the magnetic separator.

The main advantage of this configuration is the ability to operate in continuous mode by keeping the magnetic nanocatalysts retained in the reactor, while the new effluent is continuously charged into the reactor for treatment.

6.2.3 Operation of a magnetic reactor for wastewater treatment

An SBR (5-L) reactor coupled to an internal magnetic separation unit was operated under optimum conditions and evaluated in real water samples taken from the effluent of a biological reactor of an urban WWTP located in Calo-Milladoiro (A Coruña, Spain) (Table A6.1). A wastewater sample was collected and stored in a brown glass bottle at 4 °C.

The operation consists of an initial feeding of 2 L of the secondary effluent spiked with a wide range of micropollutants (E1, E2, EE2, BPA, CBZ, IBP and SMX) added at an initial concentration of 350 μg L^{-1} (each) and 750 mg Fe L^{-1} of Fe_3O_4@PAA/SBA-15 nanocomposite (1.04 g Fe_3O_4 L^{-1}) and pH 3, previously established in Section 4.3.6, Chapter 4, for the optimal removal of microcontaminants by magnetic nanocatalysts supported in SBA-15 mesoporous materials. Individual stock solutions (1 mg ml^{-1}) of each compound were prepared in acetonitrile (AcN) and stored in the dark at 4 °C.

Catalytic test cycles start with the addition of 400 mg L^{-1} of H_2O_2, followed by a reaction time of 6 h under continuous stirring. Aliquots were periodically withdrawn for high performance liquid chromatography (HPLC) and TOC measurements (Section 2.3, Chapter 2). The final separation step of the magnetic catalysts was performed using a bar magnet included in the pneumatic cylinder system previously described in Section 6.2.2. The treated effluent was discharged and fresh medium with the selected contaminants was added for a new cycle of nanocatalyst reuse. Scanning electron microscopy (SEM) were evaluated for the NCs before use and after reuse cycles.

6.2.4 Operation of a magnetic photocatalytic reactor

In the previous magnetic SBR (Figure 6.1) photocatalytic experiments were performed for the removal of a model dye (Orange II, OII; Chapter 5), together with an additional photocatalytic reactor (Figure 6.6). The photocatalytic operation

consists of an initial feeding of 2 L of the reaction medium at pH 7 with OII at a concentration of 25 mg L^{-1}, in combination with 100 mg L^{-1} of Fe_3O_4/ZnO nanophotocatalyst and 100 mg L^{-1} of H_2O_2 (operational conditions previously established in Chapter 5), followed by a reaction phase of 120 min under continuous agitation and pumping through a 365 nm wavelength UVA (15 W) lamp, with an effective reaction volume of 0.7 L.

The treated effluent was discharged, and absorbance measurements in a UV-Vis spectrophotometer were carried out to monitor color removal of OII (λ=473 nm) (Section 2.3, Chapter 2). The degradation yield (%) was determined as the extent of color disappearance, calculated by Equation 3. The reuse of the Fe_3O_4/ZnO NC was evaluated in subsequent cycles under the same optimization conditions. Finally, lamp radiation power was measured with a UV light meter PCE Group Iberica S. L. (Tobarra, Spain), model UVA-UVB PCE-UV34.

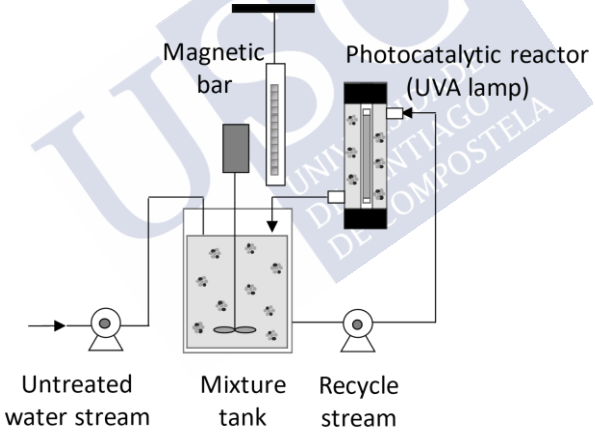

Figure 6.6 Magnetic reactor with internal magnetic separation system coupled to a photocatalytic reactor.

6.3 Results and discussion

6.3.1 Comparison of the magnetic separation unit in the reactor performing the decolorization of RB19

The potential reuse of the catalyst was evaluated by conducting 10 cycles of RB19 decolorization by heterogeneous Fenton treatment, according to the three different magnetic separation strategies described above (internal bar and external pipes and rotary systems). The oxidative capacity of Fe_3O_4@PAA/SBA-15 mNPs was independently evaluated in the degradation of RB19 with optimized concentrations of H_2O_2 (100 mg L^{-1}), catalyst (200 mg L^{-1}) and dye (25 mg L^{-1}), in a 2 L reactor volume.

First, the reactor was operated sequentially with the internal separation magnetic bar (Figure 6.1) and with the external pipes magnetic system (Figure 6.3), according to the fill-and-draw principle, which consists of the following steps: fill, react, magnetic retention of the catalyst and withdraw of the reaction medium. Finally, a magnetic rotary magnetic system was also evaluated under the same conditions RB19 decolorization conditions (Figure 6.4). The decolorization results obtained after ten cycles of reuse of mNPs for each magnetic separation unit are shown in Figure 6.7 below.

The obtained results show that the decolorization of RB19 in the three reactors through ten cycles of catalyst reuse reached high percentages, in the range of 98.8-100.0% for reactor A, 85.6-100.0% for reactor B and 87.5-100% for reactor C. The results of Fe_3O_4@PAA/SBA-15 reuse demonstrated not only the viability of the application of these superparamagnetic nanocatalysts in successive cycles without affecting the properties of the material, but also the technical feasibility for the operation of magnetic separation devices, which do not require an electrical power supply as electromagnets.

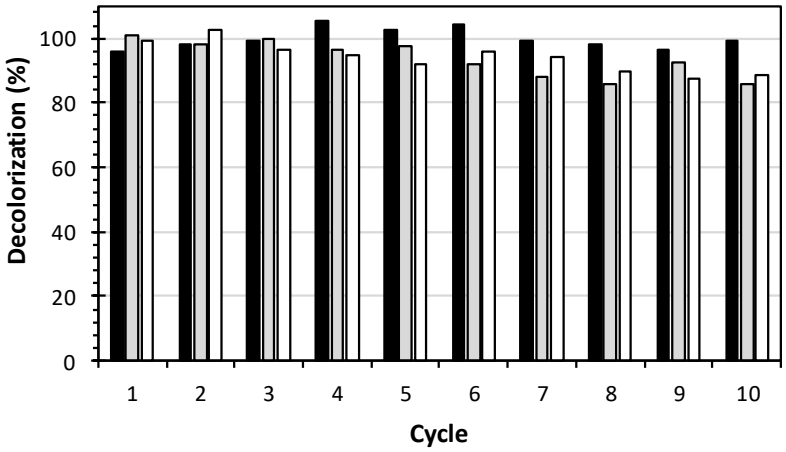

Figure 6.7 RB19 decolorization cycles (%) of heterogeneous Fenton oxidation processes during operation of different magnetic separation units: A) Internal magnetic separation (Black bars), B) External separation (Gray bars) and C) External rotary magnetic separation device (White bars). Operational conditions: Fe_3O_4@PAA/SBA-15 nanocomposite (NC): 200 mg L^{-1}, H_2O_2: 100 mg L^{-1}, RB19: 25 mg L^{-1}.

The toroidal magnets that make up the magnetic separation unit are permanently aligned and coupled with alternating polarity. Figure 6.2 shows a simulation of the axial cut of the magnetic arrangement, with a magnetic field in the range of 0.05 to 1.2 T.

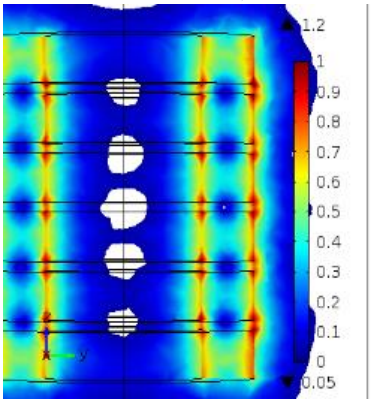

Figure 6.2 Modelling of magnetic fields (T) produced by alternate polarity configuration of the magnet array.

In the selected alternate arrangement of the magnets with the poles face to face, the field lines extend to find the opposite pole, and consequently, the area of high gradient is notably higher. In the case of series arrangement, the magnetic field reaches high values only in the spaces between the individual magnets and at the top and bottom of the separation unit, so the retention of mNPs would be not so efficient. However, as can be seen in Figure 6.7, the color removal efficiency decreased from cycle 7 for both external magnetic separation units, reaching decolorization percentages of 85.6 and 88.5%, respectively. It is important to note that, in the internal magnetic separation system, the color removal results were maintained during the ten reuse cycles of the catalyst (99.1% of RB19 decolorization in cycle 10). The efficiency of the pollutant removal depends directly on the stability of the operation. In other words, the stability of the reaction and separation system as a whole, since if the magnetic nanocatalysts are not well retained and, therefore, are eliminated in the reactor effluent, in the consecutive oxidation cycle the concentration of catalysts will not be optimal, which will lead to a progressive loss of system efficiency.

Therefore, it is important to ensure the retention of the nanocatalyst in the reaction system and to ensure that the magnetic separation units are fully effective for this purpose. Therefore, ICP-OES was performed in the effluent of cycles 1, 5 and 10 for each reactor configuration after each decolorization stage in order to determine the possible catalyst loss expressed as iron concentration (mg L^{-1} of Fe). The results obtained are summarized in Table 6.2.

Table 6.2 Results of iron concentration (mg L^{-1} of Fe) in the effluent after 2 h of heterogeneous Fenton oxidation during the cycles of Fe_3O_4@PAA/SBA-15 catalyst reuse in different magnetic separation units: A) Internal bar separation, B) External pipes separation and C) External rotary magnetic separation device

Reactor system	Cycle	Fe (mg L^{-1})
A) Internal bar separation	1	0.056 ± 0.003
	5	0.047 ± 0.001
	10	0.040 ± 0.0001

B)	External pipes separation	1	0.311 ± 0.024
		5	0.148 ± 0.005
		10	0.067 ± 0.004
C)	External rotatory separation	1	0.163 ± 0.002
		5	0.077 ± 0.004
		10	0.126 ± 0.022

The nanocatalyst was detected in the effluent as dissolved Fe (mg L^{-1}), as confirmed by the ICP-OEs analysis. The results included in Table 6.2 show that the optimal magnetic separation unit is the internal bar separation equipment, with a total iron concentration in the effluent in the range of 0.04-0.056 mg L^{-1} in the cycles 1, 5 and 10, followed for the both external magnetic separation systems with a range of Fe concentration between 0.067 and 0.311 mg L^{-1} in the reactor effluent.

The accumulation of NC over successive reuse cycles during the operation of the external rotary type of separation is the main drawback detected during use (4.25% of catalyst was retained inside the magnetic separation unit after ten cycles). However, the catalyst loss in the effluent does not exceed 1.95% (0.47% of Fe) in any case. This can be also attributed to the more stable dispersion of the NC and better separability compared to free mNPs (Zubir et al. 2014).

6.3.2 SBR coupled to the internal magnetic separation system as effective post-treatment of micropollutants in wastewater

Fenton-like oxidation experiments were scaled to a 5-L SBR combined with an internal pneumatic magnetic bar system, previously described in Section 6.2.2. The operation starts with an initial loading into the reaction tank of 2 L of secondary effluent from a WWTP at pH 3 and spiked with E1, E2, EE2, BPA, CBZ, IBP and SMX at an initial concentration of 350 µg L^{-1} (each) and in combination with 750 mg Fe L^{-1} of Fe_3O_4@PAA/SBA-15 NC and 400 mg L^{-1} of H_2O_2. The reuse of the NC in the magnetic reactor was evaluated in 5 catalytic cycles.

After each treatment, the NC was retained in the stirred glass reactor with the internal bar magnetic separator. Figure 6.8 shows the magnetic reactor system

before and after the magnetic nanocatalyst separation once the reaction is complete. The treated effluent was then discharged and a new fresh medium containing each contaminant was fed. Before starting the subsequent photodegradation process, the internal magnetic separator was removed, and the NC was re-dispersed in the medium, as previously described in Figure 6.1.

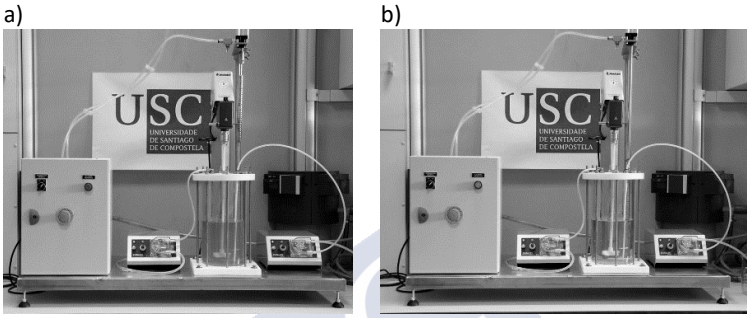

Figure 6.8 Magnetic catalytic reactor (5-L) before (a) and after (b) the introduction of the rod into the reactor. The system includes a peristaltic feeding pump, stirring unit, internal magnetic separator and pneumatic cylinder, peristaltic discharge pump and PLC.

After 6 h of reaction, full removal of IBP was obtained in all reaction cycles, while the transformation percentages achieved in the first cycle for the rest of the contaminants range relative low values (30.74-45.91%) compared to the successive oxidation cycles (Table 6.3). This can be attributed to the fresh NC stock which can be covered by excess silica dust or chemicals from the synthesis and that acts as a screen obstructing the contact between iron deposited in the NC and H_2O_2 to generate the ·OH radicals responsible for the oxidation reaction.

Table 6.3 Heterogeneous Fenton performance of Fe_3O_4@PAA/SBA-15 NC under optimal conditions in a magnetic reactor for the removal of E1, E2, EE2, BPA, CBZ, IBP and SMX (each at 3500 μg L^{-1}) after 2 h of residence time

Cycle	E1	E2	EE2	BPA	CBZ	IBP	SMX
1	41.18	30.74	45.47	45.91	34.28	100.00*	38.31
2	95.00	100.00*	81.99	71.43	66.61	100.00*	75.58
3	100.00*	100.00*	86.12	91.98	87.54	100.00*	87.41
4	84.66	100.00*	83.34	83.18	74.85	100.00*	90.32

5	87.66	100.00*	72.42	85.76	78.11	100.00*	n. d.**

*lower limit of detection (LOD) in the reactor effluent
**no data available

The transformation results indicate improved catalytic performance of the reactor in some cases with respect to the smaller scale (10 mL) experiments carried out in Chapter 4 for the removal of estrogens E1 (84.86%), E2 (88.18%) and EE2 (86.51%), BPA (58.29 %) and SMX (100%) under the same reaction conditions (350 µg L^{-1} of each contaminant, 750 mg Fe L^{-1} of Fe_3O_4@PAA/SBA-15 NC and 400 mg L^{-1} of H_2O_2). IBP is one of the most consumed non-steroidal anti-inflammatory drugs (NSAIDs) in the world, detected in WWTP effluents in concentrations reaching µ L^{-1} (Petrović et al. 2005).

Several reports have studied their removal from water through different treatments achieving relatively high removal rates, such as adsorption, ultrasonic irradiation, biodegradation, nanofiltration, coagulation-flocculation, ozonation and other advanced oxidation processes (AOPs) (Bhadra et al. 2017, Méndez-Arriaga et al. 2008, Joss et al. 2006, Vergili 2013, Vieno et al. 2006, Huber et al. 2003). In this sense, Adityosulindro et al. (2018) carried a far-reaching work, in which the elimination of IBP by Fenton heterogeneous catalysis reaches values of 88% after 3 hours of reaction, using Fe-zeolite (4.8 g L^{-1}), excess of H_2O_2 and pH 4.3. These experimental conditions implied a high concentration of catalyst and longer reaction time compared to the results of IBP elimination obtained in the present study.

From the second reuse cycle, an improvement in the elimination yield of all the selected microcontaminants has been achieved, reaching transformation values between 66.61 and 100%, with the lowest value corresponding to the CBZ elimination percentage (cycle 2). The highest transformation rates for almost all pollutant cases were obtained after cycle 3 of Fenton-like oxidation, where E1, E2 and IBP were not detected in the effluent (Figure 6.9).

Compared with the other selected contaminants removal results, EE2 (72.42-81.99%), CBZ (66.61-87.54%) and SMX (75.58-90.32%) reached high percentages, but to a lesser extent than E1 (95.00-100.00%, E2 (100.00%), BPA (71.43-91.98%) and IBP (100.00%) conversion starting from the second cycle (Table 6.3). This can be attributed to the different chemical structures and functional groups present, which

gives them a recalcitrant chemical character. For example, EE2 is a widely used synthetic estrogen present in contraceptive pills and has been reported to be more resistant than natural estrogens during elimination in water treatment (Hwang et al. 2008). Clouzot et al. (2008) investigated the biodegradation of EE2 and attribute the recalcitrant nature of the molecule to the addition of an ethyl group at position C17 on the parent molecule of the natural hormone E2.

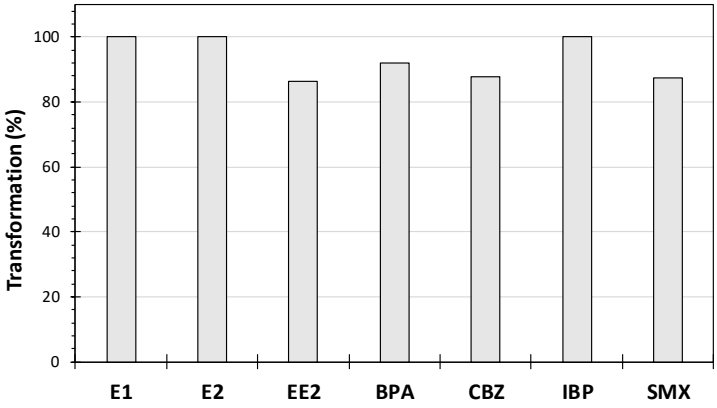

Figure 6.9 Transformation (%) of E1, E2, EE2, BPA, CBZ, IBP and SMX (each at 350 µg L^{-1}) after 2 h of heterogeneous Fenton treatment in the third cycle of an SBR operation.

Additionally, the attack of hydroxyl radicals produced by the reaction between H_2O_2 and ferrous ions (Fe^{2+}) is not unique to each compound, but is used in the degradation of the total mixture of the seven pollutants added and even to the organic matter present in the water matrix from the secondary effluent of the WWTP.

An important observation is the fact that the mineralization obtained in the third cycle did not decrease, with a TOC elimination of 12.31%. Thus, the composition of the remaining organic solution after 6 hours of treatment can be directed to the non-degraded pollutants or even to their by-products. Finally, Fe_3O_4@PAA/SBA-15 NCs was analyzed by SEM before and after its application in five different catalytic oxidation cycles. Figure 6.10 confirms that the change in NC morphology is negligible after five reuse cycles.

Therefore, the catalytic performance of Fe_3O_4@PAA/SBA-15 NC did not show a significant decrease of up to five cycles, demonstrating that it is possible to fully recover the catalyst by means of the magnetic field, which ensures reuse of the catalyst in different cycles and maintenance of a prolonged operation without the need to add a new catalyst.

a) b)

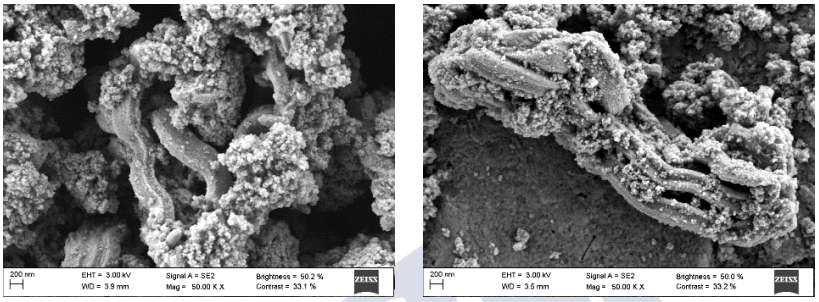

Figure 6.10 SEM images of Fe_3O_4@PAA/SBA-15 before (a) and after (b) five reuse cycles.

6.3.3 Photocatalytic magnetic SBR with internal magnetic separation system for the color removal of a model dye

The catalytic oxidation cycles of OII solution (25 mg L^{-1}) was carried out in sequential operated magnetic reactor at neutral pH (Figure 6.11). OII conversion was determined after continuous stirring for 2 h, and the results are shown in Figure 12. As can be seen in Figure 6.12, the OII transformation reached more than 65% for all oxidation cycles.

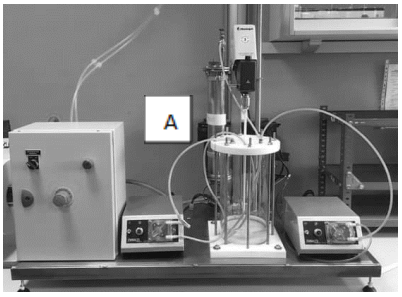

Figure 6.11 Magnetic photocatalytic reactor (5-L) comprising a photoreactor unit (A) with UVA lamp.

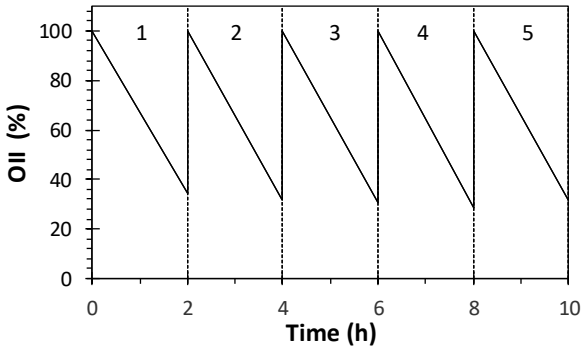

Figure 6.12 Decolorization yield in subsequent cycles of Fe_3O_4/ZnO heterogeneous photocatalysis treatment after 2 h for the color removal of OII (25 mg L^{-1}). Catalyst and H_2O_2 dosage of 100 mg L^{-1} and pH 7.

Compared to OII removal results obtained in Chapter 5, between 52.11 and 63.56% of OII decolorization, under the same catalyst and H_2O_2 concentrations (100 mg L^{-1}), an improvement of the results has been observed. This can be attributed to better matrix homogenization due to mechanical agitation and the fact that the radiation power measured for the photoreactor lamp was twice as high (4 mW cm^{-2}) as the radiation using the UVP Pen-Ray® lamp (1.57 mW cm^{-2}), which implies higher incident radiation per gram of photocatalyst.

6.4 Conclusions

This study aims to take a step forward in the application of nanostructured magnetic materials. Moreover, the retention of these novel particles after each reaction stage is mandatory, guaranteeing the discharge of the treated effluent free of contaminants.

A preliminary comparison between different magnetic reactors was provided, focusing on the development of effective magnetic separation units to solve the problem of magnetic nanocatalyst retention. Regarding the selection of best magnetic configuration technology, magnets array is a key parameter to increase magnetic retention. Results reveal that permanently aligned and coupled with alternating polarity magnets present a magnetic field capable of performing almost complete catalysts recovery. In this sense, the best configuration selected was the

internal separation device, which consists of a pneumatic cylinder with a magnetic bar inside the reactor, reaching almost complete retention of the employed magnetic nanocatalysts. Through the operation of this internal magnetic separation system coupled to an SBR, different oxidation assays were carried out by applying heterogeneous Fenton and photocatalysis as AOPs, demonstrating also the feasibility of reusing the selected catalysts for the treatment of highly compounds present in water.

6.5 References

Adityosulindro, S., Julcour, C. and Barthe, L. (2018) Heterogeneous Fenton oxidation using Fe-ZSM5 catalyst for removal of ibuprofen in wastewater. Journal of Environmental Chemical Engineering 6(5), 5920-5928.

Ahmari, H., Zeinali Heris, S. and Khayyat, M.H. (2018) Experimental investigation of new photocatalytic continuous coaxial cylinder reactor for elimination of linear alkylbenzene sulfonic acid from waste water using nanotechnology. Journal of Molecular Liquids 264, 165-171.

Arivizhivendhan, K., Mahesh, M., Boopathy, R. and Sekaran, G. (2016) A novel method for the extraction of prodigiosin from bacterial fermenter integrated with sequential batch extraction reactor using magnetic iron oxide. Process Biochemistry 51(10), 1731-1737.

Bhadra, B.N., Ahmed, I., Kim, S. and Jhung, S.H. (2017) Adsorptive removal of ibuprofen and diclofenac from water using metal-organic framework-derived porous carbon. Chemical Engineering Journal 314, 50-58.

Chen, G., Liu, J., Yao, J., Qi, Y. and Yan, B. (2017) Biodiesel production from waste cooking oil in a magnetically fluidized bed reactor using whole-cell biocatalysts. Energy Conversion and Management 138, 556-564.

Clouzot, L., Marrot, B., Doumenq, P. and Roche, N. (2008) 17α-Ethinylestradiol: An endocrine disrupter of great concern. Analytical methods and removal processes applied to water purification. A review. Environmental Progress 27(3), 383-396.

He, Z., Gao, C., Qian, M., Shi, Y., Chen, J. and Song, S. (2014) Electro-Fenton process catalyzed by Fe3O4 magnetic nanoparticles for degradation of CI Reactive Blue 19 in aqueous solution: operating conditions, influence, and mechanism. Industrial & Engineering Chemistry Research 53(9), 3435-3447.

Huber, M.M., Canonica, S., Park, G.Y. and Von Gunten, U. (2003) Oxidation of pharmaceuticals during ozonation and advanced oxidation processes. Environmental Science and Technology 37(5), 1016-1024.

Hwang, S., Lee, D.-I., Lee, C.-H. and Ahn, I.-S. (2008) Oxidation of 17α-ethinylestradiol with Mn (III) and product identification. Journal of Hazardous Materials 155(1-2), 334-341.

Joss, A., Zabczynski, S., Göbel, A., Hoffmann, B., Löffler, D., McArdell, C.S., Ternes, T.A., Thomsen, A. and Siegrist, H. (2006) Biological degradation of pharmaceuticals in municipal wastewater treatment: proposing a classification scheme. Water Research 40(8), 1686-1696.

Méndez-Arriaga, F., Torres-Palma, R., Pétrier, C., Esplugas, S., Gimenez, J. and Pulgarin, C. (2008) Ultrasonic treatment of water contaminated with ibuprofen. Water Research 42(16), 4243-4248.

Moldes-Diz, Y., Eibes, G., Vazquez-Vazquez, C., Fondado, A., Mira, J., Feijoo, G., Lema, J.M. and Moreira, M.T. (2018) A novel enzyme catalysis reactor based on superparamagnetic nanoparticles for biotechnological applications. Journal of Environmental Chemical Engineering 6, 5950-5960.

Ou, Z., Pan, J., Tang, L. and Shi, H. (2019) Continuous enantiomer-selective acylation reaction of 1-phenylethanamine in a magnetic fluidized bed reactor system (MFBRS). Journal of Chemical Technology & Biotechnology 94(6), 1951-1957.

Petrović, M., Hernando, M.D., Díaz-Cruz, M.S. and Barceló, D. (2005) Liquid chromatography–tandem mass spectrometry for the analysis of pharmaceutical residues in environmental samples: a review. Journal of Chromatography A 1067(1), 1-14.

Tang, S.C. and Lo, I.M. (2013) Magnetic nanoparticles: essential factors for sustainable environmental applications. Water Research 47(8), 2613-2632.

Vergili, I. (2013) Application of nanofiltration for the removal of carbamazepine, diclofenac and ibuprofen from drinking water sources. Journal of Environmental Management 127, 177-187.

Vieno, N., Tuhkanen, T. and Kronberg, L. (2006) Removal of pharmaceuticals in drinking water treatment: effect of chemical coagulation. Environmental Technology 27(2), 183-192.

Wang, N., Zhang, X., Wang, Y., Yu, W. and Chan, H.L.W. (2014) Microfluidic reactors for photocatalytic water purification. Lab on a Chip 14(6), 1074-1082.

Zhou, C., Wang, B., Ma, C., Song, Z., Zeng, Z., Xiang, J., Hu, S., Su, S. and Sun, L. (2015) Gaseous elemental mercury removal through heterogeneous Fenton-like processes using novel magnetically separable $Cu_{0.3}Fe_{2.7-}$ $xTixO_4$ catalysts. Fuel 161, 254-261.

Zubir, N.A., Yacou, C., Motuzas, J., Zhang, X. and Da Costa, J.C.D. (2014) Structural and functional investigation of graphene oxide-Fe_3O_4 nanocomposites for the heterogeneous Fenton-like reaction. Scientific Reports 4, 4594.

6.6 Annex

Table A6.1 Composition of the secondary effluent

Parameter	Value
Chemical oxygen demand (**COD**)	86.2 mg L^{-1}
Total organic carbon (**TOC**)	8.58 mg L^{-1}
Total nitrogen (**TN**)	2.33 mg L^{-1}
Total suspended solids (**TSS**)	0.08 mg mL^{-1}
pH	6.98
Conductivity	104.7 µS cm^{-1}
Cations	
K^+	4.71 mg L^{-1}
Mg^{2+}	2.068 mg L^{-1}
Ca^{2+}	6.89 mg L^{-1}
Na^+	16.75 mg L^{-1}
NH_4^+	0.75 mg L^{-1}
Anions	
Cl^-	14.18 mg L^{-1}
NO^{2-}	0.06 mg L^{-1}
Br^-	0.37 mg L^{-1}
NO^{3-}	3.29 mg L^{-1}
PO_4^{3-}	2.21 mg L^{-1}
SO_4^{2-}	9.86 mg L^{-1}

USC
UNIVERSIDADE
DE SANTIAGO
DE COMPOSTELA

7. Chapter 7

NANOCATALYSTS TOXICITY ASSESSMENT

SUMMARY

Nanoparticles are not only chemical entities with a specific chemical composition, but can also undergo transformations in the environment. Accordingly, it is necessary to determine the different species formed in order to understand and predict their behavior and effects. This is why the strategy for the use of synthetic nanoparticles must respond to the potential associated impacts, especially in the area of risk assessment. Within the context of toxicity, the need for analytical methods for the detection, characterization and quantification of these released species becomes evident. In this study, the potential geno and cytotoxicity of nanosized magnetic iron-based oxide particles used in the treatment of contaminated effluents through chemical catalysis processes such as Fenton reaction or photocatalysis was investigated using simple methods for the quantitative evaluation of DNA degradation and human cells metabolism disorder. The selected magnetic nanoparticles (mNPs) were free and immobilized onto silica mesoporous SBA-15 magnetite (Fe_3O_4), silica, poly (acrylic acid) and polyethylenimine coated magnetite (Fe_3O_4@SiO_2, Fe_3O_4@PAA and Fe_3O_4@PEI) and two different magnetic nanocomposites (mNCs) with titanium dioxide (TiO_2) and zinc oxide (ZnO). The results obtained highlight the need to act with caution during the use and recovery of these nanomaterials manufactured on the basis of the results observed in terms of DNA oxidation and cell damage. This chapter was developed thanks to a research stay at the Centre of Biotechnology and Fine Chemistry (CBQF), Faculty of Biotechnology in Universidade Católica Portuguesa (Porto, Portugal).

OUTLINE

7.1 Introduction

In the last decade, research has increased with the application of engineering nanomaterials to the treatment of industrial wastewater by means of different advanced oxidation processes (AOPs) such as heterogeneous Fenton oxidation or heterogeneous photocatalysis have been carried out (Munoz et al. 2015, Farrokhi et al. 2014). Moreover, the use of magnetic nanoparticles based on iron oxide as solid catalysts present great advantages, such as unique magnetic properties that allow easy recovery and reuse when applying a magnetic field, as it has been mentioned throughout the previous chapter. However, these heterogeneous processes must guarantee the complete retention of these nanoparticles and prevent their leaching, as it has been mentioned throughout the previous chapters.

Numerous studies summarize the current understanding of toxicity of engineered nanoparticles to representatives of various trophic levels, including bacteria, plants, and multicellular aquatic/terrestrial organisms, to highlight important challenges within the field of econanotoxicity (Maurer-Jones et al. 2013, Sharma et al. 2014, Monikh et al. 2019, Liu and Tang 2020). Moreover different works have focused on the investigation of the potential toxicity to human health associated with these nanomaterials (Marambio-Jones and Hoek 2010, Oberdörster et al. 2005). Based on an evaluation of the limited data currently available, Oberdörster et al. (2005) present a broad data gathering strategy in the development of a risk assessment process for nanomaterials. This study includes oral, dermal, inhalation, and injection routes depending on use patterns, considering the physicochemical characteristics, *in vitro* and *in vivo* assays as key parameters of the toxicity detection strategy.

Nevertheless, the study of the potential ecological risks of the release of nanomaterials into the environment is a necessary and complementary research area in the perspective of risk analysis. In this sense, one of the most significant reported methods for estimating the potential effects of NP is an *in vitro* assay capable of measuring DNA degradation by electrophoresis (Rivero et al. 2005). Another parameter is the evaluation of cytotoxicity, in which possible cytotoxic agents are tested by determining the number of living cells using the 2,3-bis-(2-methoxy-4-nitro5-sulfophenyl)-2H-tetrazolium-5-carboxanilide sodium salt (XTT)

colorimetric assay (Roehm et al. 1991, Janus et al. 2019). Therefore, the present study compares different magnetite-based nanocatalysts previously studied in Chapters 4-5, in order to investigate the impact that the physicochemical properties of these nanocatalysts can cause after direct exposure with a specific DNA solution and on the mitochondrial cell function of two different human cell lines before their accumulation or penetration into the membrane.

7.2 Materials and methods

7.2.1 Nanostructured catalysts

Selected Fenton-like and photocatalysts (listed in Table 7.1) were previously described in Chapters 4-5.

Table 7.1 Magnetic nanoparticles (mNPs) and nanocomposites (mNCs) characteristics.

	Catalyst	Characteristics
Fenton catalysts (Chapter 4)	Fe_3O_4	Magnetite magnetic nanoparticles (mNPs) stabilized in TMAOH
	Fe_3O_4@SiO_2	Silica coated magnetite mNPs
	Fe_3O_4@PAA	Magnetite stabilized with Poly (acrylic acid) (PAA) mNPs
	Fe_3O_4@PEI	Polyethylenimine (PEI; 25 kDa) coated magnetite mNPs
	Fe_3O_4@SiO_2/SBA-15	Silica coated mNPs supported onto SBA-15
	Fe_3O_4@C/SBA-15	Fe_3O_4@C mNPs functionalized with carboxylic groups supported onto SBA-15
	Fe_3O_4@PAA/SBA-15	PAA-coated mNPs supported onto SBA-15
	Fe_3O_4@PEI/SBA-15	PEI-coated mNPs supported onto SBA-15
Photocatalysts (Chapter 5)	Fe_3O_4/TiO_2	Titanium dioxide magnetic nanocomposite (mNC)
	Fe_3O_4/ZnO	Zinc oxide mNC
	TiO_2	Titanium dioxide NPs
	ZnO	Zinc oxide NPs

Table 7.2 summarize the size and zeta potential values of the chosen catalysts corresponding to the working pH of geno and cytotoxicity assays.

Table 7.2 Size and zeta potential of nanostructured catalysts at pH 7

	Catalyst	Size* (nm)	Zeta potential (mV)
Fenton catalysts	Fe_3O_4	8.2	-45.2
	Fe_3O_4@SiO_2	20	-24.2
	Fe_3O_4@PAA	7.6	-40.1
	Fe_3O_4@PEI	10.9	4.7
	Fe_3O_4@SiO_2/SBA-15	-	-20.65
	Fe_3O_4@C/SBA-15	-	-31.96
	Fe_3O_4@PAA/SBA-15	-	-24.04
	Fe_3O_4@PEI/SBA-15	-	2.89
Photocatalysts**	Fe_3O_4/TiO_2	150-250	-40.7
	Fe_3O_4/ZnO	200-300	-38.5
	TiO_2	40-45	-21.6
	ZnO	10-15	-25.9

*Catalysts average diameter were previously estimated in Chapter 4 and 5 (Characterization results section) for Fenton catalyst and photocatalysts, respectively.

**Photocatalyst zeta potential values were previously calculated in Chapter 5 at pH 7

***SBA-15 mesoporous silica matrix presents an average diameter between 1-2 µm.

7.2.2 Genotoxicity assay

An *in vitro* assay was performed to determine DNA degradation by electrophoresis testing (Silva et al. 2017). The test consists of direct exposure of the selected nanomaterials (Table 7.1) with a specific DNA solution to estimate the pro-oxidant effects of this nanocomposite. DNA from the calf thymus (Sigma, Germany) at 0.025 mg mL^{-1} was prepared and stored at 4°C for up to seven days. This DNA solution was incubated in the presence of different concentrations of the selected catalysts (0.0125-1 g L^{-1}) for 1 h at 37 °C, prior to the electrophoresis assay. A positive DNA control (without catalyst) was also performed in a parallel test.

Samples of each DNA-nanocatalyst solution (10 µL) were mixed with loading buffer (1:4; 25 mg bromophenol blue, 10 mL Tris-EDTA 1x buffer and 20 mL of glycerol; pH 8) and the electrophoresis test was performed on 0.75% (w v^{-1}) agarose gel (Nztech, Portugal) prepared with Tris-Acetate-EDTA buffer (TAE; Grisp, Portugal) and 0.03 µL mL^{-1} of GreenSafe Premium (Nztech, Portugal). Tests were conducted over 1.25 h at 150 mV in PowerPac Universal (BioRad, USA). The resulting DNA bands

were determined using a molecular imager GelDOC XR+ (BioRad, USA) and analysed with Image Lab™ Software v5.1. The results were expressed as the percentage of DNA inhibition, calculated as follows,

$$\text{DNA degradation (\%)} = 100 - \frac{\text{Intensity}_{\text{sample}}}{\text{Intensity}_{\text{DNA control}}} \text{ x } 100 \quad (1)$$

where $\text{Intensity}_{\text{sample}}$ is the intensity of the band area of each sample and $\text{Intensity}_{\text{DNA-control}}$ is the intensity measured manually from the control band of the DNA solution. To ensure reproducibility of the assay, a duplicate of the sample DNA solution was performed in each case. In addition, the electrophoresis band sample was carried out in duplicate, obtaining four replicates for each sample evaluated.

7.2.3 *In vitro* cytotoxicity assay

In order to investigate the impact that different concentrations (0.05-1 g L^{-1}) of the selected nanocatalyst (Table 7.1) have on the metabolic activity of cells, two different human cell lines were considered: HaCaT from human Keratinocytes and Caco2 from human colonic Epithelial, using the colorimetric assay based on 2,3-bis-(2-methoxy-4-nitro5-sulfophenyl)-2H-tetrazolium-5-carboxanilide sodium salt (XTT). The tests were conducted as previously described by Machado et al. (2012), with minor modifications. Each sample (100 µL) prepared in phosphate buffered saline (PBS) was incubated for 24 h at 37°C in a CO_2 incubator on a well-microplate and in the presence of both cell lines (HaCaT and Caco2) separately. Then, 25 µL of XTT solution was introduced directly into each well and incubated again under the same previous conditions for 2 h. All experiments were carried out in quintuplicate.

Finally, orange colour from reduced XTT was quantified by spectrophotometric analysis using optical density measurements at 485 nm (OD_{485}), in a well-microplate reader (FLUOstar Optima, BMG Labtech, USA). A positive control test was performed using a culture medium without nanocatalysts and another with selected mNPs and mNCs and without cells. The results were expressed as a percentage of metabolic inhibition described above by Silva et al. (2016), expressed as follows,

$$\text{Inhibition (\%)} = 100 - \frac{\text{OD}_{\text{sample}}}{\text{OD}_{\text{positive control}}} \text{ x } 100 \quad (2)$$

where OD_{sample} is the optical density of each sample and $OD_{positive\text{-}control}$ is the optical density from the control band of the DNA solution.

7.3 Results and discussion

7.3.1 Genotoxicity

The results of DNA degradation after incubation in the presence of different nanostructured catalysts are displayed in Figures 7.1-7.33. The results obtained indicate that, in general, minor DNA alterations were observed (less than 14.63% in all cases). In the case of magnetite-based nanoparticles (mNPs; Figure 7.1), the highest degradation percentages were obtained for Fe_3O_4@SiO_2 with 11.15% DNA degradation for a nanoparticle concentration of 0.025 g L^{-1}.

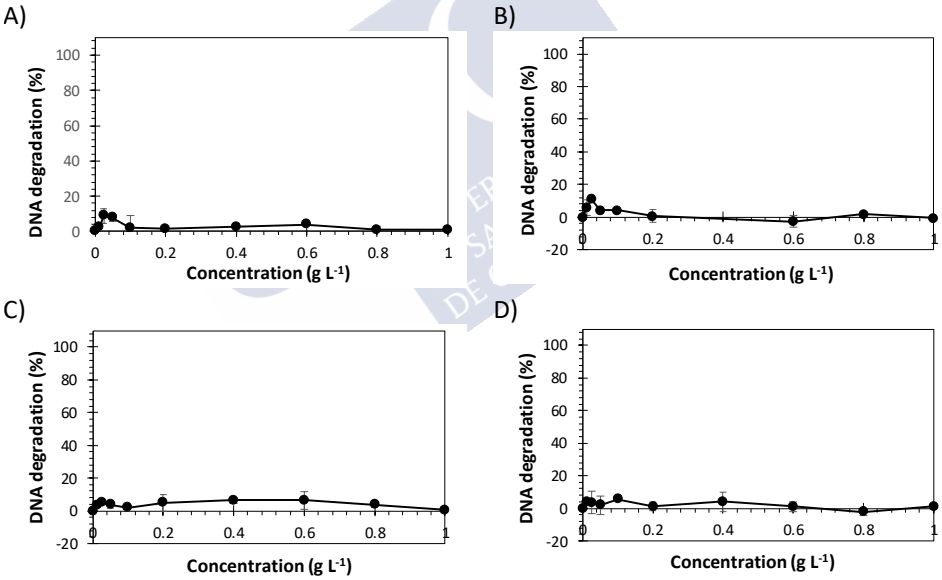

Figure 7.1 Relative effect of DNA degradation caused by A) Fe_3O_4-TMAOH, B) Fe_3O_4@SiO_2, C) Fe_3O_4@PAA and D) Fe_3O_4@PEI mNPs exposure at a concentration of 0.0125-1 g L^{-1}.

At low concentrations (0.0125-0.05 g L^{-1}), Fe_3O_4 mNPs also have a negative effect on DNA stability. In the case of the magnetite covered with the different

stabilizers (PAA and PEI), a similar effect was observed. In addition, in the case of PAA mNPs, damage alterations were also observed at intermediate concentrations (0.2-0.8 g L^{-1}) but with DNA degradation values lower than 6.38% in all cases.

With respect to magnetic mesoporous silica NCs (SBA-15 NCs), DNA alterations were detected both at low concentrations (0.0125-0.05 g L^{-1}) and intermediate concentrations (Figure 7.2); between 0.1 and 0.2 g L^{-1} for Fe_3O_4@SiO_2/SBA-15 reaching DNA degradation values of 9.14% for 0.1 g L^{-1}. For Fe_3O_4@PAA/SBA-15, a higher DNA degradation was observed at 0.6 g L^{-1} with a percentage of 7.17%, while in the case of Fe_3O_4@PEI/SBA-15 NCs DNA degradation reaches the maximum value for the highest concentration (14.63% at 1 g L^{-1}). Therefore, the effect of nanoparticle concentration on increased DNA degradation was detected.

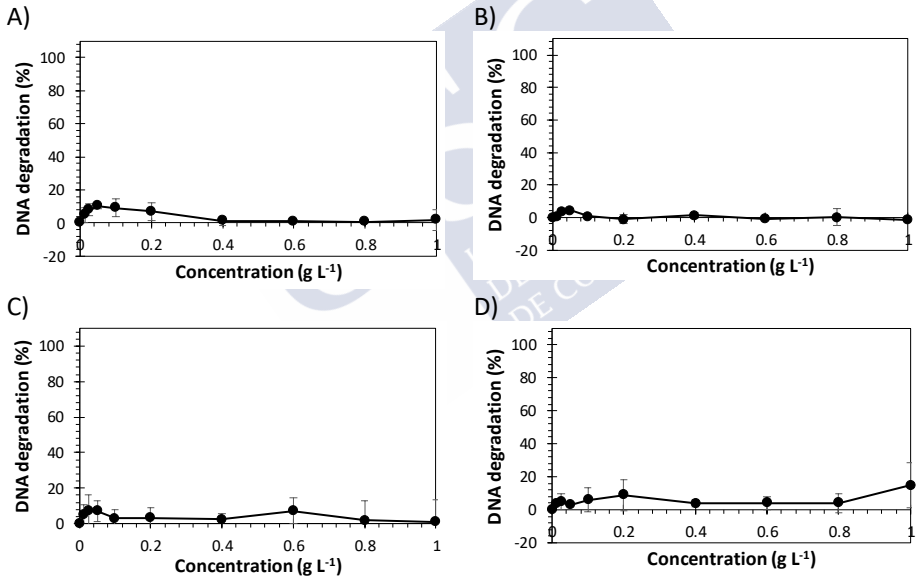

Figure 7.2 Relative effect of DNA degradation caused by A) Fe_3O_4@SiO_2/SBA-15, B) Fe_3O_4@C/SBA-15, C) Fe_3O_4@PAA/SBA-15 and D) Fe_3O_4@PEI/SBA-15 mNCs exposure in a concentration of 0.0125-1 g L^{-1}.

Finally, Figure 7.3 shows the results of DNA degradation after incubation in the presence of selected nanophotocatalyst (Fe_3O_4/TiO_2, Fe_3O_4/ZnO, TiO_2 and ZnO) at concentration between 0.0125 and 1 g L^{-1}.

Minor DNA alterations were observed at low (0.0125-0.025 g L^{-1}) and intermediate concentrations (0.2-0.4 g L^{-1}) for Fe_3O_4/ZnO NC, reaching the highest rate of DNA degradation (8.73%) at a concentration of 0.0125 g L^{-1}. While for Fe_3O_4/TiO_2 NC and both TiO_2 and ZnO NPs, negligible DNA damage was observed within the concentration range studied (less than 5% of DNA degradation). From these results, for a concentration of 0.1 g L^{-1} of Fe_3O_4/ZnO (operational conditions previously established in Chapter 5 as optimal NC concentration and applied for the operation of the magnetic sequential batch reactor (SBR)), no significant DNA degradation (1.56%) was observed.

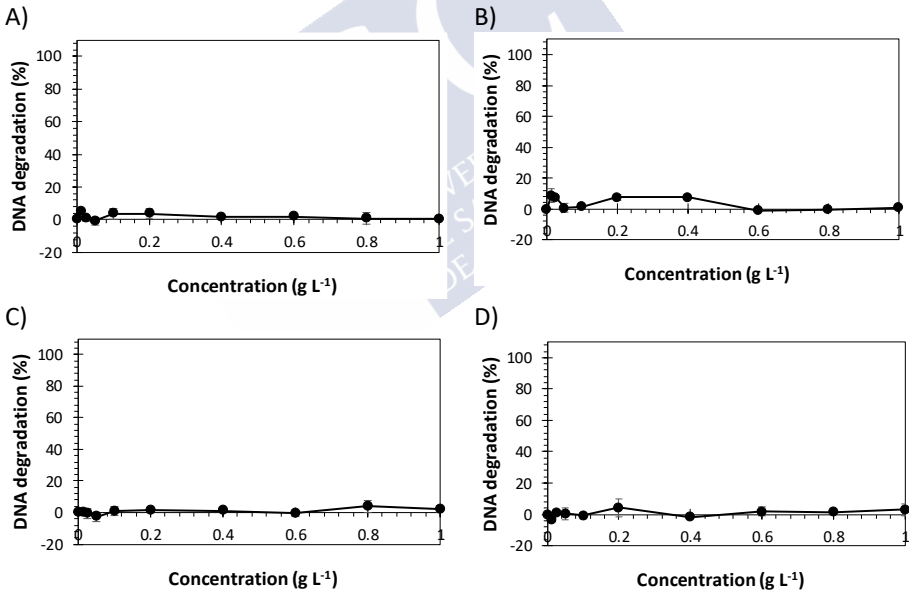

Figure 7.3 Relative effect of DNA degradation caused by A) Fe_3O_4/TiO_2, B) Fe_3O_4/ZnO, C) TiO_2 and D) ZnO nanocatalysts exposure in a concentration of 0.0125-1 g L^{-1}.

Therefore, safety considerations of Fe_3O_4/ZnO and Fe_3O_4@PAA/SBA-15, which were selected in Chapters 4 and 5 as promising catalysts for Fenton-like and

photocatalysis processes, were evaluated by studying their potential genotoxicity. Using optimal concentrations of 0.1 g L^{-1} of Fe_3O_4/ZnO and 3.12 g L^{-1} of Fe_3O_4@PAA/SBA-15 mNC (750 mg Fe L^{-1}) for its prospective application in the magnetic SBR, it can be considered that there is no significant DNA degradation.

7.3.2 Cytotoxicity

The XTT cell proliferation colorimetric assay is a widely used quantitative method for the evaluation of potential cytotoxic agents by determining the number of living cells. External agents can induce damage to cell membranes and lead to interruption of the respiratory chain, resulting in the inactivation of the dehydrogenase mitochondrial enzymatic system and cell death. Only mitochondria of viable cells are capable of reducing XTT to form an orange coloured water-soluble dye by reducing tetrazolium salt. The number of active metabolic cells is proportional to the absorbance of the dye, spectrophotometrically measured. Cell viability was calculated as the ratio of the OD_{485} mean obtained for each sample to that of the positive control (equation 2).

The toxicity results obtained for the mNPs (Fe_3O_4, Fe_3O_4@PAA, Fe_3O_4@SiO_2 and Fe_3O_4@PEI XTT assays at different concentrations (0.0125-1 g L^{-1}) after their incubation with two different human cell lines (HaCaT and Caco2) are depicted in Figure 7.4.

Several studies have reported the use of different model cell lines (A431, HeLa, HepG2) to investigate the cytotoxicity of NPs and their underlying molecular mechanisms (Kaur and Tikoo 2013, Lankoff et al. 2012, Foldbjerg et al. 2011). Most of these studies were carried out using the MTT assay based on the use of tetrazolium salt (3-(4,5-dimethyl-2-thiazolyl)-2,5-diphenyl tetrazolium bromide) for the mitochondrial activity measurement.

Nonetheless, this method has a critical drawback, the insoluble formazan produced, which requires dissolution of the dye to measure it, as XTT produces a soluble dye that simplifies the process. Caco2 is an intestinal human cell line derived from a colon adenocarcinoma, while HaCaT is a spontaneously immortalized human epithelial cell line from adult skin. The results are expressed as a percentage of metabolic inhibition in mitochondrial function for both cell lines.

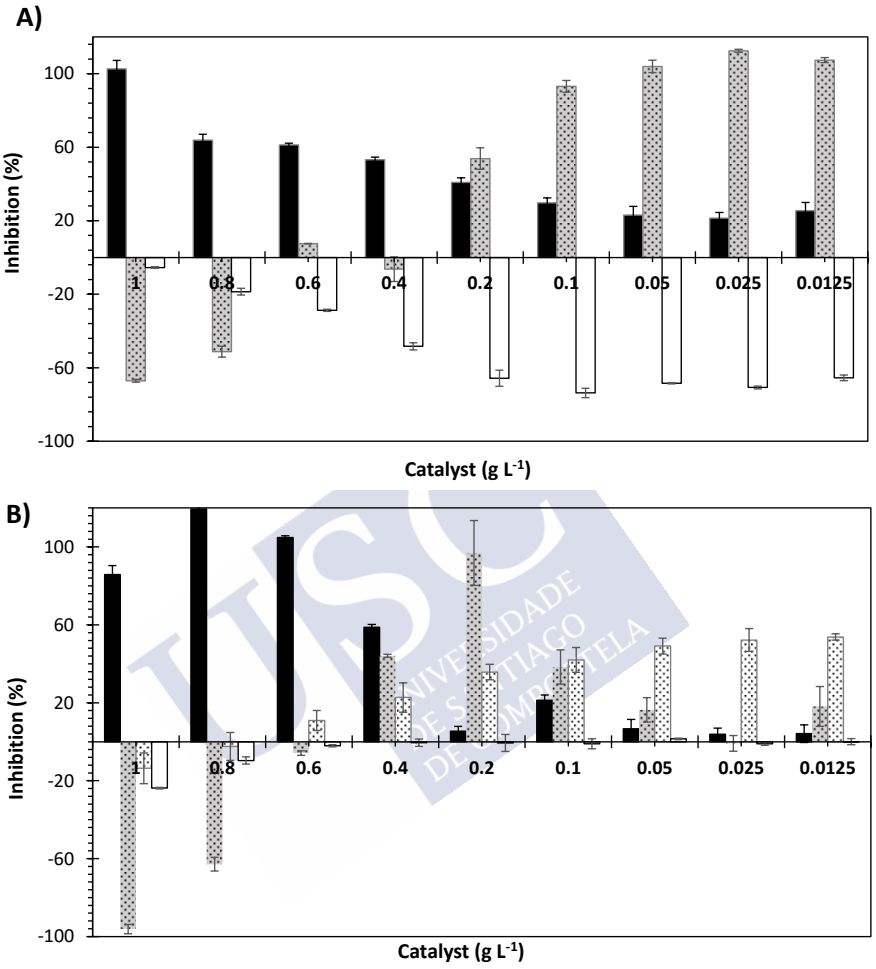

Figure 7.4 Inhibitory effect (%) of Fe_3O_4-TMAOH (black bars), Fe_3O_4@PAA (gray dot bars), Fe_3O_4@SiO_2 (white dot bars) and Fe_3O_4@PEI (white bars) mNPs on mitochondrial activity of the HaCaT cell line (A) and the Caco2 cell line (B), exposed to different concentrations (0.0125-1 g L^{-1}) during 24 h and measured by the colorimetric XTT assay.

Figure 7.4 shows an inhibitory effect on cell metabolism caused mainly by Fe_3O_4 mNPs. Metabolic inhibition increases as the concentration of mNPs increases for

both cell lines HaCaT and Caco2, achieving 100% metabolic inhibition at the highest concentration values. In the case of Fe_3O_4@PAA mNPs, for both cell cultures, high inhibition percentages are obtained at low catalyst concentrations, while at low concentration values an opposite trend can be observed, achieving negative inhibition values.

Fe_3O_4@SiO_2 mNPs show a similar trend, but to a lesser extent (Figure 7.4). For Fe_3O_4@PEI, only an increase in metabolic activity was detected as the concentration of nanostructured catalyst decreased. This effect can be attributed to the PEI polymer stabilizer, which contributes to the cellular activity of HaCaT, while for Caco2 it seems to have no effect.

Mesoporous silica structured catalyst results are depicted in Figure 7.5. In general, mNCs have an inhibitory effect on HaCaT cells, reaching values of 67.79%, corresponding to Fe_3O_4@C/SBA-15 at the lowest concentration (0.0125 g L^{-1}) (Figure 7.5). Fe_3O_4@PEI/SBA-15 mNC also present a negative effect on HaCaT cell metabolism, reaching the highest values (22.91-47.52%) at high concentrations (0.05-1 g L^{-1}). For the rest of mNCs, there is hardly any inhibitory effect on HaCaT metabolism.

For the Caco2 cell line, the tendency to increase the percentage of metabolic inhibition is maintained as the concentration increases in the case of Fe_3O_4@PEI/SBA-15 mNC. In addition, an increase in inhibition is also observed at low concentrations of Fe_3O_4@SiO_2/SBA-15 (0.0125-0.1 g L^{-1}), while at high concentrations even negative values are obtained. The rest of mNCs do not seem to have a remarkable effect on this cell line, with values below 5.97% (Figure 7.5).

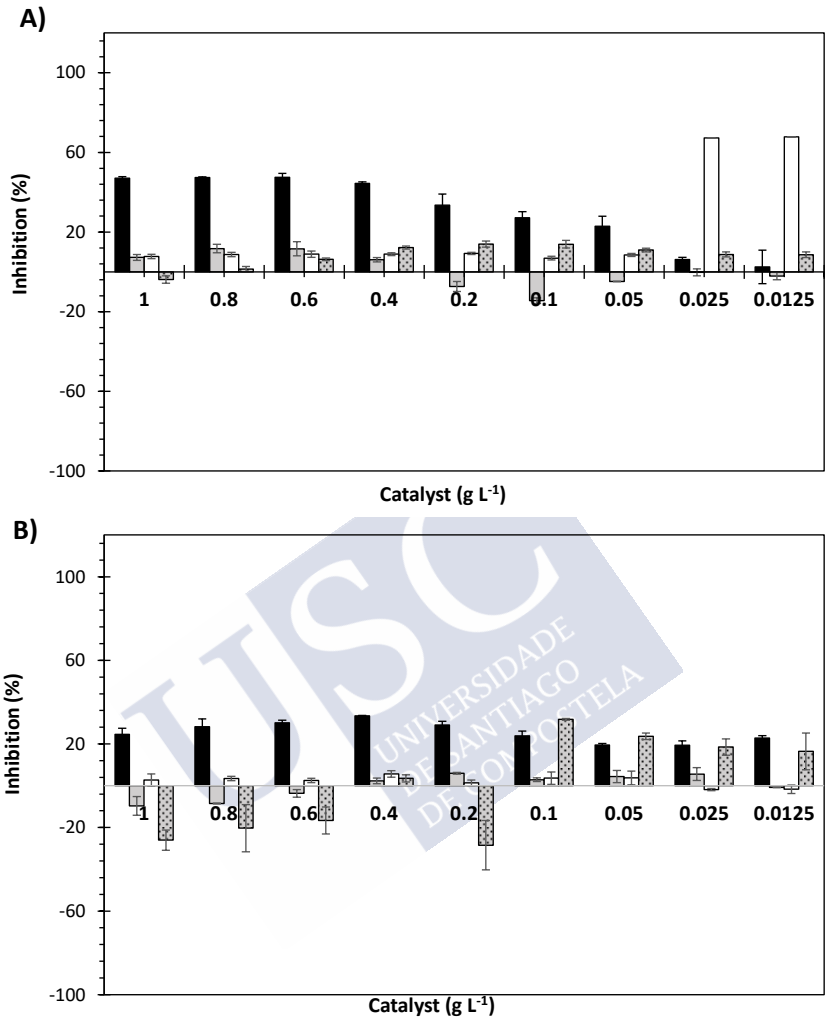

Figure 7.5 Inhibitory effect (%) of Fe_3O_4@PEI/SBA-15 (black bars), Fe_3O_4@PAA/SBA-15 (gray bars), Fe_3O_4@C/SBA-15 (white bars) and Fe_3O_4@SiO_2/SBA-15 (gray dot bars) mNCs on mitochondrial activity of the HaCaT cell line (A) and the Caco2 cell line (B), exposed to different concentrations (0.0125-1 g L^{-1}) for 24 h and measured by the colorimetric XTT assay.

Finally, Figure 7.6 shows the results obtained for the photocatalysts (TiO_2, ZnO, Fe_3O_4/TiO_2 and Fe_3O_4/ZnO) in a range of concentrations between 0.05-1 g L^{-1}. Both

TiO_2 and ZnO NPs and Fe_3O_4/TiO_2 mNC show no metabolic inhibition in HaCaT and Caco2 cells, while Fe_3O_4/ZnO NCs revealed toxic effects at all NCs doses (0.05-1 g L^{-1}) to a certain extent, ranging from 10.30 to 22.41% of metabolic inhibition.

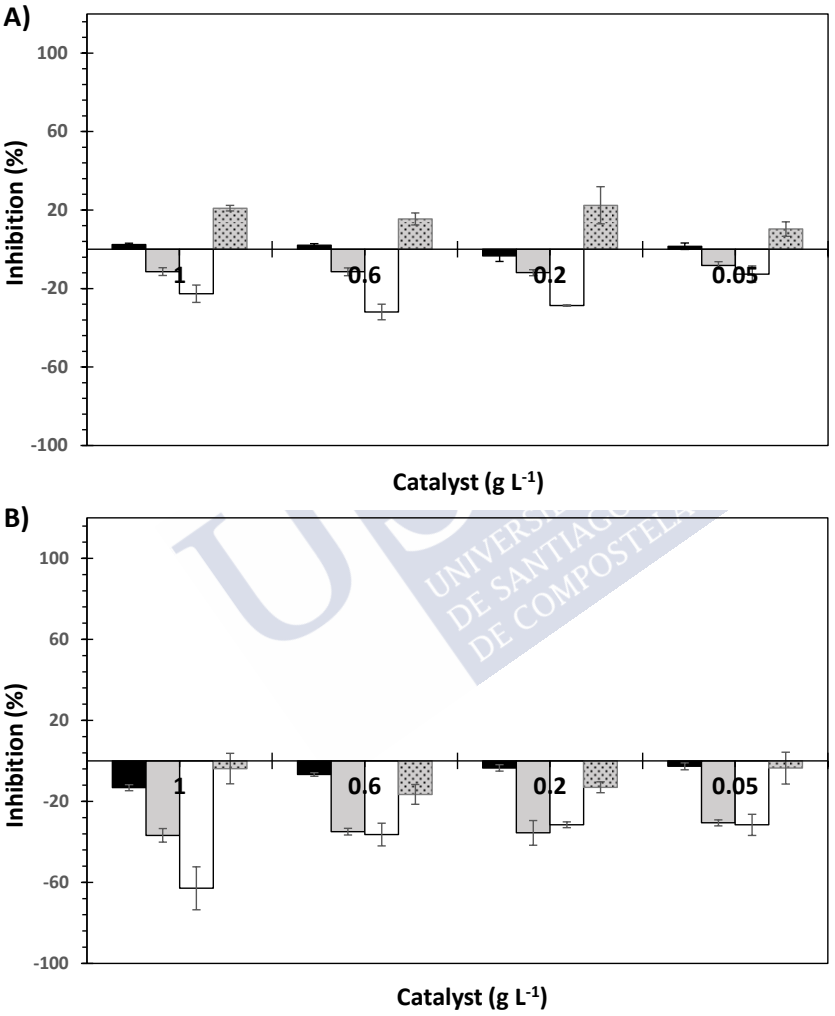

Figure 7.6 Inhibitory effect (%) of TiO_2 (black bars), ZnO (gray bars), Fe_3O_4/TiO_2 (white bars) and Fe_3O_4/ZnO (gray dot bars) nanophotocatalysts on mitochondrial activity of the HaCaT cell line (A) and the Caco2 cell line (B), exposed to different concentrations (0.05-1 g L^{-1}) for 24 h and measured by colorimetric XTT assay.

These findings point that the presence of magnetite in combination with ZnO induces an increase in the metabolic inhibition of HaCaT cells. On the other hand, neither of the two catalysts shows metabolic inhibition in Caco2 cells. On the contrary, experimental data suggest that all the nanostructured catalysts studied induce a growth of cellular metabolic activity in the Caco2 cell line, reaching negative values of metabolic activity in the range of 2.68-62.92% for all concentrations of NPs. From the viability study of Caco2 cells, a greater trend in metabolic activity can be observed as the concentration of catalysts increases, while in HaCaT cells the activity seems to be quite stable in each case.

7.4 Conclusions

The production and use of engineered nanoparticles has continued to increase in recent years, making environmental release almost certain. Therefore, recent efforts to characterize the toxicity of engineered nanoparticles have focused on environmental implications. In this sense, this work contributes to the understanding of the potential effects on genotoxicity and cytotoxicity of different nanostructured magnetite-based catalysts in a wide range of concentrations. Therefore, this study underlines the importance of further research on the mechanisms and factors that increase toxicity to improve the use of nanomaterials and awareness of their disposal.

7.5 References

Farrokhi, M., Hosseini, S.-C., Yang, J.-K. and Shirzad-Siboni, M. (2014) Application of ZnO–Fe_3O_4 nanocomposite on the removal of azo dye from aqueous solutions: kinetics and equilibrium studies. Water, Air, & Soil Pollution 225(9), 2113.

Farrokhi, M., Hosseini, S.-C., Yang, J.-K. and Shirzad-Siboni, M. (2014) Application of ZnO-Fe_3O_4 nanocomposite on the removal of azo dye from aqueous solutions: kinetics and equilibrium studies. Water, Air, & Soil Pollution 225(9), 2113.

Foldbjerg, R., Dang, D.A. and Autrup, H. (2011) Cytotoxicity and genotoxicity of silver nanoparticles in the human lung cancer cell line, A549. Archives of Toxicology 85(7), 743-750.

Foldbjerg, R., Dang, D.A. and Autrup, H. (2011) Cytotoxicity and genotoxicity of silver nanoparticles in the human lung cancer cell line, A549. Archives of Toxicology 85(7), 743-750.

Janus, Ł., Piątkowski, M., Radwan-Pragłowska, J., Bogdał, D. and Matysek, D. (2019) Chitosan-based carbon quantum dots for biomedical applications: synthesis and characterization. Nanomaterials 9(2), 274.

Janus, Ł., Piątkowski, M., Radwan-Pragłowska, J., Bogdał, D. and Matysek, D. (2019) Chitosan-based carbon quantum dots for biomedical applications: Synthesis and characterization. Nanomaterials 9(2), 274.

Kaur, J. and Tikoo, K. (2013) Evaluating cell specific cytotoxicity of differentially charged silver nanoparticles. Food and Chemical Toxicology 51, 1-14.

Kaur, J. and Tikoo, K. (2013) Evaluating cell specific cytotoxicity of differentially charged silver nanoparticles. Food and Chemical Toxicology 51, 1-14.

Lankoff, A., Sandberg, W.J., Wegierek-Ciuk, A., Lisowska, H., Refsnes, M., Sartowska, B., Schwarze, P.E., Meczynska-Wielgosz, S., Wojewodzka, M. and Kruszewski, M. (2012) The effect of agglomeration state of silver and titanium dioxide nanoparticles on cellular response of HepG2, A549 and THP-1 cells. Toxicology Letters 208(3), 197-213.

Lankoff, A., Sandberg, W.J., Wegierek-Ciuk, A., Lisowska, H., Refsnes, M., Sartowska, B., Schwarze, P.E., Meczynska-Wielgosz, S., Wojewodzka, M. and Kruszewski, M. (2012) The effect of agglomeration state of silver and titanium dioxide nanoparticles on cellular response of HepG2, A549 and THP-1 cells. Toxicology Letters 208(3), 197-213.

Liu, N. and Tang, M. (2020) Toxic effects and involved molecular pathways of nanoparticles on cells and subcellular organelles. Journal of Applied Toxicology 40(1), 16-36.

Liu, N. and Tang, M. (2020) Toxic effects and involved molecular pathways of nanoparticles on cells and subcellular organelles. Journal of Applied Toxicology 40(1), 16-36.

Machado, I., Lopes, S.P., Sousa, A.M. and Pereira, M.O. (2012) Adaptive response of single and binary Pseudomonas aeruginosa and Escherichia coli biofilms to benzalkonium chloride. Journal of Basic Microbiology 52(1), 43-52.

Machado, I., Lopes, S.P., Sousa, A.M. and Pereira, M.O. (2012) Adaptive response of single and binary Pseudomonas aeruginosa and Escherichia coli biofilms to benzalkonium chloride. Journal of Basic Microbiology 52(1), 43-52.

Marambio-Jones, C. and Hoek, E.M. (2010) A review of the antibacterial effects of silver nanomaterials and potential implications for human health and the environment. Journal of Nanoparticle Research 12(5), 1531-1551.

Marambio-Jones, C. and Hoek, E.M. (2010) A review of the antibacterial effects of silver nanomaterials and potential implications for human health and the environment. Journal of Nanoparticle Research 12(5), 1531-1551.

Maurer-Jones, M.A., Gunsolus, I.L., Murphy, C.J. and Haynes, C.L. (2013) Toxicity of engineered nanoparticles in the environment. Analytical Chemistry 85(6), 3036-3049.

Maurer-Jones, M.A., Gunsolus, I.L., Murphy, C.J. and Haynes, C.L. (2013) Toxicity of engineered nanoparticles in the environment. Analytical Chemistry 85(6), 3036-3049.

Monikh, F.A., Chupani, L., Vijver, M.G., Vancová, M. and Peijnenburg, W.J. (2019) Analytical approaches for characterizing and quantifying engineered nanoparticles in biological matrices from an (eco) toxicological perspective: old challenges, new methods and techniques. Science of the Total Environment 660, 1283-1293.

Monikh, F.A., Chupani, L., Vijver, M.G., Vancová, M. and Peijnenburg, W.J. (2019) Analytical approaches for characterizing and quantifying engineered nanoparticles in biological matrices from an (eco) toxicological perspective: old challenges, new methods and techniques. Science of the Total Environment 660, 1283-1293.

Munoz, M., de Pedro, Z.M., Casas, J.A. and Rodriguez, J.J. (2015) Preparation of magnetite-based catalysts and their application in heterogeneous Fenton oxidation - A review. Applied Catalysis B: Environmental 176-177, 249-265.

Munoz, M., de Pedro, Z.M., Casas, J.A. and Rodriguez, J.J. (2015) Preparation of magnetite-based catalysts and their application in heterogeneous Fenton oxidation - A review. Applied Catalysis B: Environmental 176-177, 249-265.

Oberdörster, G., Maynard, A., Donaldson, K., Castranova, V., Fitzpatrick, J., Ausman, K., Carter, J., Karn, B., Kreyling, W. and Lai, D. (2005) Principles for characterizing the

potential human health effects from exposure to nanomaterials: elements of a screening strategy. Particle and Fibre Toxicology 2(1), 8.

Oberdörster, G., Maynard, A., Donaldson, K., Castranova, V., Fitzpatrick, J., Ausman, K., Carter, J., Karn, B., Kreyling, W. and Lai, D. (2005) Principles for characterizing the potential human health effects from exposure to nanomaterials: elements of a screening strategy. Particle and Fibre Toxicology 2(1), 8.

Rivero, D., Pérez-Magariño, S., González-Sanjosé, M.L., Valls-Belles, V., Codoñer, P. and Muñiz, P. (2005) Inhibition of induced DNA oxidative damage by beers: Correlation with the content of polyphenols and melanoidins. Journal of Agricultural and Food Chemistry 53(9), 3637-3642.

Rivero, D., Pérez-Magariño, S., González-Sanjosé, M.L., Valls-Belles, V., Codoñer, P. and Muñiz, P. (2005) Inhibition of induced DNA oxidative damage by beers: Correlation with the content of polyphenols and melanoidins. Journal of Agricultural and Food Chemistry 53(9), 3637-3642.

Roehm, N.W., Rodgers, G.H., Hatfield, S.M. and Glasebrook, A.L. (1991) An improved colorimetric assay for cell proliferation and viability utilizing the tetrazolium salt XTT. Journal of Immunological Methods 142(2), 257-265.

Roehm, N.W., Rodgers, G.H., Hatfield, S.M. and Glasebrook, A.L. (1991) An improved colorimetric assay for cell proliferation and viability utilizing the tetrazolium salt XTT. Journal of Immunological Methods 142(2), 257-265.

Sharma, V.K., Siskova, K.M., Zboril, R. and Gardea-Torresdey, J.L. (2014) Organic-coated silver nanoparticles in biological and environmental conditions: fate, stability and toxicity. Advances in Colloid and Interface Science 204, 15-34.

Sharma, V.K., Siskova, K.M., Zboril, R. and Gardea-Torresdey, J.L. (2014) Organic-coated silver nanoparticles in biological and environmental conditions: fate, stability and toxicity. Advances in Colloid and Interface Science 204, 15-34.

Silva, S., Costa, E.M., Mendes, M., Morais, R., Calhau, C. and Pintado, M. (2016) Antimicrobial, antiadhesive and antibiofilm activity of an ethanolic, anthocyanin-rich blueberry extract purified by solid phase extraction. Journal of Applied Microbiology 121(3), 693-703.

Silva, S., Costa, E.M., Mendes, M., Morais, R., Calhau, C. and Pintado, M. (2016) Antimicrobial, antiadhesive and antibiofilm activity of an ethanolic, anthocyanin-rich

blueberry extract purified by solid phase extraction. Journal of Applied Microbiology 121(3), 693-703.

Silva, S., Costa, E.M., Vicente, S., Veiga, M., Calhau, C., Morais, R.M. and Pintado, M.E. (2017) DNA agarose gel electrophoresis for antioxidant analysis: Development of a quantitative approach for phenolic extracts. Food chemistry 233, 45-51.

Silva, S., Costa, E.M., Vicente, S., Veiga, M., Calhau, C., Morais, R.M. and Pintado, M.E. (2017) DNA agarose gel electrophoresis for antioxidant analysis: Development of a quantitative approach for phenolic extracts. Food Chemistry 233, 45-51.

USC
UNIVERSIDADE
DE SANTIAGO
DE COMPOSTELA

8. Chapter 8

GENERAL CONCLUSIONS

The work developed in the present Thesis contributes to the application of post-treatment technologies as a promising solution to increase the removal of organic micropollutants in wastewater effluents.

On the one hand, exploring the oxidative potential of immobilized enzymes as biocatalysts approach. The second proposed technology consisted on the removal of persistent contaminants through the application of the heterogeneous Fenton. In addition, photocatalysis oxidation using iron-based nanomaterials was also validated as a promising technology in this field.

Finally, one of the main outcomes of this Thesis addressed the development of reactors under different configurations, with the aim of integrating the reaction stage with the magnetic separation stage that ensures the retention of the catalyst in the system.

The main conclusions drawn from this thesis are listed below.

ENZYME-ASSISTED OXIDATION

- Efficient covalent immobilization of two different laccases from *Myceliophthora thermophila* (*Mt*) and *Trametes versicolor* (*Tv*) and versatile peroxidase (VP) from *Bjerkandera* sp onto nano and microsupports (fsNP and fsMP).

- Immobilized laccase showed a broader pH and temperature ranges, and satisfactory stability in secondary effluents.

- The different biocatalysts were applied for the removal of two model dyes and *Mt* laccase immobilized onto fsNPs and fsMPs was selected for the removal of BPA and E1, E2 and EE2 estrogens from phosphate buffer medium and from the secondary effluent of a wastewater treatment plant with high transformation values.

- The biocatalysts were easily recovered using different configurations of enzymatic reactor.

- The enzymatic reactor coupled to the polymeric membrane was effective in the removal of the target pollutant thanks to partial adsorption and enzymatic transformation.

- The consecutive use of the biocatalyst during the removal assays did not affect their removal capacity allowing their reuse for at least ten cycles.

- The decrease of the enzymatic activity did not lead to a reduction of the removal percentage, suggesting that the initial enzyme activity could be reduced to lower the operational costs.

- Ezymatic reactor system shows a great potential for the removal of water contaminants.

HETEROGENEOUS FENTON

- The central composite design selected as the Response Surface Methodology allowed to determine the optimal conditions to perform dye degradation.

- The influence of the main operational variables, such as the concentrations of mNPs and hydrogen peroxide (H_2O_2), were evaluated in order to optimize the degradation conditions of RB19.

- From the outcomes of the analysis of RB19 decolorization, it was proven that nanocatalyst stabilization plays a crucial role.

- Selected Fe_3O_4@PAA mNPs as optimal nanocatalysts, exhibit good structural stability and can be easily separated by a magnetic field.

- The immobilization of the mNPs onto a mesoporous silica matrix confers the nanocatalyst excellent properties as Fenton-like catalyst.

- High efficiency have been achieved in the removal of organic microcontaminants through the recovery and complete reuse of nanocatalysts.

PHOTOCATALYSIS OXIDATION

- Two different nanostructured photoactive materials based on hybrid NCs, Fe_3O_4/ZnO and Fe_3O_4/TiO_2, have been prepared and evaluated for wastewater treatment applications.

- Degradation experiments were performed with the aim of explore its photocatalytic activity for the removal of a variety of water pollutants.

- Results have demonstrated the feasibility of these mNCs as photocatalysts for water treatment in the presence of UV-light.

- Results also suggest that various operating parameters such as type of photocatalyst and contaminant, among other parameters, may influence the photocatalytic oxidation process.

- Immobilization of the selected semiconductor materials on magnetic solid supports reduces catalyst activity and decreases microcontaminant removal performance.

- The optimization of these conditions is crucial from the perspective of efficient design and application of heterogeneous photocatalysis processes.

- Removal experiments were carried out by reusing the photocatalyst during ten oxidation cycles

OPERATION OF DIFFERENT CONFIGURATIONS OF CATALYSIS REACTORS

- A comparison between different magnetic reactors was provided, focusing on the development of effective magnetic separation units to solve the problem of magnetic nanocatalyst retention.

- Magnets array is a key parameter to increase magnetic retention in the mangetic separation unit.

- Permanently aligned and coupled with alternating polarity magnets present a magnetic field capable of perform almost complete catalysts recovery.

- Internal separation device, which consists of a pneumatic cylinder with a magnetic bar inside the reactor, was selected as the optimal configuration.

- Almost complete retention of the employed magnetic nanocatalysts was achieve during the operation of the magnetic reactor coupled with the internal magnetic unit.

- Oxidation assays were carried out by applying heterogeneous Fenton and photocatalysis as AOPs, through the operation of this internal magnetic separation system coupled to an SBR, demonstrating also the feasibility of reusing the selected catalysts for the treatment of highly compounds present in real water matrices.

OPERATION OF DIFFERENT CONFIGURATIONS OF CATALYSIS REACTORS

- The potential geno and cytotoxicity of nanosized magnetic iron-based oxide particles used in the treatment of contaminated effluents through chemical catalysis processes such as Fenton reaction or photocatalysis was investigated using simple methods for the quantitative evaluation of DNA degradation and human cells metabolism disorder.

- The selected magnetic nanoparticles (mNPs) were free and immobilized onto silica mesoporous SBA-15 magnetite (Fe_3O_4), silica, poly (acrylic acid) and polyethylenimine coated magnetite (Fe_3O_4@SiO_2, Fe_3O_4@PAA and Fe_3O_4@PEI) and two different magnetic nanocomposites (mNCs) with titanium dioxide (TiO_2) and zinc oxide (ZnO).

- The results obtained highlight the need to act with caution during the use and recovery of these nanomaterials manufactured on the basis of the results observed in terms of DNA oxidation and cell damage.

- This study underlines the importance of further research on the mechanisms and factors that increase toxicity to improve the use of nanomaterials and awareness of their disposal.

USC
UNIVERSIDADE
DE SANTIAGO
DE COMPOSTELA

LIST OF PUBLICATIONS

Journal publications

Gamallo, M., Fernández, L., Vázquez-Vázquez, C., Fondado, A., Mira, J., Feijoo, G. and Moreira, M.T. (2019). Development of a Novel Magnetic Reactor Based on Nanostructured Fe_3O_4@PAA as Heterogenous Fenton Catalyst. *Catalysts,* 9 (1), 18 Doi: 10.3390/catal9010018.

Gamallo, M., Moldes-Diz Y., Eibes G., Feijoo G., Lema, J.M. and Moreira, M.T. (2018). Sequential reactors for the removal of endocrine disrupting chemicals by laccase immobilized onto fumed silica microparticles. *Biocatalysis and Biotransformation*, 36 (3), 254-264. Doi: 10.1080/10242422.2017.1316489.

Fernández, L., Gamallo, M., González-Gómez, M. A., Vázquez-Vázquez, C., Rivas, J., Pintado, M., and Moreira, M. T. (2019). Insight into antibiotics removal: Exploring the photocatalytic performance of a Fe_3O_4/ZnO nanocomposite in a novel magnetic sequential batch reactor. *Journal of environmental management*, *237*, 595-608.

Moldes-Diz, Y., Gamallo, M., Eibes, G., Vargas-Osorio, Z., Vazquez-Vazquez, C., Feijoo, G., Lema, J. M. and Moreira, M. T. (2018). Development of a superparamagnetic laccase nanobiocatalyst for the enzymatic biotransformation of xenobiotics. *Journal of Environmental Engineering*, 144 (3), 04018007.

Book chapters

Gamallo, M., Fernández, L., Feijoo, G. and Moreira, M. T. (2020). Nano-based technologies for environmental soil remediation. In Nanomaterials for Sustainable Energy and Environmental Remediation, 307-331. Elsevier.

Gamallo, M., Moldes-Diz, Y., Taboada-Puig, R., Lema, J.M., Feijoo, G. and Moreira, M.T. (2018). Chapter 6: Textile wastewater treatment by advanced oxidation processes: a comparison study. *Life-cycle Assessment of Wastewater Treatment*, Editor: Mu Naushad**.** Vol 1, 93-116.

Patent

Gamallo, M., Moldes-Diz, Y., Eibes, G., Vázquez-Vázquez, C., Fondado, A., Mira, J., Lema, J.M., Feijoo, G. and Moreira, M.T. Procedimiento y sistema de eliminación de microcontaminantes mediante reactor con nanopartículas magnéticas y unidad de separación externa. ES 2670712B2.

Conference proceedings

Oral contributions

Gamallo, M., Fernández, L., Vázquez-Vázquez, C., Feijoo, G., Moreira, M.T. Oxidación avanzada basada en procesos Fenton para la eliminación de contaminantes presentes en agua. I Simposio Novedar: Presencia y eliminación de microcontaminantes en agua (Santiago de Compostela, Spain; 2019).

Gamallo, M., Fernández, L., Vázquez-Vázquez, C., Feijoo, G. and Moreira, M.T. Magnetic Fe_3O_4 nanoparticles stabilized with poly(acrylic acid) as heterogeneous-Fenton catalyst for water decolorization. International Conference on Nanotechnology based Innovative Applications for the Environment, NINE (Naples, Italy; 2019)

Gamallo, M., Silva, S., Pintado, M.E., Feijoo, G., M.T. Moreira. Genotoxicity analysis of different magnetite-based nanoparticles applied in chemical catalysis processes. 13th International Chemical and Biological Engineering Conference, CHEMPOR (Aveiro, Portugal; 2018).

Gamallo, M., Vázquez-Vázquez, C., Lema, J.M., Feijoo, G. and Moreira, M.T. Benchmarking of different magnetic nanoparticles as nano-sized Fenton catalysts. Ecotechnologies for Wastewater Treatment, EcoSTP 2018 (London, Canada).

Gamallo, M., Moldes-Diz Y., Fernández, L., Fondado, A., Mira, J., Lopez-Quintela, M.A., Vázquez-Vázquez, C., Lema, J.M., Feijoo, G. and Moreira, M.T. Evaluating innovative advanced oxidation systems based on chemical and biochemical nanoparticles aiming at removal of dyes and endocrine disrupting chemicals. Comunicación oral. II Simposio Investigación en Tecnologías Ambientales (Santiago de Compostela, Spain; 2018).

Poster contributions

Gamallo, M., Moldes-Diz Y., Eibes G., Feijoo G., Lema, J.M., Moreira, M.T. Enzyme immobilized onto Magnetized and non-Magnetized Microparticles as

biocatalysts for the removal of anionic and cationic model dyes. II Jornadas Españolas de Biocatálisis, JEB (Oviedo, Spain; 2018).

Gamallo, M., Moldes-Diz Y., Eibes G., Feijoo G., Lema, J.M., Moreira, M.T. Heterogeneous Fenton catalytic removal of Reactive Blue 19 based on the potentiality of magnetite nanoparticles. 10th World Congress of Chemical Engineering (Barcelona, Spain; 2017).

Gamallo, M., Moldes-Diz Y., Eibes G., Lema, J.M., Feijoo G., Moreira, M.T. Envisaging the potentiality of enzyme immobilized on micro and nanoparticles for the removal of endocrine disruptor compounds. 1st International Conference Bioresource Technology for Bioenergy, Bioproducts & Environmental Sustainability Biorestec (Sitges, Spain; 2016).

USC
UNIVERSIDADE
DE SANTIAGO
DE COMPOSTELA

ACKNOWLEDGEMENTS

This research was supported by two projects: Chemical and biochemical catalysis reactors ruled by nanosize Metal OxiDes, Enzyme Nanoparticles and Atomic Clusters applied for the removal of emerging contaminants (MODENA), Project CTQ2016-79461-R granted by Spanish Ministry of Science and Innovation and HP-NANOBIO project, PID2019-111163RB-100.

I would like to thank my thesis directors Maite and Sindo for giving me the opportunity to carry out this thesis and for their kind support all these years.